

Harmonic Resonances in Nonlinear Josephson Junction Circuits: Experimental and Analytical Studies

by

Amy Elizabeth Duwel

Submitted to the Department of Electrical Engineering and
Computer Science

in partial fulfillment of the requirements for the degree of

Doctor of Philosophy in Electrical Engineering

at the

MASSACHUSETTS INSTITUTE OF TECHNOLOGY

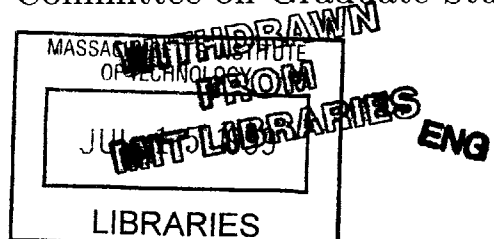
May 1999
[June 1999]

© Massachusetts Institute of Technology 1999. All rights reserved.

Author
Department of Electrical Engineering and Computer Science
May 17, 1999

Certified by
T. P. Orlando
Professor
Thesis Supervisor

Accepted by
Arthur C. Smith
Chairman, Department Committee on Graduate Students



Harmonic Resonances in Nonlinear Josephson Junction Circuits: Experimental and Analytical Studies

Amy Elizabeth Duwel

Submitted to the Department of Electrical Engineering and Computer Science
on May 17, 1999, in partial fulfillment of the requirements for the degree of
Doctor of Philosophy in Electrical Engineering

Abstract

This thesis presents a study of resonance dynamics in circuits of superconducting Josephson junctions. The Josephson junction is an intrinsically nonlinear device which, under certain conditions, can exhibit harmonic oscillations. This research begins with the dynamics of Josephson junctions connected in parallel with either periodic (ring geometry) or open-ended (row geometry) boundary conditions. Previous studies of the single ring system have established the existence of periodic, quasi-periodic, and even sub-harmonic resonances in this system, while only periodic resonances have been observed in the single row systems. The measurements and analysis presented here add sub- and super-harmonic resonances to the long row systems. They also show that the collective oscillations of junctions in very long systems are only slightly perturbed by the boundaries and thus resemble the solutions of ring systems.

The dynamics of both open-ended and ring arrays become particularly rich when two such arrays are inductively coupled. For symmetrically coupled rows, the harmonic and sub-harmonic resonances split into two frequencies, corresponding to in-phase and anti-phase oscillations. This is observed in both experiments and numerical simulations. An ansatz for the phase solutions at resonance is used to derive the two natural frequencies from the coupled nonlinear equations. Inductively coupled rings can be analyzed in the same way if they have identical numbers of trapped fluxons. When this is not true, the solutions to the coupled ring system are more complex. Through DC measurements and numerical simulations, a survey of some new and unexpected dynamical states is presented. A preliminary analysis is used to discuss those features of the data which are related to resonances in the dynamical system.

Finally, a portion of this research is dedicated to obtaining useful AC power from Josephson junction circuits operating at resonance. The parallel row is first considered, along with the possibility of increasing the power by using the in-phase mode of inductively coupled rows. A new system with three junctions per cell (triangular cell) is also considered. Both single triangle-cell rows as well as large two-dimensional arrays are shown to have sharp resonance steps in DC measurements. AC power is coupled from these arrays to an on-chip detector junction, which responds by showing Shapiro steps in its DC current-voltage characteristic. The possibilities for future improvement in this design are discussed.

Thesis Supervisor: T. P. Orlando, Professor of Electrical Engineering

Acknowledgments

My education at MIT has been shaped by the many great people around me. My colleagues and advisors have become not only the people that I have learned most from academically, but also my closest friends. I am grateful to have known and learned from such a wonderful group of people.

My advisor, Professor Terry Orlando, has done his job with a thoughtfulness and sincerity that I will always appreciate. I am so thankful for the encouragement that I have received. Terry's concern for my academic confidence improved everything that I did. He has also given me every opportunity available, with attention to my education as well as my personal and academic growth. My advisor deserves the most credit for making MIT a wonderful learning and growing and happy experience for me.

I am honored to have learned from Professor Steven Strogatz, who in addition to being one of the great leaders in his field, is a fantastic teacher. I thank Steve for guiding my research and helping to connect it to a bigger picture. I admire Steve for advising with humility and respect for everyone and for every question. I have thoroughly enjoyed his enthusiasm, and hope to continue learning from him.

I thank my colleague and friend, Enrique Trías. He has become one of my academic heroes. Enrique has generously shared so much knowledge, insight, and perspective with me. I feel always indebted to his generous help over the years. I could not have learned so many things without him. As friends, we have shared many experiences together during these years. I will enjoy the photos of those great trips after conferences and especially Europe. Thank you Enrique, again.

To Professor Shinya Watanabe, my other intellectual hero and friend, I owe so many thanks. Working together has been completely enjoyable and productive. I feel lucky to have someone so patient and incredibly intelligent to work with. I admire the energy and the sincerity he puts into his job and his life. I am inspired by, and thoroughly happy to know Shinya, and I thank him for all that he has taught me.

Dr. Herre van der Zant has been my unofficial second advisor, even after leaving

MIT. I thank Herre for all of the care that he put into teaching me and helping me to begin here. I based my work on his, and continue to learn from him. Herre made so many things possible for me, and was still such a warm, funny, and truly caring person to know. I am grateful to have had such a talented and motivated scientist sharing his work and his friendship with me.

I thank Steve Patterson, who is not an official member of our group, but whose contributions to my work and my life here have been valuable. Steve is that person around who knows everything that we are supposed to know, and is happy to share it with his colleagues. Steve has been there for me with many answers, for all of the last-minute panics, and as a great friend.

I would also like to thank Professor Millie Dresselhaus and Professor Hans Mooij for serving on my committee. I am truly honored to have such great scientists to read my thesis and help me to improve it. I thank them for all of the advice and encouragement.

I thank the members of my group, who have made this a learning environment as well as a warm and caring atmosphere. Thank you to Juanjo Mazo, for answering so many little questions and for bringing such sincerity and a sense of humor to our hallway. Thank you to Lin Tian for patiently teaching us and contributing so much. Thank you to Donald Crankshaw for all of the extra favors and the hard work. Thank you to David Carter, who I so often looked to for advice. Thank you also to Mark Schweitzer, who I still miss as my office-mate.

I thank two special members of our group, Pieter Heij and Sebastiaan Várdy of Delft. I loved working with such fun and motivated people. Pieter and Sebastiaan both worked so hard and brought out the best in all of us. I also thank John Weisenfeld and Steven Yeung of Cornell University for a great collaboration. Their talents and enjoyable personalities came through and helped our project immensely.

I have enjoyed a close collaboration with Dr. Stan Yukon and Dr. Nathaniel Lin. Thank you to Stan for the patience, creativity, and incredible intelligence shared with me. Thank you to Nathaniel for the hard work and attentiveness while teaching me. The collaboration with Dr. Pasquilina Caputo has been productive and enjoyable

as well. Thank you to Lilli for being such a great friend and colleague. Thank you to Professor Alexey Ustinov for sharing his knowledge with me and being such a thoughtful host.

I thank my collaborators at University of Maryland, Professor Chris Lobb, Dr. Paola Barbara, and especially Dr. Fred Cawthorne. Their generous and collaborative attitudes toward scientific research are what make progress possible. I have learned more from them in small conversations than hours in a journal could provide.

I thank HYPRES for help to me well beyond any business protocol might demand. John Coughlin, Masoud Radpavar, and Oleg Mukhanov have been especially helpful.

I have made many friends at MIT whose support and encouragement helped me to succeed. Thank you to Olga Arnold, Emily Warlick, Rich Perelli, and Angela Mickunus. I also thank my friends who helped me to relax outside of MIT. Thank you to Tu-anh Phan, Sarah Spratt, Natasha Baihly, and Hua Yang. I especially thank Danielle Demko and Aman Garcha, who have always been there for me.

I thank my all of my family for their love and support. I am especially grateful to my mother, Grace Lehua Gustin, who has been there for me since the first step. I also thank my grandfather, Loren Forrester, who helped me to chose this step.

My most special thanks and dedication are to Carl Pallais. For all of my years at MIT, and for the many years to come, I thank Carl. During my hard work, I needed the healthy perspective that Carl has helped me to keep. I have remembered how lucky I am to be here at MIT. I will always feel fortunate that I was able to share it with Carl, and that I have the love and friendship of such a great person.

The author wishes to thank MIT and the Cronin Fund Fellowship for support, as well as the GE Fellowship for the Future and the NSF Fellowship program. This research was also supported by grant DMR-9610042.

Contents

1	Introduction	9
2	Background	12
2.1	The Josephson Junction	12
2.2	Coupled Josephson Junctions	18
3	Single Rings and Rows	24
3.1	Resonant States	24
3.1.1	Simulations: Single Rings	25
3.1.2	Experiments: Single Rings	34
3.1.3	Experiments: Single Rows	39
3.2	Analysis	42
3.2.1	Modal equations for single rings	43
3.2.2	Energy balance for single rings	48
3.3	Rings Experiments: Negative Differential Resistance	54
3.4	Summary of Results for Single Rings and Rows	61
4	Coupled Rings and Rows	64
4.1	System and governing equations	64
4.2	Coupled Rows: Data and Simulations	68
4.3	Analysis for in-phase and anti-phase solutions	78
4.4	Coupled Rings: Data and Simulations of non-voltage locked states . .	82
4.5	Analysis for Resonances in Coupled Rings	97

4.5.1	Coupled Rings with $M_1 = M_2$	101
4.5.2	Coupled Rings with $M_1 \neq M_2$	103
4.5.3	Energy balance for coupled rings	109
4.6	Summary of the results on Coupled Systems	113
5	Josephson Junction Arrays as Oscillators	115
5.1	Underdamped Parallel Arrays	118
5.1.1	Simulations and phase solutions	118
5.1.2	Analysis of super-harmonics	122
5.1.3	Power at resonances	130
5.2	Triangular Arrays	132
5.2.1	DC Measurements	132
5.2.2	AC Measurements: on-chip and off-chip	136
5.3	Conclusions	144
6	Future Work	145
A	Experimental Parameters	148
B	Modal Expansion of Sine Terms	150
C	Superharmonic Resonances from Modal Equations	154
D	Publications and Conference Proceedings	156
E	Selected Reprints	158

List of Figures

2-1	Schematic of SIS Josephson junction	12
2-2	RSJ model of a junction	14
2-3	Single pendulum	16
2-4	Chain of coupled pendula	19
2-5	Open-ended array of Josephson junctions	19
2-6	Ring array of Josephson junctions	22
2-7	Ring of coupled pendula	23
3-1	Simulated IV for $N = 8$ ring	26
3-2	Simulated phase of junction versus time for Eck step	28
3-3	Simulated voltages of junctions versus time for Eck step	29
3-4	Simulated IV curve for $N = 8$ ring with $M = 1$	32
3-5	Simulated junction phase versus time on a substructure	33
3-6	Simulated junction phase versus time on an HV step	33
3-7	Schematic of $N = 8$ ring array	34
3-8	Experimental IV of $N = 8$ ring with $M = 1$	36
3-9	Experimental IV of $N = 8$ ring with $M = 0, 1, 2, 3, 4$	37
3-10	Experimental dispersion relation for $N = 8$ ring	38
3-11	Experimental IV curve of $N = 54$ junction row	39
3-12	Step voltages versus frustration for $N = 54$ junction row	40
3-13	Symbolic representation of modal coupling	47
3-14	Schematic of two junctions in a discrete ring system	48
3-15	Power balance constraint for two modes in a single ring	52

3-16	Power balance constraint for two modes plotted with resonance curve	53
3-17	Experimental IV for $N = 8$ ring with $M = 3$, showing negative differential resistance	54
3-18	IV curve showing hysteresis of negative differential resistance feature	55
3-19	Voltage of negative differential resistance feature versus temperature .	57
3-20	Slope of negative differential resistance feature versus temperature . .	58
3-21	IV curves of $N = 8$ ring with $M = 4$ showing negative differential resistance feature	59
3-22	Summary of resonant states in single rings	62
4-1	Schematic of inductively coupled rings	65
4-2	Schematic of inductively coupled rows	66
4-3	Experimental IV of $N = 54 \times 2$ row system	68
4-4	Step voltages versus frustration for $N = 54 \times 2$ coupled rows	69
4-5	Simulated IV curve for $N = 54 \times 2$ coupled rows	72
4-6	Simulated phase solutions versus time on Eck step of $N = 54 \times 2$ coupled rows	76
4-7	Simulated phase solutions versus j on Eck step of $N = 54 \times 2$ coupled rows	77
4-8	Simulated voltages of Eck steps versus frustration for $N = 54 \times 2$ coupled rows	81
4-9	Experimental IV for coupled rings with $N = 4$	84
4-10	Simulated IV for coupled rings with $N = 4$	85
4-11	Simulated voltage versus time for coupled rings on non-voltage locked state	87
4-12	FFTs of coupled ring solutions	89
4-13	FFTs showing relative phases of coupled ring solutions	90
4-14	Phase portraits showing relative phases of coupled ring solutions . . .	91
4-15	Measured IV curve of $N = 4$ coupled rings	93
4-16	Simulated IV for coupled rings with $N = 51$	94

4-17	Space-time plot of kink/ anti-kink motion for coupled rings with $N = 54$	96
4-18	Step voltages of coupled rings versus theory	108
4-19	Power balance constraint for coupled rings	112
5-1	Simulated IV for $N = 54$ junction array	119
5-2	Phase versus time on substructures in $N = 54$ junction array	120
5-3	FFT of phase solutions on substructures in $N = 54$ junction array	121
5-4	Amplitudes of $m = 1$ and $m = 2$ steps in $N = 54$ junction array, versus frustration	128
5-5	Single triangular cell	132
5-6	Schematic of triangular row	133
5-7	Measured IV curves of single triangular cell and of triangle row	134
5-8	Step voltage versus field for triangular row	135
5-9	Triangular array coupled to detector junction	136
5-10	IV curves of detector junction showing Shapiro steps	138
5-11	IV curve of triangular array showing bandwidth for radiation	140
5-12	Schematic of triangular array coupled to finline antenna	142
5-13	Measurement of triangular array power	143
A-1	Measurement of $N = 8$ ring showing gap voltage	149

List of Tables

- 2.1 PENDULUM ANALOG OF JOSEPHSON JUNCTION 17
- 3.1 PARAMETERS FOR M=3 NEGATIVE RESISTANCE DATA 60
- 3.2 PARAMETERS FOR M=4 NEGATIVE RESISTANCE DATA 60
- 5.1 JOSEPHSON JUNCTION OSCILLATORS 117

Chapter 1

Introduction

The Josephson junction is a nonlinear electronic oscillator and constitutes the basic element of superconducting circuits. As such, networks of superconducting Josephson junctions are of interest as possible high frequency oscillator sources as well as model systems for the study of coupling between nonlinear oscillators. In this research, we will consider a few related network configurations from both of these perspectives.

Most of this work is concerned with the dynamics of Josephson oscillators connected electrically in parallel and biased by a constant DC current. This system is an ideal experimental realization of the discrete sine-Gordon equation. The discrete sine-Gordon equation has been used to model dislocations [1], magnetic and ferromagnetic domain walls [2], and chains of coupled pendula [3, 4]. The coupling of nonlinear oscillators in general is important to many other fields, including biologists who study the dynamics of collective ion channel gating [5] or the synchronous neuronal activity associated with seizures [6], as well as microwave circuit designers who require phase-locking between arrays of Gunn diodes [7].

A particularly fascinating and useful aspect of discrete sine-Gordon systems is the fact that traveling wave solutions dominate the dynamics. In certain parameter regimes, localized solitary waves called solitons can travel through the arrays, relatively unscathed by damping effects or even by collisions with other solitons. For other ranges of parameter space, uniform traveling waves are excited with only a DC input. The majority of this research focuses on the regime where uniform traveling

waves are excited, although the soliton regime is also explored. In our junction arrays, the traveling waves appear at particular resonance frequencies, which have been predicted analytically [8, 9]. As a starting point, we confirm some previous studies in systems with periodic boundaries (rings) as well as long open-ended rows. Both experiments and numerical simulations are used to characterize the solutions which are compared with previous work [8, 10, 11]. Experimentally, we find new resonances in the rows and develop an analysis to predict these resonant frequencies. Experiments also show a unique new structure in the data from rings, which is characterized and discussed. Finally, we present a spatial modal analysis with which several different periodic and quasi-periodic solutions to these systems can be considered. This analysis is well-connected to the previous work, and the combination enables very complete description of the traveling wave solutions in the sine-Gordon system.

The analysis is next extended to include two symmetrically coupled discrete sine-Gordon systems. No previous experimental or analytical results were available for this system, although the continuous counterpart has been the subject of several studies [12, 13, 14, 15]. In our discrete system, measurements show a splitting of the original resonance frequencies. Numerically we observe that these two resonances correspond to the in-phase and anti-phase states which can be expected from symmetrically coupled oscillators. In addition, we observe phase-locked states even while the systems exhibit quasi-periodic oscillations. We view these coupled arrays as a model system for studying the spatiotemporal dynamics of coupled oscillators.

One very good reason to focus on the traveling wave solutions is their desirability in practical applications of the Josephson system. The final chapter of this thesis introduces the possibility for using phase-locked arrays of Josephson junctions as high-frequency oscillator sources. Long Josephson junctions are already in use as detectors and mixers of the THz frequency radiation from astronomical sources. In addition, the communications industry and electronic warfare technology increasingly demand high frequency solid state systems. However, for frequencies above 400 GHz, semiconductor sources generate power levels of less than 1 mW [7, 17] and are not tunable. Tunable oscillators in this frequency range can be made from Josephson

junction arrays, which are theoretically capable of mW power levels [18]. To date, measurements of Josephson oscillators yield power levels of 0.85 mW at 240 GHz [19]. Although solid-state sources generally offer lower power levels than many applications requirements, the advantages of compactness and integrability motivate continued research.

We apply the analytical expressions developed in previous chapters to the problem of how much AC power can be obtained from our devices, and how to improve this maximum. We explore a new configuration which may be more suited to the oscillator application, and discuss the mode of operation. Finally, we measure both the DC and AC properties of a Josephson oscillator and assess its performance.

Chapter 2

Background

2.1 The Josephson Junction

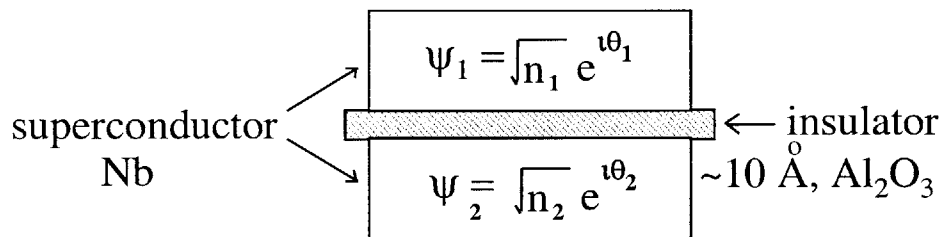


Figure 2-1: Schematic of an SIS Josephson junction.

Superconducting Josephson junctions are based on the tunneling of superelectrons (Cooper pairs) through an insulating barrier. Low temperature SIS (superconductor-insulator-superconductor) junctions can now be fabricated commercially. The geometry of a typical device is shown in Fig. 2-1. Our junctions are made at HYPRES [20] and use Nb-AlO_x-Nb. Since niobium becomes superconducting below about 9 K, our junctions operate between 4.2 K and 9 K. In the superconductor, all of the paired electrons behave coherently and can be described by a single macroscopic wavefunc-

tion, Ψ . The magnitude of this wavefunction decays exponentially in the insulating region. However, if the insulator is thin enough, there will be some overlap of the wavefunctions from the two superconductors. Associated with this overlap is a tunneling current, as predicted by Brian Josephson in 1962. It can be shown that in the absence of any scalar or vector potentials, the density of the supercurrent J_s depends on the difference between the phases of the macroscopic wavefunctions in the two superconductors.

$$J_s = J_c \sin(\theta_1 - \theta_2) \quad (2.1)$$

where J_c is the critical current density of the junction, and it decays exponentially with the thickness of the insulator. In the presence of a magnetic field, the superconductor phase depends on the choice of magnetic gauge, \mathbf{A} . However, we can define a gauge invariant phase difference

$$\phi = \theta_1 - \theta_2 - \frac{2\pi}{\Phi_o} \int_1^2 \mathbf{A} \cdot d\mathbf{l} \quad (2.2)$$

where the integral is taken across the oxide. With this definition, the equation for the superconducting tunneling current J_s is also gauge-invariant:

$$J_s = J_c \sin(\phi). \quad (2.3)$$

With the approximation that the current and phase are uniform over the cross-section of the junction, we can derive the lumped-element current-phase relation [21]

$$I_s = I_c \sin \phi(t). \quad (2.4)$$

It can also be shown that a time-dependent phase difference results in a voltage across the junction [21]

$$\frac{d\phi}{dt} = \frac{2\pi}{\Phi_o} v. \quad (2.5)$$

The quantity $\Phi_o = h/2e = 2.07 \times 10^{-15} \text{ T}\cdot\text{m}^2$ is referred to as a flux quantum. In equation (2.4), we see that the superelectrons can carry a maximum current of I_c .

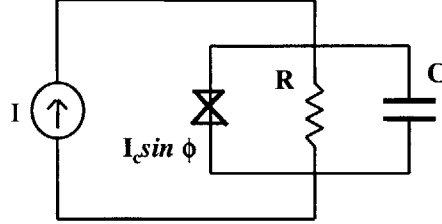


Figure 2-2: RSJ model of a junction.

When more DC current is applied to the junction, it must be carried by normal electrons, which dissipate energy. The lumped-element model for the Josephson tunneling junction includes a superelectron current path in parallel with a normal resistive path R_n . In addition, a capacitive path C must be included due to the geometry of the device. This resistively and capacitively-shunted-junction (RSCJ) model is sketched in Fig. 2-2.

Referring to Fig. 2-2, Kirchhoff's current law requires that

$$I = I_c \sin \phi + \frac{v}{R_n} + C \frac{dv}{dt}. \quad (2.6)$$

In our models of the junction, we use the normal-state resistance R_n of the junction for the RSJ resistor. However, when the junction voltage is below the superconducting gap voltage, $2\Delta/e$, (called the sub-gap region), the dynamic resistance can be quite different from R_n . A more accurate piece-wise linear model (in which the sub-gap resistance is different from R_n) is sometimes used in the literature [21]. In addition, a resistive shunt can be placed in parallel with the junction. This shunt resistance is usually smaller than the junction intrinsic resistance and allows the experimentalist to better control the damping.

We note that the supercurrent branch has the voltage-current relation of a non-

linear inductor, since

$$\frac{dI_s}{dt} = I_c \dot{\phi} \cos \phi = \left(\frac{2\pi I_c}{\Phi_o} \right) v \cos \phi. \quad (2.7)$$

For this reason, the quantity $L_J = \Phi_o/2\pi I_c$ is called the Josephson inductance.

Writing the voltage in terms of the phase difference and normalizing time, we obtain:

$$\ddot{\phi} + \Gamma \dot{\phi} + \sin \phi = I_b \quad (2.8)$$

where $\Gamma = \sqrt{L_J/(R_n^2 C)}$. We normalized the current to I_c , the voltage to $I_c R_n$, and the time to $\sqrt{L_J C}$. Alternatively, the time can be normalized to L_J/R_n , since there are two time constants in the problem. The ratio of these two time constants (squared) defines the Stewart-McCumber parameter, $\beta_c = R_n^2 C/L_J = \Gamma^{-2}$. In this form, the left-hand side of equation (2.8) represents the normalized RCSJ junction current. At times it is convenient to represent the normalized junction current on the left-hand-side of equation (2.8) as

$$\mathcal{N}[\phi] = \ddot{\phi} + \Gamma \dot{\phi} + \sin \phi \quad (2.9)$$

Equation (2.8) is the same equation which describes the motion of a single damped pendulum, drawn in Fig. 2-3. The variable ϕ gives the angle of the pendulum, the quantity Γ (or β_c) gives the degree of damping in the system, and the applied current I_b is analogous to the applied torque. Table 2.1 details the correspondence. For a pendulum with no applied torque but with an initial angle, the nature of pendulum's subsequent motion in time depends strongly on the damping. For $\Gamma > 1$ which is $\beta_c < 1$ (overdamped), the angle is a smoothly decaying exponential. For $\Gamma < 1$ (underdamped), the response is an oscillation in time with a slowly decaying amplitude. When $\Gamma = 1$ the pendulum is critically damped and the angle also decays exponentially. When an AC force is applied to the pendulum, the response is a combination of the homogeneous solution described above and the particular solution, which follows the drive. It is the amplitude of oscillations in the particular solution which are usually of interest, since the homogeneous solution decays exponentially in time. This amplitude also depends strongly on the damping. In mechanics, the degree of

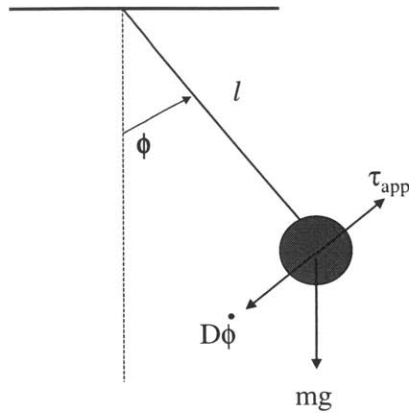


Figure 2-3: A single pendulum, which is a mechanical analog for the superconducting Josephson junction. The external forces include an applied torque, a gravitational restoring force, and damping, which may result from motion in a viscous medium.

damping is usually described in terms of a quality factor, Q . This is related to the Stewart-McCumber parameter by $Q^2 = \beta_c$.

Table 2.1: PENDULUM ANALOG OF JOSEPHSON JUNCTION

Junction	Pendulum
$C\ddot{\phi} = (2\pi/\Phi_o)I - \dot{\phi}/R - (2\pi/\Phi_o)I_c \sin \phi$	$ml^2\ddot{\phi} = \tau_{\text{app}} - D\dot{\phi} - mgl \sin \phi$
applied current, I capacitance, C resistance, R Josephson current, $\sin \phi$	applied torque, τ_{app} mass, m viscous damping, D gravitational force, $\sin \phi$
Normalized Equations $\ddot{\phi} + \Gamma\dot{\phi} + \sin \phi = I_b$	

2.2 Coupled Josephson Junctions

To introduce coupled Josephson junctions, we first consider the coupled pendulum chain of Fig. 2-4, since this system is slightly easier to visualize. This analog for coupled Josephson junctions was suggested by [4] and is discussed in more detail in [22]. The pendula in Fig. 2-4 are coupled by torsional springs and rotate in the y-z plane. If the two ends of a torsional spring are twisted with respect to each other, then the spring will exert a restoring force proportional to the twist: $F = -k\Delta\phi$. For example, if an extra torque is applied only to pendulum j , trying to turn it over, then the springs tend to pull it back in line with its neighbors. This nearest-neighbor coupling is added into the force-balance equation for the pendulum

$$ml^2\ddot{\phi} + D\dot{\phi} + mgl \sin \phi - \tau_{\text{app}} = \kappa(\phi_{j+1} + \phi_{j-1} - 2\phi_j). \quad (2.10)$$

The ends of the chain can be fixed with a non-zero twist between them. If the springs are very strong, the the twist applied to the ends will distribute evenly throughout the chain. If the springs are weak, then the twist applied to the ends affects only a few pendula near the boundaries (in the static solution). The dynamics in these two regimes can be quite different and interesting, as we will see.

Josephson junctions can be similarly coupled to each other through a circuit. The junctions are connected in parallel, as in Fig. 2-5. A constant magnetic field is applied and flux threads the loops of the array. However, the phase of the macroscopic wavefunction in the superconducting wires depends on this magnetic vector potential through the supercurrent equation [21]. When the superconductor phases are integrated around the closed loop of a single cell, the relationship simplifies to [21]

$$\phi_{j+1} - \phi_j = \frac{2\pi\Phi_j}{\Phi_o} + 2\pi n. \quad (2.11)$$

Thus the magnetic flux threading a loop Φ_j couples the gauge-invariant phases of the junctions. If the phases ϕ_{j+1} and ϕ_j are different by exactly 2π , then the flux in the cell is Φ_o . This quantized unit is often called a fluxon or a vortex. The presence

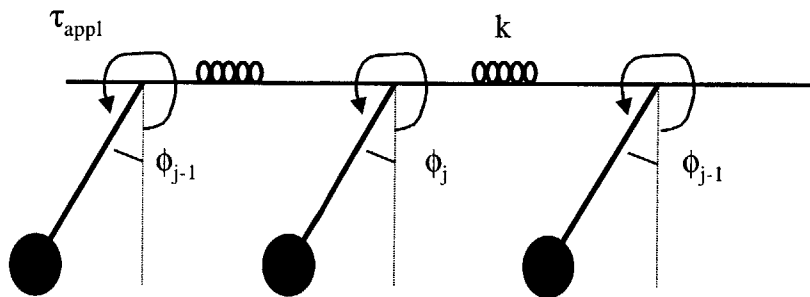


Figure 2-4: Chain of coupled pendula.

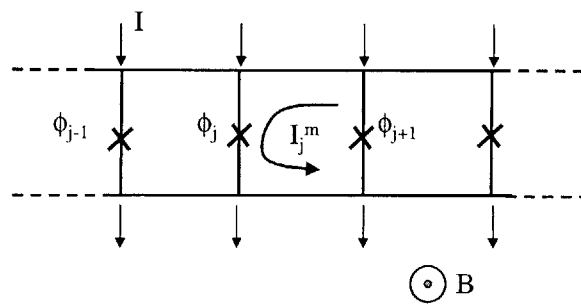


Figure 2-5: An open-ended row of identical Josephson junctions. The junctions are indexed by j , and the phase difference across junction j is ϕ_j . Magnetic field is applied into the page.

of a single vortex in a cell of the array is analogous to having a 2π twist between adjacent pendula in the linear chain. The term $2\pi n$ (n is an integer) in equation (2.11) arises from the fact that the phases are circular variables and differences of $2\pi n$ are physically indistinguishable. We will neglect this term in our circuit equations.

The total flux threading any loop (Φ_j^m) must also be equal to the sum of the applied external flux (Φ_{app}) and any induced flux. The induced flux in loop j is either due to its own mesh (circulating) current I_j^m and self-inductance $L_{j,j}$, or to the mesh current and mutual inductance with a neighboring cell. Including all mutual inductances, then, we write the flux in loop j as:

$$\Phi_j^m = \Phi_{app} + \sum_{i \in \langle N \rangle} L_{i,j} I_i^m. \quad (2.12)$$

The sum is over all N junctions. In analytical calculations, we sometimes include only self-inductances and write $L_{j,j} = L_s$. When possible, nearest neighbor inductances are also included as $L_{j,j\pm 1}/L_s = -M_h$, so that $M_h > 0$.

Finally, applying Kirchoff's current law at the node above junction j gives:

$$\mathcal{N}[\phi_j] - I_b = \frac{1}{I_c} (I_j^m - I_{j-1}^m) \quad (2.13)$$

where $\mathcal{N}[\phi_j] = \ddot{\phi}_j + \Gamma \dot{\phi}_j + \sin \phi_j$ is the normalized junction current defined in (2.9).

¹ The differences of mesh currents can be written in terms of phases using equations (2.12) and (2.11). If we include only self-inductances, then we can write

$$\frac{1}{I_c} (I_j^m - I_{j-1}^m) = \frac{1}{L_s I_c} (\Phi_j - \Phi_{j-1}) = \frac{\Phi_o}{2\pi I_c L_s} (\phi_{j+1} - 2\phi_j + \phi_{j-1}) = \Lambda_j^2 \nabla^2 \phi_j \quad (2.14)$$

¹Note that the *difference* of mesh currents on the right side of equation (2.13) is well defined. However the mesh current of an *individual* cell will not have a physical meaning unless some reference mesh is set equal to zero. This situation is more familiar in the context of voltages, and it is just the same. We must chose a reference point, in this case a reference mesh, and the other mesh currents are well defined with respect to this reference. In our open-ended network, we expect that for the last (boundary) cell of the array, the mesh current in this cell is equal to the branch current through the last junction. The natural reference mesh current, then, is the mesh of an imaginary cell neighboring the real end cell of the array. It is this mesh current which we set equal to zero. For ring arrays with periodic boundary conditions, the mesh current on the inner superconducting ring will be assumed to be zero.

where ∇^2 is the discrete Laplacian operator and $\Lambda_j^2 = L_j/L_s$. Combining these two equations we can write the equation of motion for the phase of junction j as

$$\ddot{\phi}_j + \Gamma \dot{\phi}_j + \sin \phi_j = \Lambda_j^2 \nabla^2 \phi_j + I_b. \quad (2.15)$$

At the boundaries of the open-ended system, the mesh current is equal to the sum of the junction current and the bias current I_b , and equation (2.15) will be slightly different. In order to write the same equation for every junction, j , we can invent dummy junctions $j = 0$ and $j = N + 1$ and define the boundary conditions to be

$$\phi_0 = \phi_1 - 2\pi f \quad \text{and} \quad \phi_{N+1} = \phi_N + 2\pi f \quad (2.16)$$

The parameter $f = \Phi_{app}/\Phi_o$ is called the frustration of the system.

Equation (2.15) is exactly analogous to the equation (2.10) for the chain of coupled pendula. The parameter Λ_j^2 plays the role of the spring constant coupling the pendula. The size of Λ_j^2 determines the influence of the neighboring junctions $\phi_{j\pm 1}$ on ϕ_j . When Λ_j^2 is small, static solutions show that the magnetic field penetrates only a few cells into the array [23] (depending on the strength of the field as well). This is analogous to the case of a weak spring in the chain of pendula. A strong spring corresponds to a large Λ_j^2 . For this reason, the parameter Λ_j^2 is called the penetration depth or the discreteness parameter.

In contrast, the ring system has the following boundary conditions

$$\phi_{j+N} = \phi_j + 2\pi M \quad (2.17)$$

where M is any integer. Although junctions ϕ_j and ϕ_{j+N} are physically the same, the phase variable is circular and only physically defined modulo 2π . This boundary condition expresses the possibility that magnetic flux is trapped in the superconducting ring. The sum of the flux in every cell gives the total trapped flux in the ring

$$\sum_{j=\langle N \rangle} \Phi_j = \phi_{N+1} - \phi_1 = 2\pi M \quad (2.18)$$

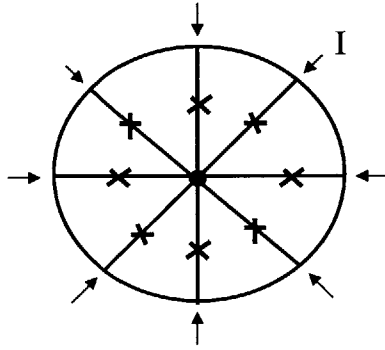


Figure 2-6: A ring of identical Josephson junctions. DC current is injected at the nodes indicated by arrows, and is extracted from the center node.

and this flux must be quantized. M is the number of flux quanta. Comparing with the open-ended system, we see that this restricts the frustration to $f = M/N$.

To visualize the trapped quantized flux in a ring, the pendulum analogy is again helpful. The coupling between junctions is mechanically modeled by torsional springs. When one pendulum is overturned, the neighboring pendula exert a restoring force through the torsional springs. If the boundaries are closed after a pendulum is overturned, then a “kink” is trapped in the system. If the springs are weak (small Λ_j^2), the kink stays localized around one pendulum. If the springs are strong (large Λ_j^2), the kink spreads out over many pendula. Figure 2-7 depicts a coupled pendulum ring with one trapped kink.

Since the system is discrete, its properties are periodic with period $f = 1$ ($M = N$). This property is easily understood by considering the pendulum ring. If all N pendula are overturned before closing the boundaries, the system is exactly the same as if no pendula had been overturned. Likewise, overturning only one pendulum produces the same physical system as overturning $N + 1$ pendula.

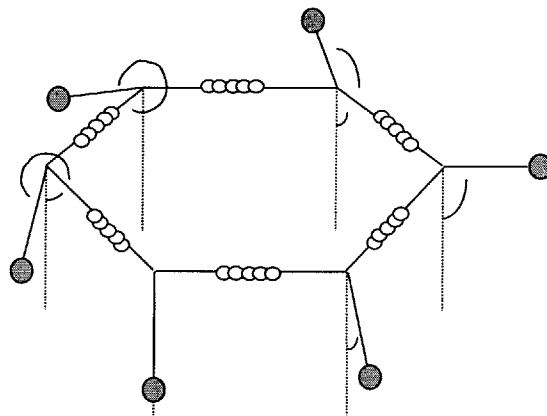


Figure 2-7: Mechanical analog of Josephson ring: a ring of pendula coupled by torsional springs. A single kink is trapped in this ring.

Chapter 3

Single Rings and Rows

In this chapter we will use numerical simulations and experimental measurements to introduce single rings and open-ended rows of Josephson junctions. Some typical dynamical states will be reviewed in Section 3.1. New results on single rows are presented in Section 3.1.3. Section 3.2 describes two new analytical approaches for resonances in single rings. In Section 3.3, we present some recent measurements on single rings which show a fascinating negative differential resistance. Finally, Section 3.4 is a summary of the chapter.

3.1 Resonant States

The discrete sine-Gordon equation is physically realized by the ring of Josephson junctions connected in parallel, as shown in Fig. 2-6. The dynamics of this system have been studied extensively both experimentally [8, 10, 11] and analytically [9, 11, 26]. Those results provide a strong background and an important starting point for this research. Therefore, some of those results will be reviewed through examples in this section. Numerical simulations will be used so that the dynamical solutions can be discussed in detail. The current versus voltage (IV) characteristics of single rings are also measured experimentally. Example IV characteristics of single row arrays are also presented and compared with ring results. We find a new resonance feature in row arrays, which we characterize and discuss.

3.1.1 Simulations: Single Rings

The governing equations which model our arrays were derived by applying Kirchhoff's current laws and using the RSCJ model for the current through a single junction. We normalize the current to I_c , the voltage to $I_c R_n$, and time to $\sqrt{L_J C}$ (inverse plasma frequency). The equations are given in terms of the gauge-invariant phase differences across the junctions, ϕ_j , where $j = 1, \dots, N$ indexes the junction's position. For simplicity we neglect all the cell inductances except the self-inductance, which results in the damped, driven, discrete sine-Gordon model, equation (2.15):

$$\ddot{\phi}_j + \Gamma \dot{\phi}_j + \sin \phi_j = I_b + \Lambda_J^2 (\phi_{j+1} - 2\phi_j + \phi_{j-1}) \quad (3.1)$$

for $j = 1, \dots, N$ and $\Gamma = \beta_c^{-1/2}$. Our numerical code can include longer range inductances as necessary, up to the full inductance matrix [30]. However, our analysis in the next sections use mainly (3.1). Simulating the same equations allows us to make a direct comparison with our analysis. The simpler system not only illuminates the essential mechanism responsible for the observed steps but also reproduces the measurements reasonably well, as we will show.

With only self-inductance, the boundary conditions for the ring are

$$\phi_{j+N}(t) = \phi_j(t) + 2\pi M \quad (3.2)$$

for all t where M is an integer. The fourth-order Runge-Kutta scheme with a time-step $\Delta t = 1$ is used for integrating the system. The instantaneous voltage at junction j is simply proportional to the rate of the change of ϕ_j , and is given in our normalization by

$$V/I_c R_n = \Gamma d\phi_j/dt. \quad (3.3)$$

With (3.1–3.3), current-voltage characteristics are numerically obtained at various M values using the parameters Λ_J and Γ from our experiments. Figure 3-1 shows the results for $M = 2$ and $N = 8$. The parameters are $\Lambda_J^2 = 4.29$ and $\Gamma = 0.088$ ($\beta_c = 162$). For an array with $N = 8$ Josephson junctions, this parameter regime

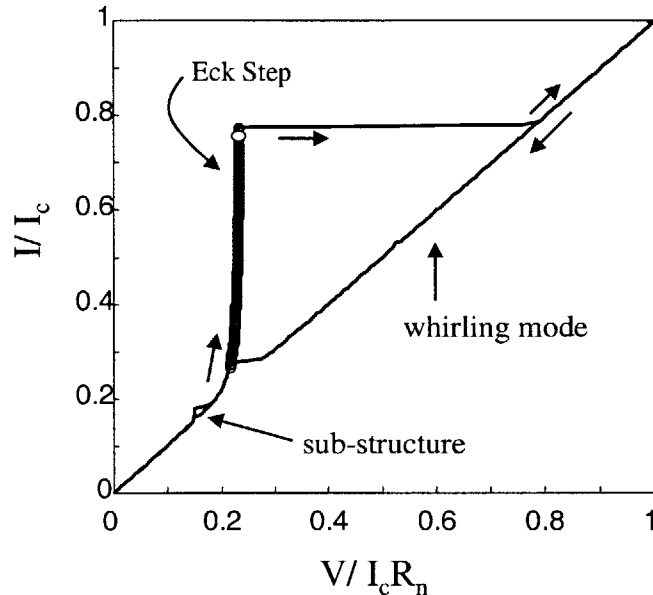


Figure 3-1: Numerically simulated IV curve of an $N = 8$ ring. The parameters are $M = 2$, $\Lambda_J^2 = 4.29$, and $\Gamma = 0.088$ ($\beta_c = 162$).

corresponds to a pendulum system with strong springs, so that the trapped kinks will be spread out across the chain in the static solution. The dynamical solutions of this system are explored for a range of applied force (I_b).

The bias current is increased in normalized steps of 0.001, and the values of $\dot{\phi}_j(t)$ are calculated. A time and spatial average is calculated to give the DC voltage shown, $V/I_c R_n$. As the current is increased from zero, the voltage increases linearly. For this $M = 2$ case, we see no critical current in the IV curve. In the mechanical picture, the applied torque immediately causes the pendula to rotate over the top. The average rotation rate increases with applied torque. However, in the bias current range from about $I/I_c = 0.15 - 0.18$, the voltage deviates from the linear path and a small step appears in the IV curve. This point is marked “sub-structure” in Fig. 3-1. The reason for this label will be explained. As the current is further increased, a much larger deviation from the linear path appears in the range $I/I_c = 0.3 - 0.8$. The points along this step are darkened for emphasis, and the step is marked “Eck step”. On

the Eck step, the voltage is nearly constant for a large range of current. This implies that the applied torque in the pendulum system does not increase the rotation rate of the pendula. So where does the input energy go?

We study the individual phase solutions of the junctions to learn more about the dynamics on this step. A point near the top of the Eck step has been marked with an open circle. At this bias current ($I/I_c = 0.76$), the voltage is $V/I_c R_n = 0.23$. Figure 3-2 shows the phase of junction $j = 1$ versus time. The phase is periodically increasing in increments of 2π . However, just after the pendulum turns over, the phase swings back a little before turning over again. The average rate of increase of ϕ_j (the slope in Fig. 3-2) is proportional to the frequency at which the pendulum overturns. Each pendulum in the array exhibits this behavior, except that there is a time delay between pendula. The solution for $\dot{\phi}_j$ is also calculated and shown in Fig. 3-3. The solution consists of a single harmonic oscillation in time. There is a constant phase shift between adjacent pendula which corresponds to the trapped twists spread uniformly across the array. For $M = 2$, the phase shift between $\dot{\phi}_1$ and $\dot{\phi}_3$ is 180° , as shown in the figure. As required by the Josephson relation, the DC offset of $\dot{\phi}_j$ is equal to the slope of ϕ_j in Fig. 3-2. Although the FFT is not shown, we find that the frequency of the oscillation in Fig. 3-3 is also equal to the DC voltage.

On the Eck step, then, a traveling wave with wavenumber $k = 2\pi M$ is excited in the array. The pendula (junctions) oscillate in time, with a constant phase-shift k between them. The frequency of the oscillation is equal to the (normalized) DC voltage. What determines this DC voltage? Previous authors have determined that the excited wave can be thought of as a lattice vibration [8, 9]. The chain of coupled pendula form a discrete lattice and can support vibrations. The combination of two trapped kinks and an applied torque drives the $k = 2\pi M$ vibrational mode to become excited. Since the system is discrete, dispersion is expected. That is, waves with different wavenumbers should travel with different speeds. This means that both the frequency of oscillation and the DC voltage of the Eck step should be different for different M . This is exactly what is observed [8, 11].

In the Josephson system, the phase oscillations correspond to oscillations of the

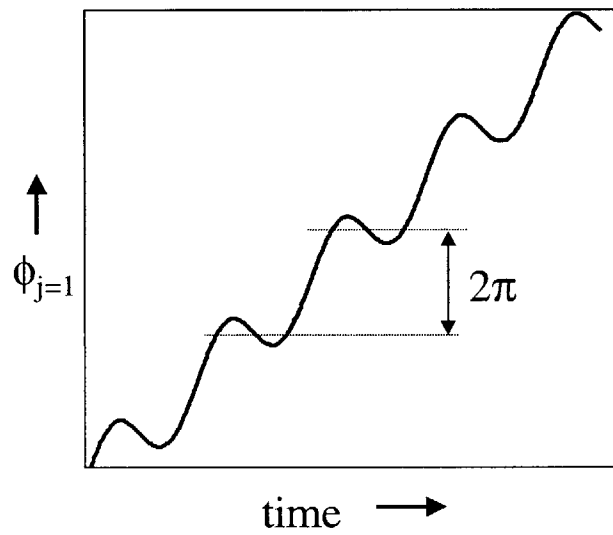


Figure 3-2: Phase of junction $j = 1$ versus time. This solution is for the IV curve of an $N = 8$ array with $M = 2$ trapped kinks, at $I/I_c = 0.76$, which is marked in Figure 3.1.

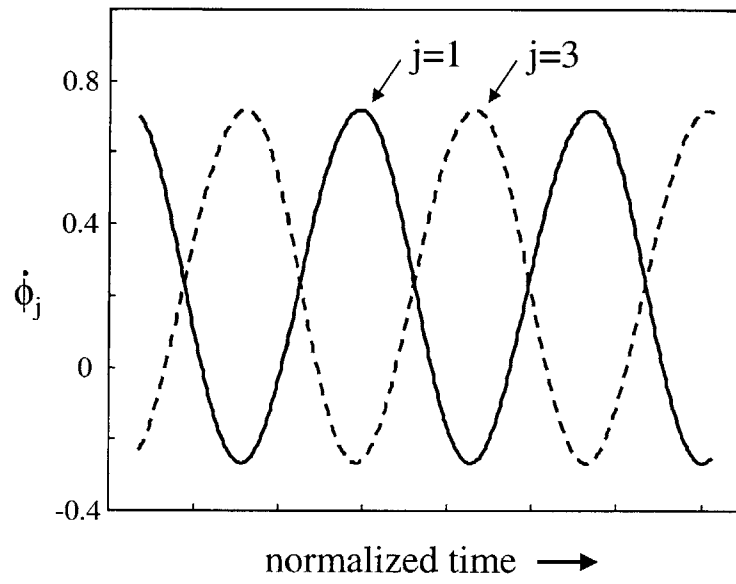


Figure 3-3: Voltages of junctions $j = 1$ (solid line) and $j = 3$ (dashed line) versus time. This solution is for the IV curve of an $N = 8$ array with $M = 2$ trapped kinks, at $I/I_c = 0.76$, which is marked in Figure 3.1.

flux in a cell of the array, since $\Phi_j = (\Phi_o/2\pi)[\phi_{j+1} - \phi_j]$. Therefore, in the Josephson array, the excited traveling wave is electromagnetic. Propagation of the wave is characterized by a dispersion relation, which is nonlinear since the system is discrete. A similar step appears in long *continuous* Josephson junctions, and was first described by Eck [25]. Despite the differences in systems, there are enough common features to this solution that the term Eck step has survived in reference to this step of the discrete system as well [10]. By analogy with the continuous system, this step is also sometimes called a “Flux Flow Step” (FFS).

In Fig. 3-1, the Eck step loses stability at $I/I_c = 0.78$. At this point, the system switches to a linear regime with much higher voltage. The simulations (not shown) show that the pendula no longer swing back at all after overturning. The applied torque forces the pendula to rapidly whirl over the top without any time for extra oscillations. The trapped twist is still maintained as a constant phase difference between the pendula, as the chain rigidly whirls. This solution has been appropriately dubbed the “whirling mode” [31, 34] and this linear region of the IV curve is sometimes referred to as the “whirling branch”. If the current is now decreased along the whirling branch, the rotation rate of the pendula decreases linearly. The system does not switch back to an Eck-step solution until the current is very close to the bottom of the step. The inertia of the pendula causes this hysteresis. The amount of hysteresis is determined by the parameter Γ (or $\beta_c = \Gamma^{-2}$). For $\Gamma > 1$ ($\beta_c < 1$) there is no hysteresis.

In Fig. 3-4, we examine an IV curve for the same $N = 8$ ring but now with $M = 1$. This time, the sub-structure step is very large, and no Eck step appears. In addition, a new step, labeled “HV step” appears. Figure 3-5 shows the solution for $\dot{\phi}_1$ while the system is on a sub-structure. The point used is marked on the IV curve at the top of the step, at current bias $I/I_c = 0.47$ and DC voltage $V/I_c R_n = 0.12$. On this sub-structure, we see that the pendulum phase “rings” not just once, as on the Eck step, but twice in every cycle. Other substructures can be observed corresponding to even more ringing. The result is that higher harmonics are present in the $\dot{\phi}_j$ solutions. This fascinating behavior was first described for the regime where the kinks are relatively

localized compared to the size of the array [8, 9]. The applied torque forces the kinks to move through the array. After a kink passes a given pendulum, the pendulum “rings” until the next kink passes. If the motion of the kinks can phase-lock with the ringing of the pendula, a large-amplitude wave becomes excited.

The HV step solution is shown in Fig. 3-6. At the top of the step, the motion of the pendulum is quasi-periodic. That is, there are two frequencies in the solution which are not multiples of each other. This type of solution can be associated with the excitation of a kink/anti-kink pair. The step arises as an instability of the whirling branch, and the dynamics have been studied in detail in [26, 34]. The structure is called a “High Voltage” (HV) step, referring to the fact that the voltages of such steps are always higher than those of the Eck steps.

For long open-ended rows, many of the same dynamical solutions appear. In this case, externally applied magnetic field enters the array through the boundaries. The number of kinks in the array is not quantized and is continuously tunable. Therefore the spatial wavenumbers of excited resonances can be continuously tuned. In the next sections, we show experiments on single rings and single rows of underdamped junctions.

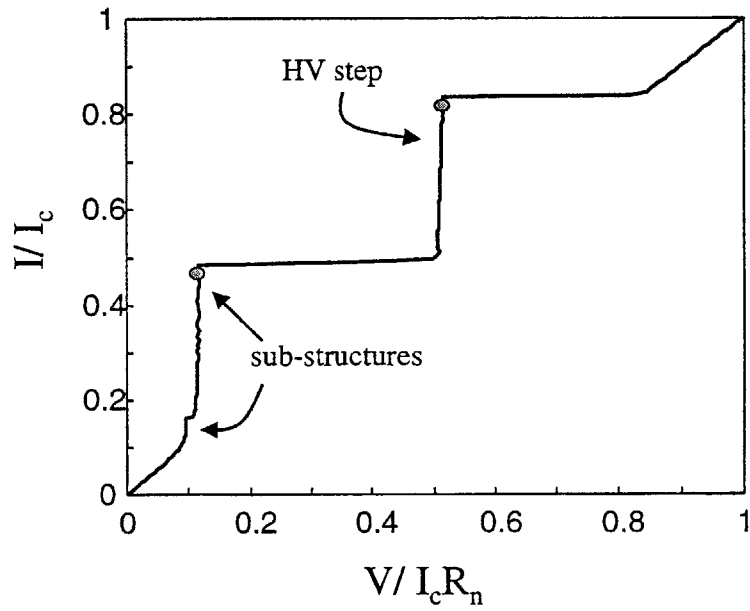


Figure 3-4: Numerically simulated IV curve of an $N = 8$ ring. The parameters are $M = 1$, $\Lambda_j^2 = 4.29$, and $\Gamma = 0.088$ ($\beta_c = 162$).

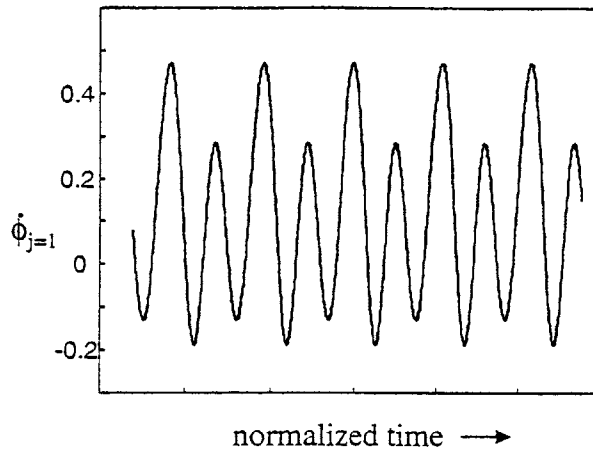


Figure 3-5: Time dynamics on a sub-structure. The point is $I/I_c = 0.47$, marked on the IV in Figure 3.4, which has $N = 8$ and $M = 1$. The solution for $\dot{\phi}_{j=1}$ is shown versus time, which is normalized. Note that the pendulum rings twice during each cycle.

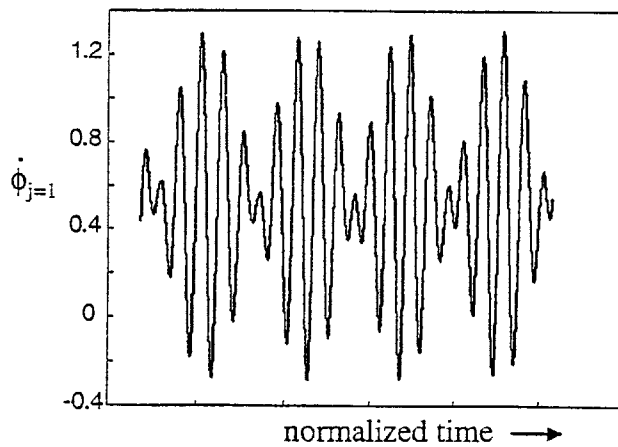


Figure 3-6: Time dynamics on an HV step. The point is $I/I_c = 0.82$, marked on the IV in Figure 3.4, which has $N = 8$ and $M = 1$. The solution for $\dot{\phi}_{j=1}$ is shown versus time.

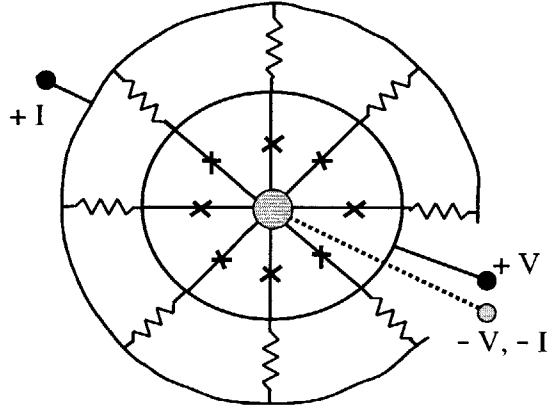


Figure 3-7: Schematic of the N=8 ring with bias resistors included.

3.1.2 Experiments: Single Rings

Since single rings have been studied extensively, new measurements of the ring system form a convenient starting point. In this section, we show measurements of a single ring array which exhibits both the expected Eck steps and some HV steps. Experimental evidence of a *new* dynamical state in single rings will be presented later in a Section 3.3. The schematic of Fig. 2-6 showed that the same bias current is applied to each junction and is withdrawn at the center node. Experimentally, this is achieved through bias resistors. In Fig. 3-7, we show a more detailed schematic of an $N = 8$ array. The outer bus-bar which delivers current to the bias resistors is a broken ring, so as to not trap flux. The layout editor KIC [24] was used for the designs, and HYPRES [20] fabricated the samples. Appendix A describes the procedure used to determine the system parameters, including the damping β_c and discreteness Λ_j^2 .

An IV curve for the ring is shown in Fig. 3-8. There is a critical current of approximately $3 \mu A$. The Eck and HV steps are marked. In this case, no sub-structures appear. The parameters of the experimental system have been estimated using the procedure outlined in Appendix A. Despite the fact that the parameters are the same

for the experiment in Fig. 3-8 and the simulation in Fig. 3-4, the solutions are not identical. In order to get a better match between experiments and simulations, we sometimes add some disorder to the critical currents. This effect is small, however; adding up to 10% disorder to the critical currents primarily causes a rounding of the tops of steps and the top of the zero voltage state. More importantly, the damping parameter used in the simulations, β_c must be lowered from the original experimental estimate (especially for the low j_c samples). This issue should be addressed in future research.

In Fig. 3-9, the IV curves for $M = 0, 1, 2, 3$ and 4 trapped kinks are shown. Recall that, in the regime where the “spring constant” is strong relative to the array size ($M\Lambda_J^2/N > 1$), the M trapped kinks impose a spatial wavelength on the system. In addition, numerical simulations of Section 3.1.1 showed that the frequency of the junction oscillations are proportional to the measured DC voltage of the Eck step. Thus, measuring the DC step voltage versus the M trapped kinks is a measure of the dispersion relation for the system. Figure 3.11 shows this data. The dispersion relation is periodic with M , due to the discreteness. The solid line is a theoretical fit. The formula for this fit was obtained from the dispersion relation for the linearized system in [8]. In normalized units, this dispersion relation is $\omega_k^2 = 4\Lambda_J^2 \sin^2(k\pi/N)$, where $k = M$ for the Eck step. In real units, the theory plotted in Fig. 3.11 is

$$V_{\text{Eck}} = V_o \sin\left(\frac{M\pi}{N}\right) \quad (3.4)$$

where $V_o = \Phi_o/2\sqrt{L_s C}$. The Eck step voltages, then, depend on the size of a cell in the array, which influences L_s , and the area of the junctions, which influences C . A derivation of this dispersion relation will be reviewed in the following sections. Formulas for the HV steps were derived in [11], and will also be reviewed as needed.

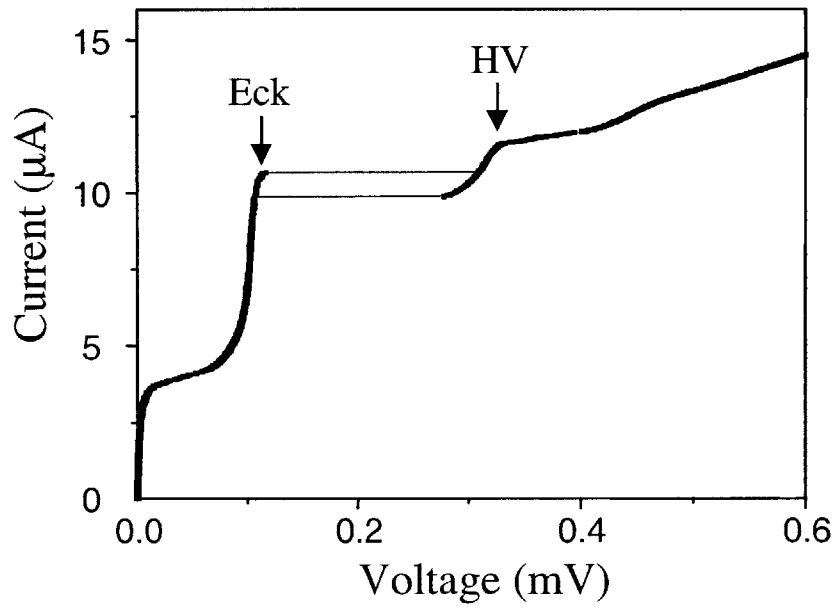


Figure 3-8: IV curve for the $N = 8$ ring with $M=1$. The Eck and HV steps are marked. The parameters are $\beta = 162$ and $\Lambda_j^2 = 4.29$.

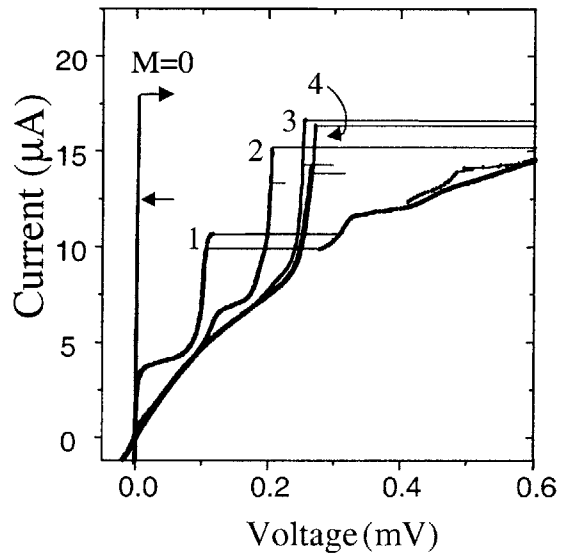


Figure 3-9: IV curves showing the Eck steps for $M = 0, 1, 2, 3, 4$ trapped kinks in an $N = 8$ ring. The curves are hysteretic, since $\beta_c = 162$. The discreteness parameter is $\Lambda_j^2 = 4.29$.

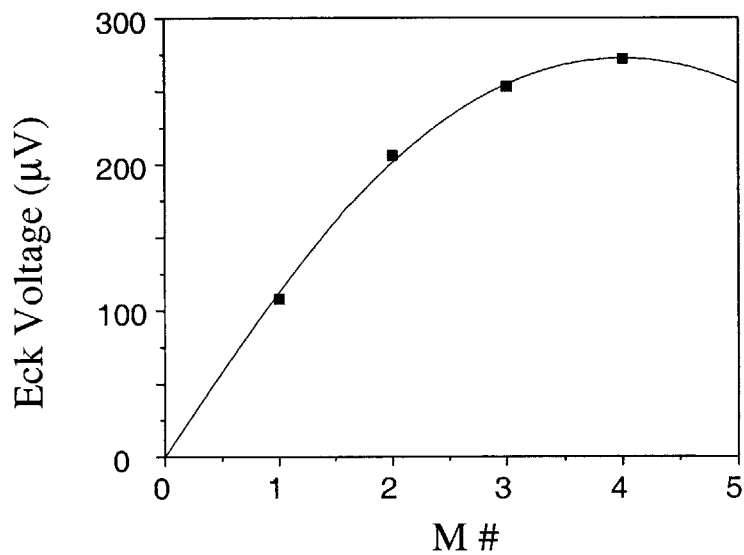


Figure 3-10: Eck voltages versus number of trapped kinks, obtained from the measured IV curves of Figure 3-9. The experimental parameters are $\beta_c = 162$ and $\Lambda_j^2 = 4.29$. The solid line is theory, and was derived in reference [8]. The theory uses $V_o = 284 \mu\text{V}$ and $M_h = 0.04$.

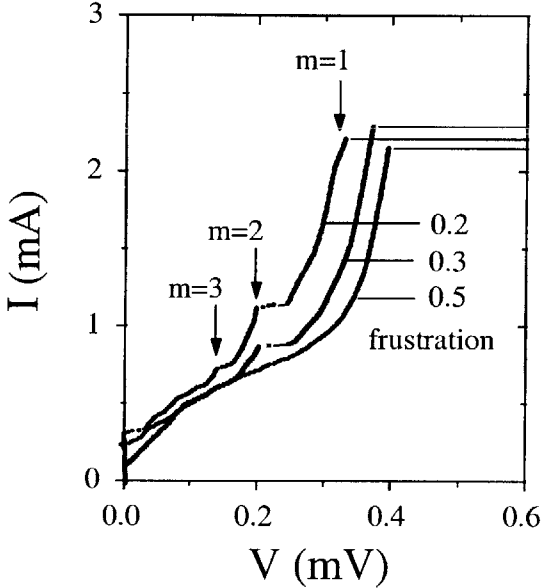


Figure 3-11: Current vs Voltage of a 54-junction array on a ground plane at three values of $f = 0.2, 0.3,$ and 0.5 . The temperature is 7.2 K so that $I_c R_n = 0.93$ mV. The three steps indicated by the arrows are labeled by m values corresponding to the number of dominant harmonics in the mode.

3.1.3 Experiments: Single Rows

In the open-ended system, the amount of flux is not quantized. We can imagine again the coupled pendula, but this time as a linear chain. The amount of applied field corresponds to twisting the ends of the chain and holding that twist fixed as the phases evolve in time. Consistent with previous measurements [10], we find that this results in a continuously tunable Eck voltage. Three example IV's are shown in Fig. 3-11 for $f = 0.2, 0.3,$ and 0.5 . This system had $N = 54$ junctions with $\beta_c = 16$ and $\Lambda_J^2 = 0.92$.

In addition to a tunable Eck step, we also see substructures appearing in the IV curve. Although these have been observed in discrete ring arrays [8], their appearance

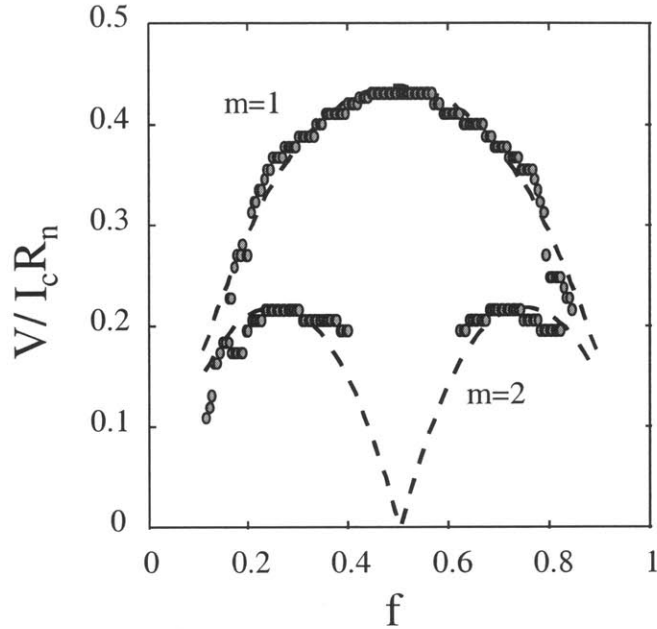


Figure 3-12: Step voltages of the 54-junction array versus the frustration f , for the modes $m = 1$ and $m = 2$. The dashed curves are plots of the dispersion relation.

in the open-ended system had not been predicted. Marked on the $f = 0.2$ IV of Fig. 3-11 are several substructures. We have designated the Eck step as the $m = 1$ step and indexed the other steps as well. The m index refers to how many times each pendulum in the array rings in between the passing of kinks.

The voltage locations of the peaks experimentally vary with f , as seen in Fig. 3-11. More systematically, we show the dependence of the first two steps in Fig. 3-12. The Eck peak voltage is found to be periodic in f with period $f = 1$ and to be approximately symmetric with respect to $f = 0.5$. This is consistent with previous observations [10]. At $f = 0.5$, the Eck step reaches its highest voltage value. For a smaller f , there is a threshold frustration, below which the Eck step does not appear. This cut-off f_{c1} , known as the lower critical field or frustration, is the minimum applied flux density for vortices to enter an array [10]. The value is quite large for our system, $f_{c1} \approx 2/(\pi^2 \Lambda_J) = 0.2$. The voltage location of the second step shows roughly the same f -periodicity and symmetry as the Eck step. This second step, however, achieves the maximum voltage near $f = 0.25$, and it disappears near $f = 0.5$ and for

approximately $f < f_{c1}$.

The Eck ($m = 1$) steps are ubiquitous in one-dimensional parallel arrays as well as in continuous long junctions. In contrast, the other steps ($m > 1$) do not appear in long continuous junctions, but do appear in discrete arrays when Λ_J is small. In our arrays, we find Λ_J must be less than unity for the $m = 2$ step to appear.

In open-ended arrays with a smaller N (which are not studied in this thesis), Fiske steps may be observed in a similar part of the IV below the Eck voltage [29]. We emphasize, however, that they are qualitatively different. Fiske resonances can be described as standing waves (cavity modes) resulting from boundary reflections. The wavelength of the modes are restricted by the boundary geometry, and consequently, the resonance voltage locations do not depend strongly on f . At a certain value of f , only even or only odd modes are excited. As N becomes large, for a given value of damping, these Fiske resonances disappear due to damping of the edge reflections. None of these features apply for the Eck step as well as the $m > 1$ steps, which are tunable in f . Thus, the new steps are expected to belong to the same family as the Eck step.

3.2 Analysis

In previous sections, we have explored the nature of the phase solutions when the system is biased on a step in the IV curve. We found that the solutions are periodic traveling waves or quasi-periodic with only a few frequencies. Various analytical techniques have been used by previous authors to obtain the voltages and oscillation frequencies at which these special wave solutions occur. For sub-structures, a perturbative analysis around a traveling kink solution yields the dispersion relation for linear lattice vibrations [8]. Phase-locking between the moving kink and the lattice waves results in the sub-structure resonances [8, 9]. For both Eck steps and sub-structures, a traveling wave ansatz has been used and harmonic balance applied to obtain the dispersion relation [32, 27]. Finally, for HV steps, a stability analysis of the whirling mode solutions predicts unstable regions of the whirling branch, resulting in quasi-periodic solutions [11].

The variety of analytical techniques which can be applied speaks for the rich dynamics of this system. In addition, each successful approach provides new insight into the nature of the dynamical solutions. Despite the range of mechanisms which may lead to the appearance of these different states, most of the solutions of interest correspond to the excitation of only one or two spatial frequencies. Therefore, in the following section, we contribute an approach which can be applied to any resonance of this type. We use a spatial modal analysis and write a set of coupled modal equations for the system. We show that *all* of the observed steps— Eck steps, sub-structures, and HV steps— can be related to resonances of the spatial modes. Finally, we present an analytical discussion of the discrete periodic array which is not aimed specifically at predicting resonances, but instead provides a conceptual insight into the system. In this discussion we enforce an energy balance in the circuit and examine the consequences.

3.2.1 Modal equations for single rings

For reference, we repeat the governing equation of our ring system:

$$\ddot{\phi}_j + \Gamma \dot{\phi}_j + \sin \phi_j = \Lambda_j^2 \nabla^2 \phi_j + \text{I}_b, \quad (3.5)$$

and the boundary condition:

$$\phi_{j+N} = \phi_j + 2\pi M. \quad (3.6)$$

The following transformation is useful for analysis.

$$\varphi_j = \phi_j - 2\pi \frac{M}{N} j. \quad (3.7)$$

At the end of the calculation, we can shift back to the variable ϕ_j . Physically, this applies a magnetic field of $2\pi M/N$ to each cell, since $\Phi_j = \phi_{j+1} - \phi_j$. Since the shift is constant in time, it will not affect the dynamics of our system. We can study the dynamics of $\varphi_j(t)$ and then shift back to $\phi_j(t)$ to later obtain the correct solution. Applying the transformation to φ_j , to equation (3.5), we obtain:

$$\ddot{\varphi}_j + \Gamma \dot{\varphi}_j + \sin[\varphi_j + (2\pi M/N)j] = \Lambda_j^2 \nabla^2 \varphi_j + \text{I}_b. \quad (3.8)$$

The boundary condition becomes $\varphi_{j+N} = \varphi_j$.

Since φ_j is periodic on a discrete lattice, we can write the discrete Fourier Series:

$$\varphi_j = \sum_{k=\langle N \rangle} P_k(t) e^{ik(2\pi/N)j}. \quad (3.9)$$

Using the Fourier series (3.9) for φ_j , we simplify the discrete Laplacian:

$$\nabla^2 \varphi_j = \sum_{k=\langle N \rangle} (-\omega_k^2) P_k(t) e^{ik(2\pi/N)j}, \quad (3.10)$$

where

$$\omega_k^2 = 4\Lambda_j^2 \sin^2(k\pi/N). \quad (3.11)$$

We also write a discrete Fourier series for the sine term, since it is periodic in j :

$$\sin[\varphi_j + (2\pi M/N)j] = \sum_{k=\langle N \rangle} F_k(t) e^{ik(2\pi/N)j}. \quad (3.12)$$

Now the governing equation for φ_j can be written as the coupled amplitude equations:

$$\ddot{P}_k + \Gamma \dot{P}_k + F_k = -\omega_k^2 P_k, \quad k \neq 0 \quad (3.13)$$

$$\ddot{P}_0 + \Gamma \dot{P}_0 + F_0 = I_b, \quad k = 0 \quad (3.14)$$

In Appendix B, the details for writing the Fourier series coefficients F_k in terms of P_k are provided. Similar calculations were used in reference [27]. In the analysis, the $|P_k|$ are formally assumed to be so small that higher order Bessel functions can be neglected and only linear terms in P_k need to be included. With these assumptions, which can be checked using simulations, we obtain (for $M \neq 0$):

$$F_0 = -\frac{1}{2} p_M \sin(P_0 - \theta_M) \quad (3.15)$$

$$F_M = \frac{1}{2} [-ie^{iP_0} + \frac{1}{2} P_{2M} e^{-iP_0}] \quad (3.16)$$

$$F_k = \frac{1}{2} [P_{k-M} e^{iP_0} + P_{k+M} e^{-iP_0}] \quad k \neq 0, M. \quad (3.17)$$

In the calculations and in equation (3.15), we write P_k in polar coordinates as $P_k = (-i/2)p_k e^{i\theta_k}$. Putting these back into the amplitude equations (3.13- 3.14), we obtain:

$$\ddot{P}_0 + \Gamma \dot{P}_0 - \frac{1}{2} p_M \sin(P_0 - \theta_M) = I_b \quad (3.18)$$

$$\ddot{P}_M + \Gamma \dot{P}_M + \omega_M^2 P_M + \frac{1}{2} [-ie^{iP_0} + P_{2M} e^{-iP_0}] = 0 \quad (3.19)$$

$$\ddot{P}_k + \Gamma \dot{P}_k + \omega_k^2 P_k + \frac{1}{2}[P_{k-M}e^{iP_0} + P_{k+M}e^{-iP_0}] = 0 \quad k \neq 0, M. \quad (3.20)$$

The coupled modal equations above can be used to discuss the features of our data. We will consider them one at a time.

First, the equation (3.18) is similar to the single pendulum equation, except that the effective I_c is modulated by the amplitude of P_M . This equation is the only one which has a DC solution in time, since it contains a DC driving force. Taking the DC terms in equation (3.18) will give the time-averaged IV characteristics. In the literature, we find a perturbative solution to equation (3.18) for small values of the quantity Γ/I_b [33]. When the bias is well beyond the critical current, the first order solution is just $P_0(t) = \nu t + \theta$, where $\nu = I_b/\Gamma$ and θ is an integration constant.

Next, consider the $k = M$ equation. We can think of P_0 as a driving function. When $P_0 = \nu t + \theta$, the drive is simple. The amplitude of P_M becomes large when $\nu = \omega_M$. The amplitude of P_M in turn affects the $k = 0$ equation and the IV characteristic. This is how we can understand the Eck peak appearing in the IV. Since this looks like a linear oscillator, we expect that when $\nu < \omega_M$, $\theta = \theta_M$. When $\nu = \omega_M$, $\theta = \theta_M + \pi/2$, and for $\nu > \omega_M$, $\theta = \theta_M + \pi$. Also, this equation implies that there might be an additional resonance at $\nu = \omega_M \pm \omega_{2M}$, if the amplitude of P_{2M} is excited. The \pm reflects possible phase differences of the drive. Exactly following [34], a two-time analysis of the solutions near this frequency should be pursued to confirm that this is indeed a resonance. A resonance at the DC voltage of $\nu = \omega_M + \omega_{2M}$ could loosely be associated with the excitation of M kink/anti-kink pairs, and would be identified as an HV step in the DC IV characteristic.

Finally equation (3.20) is identical to those for the whirling mode instabilities of reference [11] when $P_0 = \nu t$. At DC voltages such that $\nu = \omega_k + \omega_{k+M}$, mode P_k becomes large and an HV step appears in the IV. The excitation of mode P_k can be associated with k kink/anti-kink pairs in the system, so that the total number of anti-kinks is k while the total number of kinks is $k + M$. Likewise, the mode P_k can become large when $k - M$ pairs are excited in the system. Then the total number of kinks is k while the number of anti-kinks is $k - M$, and the corresponding HV step

would appear at $\nu = \omega_k + \omega_{k-M}$.

The analysis of Watanabe and van der Zant in reference [11] was constructed so that the amplitude P_k was a Fourier mode of a *perturbation* to the basic solution $\phi^* = \nu t$. Therefore, if one modal amplitude P_k resonates, the perturbation is large and the solution will deviate from this basic solution. Although the present analysis is not formally constructed as a stability analysis and the P_k 's do not need to be infinitesimal up to equations (3.13- 3.14), the truncation in equations (3.15- 3.17) is based on linearization. Therefore, the resulting system (3.18- 3.20) yield results consistent with the previous stability analysis, as we have seen.

Because the k -th mode is coupled only to $k \pm M$ modes in (3.18- 3.19), some junctions are decoupled from P_0 completely, depending on the combination of N and M . For instance, a situation with $N = 8$ and $M = 2$ is illustrated in Fig. 3-13 where junctions with odd indices do not interfere with P_0 . Because the DC IV characteristic is determined from (3.18), it implies that those decoupled modes do not affect the IV. Of course, this is an artifact made by truncating the coupling terms F_k as in (3.15- 3.17). The truncated equations (3.18- 3.20) are not complete enough to explain why a step might appear in the IV curve when such modes are excited. On the other hand, improving the truncated system by including more coupling terms in the modal equations (3.13- 3.14) would make the resulting system so complicated that they no longer provide any valuable insight. Instead, we will simply note that the limitation of the above analysis and use a different approach in the next section to discuss effects of all the modes on the IV.

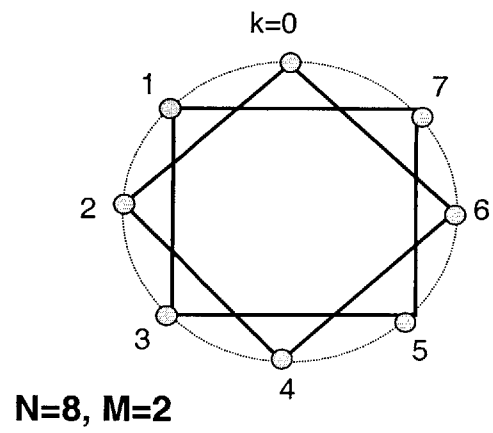


Figure 3-13: Symbolic representation of modal coupling

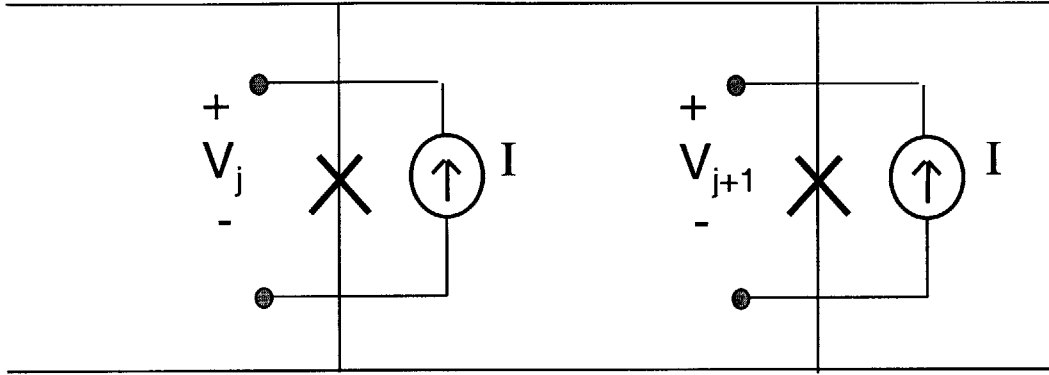


Figure 3-14: Schematic of two junctions within a discrete ring system. Current is injected uniformly via identical current sources at each junction. The voltage across junction j is denoted by V_j .

3.2.2 Energy balance for single rings

For a system in steady state, the average power supplied by the source should be equal to the average power dissipated in the system. In Figure 3-14, we show a schematic of a few junctions in our ring system, as they are modeled in simulations. Equal current sources are applied to each junction.

The instantaneous power supplied by any one source, at junction j for example, is just $V_j I$, since the voltage across the source is $V_j(t)$. Since we are interested in the average power, we will eventually need to take a time average of the function. For now we will denote the time average as $\langle V_j \rangle$. Then the total power φ_s supplied by the sources is:

$$\varphi_s = I \sum_{j=\langle N \rangle} \langle V_j \rangle \tag{3.21}$$

This must equal the total power absorbed by the passive impedances. Using

the RSJ model of the junction, each junction has a passive impedance of R , with a complex voltage across this element of V_j . Then the average power dissipated in each junction is $\langle V_j^2 \rangle / R$. The total power dissipated in all of the passive elements is then

$$\wp_R = \frac{1}{R} \sum_{j=\langle N \rangle} \langle V_j^2 \rangle. \quad (3.22)$$

Since $V_j = \dot{\varphi}_j(\Phi_o/2\pi)$, then equation 3.9 gives

$$V_j = \frac{\Phi_o}{2\pi} \sum_{k=\langle N \rangle} \dot{P}_k e^{ik(2\pi/N)j} \equiv \sum_{k=\langle N \rangle} v_k e^{ik(2\pi/N)j}. \quad (3.23)$$

Using this, we can simplify the expressions for both \wp_s and \wp_R . First, it is helpful to recall that since both the voltage and the superconducting phase must be real functions, then $v_k^* = v_{-k}$, which implies that $v_0^* = v_0$. We will also use the identity:

$$\sum_{j=\langle N \rangle} e^{ik(2\pi/N)j} = \begin{cases} N, & k = 0, \pm N, \pm 2N, \dots \\ 0, & \text{otherwise} \end{cases} \quad (3.24)$$

Starting with the sum in \wp_s , we have

$$\begin{aligned} \sum_{j=\langle N \rangle} \langle V_j \rangle &= \sum_{j=\langle N \rangle} \sum_{k=\langle N \rangle} \langle v_k \rangle e^{ik(2\pi/N)j} \\ &= \sum_{k=\langle N \rangle} \langle v_k \rangle \sum_{j=\langle N \rangle} e^{ik(2\pi/N)j} = \sum_{k=\langle N \rangle} \langle v_k \rangle N \delta_{k,0} = N \langle v_0 \rangle. \end{aligned} \quad (3.25)$$

The sum in \wp_R also simplifies to

$$\begin{aligned} \sum_{j=\langle N \rangle} \langle V_j^2 \rangle &= \sum_{j=\langle N \rangle} \left\langle \left[\sum_{k=\langle N \rangle} v_k e^{ik(2\pi/N)j} \right]^2 \right\rangle \\ &= \sum_{j=\langle N \rangle} \left\langle \sum_{k=\langle N \rangle} \sum_{l=\langle N \rangle} v_k v_{-l}^* e^{i(k+l)(2\pi/N)j} \right\rangle = N \sum_{k=\langle N \rangle} \langle |v_k|^2 \rangle. \end{aligned} \quad (3.26)$$

This is just the discrete version of Parseval's relation. Then the power balance $\wp_s = \wp_R$ gives

$$I\langle v_0 \rangle = \frac{1}{R} \sum_{k=\langle N \rangle} \langle |v_k|^2 \rangle. \quad (3.27)$$

If the current is normalized to $I_b = I/I_c$ and the voltage is normalized to $\mathcal{V}_k = v_k/(I_c R)$, then equation(3.27) becomes

$$I_b \langle \mathcal{V}_0 \rangle = \sum_{k=\langle N \rangle} \langle |\mathcal{V}_k|^2 \rangle. \quad (3.28)$$

For the vector $\vec{\mathcal{V}} = \sum_k \mathcal{V}_k$, the length of $\vec{\mathcal{V}}$ is just $\|\vec{\mathcal{V}}\| = [\sum_k |\mathcal{V}_k|^2]^{1/2}$. Equation (3.28) implies that the time average of the total magnitude of $\vec{\mathcal{V}}$ is constrained to a surface. We can see this better by rearranging the equation and completing the square:

$$\left\langle \left(\mathcal{V}_0 - \frac{I_b}{2} \right)^2 \right\rangle + \langle |\mathcal{V}_1|^2 \rangle + \langle |\mathcal{V}_2|^2 \rangle \cdots + \langle |\mathcal{V}_{N-1}|^2 \rangle = \left(\frac{I_b}{2} \right)^2 \quad (3.29)$$

In two dimensions, the surface is a circle and in three dimensions the surface is a sphere. The radius of the surface is determined by the value of the bias current. For a given bias current, an increase in the time average power of one component \mathcal{V}_k requires a decrease of another.

This geometric picture improves our understanding of some of the resonance features in the IV curves. In fact, the intuitive arguments offered by many authors to qualitatively explain the Eck step are made more precise and logical by this calculation. These authors note that on the Eck step the AC oscillations of the junctions become larger as the current is increased, while the DC voltage does not increase. Using the above geometric picture, we can make this argument more clearly. On the Eck step, we need only consider the amplitudes of P_0 and P_M , or the corresponding \mathcal{V}_0 and \mathcal{V}_M . In this two-dimensional space, the magnitude of $\vec{\mathcal{V}}$ is constrained to a circle, as depicted in Fig. 3-15. If \mathcal{V}_M becomes larger (due to a resonance in this case), then for a given current, \mathcal{V}_0 must decrease. On the other hand, if current is increased, we cannot tell the relative increases of \mathcal{V}_0 and \mathcal{V}_M – this information must come from the specific equations which couple \mathcal{V}_0 and \mathcal{V}_M (P_0 and P_M) to each other and to I_b .

To first order, these modal equations have been obtained in the last section.

Combining the modal equations with the power balance constraint results in an interesting qualitative picture of the Eck step ($k = M$ resonance). Equation (3.19) looks like a damped oscillator, with a sinusoidal driving when $P_0 = \nu t$. The response will go as $P_M = p e^{i\nu t}$. Ignoring the P_{2M} drive for now, we know how to calculate the resonance curve for $p(\nu)$ from the transfer function of (3.19). Then the time average value $\langle P_M \rangle = p/\sqrt{2}$, and $\langle \mathcal{V}_M \rangle = p\nu/\sqrt{2}$. Also, for $P_0 = \nu t$, we have $\langle \mathcal{V}_0 \rangle = \nu$. Thus the modal equation (3.19) can be used as an additional constraint on the relationship between $\langle \mathcal{V}_0 \rangle$ and $\langle \mathcal{V}_M \rangle$, and can be plotted with the power balance constraint. In Fig. 3-16, for a given bias current, the values of $\langle \mathcal{V}_0 \rangle$ and $\langle \mathcal{V}_M \rangle$ are found from the intersection of the circle with the resonance curve. For small currents, only $\langle \mathcal{V}_0 \rangle$ is nonzero. As the bias current increases, the DC voltage increases. However, as the DC voltage begins to approach the resonance of P_M , $\langle \mathcal{V}_M \rangle$ grows and the DC voltage no longer increases linearly with current. The plot in Fig. 3-16 was made for the normalized values $\omega_M = 0.2$, $\Gamma = 0.05$, and $I_b = 0.02, 0.1, 0.2, 0.4$. In experiments and simulations, steps begin to appear at normalized values of $I_b \approx 1/N$. In the plot and the inset, we can see that the resonance peak predicted by the modal equations is on a much larger scale.

This approach to interpreting the relationship between the input current, the DC voltage and the AC amplitudes will not be quantitatively accurate. For more quantitative results, the ansatz approach to be described in Section 5.1.2 is more accurate and can even be used to calculate the IV curve [47]. The advantage of the power balance constraint is that it is independent of the modal analysis. It derives only from the fact that the system is discrete and periodic. However, further constraints (like a resonance curve obtained from the modal equations) must be added to get more information about the dynamics of the system. The accuracy of the information obtained depends on the accuracy of the constraint added. In the case of a single ring on a resonant step, we will show in the next section that other methods can be more quantitatively accurate in terms of predicting the IV curve as well as the AC amplitudes. Some systems (like the coupled rings in Chapter 4) may be too

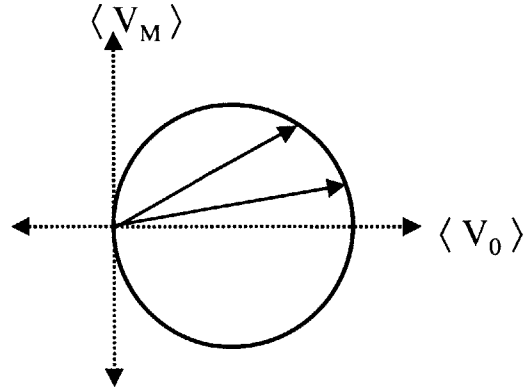


Figure 3-15: For a fixed I_b , when only $\langle V_0 \rangle$ and $\langle V_M \rangle$ are non-zero, their magnitudes are confined to a circle.

complicated for the ansatz approach to work. In these cases, a combination of the power balance constraint and a simple modal analysis may provide some insight. In addition, the power balance constraint can be applied independent of whether any spatial modes are at resonance in the system.

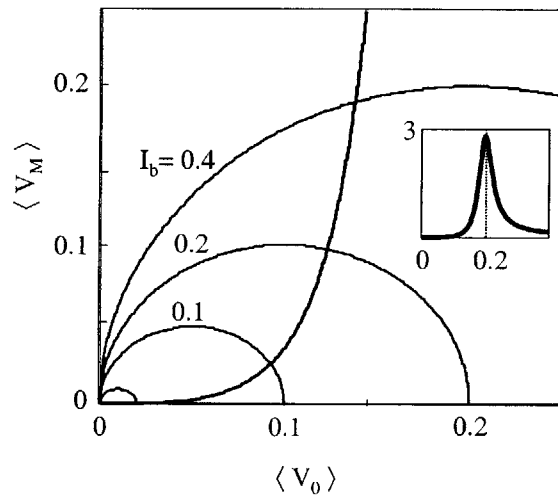


Figure 3-16: As I_b is increased, the radius of the circle which relates $\langle V_0 \rangle$ and $\langle V_M \rangle$ increases and its center shifts. The magnitudes of $\langle V_0 \rangle$ and $\langle V_M \rangle$ are also related by the resonance curve, shown in the inset. The intersection of the resonance curve with the circles will give the solution to $\langle V_0 \rangle$ and $\langle V_M \rangle$ for a given bias current.

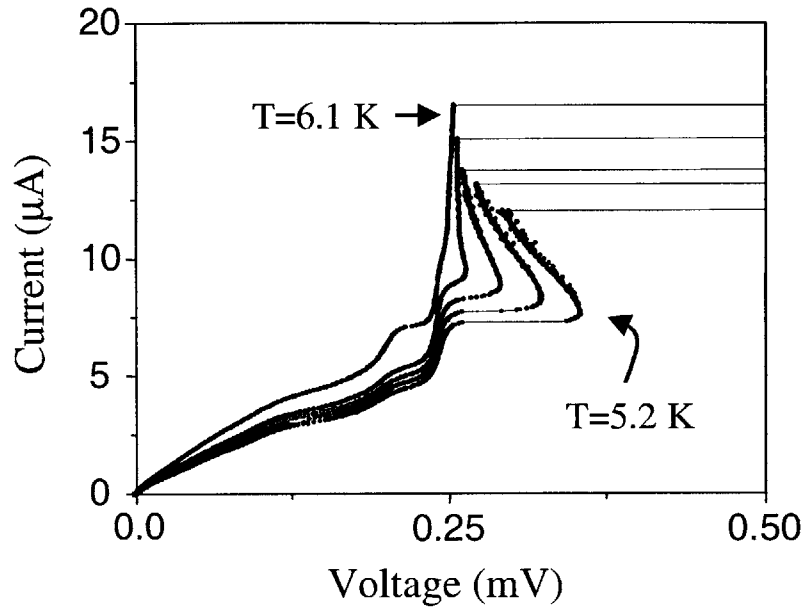


Figure 3-17: Negative differential resistance features of the IV for an $N = 8$ ring with $M = 3$ kinks. At $T = 6.1$ K, the IV looks normal. As the temperature is lowered, the negative resistance appears. The temperatures for the IV curves are, in order, $T = 6.1, 5.5, 5.4, 5.3, 5.2$ K. The corresponding parameters are listed in Table 3.1.

3.3 Rings Experiments: Negative Differential Resistance

In the single ring system, our experiments reveal a new structure in the IV which has not been reported before. Although we can not yet offer an explanation of this data, we will describe the structure in detail since it has appeared in two separate samples and over a range of parameters.

As described in the previous section, a ring with M trapped kinks will exhibit an Eck step whose voltage depends nonlinearly on M . When the Eck step becomes unstable, the system usually switches to either the whirling branch or an HV step. In recent experiments, however, a new structure appears at the top of the Eck step. Figure 3-17 shows several IV curves for an $N = 8$ ring with $M = 3$ kinks trapped. At

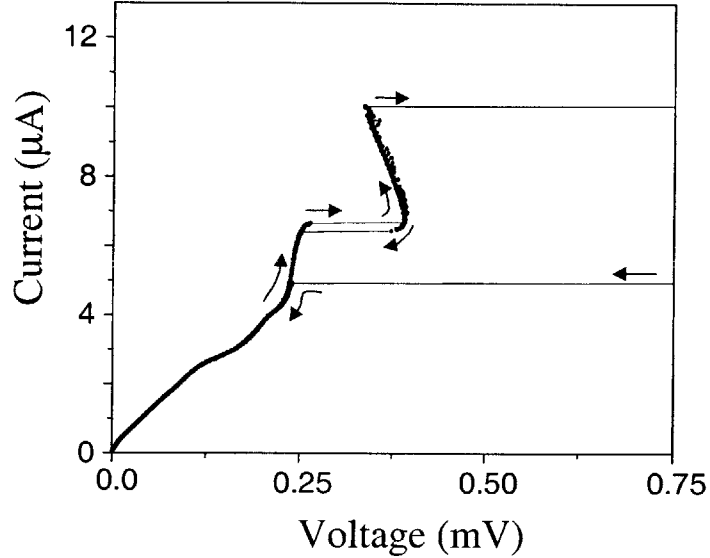


Figure 3-18: IV curve for an $N = 8$ ring with $M = 3$ trapped fluxons. The temperature is $T = 4.9$ K, giving $\Lambda_J^2 = 2.32$ and $\Gamma = 0.058$ ($\beta_c = 299$). There are two hysteresis loops. Arrows mark the direction of increasing and decreasing bias current while the data was measured.

$T = 6.1$ K, the usual Eck step appears. When the maximum current of the Eck step is reached, the system switches over to the whirling branch, which is not included in this plot. At $T = 6.1$ K, we estimate the damping to be $\beta_c = 240$ and the discreteness to be $\Lambda_J^2 = 2.9$. As the temperature is lowered (making the kinks more localized and the system more underdamped), a new structure appears at the top of the Eck step. The striking characteristic of this feature is its *negative* slope. Four IV curves with this structure are included in Fig. 3-17. The parameters for the data are listed in order in Table 3.1. As the temperature is decreased, the maximum voltage of this feature increases. The slope, the negative differential resistance, also changes with temperature. If lines are drawn to fit the negative slopes for each temperature, they all seem to intersect at a single point corresponding to the $M = 3$ Eck voltage and a current of approximately $15 \mu A$.

In Fig. 3-18, we show a close-up of the negative resistance feature at $T = 4.9$ K.

There are two hysteresis loops. The larger one is between the part of the IV shown in this plot and the normal-state resistive branch, which is off of the plot at much higher voltages. The second hysteresis loop is between the Eck step and the negative resistance feature. Arrows mark the direction of increasing and decreasing bias current while the data was measured. The size of the hysteresis loop measured between the negative resistance feature and the Eck step is very sensitive to temperature. At higher temperatures (*e.g.* $T = 5.5$ and $T = 5.4$ K in Fig. 3-17), no hysteresis is measured. The presence of the hysteresis makes it difficult to ascertain the *precise* value of the voltage at the tip of the negative resistance feature (since sometimes the system may switch states due to noise). However, the data for the tip voltage in Fig. 3-19 shows a clear trend. At higher temperatures when the negative differential resistance feature does not appear, we plot the Eck step voltage instead (as circles) for reference. At lower temperatures, the tip voltage begins to decrease again. The inset shows two example IV curves with dotted lines to indicate the points used for the maximum voltage data. In Fig. 3-20, we also examine the slope of the negative differential resistance feature as a function of temperature. At high temperatures where the feature does not appear, we plot the Eck step slope, again as a circle. The inset shows the portion of the IV curve used for the slope fit.

In both Fig. 3-19 and Fig. 3-20, we see that the voltage along the negative differential resistance feature is extremely sensitive to temperature in comparison with the Eck step data. Small controlled changes in temperature influence that portion of the IV curve drastically. This may explain the appearance of more noise in the measured voltage along the negative differential resistance data. This voltage noise most likely reflects our ability to experimentally control the array temperature to within approximately ± 0.005 K.

Negative differential resistance features also appeared in an $N = 8$ ring when $M = 4$ (Fig. 3-21). The parameters for the data are listed in Table 3.2. The interesting changes in slope with temperature are different in this case. In fact, at a temperature of 5.5 K, the slope tilts back in the positive direction. A negative resistance feature has also been observed in an $N = 9$ ring with $M = 2$, but persists over a much

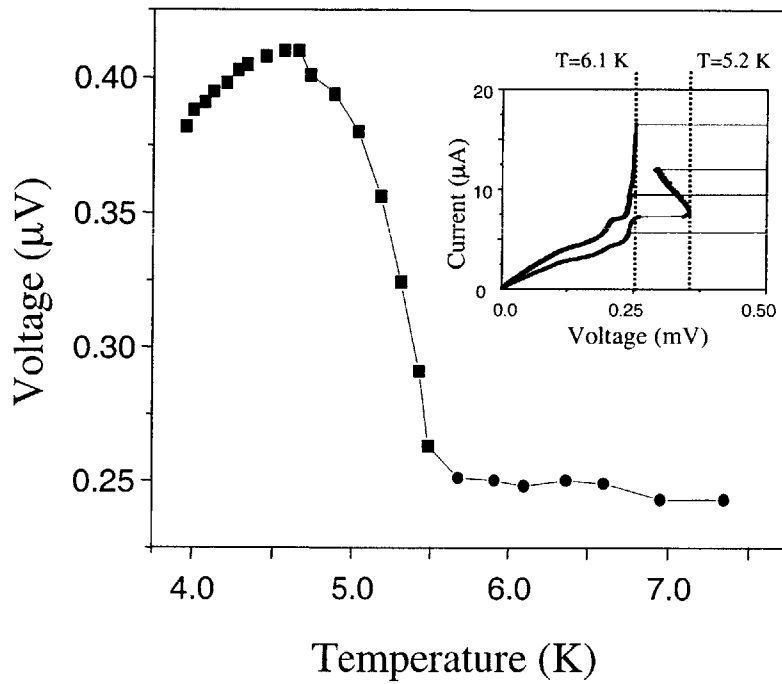


Figure 3-19: Squares show the voltage at the tip of the negative resistance feature, versus temperature. The data is for the $N = 8$ ring with $M = 3$. At high temperatures when the feature does not appear, the Eck step voltage is included (as a circle) for reference. The inset shows two example IV curves with the maximum voltage marked.

narrower range of temperatures.

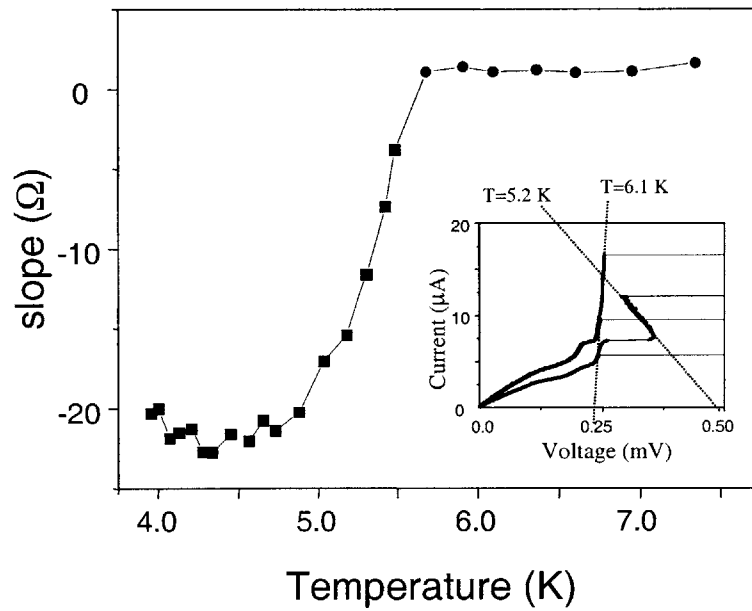


Figure 3-20: Squares show the slope of the negative resistance feature versus temperature. The data is for the $N = 8$ ring with $M = 3$. At high temperatures when the feature does not appear, the Eck step slope is included (as a circle) for reference. The inset shows an example of the portion of the IV curve used for the slope data.

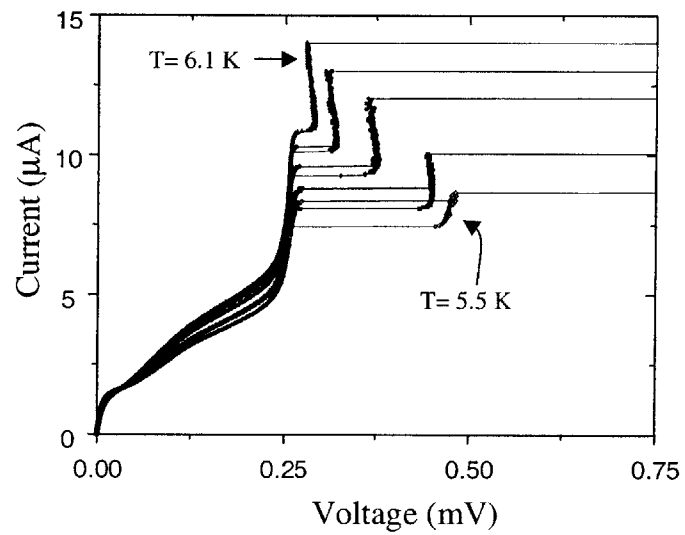


Figure 3-21: Negative resistance features of the IV for an $N = 8$ ring with $M = 4$ kinks. The temperatures for the IV curves are, in order, $T = 6.1, 6.0, 5.9, 5.7, 5.5$ K. The corresponding parameters are listed in Table 3.2.

Table 3.1: PARAMETERS FOR M=3 NEGATIVE RESISTANCE DATA

T (K)	Λ_J^2	β_c	Γ
6.1	2.86	242	0.0643
5.5	2.53	274	0.0604
5.4	2.51	277	0.0601
5.3	2.46	282	0.0596
5.2	2.42	287	0.0590

Table 3.2: PARAMETERS FOR M=4 NEGATIVE RESISTANCE DATA

T (K)	Λ_J^2	β_c	Γ
6.1	2.86	242	0.0643
6.0	2.78	249	0.0634
5.9	2.74	253	0.0629
5.7	2.62	265	0.0614
5.5	2.53	274	0.0604

3.4 Summary of Results for Single Rings and Rows

Discrete Josephson junction arrays with both periodic boundary conditions and open-ends have been measured and analyzed. In accordance with previous experiments, we observed several resonances in these systems, which result in steps in the measured DC IV curves. Numerical simulations have been used to study the dynamics in detail. We described the dynamics for three main resonant states: Eck steps, HV steps, and sub-structures. In the regime where the kinks are not localized compared to the system size, the phase solutions for all of these states are traveling waves. The spatial modes and frequencies of the waves vary for each resonance, and can be interpreted in terms of the motion of trapped kinks in the system. For resonances in the single ring system, a complete study, including experiments, numerics, and analysis, is presented in reference [11]. Figure 3-22 summarizes those results. The results on single rings have been reviewed in this chapter in preparation for the study of coupled systems in the next chapter.

We have added to the single rings results a new analytical approach which conceptually ties together the three different resonances and can predict the associated frequencies and voltages. The approach is a modal analysis which relies on the fact that the system is discrete and periodic. A set of coupled equations are obtained under the approximation that the modal amplitudes are small. Resonances of various spatial modes result in the steps observed in the IV curves. The advantage of this approach is that it provides a compact way of obtaining information about all three states in Fig. 3-22.

A separate but complementary analysis of the single ring system is derived from the requirement of power balance. This analysis is based on Parseval's relation. The single ring system is discrete and periodic. The energy provided to each element must be equal to the total energy contained in the *spatial* Fourier modes. This result is true whether the system is linear or nonlinear. The power balance does not provide any information about how the energy is distributed among the modes, which is importantly different for linear and nonlinear systems. Information about

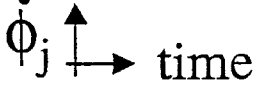


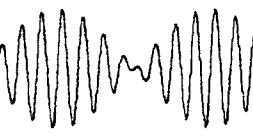
name	$\dot{\phi}_j$ 	$v = \text{step voltage}$	Physical interpretation
Eck		$v = \omega_M$	M= trapped kinks
sub-structure		$v = \omega_{mM}$	m= # ringings
HV		$v = \begin{cases} \omega_{m+M} + \omega_m \\ \omega_{m-M} + \omega_m \end{cases}$	$\left. \begin{matrix} m \\ m-M \end{matrix} \right\}$ excited pairs
$\omega_k = 2 \Lambda_j \sin (k \pi / N)$			

Figure 3-22: Summary of resonant states found in single rings.

the relative amplitudes of the various modes must come from other analyses, and we use the modal analysis as an example. Since the $k = 0$ spatial mode is related to the DC voltage, we can use this power balance requirement to consider how the distribution of energy in the modes might affect the DC IV curve.

This chapter also presents new experimental results on open-ended rows. Previously, only Eck step resonances had been observed in rows [10]. We have experimentally observed sub-structures in open-ended systems as well. Numerics show that the sub-steps correspond to “ringing” of the pendula in-between the passing kinks. Even though kinks are not trapped in the open-ended system, they travel through almost as a rigid array. This result suggests that the long open-ended rows might be treated analytically very much like the system with periodic boundary conditions. In Fig. 3-22, the Eck and sub-structure solutions for the open-ended system are obtained by replacing M with fN , since the flux is no longer quantized. A more complete discussion of the analysis of open-ended rows will be presented in Chapter 5.

Finally, we present in this chapter new experimental results showing a negative differential resistance in single rings. The new feature emanates from the Eck step and is very pronounced for a system with $N = 8$ and $M = 3$. The voltage and the slope are very sensitive to the system temperature. Due to the relatively drastic temperature dependence, it is unlikely that the feature is related to an $L_s C$ resonance of the system. This fascinating feature is not yet explained, and future work will include numerical simulations.

Chapter 4

Coupled Rings and Rows

In this chapter, we explore systems of *two* discrete rows or rings of underdamped junctions. The nonlinear dynamics of inductively coupled discrete systems is relatively uncharted. However, the continuous counterpart, stacked long Josephson junctions, have been studied experimentally [12, 13], numerically [14], and analytically [15]. An interesting feature is the phase-locking between kinks in the two systems, and the role of kink/anti-kink excitations in coupled rings. Such phase-locking has been observed in continuous ring-systems [12, 16]. We view these Josephson arrays as model systems for studying the spatiotemporal dynamics of coupled oscillators, and more specifically for exploring kink interactions in discrete lattices.

4.1 System and governing equations

The layout of the discrete coupled ring system is shown in Fig. 4-1. Current is fed into the nodes of the outer ring (shown by arrows), flows radially through the junctions and is extracted at the center island. The equivalent open-ended system is shown in Fig. 4-2. For single rings and rows, L_s represented the self-inductance of a cell in the array, and M_h is the ratio of the mutual inductance between neighboring cells and L_s . In the case of coupled rows, we must add the effect of M_v , which is defined as the ratio of the mutual inductance between adjacent cells in the two arrays to the self inductance of a single cell. The coupling of M_v is schematically included in Fig. 4-2.

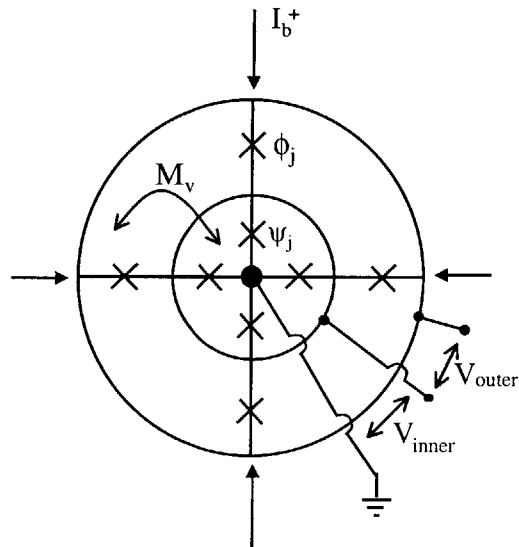


Figure 4-1: Schematic of inductively coupled ring system. A uniform current I_b is fed into each node, as indicated by arrows and is extracted from the center island. In experiments, we measure the dc voltages V_{inner} and V_{outer} . M_v is the mutual inductance between two adjacent cells of the inner and outer rings.

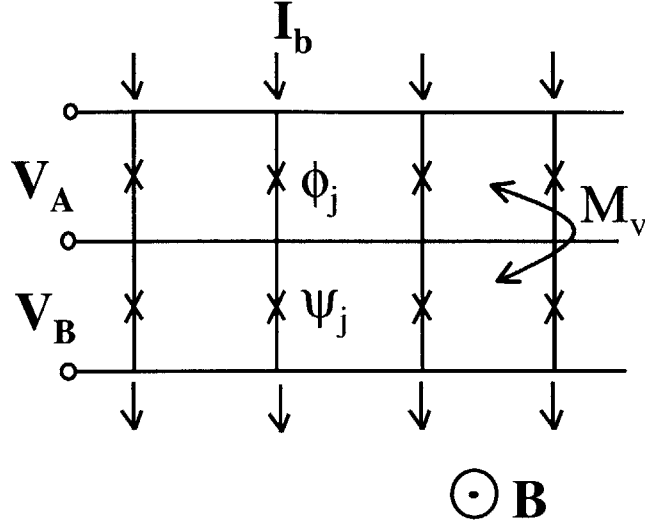


Figure 4-2: Inductively coupled rows.

In the coupled rings case, it is not possible to design a system with precisely the same geometric inductances for the inner and outer rings. Due to the geometry, we have $L_{\text{in}} < L_{\text{out}}$. (The cell inductance L_s has been replaced by L_x with “x” referring to either “in” or “out”). Therefore, M_h and M_v are different for each row, and will be replaced by $M_{h,x}$ and $M_{v,x}$. The discreteness parameters in the two systems will also be slightly different. We use $\Lambda_{\text{in}}^2 = L_J/L_{\text{in}}$ and $\Lambda_{\text{out}}^2 = L_J/L_{\text{out}}$. In simulations of coupled ring and row system, the nearest-neighbor coupling is included. However, in the analysis sections, we will sometimes neglect M_h and $M_{h,x}$ for simplicity.

We use ϕ_j and ψ_j to represent the phase of junction j in the outer ring and inner ring, respectively. The dynamics are governed by two coupled discrete sine-Gordon equations:

$$\mathcal{N}[\phi_j] - M_{h,\text{out}}(\mathcal{N}[\phi_{j+1}] + \mathcal{N}[\phi_{j-1}]) - M_{v,\text{out}}\mathcal{N}[\psi_j] = \Lambda_{\text{out}}^2 \nabla^2 \phi_j + I_b \quad (4.1)$$

$$\mathcal{N}[\psi_j] - M_{h,\text{out}}(\mathcal{N}[\psi_{j+1}] + \mathcal{N}[\psi_{j-1}]) - M_{v,\text{out}}\mathcal{N}[\phi_j] = \Lambda_{\text{out}}^2 \nabla^2 \psi_j + I_b \quad (4.2)$$

where, as before $\mathcal{N}[\varphi(t)] = \ddot{\varphi} + \Gamma\dot{\varphi} + \sin \varphi$ returns the total normalized current through a junction in response to its phase $\varphi(t)$ and $\nabla^2 \varphi_j = \varphi_{j+1} - 2\varphi_j + \varphi_{j-1}$ is the discrete Laplacian. For coupled rows, the parameters are identical and in equations (4.1- 4.2), $M_{h,x} = M_h$ and $M_{v,x} = M_v$ will be used.

At the boundaries of the open-ended system, equations (4.1- 4.2) will be different. In order to write the same equation for every junction, j , we can again invent dummy junctions $j = 0$ and $j = N + 1$ and define the following boundary conditions

$$\phi_0 = \phi_1 - 2\pi f \quad \text{and} \quad \phi_{N+1} = \phi_N + 2\pi f \quad (4.3)$$

$$\psi_0 = \psi_1 - 2\pi f \quad \text{and} \quad \psi_{N+1} = \psi_N + 2\pi f. \quad (4.4)$$

The two coupled rows have identical boundary conditions since the same external field is applied to both.

When the boundaries are made periodic, however, we find that it is possible to trap different amounts of flux in each ring. For this system, the boundary conditions become

$$\phi_{j+N} = \phi_j + 2\pi M_{\text{in}} \quad (4.5)$$

$$\psi_{j+N} = \psi_j + 2\pi M_{\text{out}} \quad (4.6)$$

where M_{in} is the integer number of flux quanta trapped in the inner ring, while M_{out} gives the number of fluxons trapped in the outer ring.

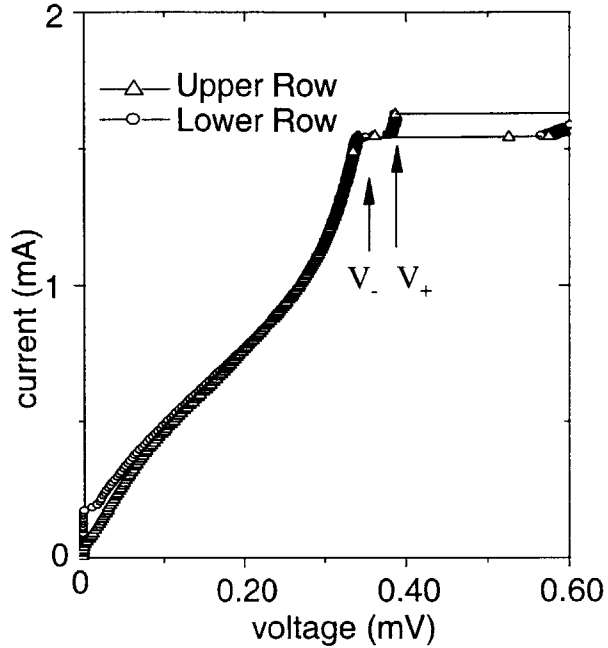


Figure 4-3: Measurements of an inductively coupled array, $N=54 \times 2$, on a ground plane. The triangles represent the voltage values measured across the top row, while the circles are voltage values across the bottom row. The measurements are taken at 8.2 K ($I_c R_n = 0.5$ mV and $f = 0.55$.)

4.2 Coupled Rows: Data and Simulations

Figure 4-3 shows the voltage across each row of a 54×2 array (above a ground plane) when the current is uniformly injected and $f = 0.55$. Two steps clearly appear in the I-V when the voltage is measured across a single row. The voltage values at the tops of the steps are labeled V_+ and V_- in the figure. Near the steps, the voltages across each row are the same, and the rows are said to be voltage-locked. When the voltage is measured across both rows, two steps are again seen, but at twice the voltage.

In Fig. 4-4, we plot the voltage positions of V_+ and V_- vs. frustration. The voltages are periodic in magnetic field, with period $f = 1$, which is an effect of the discreteness. The steps appear sharp at high values of f (near $f = 0.5$). Near $f = 0$ and $f = 1$, the steps are unstable and difficult to define. The asymmetry in the data reflects this. (The solid lines are a theoretical fit, discussed in the next section, which

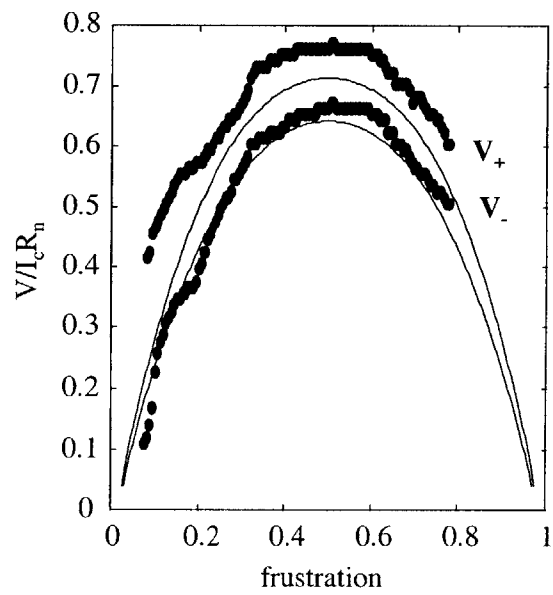


Figure 4-4: The measured voltages of both steps versus frustration, for an array of $N=54 \times 2$. This data was taken across one row of an array at $T = 8.2$ K. The solid line shows the model, with $\beta_c = 8.1$, $\Lambda_j^2 = 1.2$, $M_v = 0.13$, and $M_h = 0.13$. The voltage is normalized to $I_c R_n = 0.5$ mV.

uses parameters obtained from diagnostics.) Our devices are nearly symmetric, so that we can estimate the vertical nearest-neighbor coupling, M_v , to be approximately equal to M_h . The theory provides a qualitative picture of the data and seems to match best at high f .

The two steps appear to be stable experimentally only in a limited parameter range, with $\beta_c = 8 - 20$ and $\Lambda_J^2 = 1 - 1.5$. Although we have observed splitting in samples with much larger β_c and smaller Λ_J , we did not see voltage locking between the rows [37]. We find that, at the required temperatures, the output resistance is large, $r_o = 8.5 \Omega$. The steps appear in a voltage range of $V_- = 0.05 - 0.34$ mV and $V_+ = 0.21 - 0.39$ mV, corresponding to bandwidths of 140 MHz and 87 MHz, respectively. There is a threshold field value below which no steps appear.

Dynamical equations for the system are given in terms of the gauge-invariant phase differences across the junctions. As labeled in Fig. 4-2, we refer to the phases of junctions in the top row as ϕ_j and in the bottom row as ψ_j , where j indexes the junction's position in the array. The governing equations are derived by applying Kirchhoff's current laws and the RSJ model for the current through a single junction. With only nearest-neighbor inductances, the gauge-invariant phase differences in the upper and lower row junctions, ϕ_j and ψ_j , satisfy

$$\begin{aligned} \mathcal{N}[\phi_j] - M_h(\mathcal{N}[\phi_{j+1}] + \mathcal{N}[\phi_{j-1}]) - M_v\mathcal{N}[\psi_j] \\ = I_b + \Lambda_J^2(\phi_{j+1} - 2\phi_j + \phi_{j-1}) \end{aligned} \quad (4.7)$$

and

$$\begin{aligned} \mathcal{N}[\psi_j] - M_h(\mathcal{N}[\psi_{j+1}] + \mathcal{N}[\psi_{j-1}]) - M_v\mathcal{N}[\phi_j] \\ = I_b/I_c + \Lambda_J^2(\psi_{j+1} - 2\psi_j + \psi_{j-1}) \end{aligned} \quad (4.8)$$

respectively, where

$$\mathcal{N}[\phi(t)] \equiv \ddot{\phi} + \Gamma\dot{\phi} + \sin \phi$$

is a functional which returns the total (normalized) current through a junction in

response to its phase $\phi(t)$. Also, $\Gamma = \beta_c^{-1/2}$ and time has been normalized by $\tau = \sqrt{L_J C}$. Note that the inter-row coupling is provided only through terms involving M_v . If $M_h = M_v = 0$ (no inductive coupling), then the equations reduce to two independent discrete sine-Gordon equations. The equations (4.7- 4.8) hold for all junctions in the array, except for $j = 1$ and N . At the boundaries of the top row,

$$\begin{aligned} \mathcal{N}[\phi_1] - M_h(\mathcal{N}[\phi_2] + \mathcal{N}[\phi_1]) - M_v \mathcal{N}[\psi_1] \\ = I_b + \Lambda_J^2(\phi_2 - \phi_1 + 2\pi f) \end{aligned} \quad (4.9)$$

$$\begin{aligned} \mathcal{N}[\phi_N] - M_h(\mathcal{N}[\phi_{N-1}] + \mathcal{N}[\phi_N]) - M_v \mathcal{N}[\psi_N] \\ = I_b + \Lambda_J^2(\phi_{N-1} - \phi_N - 2\pi f) \end{aligned} \quad (4.10)$$

Similar equations hold for the lower row of junctions.

We have written Eqs. 4.7–4.10 in a form which emphasizes the spatial coupling introduced by nearest-neighbor inductances. However, to do numerical simulations, we write the system in a more compact form, similar to reference [38], which we will briefly describe. The junction phases constitute a $2N$ element vector, where the first N elements are the phases of the upper row and the last N elements are the phases of the lower row. Then the left side of Eqs. 4.7–4.10 can be expressed as the vector product of a $(2N \times 2N)$ inductance matrix, $\bar{\mathbf{M}}$, and $\mathcal{N}[\bar{\phi}]$, while the spatial derivative on the right side can be written in terms of a matrix operator. Non-zero elements of the inductance matrix produce coupling. For example, the elements $(j, 2j)$ and $(2j, j)$ are assigned a value of $-M_v$. All mutual inductances can be included by changing the inductance matrix, $\bar{\mathbf{M}}$. We retain only the nearest-neighbor terms, noting that use of the complete inductance matrix gives nearly identical results.

We use a fourth-order Runge-Kutta scheme to solve the system. In order to implement this technique, we reduce the equations to two first-order systems by making the substitution, $\bar{\mathbf{v}} = d\bar{\phi}/dt$. The coupled systems $d\bar{\mathbf{v}}/dt$ and $d\bar{\phi}/dt$ are then integrated in equal time intervals. For damping and discreteness parameters approximating those of our experimental system, numerically simulated I-V's also exhibit two voltage steps, as shown in Fig. 4-5.

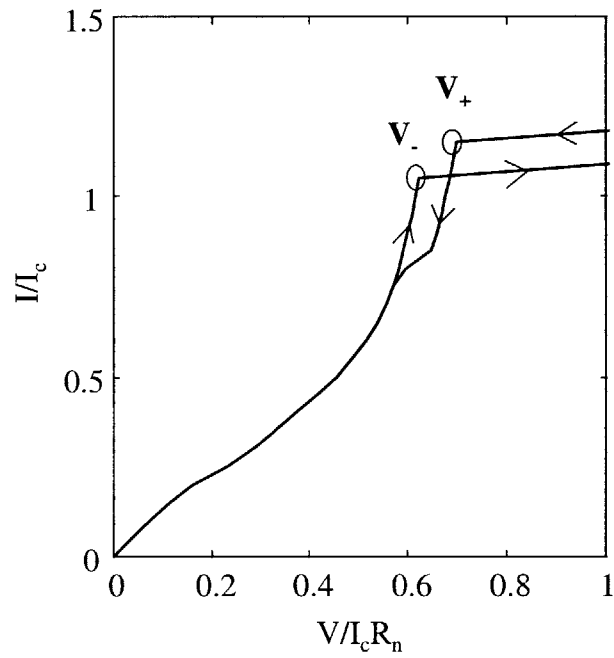


Figure 4-5: Simulated current-voltage characteristic for an inductively coupled array of 54×2 junctions at $f = 0.55$. The voltage across a single row is plotted. The parameters used are $\beta_c = 10.8$ and $\Lambda_j^2 = 1.56$.

The figure shows the voltage measured across a single row. Note that both steps appear, even when the voltage is measured across only one row. In the simulations, the voltages of both rows are identical. This contrasts with our experiments, where the voltages of the rows are different for small bias currents. There also appears to be more hysteresis on the steps than in experiments. This is perhaps because we have not included thermal fluctuations in our simulations. In experiments, thermal fluctuations cause switching, making it difficult to trace the entire step.

The numerical phase solutions, $\phi_j(t)$ and $\psi_j(t)$, provide valuable information which is not available through our experiments. We will use these to better describe the junction dynamics when the system is biased on a step and to specify the influence of magnetic field on the step voltage.

While we bias the system of 54x2 junctions at the top of a voltage step (at the points marked as V_- and V_+), Figs. 4-6(a) and (b) show the phase evolution in time for a single set of vertically adjacent junctions near the middle of the array ($j = 25$). The junction phases, $\phi_{25}(t)$ and $\psi_{25}(t)$, can be approximated by the sum of a linear function in time and a small periodic oscillation. In the V_- state (Fig. 4-6(a)), the linear part of the phase plots show an offset between the rows, while the sinusoidal part is phase-shifted. However, in the V_+ state (Fig. 4-6(b)), the rows have no relative offsets or phase-shifts, and the plots of each row are indistinguishable. A linear fit through the points shows that the average $\phi_j(t)$ and $\psi_j(t)$ have slopes proportional to the step voltage. This is consistent with the fact that the DC voltage is calculated by taking a time average of $d\phi/dt$ for the first row and $d\psi/dt$ for the second row. In the insets, we plot the voltage vs. time. The oscillation is sinusoidal, with a single frequency ω which is equal to the slope of the linear fits. We find that the oscillation becomes more complicated when the system is not biased on a step. At voltages below the lower step, more frequency components appear in the oscillation. At these voltages, there is generally a phase-shift between the rows, but it is not clear that the phase-shift remains constant in time. At voltages above the upper step, the oscillations continue at a single frequency but with much smaller amplitude. The phase solutions in this regime appear to be whirling modes, as described in Ref. [26],

and adjacent junctions in each row are always out-of-phase.

We find that the spatial distribution of phases across the array exhibits similar behavior. In Figs. 4-7(a) and (b), we plot the phase vs. junction number, at a given point in time. The function is almost linear with an approximate slope of $2\pi f$. The insets show the instantaneous voltage vs. junction number for each row. These plots are reminiscent of under-sampled sine waves. Thus, the functional form of the wave is more easily determined by examining the voltage vs. time plots of successive junctions. We find that the spatial oscillation is also sinusoidal, with a wavenumber of $2\pi f$. Again, on the lower-voltage step (Fig. 4-7(a)), the oscillations of each row are phase-shifted with respect to the other, whereas the oscillations are in-phase on the higher voltage step (Fig. 4-7(b)). Although it is more difficult to see in the figures, we find that there is again an offset between the rows for the lower step and not for the higher step.

In summary, the simulations indicate that solutions for the phases at these points of the I-V can be well approximated by

$$\phi_j(t) = \chi_j(t) + \theta + c + a \sin(\chi_j + \theta) \quad (4.11)$$

and

$$\psi_j(t) = \chi_j(t) - \theta + c + a \sin(\chi_j - \theta) \quad (4.12)$$

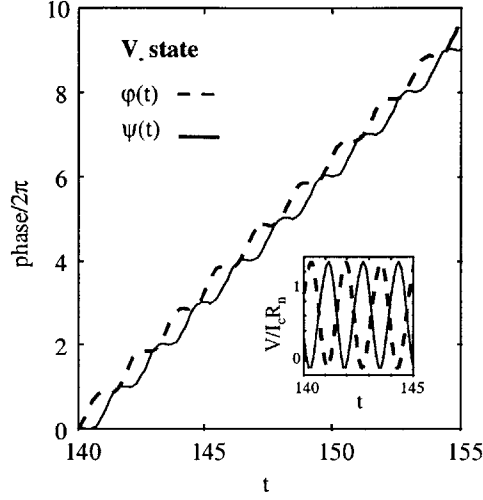
where

$$\chi_j(t) = \omega t + 2\pi f j. \quad (4.13)$$

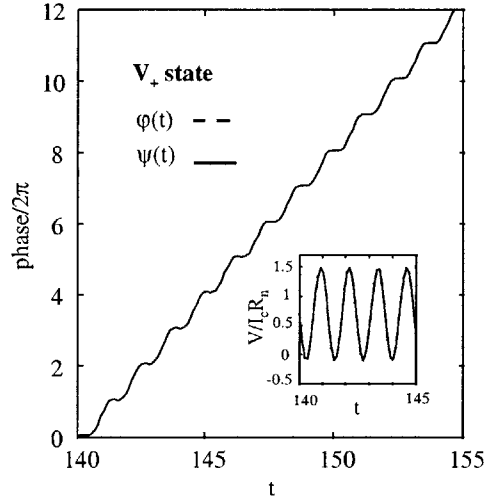
The phase difference between the rows is given by 2θ ; e.g. $\theta = 0$ for the symmetric in-phase state (V_+) and $\theta = \pi/2$ for the anti-symmetric state (V_-). The constant a represents the amplitude of the oscillations. The constant c denotes the phase difference between the linear rotating part and the sinusoidal oscillation part of the waveform.

The above traveling wave solution works well throughout most of the array. Near the array edges, we do see some reflections, and the junction oscillations no longer

look sinusoidal. However, the simulations show that these effects damp out within a few junctions from the edge.

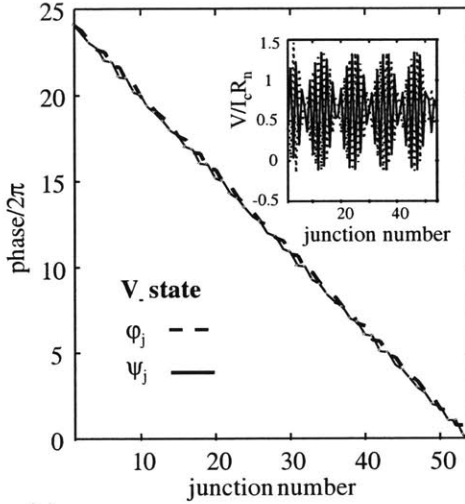


(a)

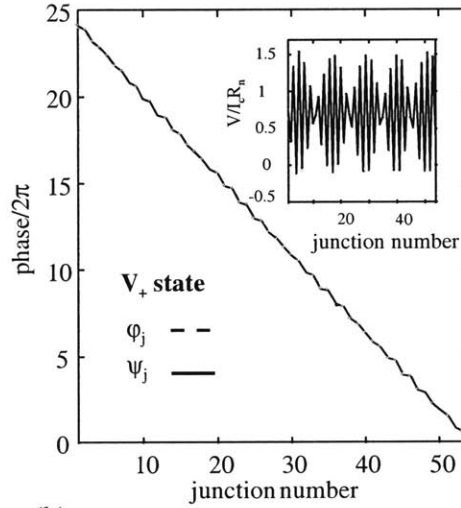


(b)

Figure 4-6: (a) Phase evolution in time near the middle of the array ($j = 25$), for the system with $N=54 \times 2$ biased at point V_- . The upper row is represented by a dashed line, while the lower row corresponds to the solid line. The inset shows the corresponding voltage vs. time for each row. (b) For the system biased at point V_+ , we show the phase evolution in time near the middle of the array ($j = 25$). Dashed and solid lines correspond to the upper and lower rows, respectively. The inset shows the corresponding voltage vs. time for each row. Time is normalized in steps of τ .



(a)



(b)

Figure 4-7: (a) Phase vs. junction number, j , at a fixed time, for the system with $N=54 \times 2$ biased at V_- . The upper row is represented by a dashed line, while the lower row corresponds to the solid line. The inset shows the corresponding voltage vs. j . (b) For the system biased at V_+ , we show the phase vs. junction number, j , at a fixed time. Dashed and solid lines correspond to the upper and lower rows, respectively. The inset shows the corresponding voltage vs. j . Since the solutions are in phase, they appear as one line in the plots.

4.3 Analysis for in-phase and anti-phase solutions

In this section we substitute the suggested solutions, Eq. 4.11, into the governing Eq. 4.7 to determine relationships among the parameters a , c , θ , ω and I_b for a given f .

To clarify the discussion, we will carry out our analysis neglecting M_h in Eqs. 4.7 and 4.8 and then at the end show how M_h can be included. Substitution of Eq. 4.11 yields

$$\begin{aligned} & \omega^2 a [\sin(\chi_j + \theta) - M_v \sin(\chi_j - \theta)] - \Gamma \omega a [\cos(\chi_j + \theta) \\ & - M_v \cos(\chi_j - \theta)] - \Gamma \omega (1 - M_v) - \omega_1^2 a \sin(\chi_j + \theta) + I_b / I_c \\ & = \sin[\chi_j + \theta + c + a \sin(\chi_j + \theta)] + M_v \sin[\chi_j - \theta + c + a \sin(\chi_j - \theta)] \end{aligned} \quad (4.14)$$

where

$$\omega_1^2 = 4\Lambda_J^2 \sin^2(\pi f). \quad (4.15)$$

The non-linear terms on the right-hand side can be expanded into a Fourier-Bessel series [39],

$$\begin{aligned} & \sin[\chi_j \pm \theta + c + a \sin(\chi_j \pm \theta)] = \\ & \sum_{m=-\infty}^{\infty} J_m(a) \sin[(m+1)(\chi_j \pm \theta + c) - mc]. \end{aligned} \quad (4.16)$$

Using this expansion, we can apply the method of harmonic balance to Eq. 4.14. This method neglects all the harmonics in Eq. 4.14 except the zeroth and the first, and balances the coefficients of these two modes. This method was previously used in the Josephson junction context in order to study a single junction [39], a simple in-phase solution of two-dimensional arrays [40], and single-harmonic solutions in two-dimensional arrays [41]. It was also applied to the study of zero-field steps and the Fiske steps in one-dimensional continuous junctions [42, 43].

After some algebraic manipulation, balancing of the DC terms yields

$$I_b = I_c(1 + M_v)[\Gamma\omega - J_1(a) \sin c]. \quad (4.17)$$

Balancing the $\cos \chi_j$ terms, we find

$$\begin{aligned} & \sin \theta [-\omega_1^2 a + \omega^2 a(1 + M_v)] + \cos \theta [-\Gamma\omega a(1 - M_v)] \\ &= \sin \theta [J_0(a)(1 + M_v) \cos c] + \cos \theta [J_0(a)(1 - M_v) \sin c] \end{aligned} \quad (4.18)$$

while balancing the $\sin \chi_j$ terms gives

$$\begin{aligned} & \sin \theta [\Gamma\omega a(1 + M_v)] + \cos \theta [-\omega_1^2 a + \omega^2 a(1 - M_v)] \\ &= \sin \theta [-J_0(a)(1 + M_v) \sin c] + \cos \theta [J_0(a)(1 - M_v) \cos c]. \end{aligned} \quad (4.19)$$

From Eq. 4.8, we obtain the same equations except θ is replaced by $-\theta$. Since Eq. 4.17 does not involve θ , it is unchanged. However, Eqs. 4.18 and 4.19 are changed, and we obtain a total of five constraints for the parameters, a , c , θ , ω and I_b/I_c for each f .

It is easy to see, however, that the five equations can never be satisfied simultaneously when $\sin \theta \neq 0$ and $\cos \theta \neq 0$. This means that the ansatz is consistent if and only if $\sin \theta = 0$ or $\cos \theta = 0$, in accordance with our numerical observation. In this case, Eqs. 4.17-4.19 reduce to

$$[\Gamma\omega - J_1(a) \sin c](1 + M_v) = I_b/I_c \quad (4.20)$$

$$\Gamma\omega a + J_0(a) \sin c = 0 \quad (4.21)$$

$$\omega^2 a(1 \pm M_v) = \omega_1^2 a + J_0(a)(1 \pm M_v) \cos c \quad (4.22)$$

where the $-$ sign is taken for $\sin \theta = 0$ (in-phase) and the $+$ sign is taken for $\cos \theta = 0$ (anti-phase). Equation 4.20 simply computes I_b once the other parameters are obtained. Thus we have only two equations for a, c, ω . The parameter c can be

eliminated from Eqs. 4.21 and 4.22, and we obtain a single equation

$$(J_0(a)/a)^2 = (\omega\Gamma)^2 + (\omega^2 - \omega_{\pm}^2)^2 \quad (4.23)$$

where

$$\omega_{\pm}^2 = \frac{\omega_1^2}{1 \mp M_v} = \frac{4\Lambda_J^2}{1 \mp M_v} \sin^2(\pi f).$$

As ω is varied, we obtain a one-parameter family of roots for a . Thus we supplement the equation with a “resonance condition” $da/d\omega = 0$, which maximizes the oscillation amplitude, a . Solved with the condition, Eq. 4.23 gives us the resonance frequency

$$\omega^2 = \omega_{\pm}^2 - \Gamma^2/2 \quad (4.24)$$

The amplitude of the oscillations is then given implicitly by

$$\left(\frac{J_0(a)}{a}\right)^2 = \omega_{\pm}^2 \Gamma^2 - \frac{\Gamma^4}{4} \quad (4.25)$$

Finally Eq. 4.20 gives the corresponding I_b . When we include horizontal nearest-neighbors in our equations, the form of the resonance frequencies, Eq. 4.24, and amplitude, Eq. 4.25 remain the same. However, ω_{\pm} is replaced by

$$\omega_{\pm}^2 = \frac{4\Lambda_J^2}{1 \mp M_v - 2M_h \cos(2\pi f)} \sin^2(\pi f). \quad (4.26)$$

In Fig. 4-8, the theory is compared with simulation results for $\beta_c = 10.8$ and $\Lambda_J^2 = 1.56$. We see that the resonant voltages are predicted well by this theory. Our experimental data in Fig. 4-4 has similar trends, but the voltage values do not match the theory as well. We have found better fits to the data by modifying the values of β_c and M_h (within the uncertainty of our diagnostic results) used for the theoretical curve.

As observed, the resonance condition we imposed appears appropriate to calculate the steps. However, one may also choose an alternative supplementary condition, $dI/d\omega = 0$. This is perhaps a more intuitive condition to calculate a step in the I-V,

but it does not lead to an analytical estimate for the frequency. Nonetheless, the roots can be found by numerically solving the algebraic system, and it is determined that the resonant frequency is extremely close to (but larger than) ω in Eq. 4.24 when Γ is small. Thus, we may choose either condition, and our results are altered little by the choice.

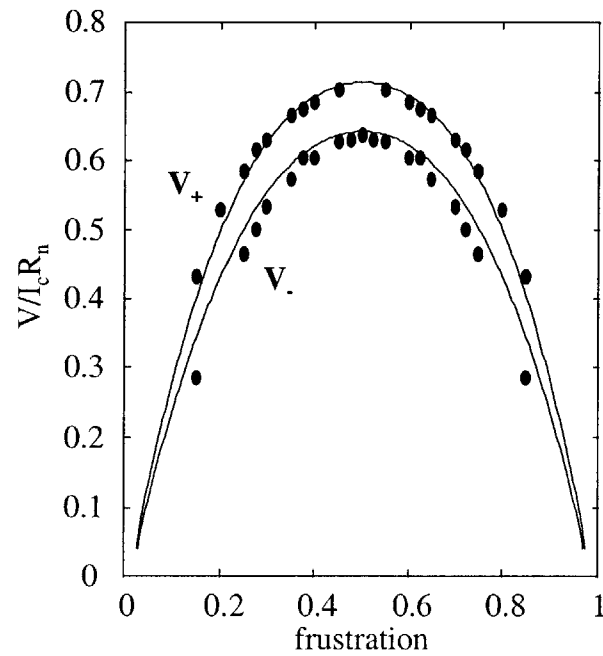


Figure 4-8: Voltage positions of flux flow steps in simulated I-V's (solid circles). The voltage is normalized to $I_c R_n$. The solid line represents the theory of Eq. 4.26.

4.4 Coupled Rings: Data and Simulations of non-voltage locked states

In the case of open-ended rows, inductive coupling between two identical rows causes a splitting of the dispersion relation. The rows tend to phase-lock and an in-phase resonance occurs at a higher frequency than the anti-phase resonance. For the case of coupled rings, the possibility of trapping different numbers of kinks in the two rings leads to new and exciting dynamics. Due to a difference in their boundary conditions, the two coupled oscillators are no longer identical. As we saw in the case of the single rings, the boundary condition determines which spatial modes can resonate in the system and at which DC voltages they will be excited. In this section, we will use experiments and numerical simulations to explore the resonances which can occur for a system of coupled rings with non-identical boundary conditions and the possibility of phase-locking between the rings.

Figure 4-1 shows a schematic of inductively coupled rings with $N = 4$. The experimental system is fabricated with a planar geometry, as shown. For this system, it is impossible to make the loops of the inner ring cells identical to those of the outer ring cells. The effect is a difference in the loop inductances for the inner and outer rings. For our system with $N = 4$, we estimate the loop self-inductances to be roughly $L_{\text{in}} = 21$ pH and $L_{\text{out}} = 26$ pH. The corresponding non-identical discreteness parameters Λ_J^2 are given as $\Lambda_x^2 = L_J/L_x$ where “x” refers to either “in” or “out”. The radius of the outer ring is $28 \mu\text{m}$, and the junctions are designed to have areas of $3 \times 3 \mu\text{m}^2$. When the system is cooled in the presence of a perpendicular magnetic field to below the superconducting transition, the total flux bounded by the continuous superconducting rings becomes trapped in units of $\Phi_o = h/2e$. A single unit of quantized flux is called a kink (or vortex) if the flux is along the applied field and an anti-kink if it is opposite. If there are $m_{\text{v,in}}$ and $m_{\text{v,out}}$ kinks in the two rings, and $m_{\text{a,in}}$ and $m_{\text{a,out}}$ anti-kinks, then the net, conserved flux in each ring is $M_{\text{in}} = m_{\text{v,in}} - m_{\text{a,in}}$ and $M_{\text{out}} = m_{\text{v,out}} - m_{\text{a,out}}$.

In Fig. 4-9, we show an example IV curve for the coupled rings when $M_{\text{in}} \neq M_{\text{out}}$.

The figure shows a close-up of the Eck steps above $I_b \approx 2.2 \mu\text{A}$. There are two kinks (drawn as open circles) trapped in the inner ring and one in the outer ring. In Fig. 4-9(a), an HV step occurs in the outer ring at $I_b = 2.75 \mu\text{A}$. Based on studies of single rings, we associate this resonance with the excitation of a kink/anti-kink pair. The step steepens as the kink and anti-kink approach their maximum speeds. Numerical simulations will be used to study the junction oscillations associated with this pair as well as the influence of the inner ring kinks on those of the outer ring.

In both experiments and numerical simulations, an intriguing observation is made: unless $M_{\text{in}} = M_{\text{out}}$, HV steps appear in only one ring at a time. Furthermore, *which ring* will have an excited pair and when depends sensitively on parameters. Figure 4-9(b) shows the IV at a slightly higher temperature, corresponding to an increase of Λ_x^2 and Γ by only 1.3 percent from the IV of Fig. 4-9(a). At this temperature an HV step appears in the inner ring instead.

We observe, for every distinct combination of $M_{\text{in}} \neq M_{\text{out}}$, a parameter regime where pairs are excited only in the outer ring, another parameter regime where pairs are excited only in the inner ring, and a transition region in temperature from one state to the other. The reason for a transition from one state to another as the parameters are varied is related to the stability of the states. In fact, we observe similar transitions among many of the possible dynamical states of the system. For a given M_{in} and M_{out} , each ring can be in one of the following states: (1) $V = 0$, (2) Eck step, (3) HV step, and (4) whirling branch (admittedly a simplified picture, for the purpose of discussion), leading to 16 possibilities for the system. Which of these possible states appears depends on both the driving current and the system parameters. In addition, more than one state can be stable for a given driving current when the system is hysteretic.

We now consider the numerical simulation of Fig. 4-10, with $M_{\text{in}} = 2$ and $M_{\text{out}} = 1$, as in the experiment of Fig. 4-9. Although the parameters used for the simulation slightly differ from those of Fig. 4-9, with Fig. 4-10 corresponding to a system with lower temperature, many of the same dynamical features appear. At a normalized current value of 0.15, both rings begin on their Eck steps. The inner ring has two

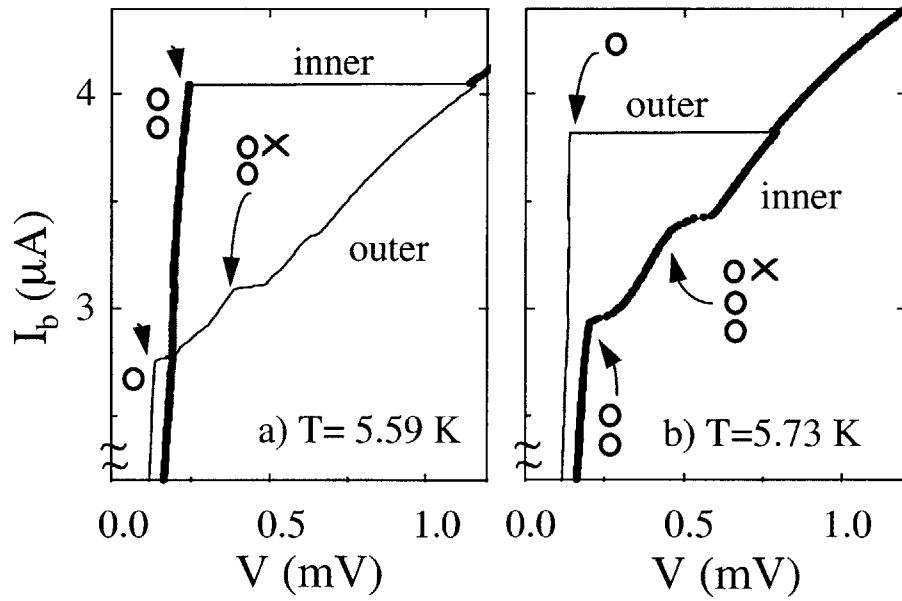


Figure 4-9: Measured IV characteristic with $N = 4$. These close-ups begin at a bias current of $2.2 \mu\text{A}$, when both rings are on Eck steps. The sample parameters are $L_{\text{out}} = 26 \text{ pH}$, $L_{\text{in}} = 21 \text{ pH}$, and $j_c(T = 0) = 83.3 \text{ A/cm}^2$. $M_{\text{in}} = 2$ and $M_{\text{out}} = 1$. (a) $T = 5.59 \text{ K}$, giving $\Gamma = 0.0507$, $\Lambda_{\text{in}}^2 = 2.67$, and $\Lambda_{\text{out}}^2 = 2.23$. A kink/anti-kink pair is excited in the outer ring at $I_b = 2.75 \mu\text{A}$, causing an HV step. (b) $T = 5.73 \text{ K}$, giving $\Gamma = 0.0514$, $\Lambda_{\text{in}}^2 = 2.74$, and $\Lambda_{\text{out}}^2 = 2.29$. A kink/anti-kink pair is excited in the inner ring at $I_b = 2.9 \mu\text{A}$.

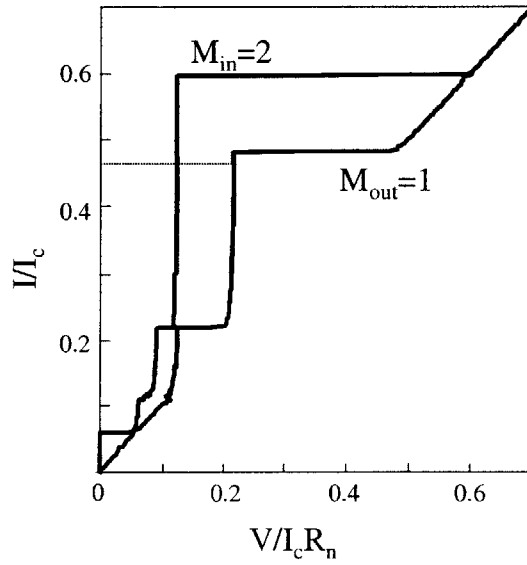


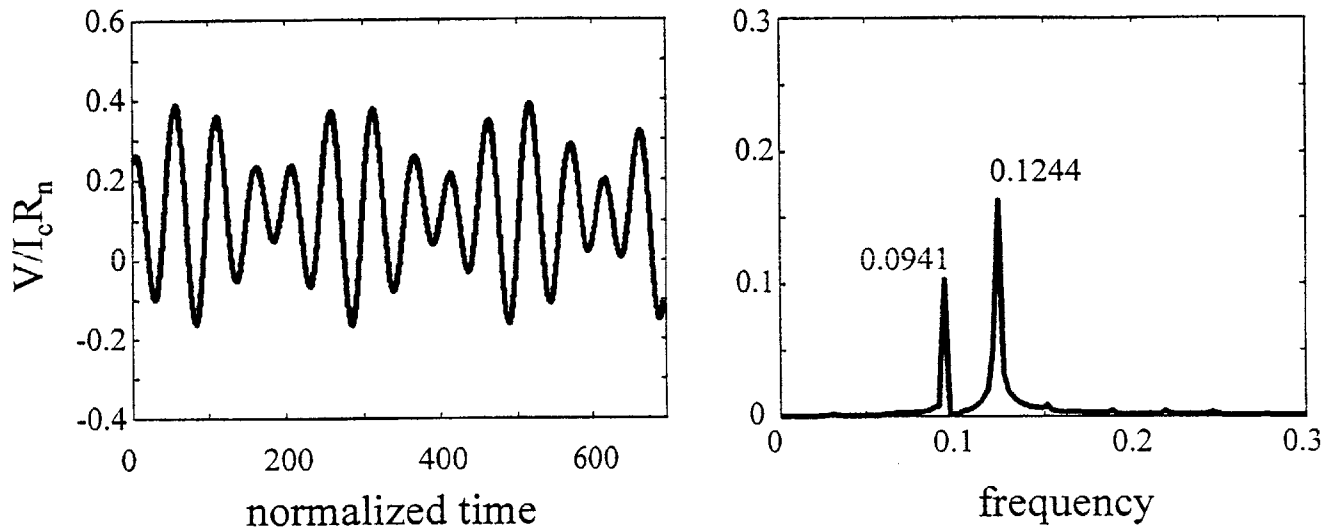
Figure 4-10: Numerical IV curve for the $N = 4$ ring with $M_{in} = 2$ and $M_{out} = 1$. The parameters are $\Lambda_{in}^2 = 2.98$, $\Lambda_{out}^2 = 2.43$, and $\Gamma = 0.048$ ($\beta_c = 429$). The phase dynamics at $I/I_c = 0.46$, which is marked by a dotted line, will be shown in detail in Figures 4-11 through 4-14.

kinks trapped while the outer ring has one kink trapped. Just above $I/I_c \approx 0.2$, the outer ring switches to an HV step, as in Fig. 4-9(a). In the simulation, the Eck voltage of the inner ring seems to be affected by this jump. For a wide range of currents, this Eck step and HV step combination is stable in the system.

Since we have access to the time-dependent solutions of the junctions, we can now study the influence of the inner ring kinks on those of the outer ring. At the normalized current of 0.46 (the dotted line in Fig. 4-10), the inner ring Eck voltage is $V_{\text{in}}/(I_c R_n) = 0.1236$ while the outer ring has its HV step at $V_{\text{out}}/(I_c R_n) = 0.2176$. Figure 4-11(a) shows the time-dependent solution for the voltage of junction 2 at $I/I_c = 0.46$. The FFT of the AC component is also included. Although the inner ring is on an Eck step, the voltage oscillations are quasi-periodic in time. Since the two frequencies are not multiples of each other, the FFT which is shown calculates only the lower frequency very accurately. Within the error, the higher of the two frequencies corresponds to the inner ring Eck voltage. The presence of the lower frequency in the inner ring solution is purely an effect of the coupling to the outer ring and it does not appear for single rings on the $M = 2$ Eck step. Figure 4-11(b) shows the time-dependent solution for the voltage of junction 2 in the outer ring. This solution is also quasi-periodic. The sum of the two frequencies $0.0941 + 0.1244 = 0.2185$ is approximately equal to the HV step voltage, 0.2176. Based on studies of HV steps in single rings [34], this type of quasi-periodic solution is expected for HV steps. The outer ring has a single trapped kink and an excited kink/anti-kink pair. The total of two kinks lead to an excitation of a $k = 2$ spatial mode and a time oscillation at 0.1244, which is the same as the inner ring oscillation for two kinks. The single anti-kink corresponds to an excitation of the $k = 1$ mode and results in a time oscillation at 0.0941. The sum of the two kinks traveling in one direction and the anti-kink moving in an opposite direction results in a voltage step at $0.0941 + 0.1244$.

In order to confirm that the two frequencies do correspond to separate excitations of $k = 1$ and $k = 2$ spatial modes, we can add and subtract the solutions of various $\dot{\phi}_j$ to eliminate modes. For the $k = 1$ mode, junctions $j = 1$ and $j = 3$ should be exactly out-of-phase. Therefore by adding the AC solutions of $\dot{\phi}_1 + \dot{\phi}_3$, the $k = 1$

(a) Inner Ring: on Eck step, $M_{in} = 2$



(b) Outer Ring: on HV step, $M_{out} = 1$

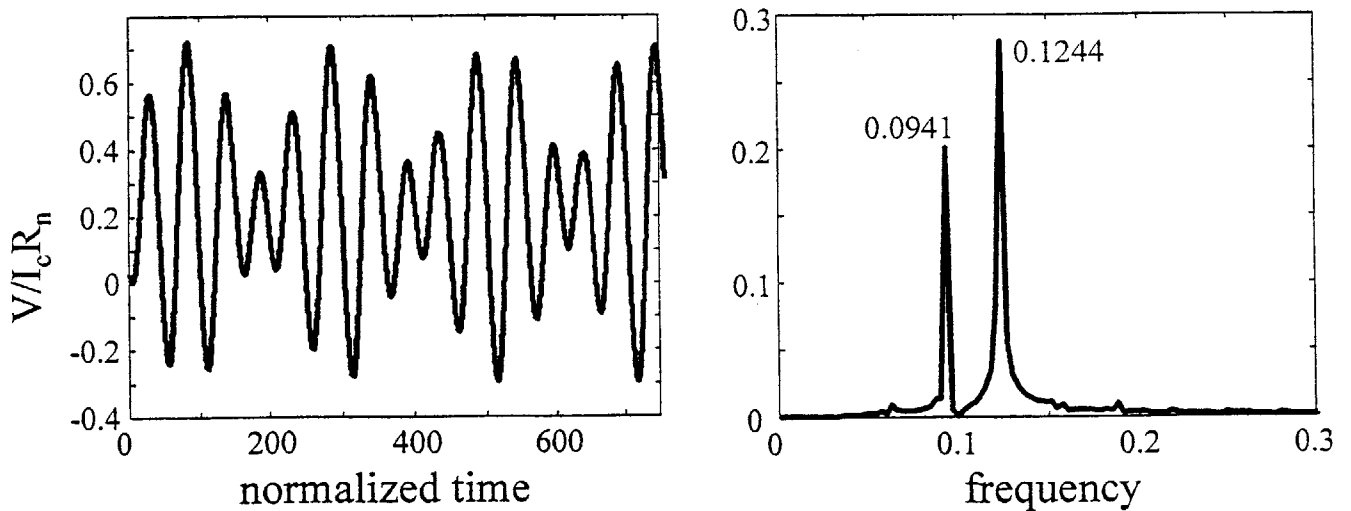


Figure 4-11: AC voltages versus time and corresponding FFTs at $I/I_c = 0.46$. (The DC component is not included in the FFT.) The signals are quasi-periodic with both rings at identical frequencies of $\omega = 0.0941$ and $\omega = 0.1244$.

mode is eliminated. As Fig. 4-12 shows, the lower frequency disappears in the FFT of $\dot{\phi}_1 + \dot{\phi}_3$, and the higher frequency corresponds to the $k = 2$ mode. Likewise, the FFT of $\dot{\phi}_1 + \dot{\phi}_2$ eliminates the $k = 2$ mode and shows that the lower frequency corresponds to an excitation of $k = 1$.

We now examine the phase relationships *between* the rings. Based on the results of coupled rows, we begin by looking for in-phase and anti-phase oscillations of corresponding junctions in the two rings. If the junctions oscillate with equal amplitudes exactly in-phase or anti-phase, then one of the sum or difference $\phi_j \pm \psi_j$ will be zero. In this case, however, we already know from Fig. 4-11(a) and (b) that although the oscillations in the two rings are at identical frequencies, their amplitudes differ. Therefore they will not exactly cancel. This is what is observed in Fig. 4-13. The anti-phase mode seems to dominate, but $\dot{\phi}_2 + \dot{\psi}_2$ does not exactly cancel since the oscillations have larger amplitude in the outer ring. In order to examine the phase relationships for oscillations of unequal amplitudes, we can also plot $\phi_j(t)$ versus $\psi_j(t)$. Since the quasi-periodic nature of the solutions can be confusing, the k -modes are separated by plotting $(\dot{\phi}_1 + \dot{\phi}_2)$ versus $(\dot{\psi}_1 + \dot{\psi}_2)$ for $k = 1$ in Fig. 4-14 and separately plotting $(\dot{\phi}_1 + \dot{\phi}_3)$ versus $(\dot{\psi}_1 + \dot{\psi}_3)$ for $k = 2$. These plots show, as does the FFT of Fig. 4-13, that the solutions are not perfectly composed of two frequencies, but that the oscillations are anti-phase in nature.

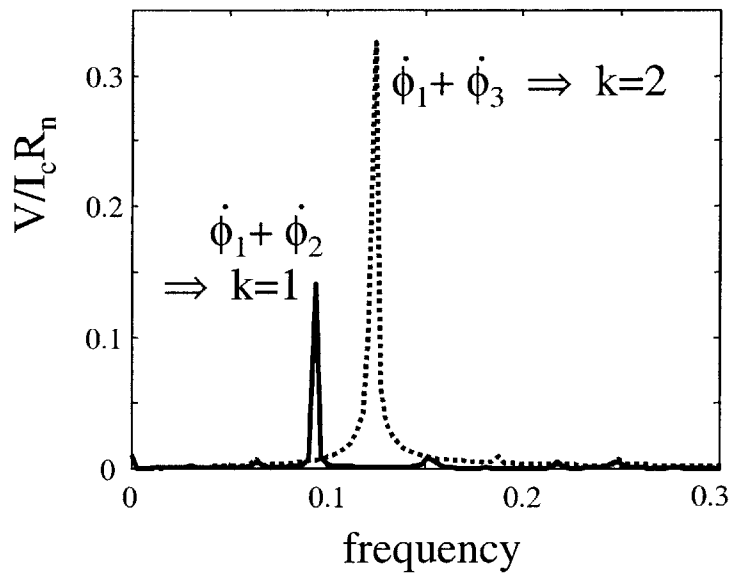


Figure 4-12: FFTs showing that the lower of the two frequency components ($\omega = 0.0941$) corresponds to an excitation of the $k = 1$ mode, while the higher of the frequencies ($\omega = 0.1244$) corresponds to $k = 2$. The $k = 1$ mode is isolated by adding $\dot{\phi}_1 + \dot{\phi}_2$, which are exactly out-of-phase for $k = 2$. Likewise, the FFT of $\dot{\phi}_1 + \dot{\phi}_3$ isolates the $k = 2$ mode. The solutions for $\dot{\phi}_j$ were obtained from the numerical simulations shown in in Figure 4-10 for $I/I_c = 0.46$.

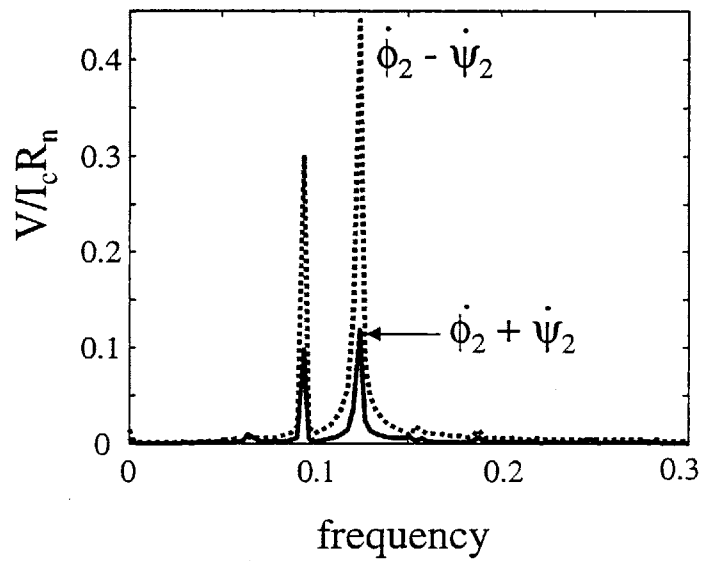


Figure 4-13: FFTs of $\dot{\phi}_2 \pm \dot{\psi}_2$, without their DC components. This plot shows that the anti-phase component is largest. The solutions for $\dot{\phi}_2$ and $\dot{\psi}_2$ were obtained from the numerical simulations shown in in Figure 4-10 for $I/I_c = 0.46$.

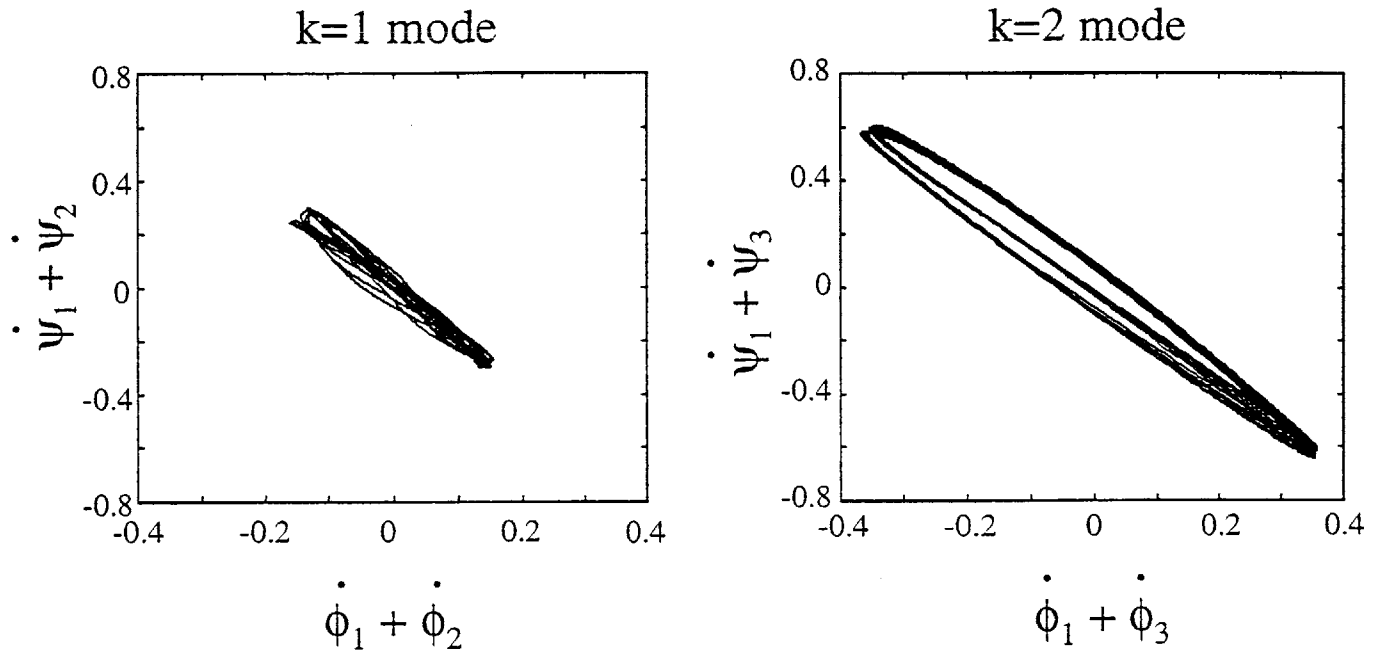


Figure 4-14: Phase relationships between the rings for the $k = 1$ mode and the $k = 2$ mode separately. The solutions for $\dot{\phi}_j$ and $\dot{\psi}_j$ were obtained from the numerical simulations shown in in Figure 4-10 for $I/I_c = 0.46$.

In Fig. 4-10, we noted a small shift in the Eck voltage of the inner ring at the point where the outer ring switched to an HV step. Such voltage shifts are typical in both experimental and numerical data on coupled rings. A clear experimental example is provided in Fig. 4-15, where $M_{\text{in}} = 1$ while $M_{\text{out}} = 0$. As the bias current is increased from zero, the single kink in the inner ring begins to move, producing an average DC voltage across the inner ring junctions. Meanwhile, the outer ring, which has no trapped kinks, remains superconducting. As the inner ring approaches a constant voltage on the Eck step, we can assume (and numerical simulations confirm) that the resonating linear waves in the inner ring excite similar waves in the outer ring as well. At approximately $I_b = 7.2 \mu\text{A}$, the outer ring's superconducting state becomes unstable and a step appears. The up path of the IV is shown separately in the left inset of Fig. 4-15. This instability is associated with the excitation of a kink/anti-kink pair.

As soon as the outer ring switches to the HV step, the voltage of the inner ring (on its Eck step) shifts to a slightly lower value. The step which appears on the up path of the outer ring IV has approximately twice the voltage of the inner ring step. This is consistent with the picture that the outer ring kink and anti-kink move at nearly equal speeds and in opposite directions, producing twice the dc voltage of the kink moving in the inner ring. The sudden shift in the inner ring Eck voltage (which is clearer in the inset) indicates that the inner ring kink slows down when a pair appears in the outer ring. This suggests that the inner ring kink may have slowed to phase lock with the kink in the outer ring.

At still higher driving current, the excited pair disappears again as the Eck step in the inner ring becomes unstable. At this point (near $7.75 \mu\text{A}$), the outer ring switches back to the superconducting state and the inner ring switches to a uniform whirling state [11]. On the down path (the right inset of Fig. 4-15 with current decreasing monotonically from $10 \mu\text{A}$), a pair is again excited in the outer ring and persists as the current bias is decreased even below $7.2 \mu\text{A}$, causing hysteresis in the IV. Surprisingly, the voltage of this HV step gradually decreases to well below twice the voltage of the inner ring Eck step. When the pair disappears from the outer ring, the inner ring

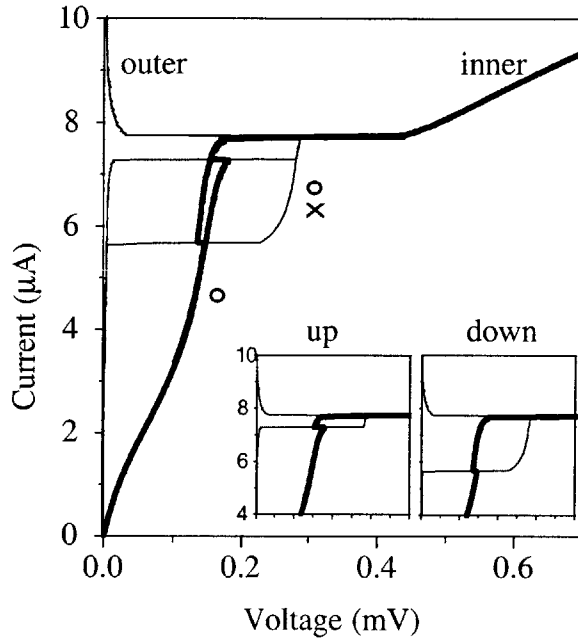


Figure 4-15: Current-voltage curves for the $N=4$ system with $M_{\text{in}} = 1$ and $M_{\text{out}} = 0$. The sample parameters are $L_{\text{in}} = 21$ pH, $L_{\text{out}} = 26$ pH, and $j_c(T = 0) = 139$ A/cm². $T = 7.22$ K, giving $\Gamma = 0.0823$, $\Lambda_{\text{in}}^2 = 2.55$, $\Lambda_{\text{out}}^2 = 2.07$.

kink speeds up again, as indicated by the shift in the Eck step voltage at $I = 5.6 \mu\text{A}$.

The experiments show two surprising results. First, a shift to a lower voltage occurs in the Eck step as soon as the outer ring is on the HV step. This adjustment of the kink velocity clearly illustrates the existence of interactions between the two rings. Second, the voltage of the Eck step is not exactly half of the voltage of the HV step. This observation indicates that not the whole array is phase-locked. We have performed many simulations to study these aspects in more detail.

In order to better understand the interactions described by the data in Fig. 4-15, we have simulated the system with parameters similar to our experiments. However, we find that simulations of systems with larger N , where the kinks are very localized and easy to identify, are the most elucidating. Figure 4-16 shows an IV characteristic from a simulation. In this case, there are $N = 51$ junctions in each ring. For a range of bias currents ($I_b < 0.57 I_c$), kink/anti-kink pairs are excited in the outer

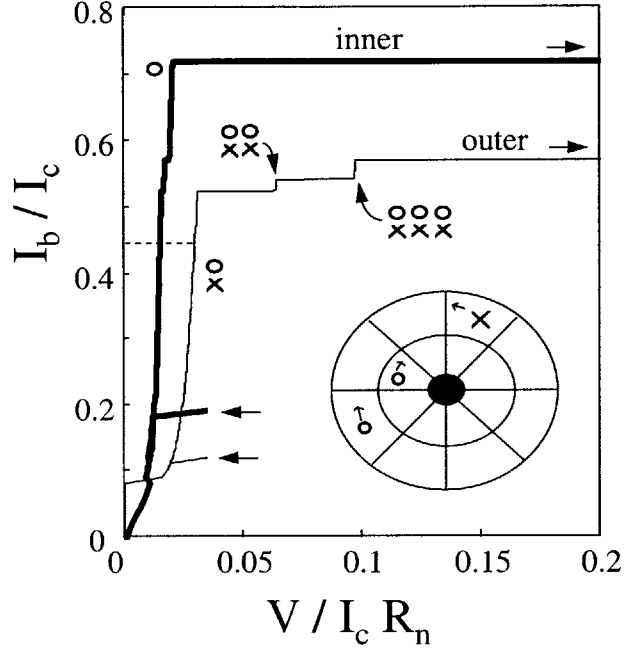


Figure 4-16: Simulated IV characteristic for parameters: $M_{\text{in}} = 1$, $M_{\text{out}} = 0$, $N = 51$, $\Gamma = 0.1$, $\Lambda_{\text{out}}^2 = 1.76$, $\Lambda_{\text{in}}^2 = 2.55$, $M_{\text{h,out}} = 0.08$, $M_{\text{v,out}} = 0.12$, $M_{\text{h,in}} = 0.12$ and $M_{\text{v,in}} = 0.17$. The nearly constant voltage steps correspond to the motion of the kinks (represented by open circles) and anti-kinks (represented by crosses) at their maximum speeds. The inset shows the relative motion of the kinks and the anti-kink for one excited pair in the outer ring.

ring. The inset shows the relative motions of the kinks and the anti-kink when one pair is excited in the outer ring.

In Fig. 4-16, we plot the average dc voltage for each ring vs. bias current. As the current is increased, the kinks move faster, and the dc voltage increases. The inner ring Eck step reaches a maximum at a voltage of $0.0151 I_c R_n$. The outer ring has zero trapped flux, but exhibits HV steps. The first step in the outer ring at $0.0297 I_c R_n$ is due to a single excited pair. As in the experiment, the voltage of the Eck step jumps to a lower voltage value when the outer ring switches to the HV step.

Along the Eck step, we find that the average voltage of the outer ring is not quite twice that of the inner ring's, indicating that the speeds of the two kinks and the anti-kink are not identical. Fig. 4-17 plots the space-time portrait of the motion

at $I_b = 0.45 I_c$. The two kinks, drawn as open circles, travel at approximately the same speed with a constant phase separation between them. Hence, we see that the coupling gives rise to phase-locking between kinks of the same sign in different rings.

A more dramatic interaction effect is the precession of the collision region between the kink and anti-kink in the outer ring. The anti-kink travels in the opposite direction and moves more slowly than the kink. As it periodically collides with the kink, the interaction perturbs its motion slightly. Because of the difference in their speeds, they collide at a different location for each revolution, and the collision region precesses around the ring, as shown from the solid line in Fig. 4-17. Slopes of the lines indicate that the speed of the kink in the inner ring is equal to the speed of the kink in the outer ring, 0.0151, while the speed of anti-kink in the outer ring is 0.0146. The difference in the kink and anti-kink speeds gives the precession rate of the kink/anti-kink collision region.

Without yet doing any analysis, we know that the speeds of kinks in the rings will be influenced by the coupling, and that at least two different speeds should be possible, depending on the phase relationships between the rings. The coupling between the kinks might allow them to move faster, at a speed approaching the “in-phase” speed (ω^+) derived for identical open-ended rows in equation (4.26). The anti-kink, which has no counterpart in the inner ring, must travel at the “anti-phase” speed (ω^-). Using equation (4.26) would over-estimate the precession by about a factor of 3, but it is not clear that this equation should be applied to rings with $M_{in} \neq M_{out}$ or that the kinks and anti-kink actually reach their maximum speeds in this case.

When the current is increased above $I_b = 0.52 I_c$, a second pair is excited in the outer ring and a voltage step appears at $0.065 I_c R_n$. At this point, the inner ring voltage shifts to a slightly higher value. Since the system is discrete, we might expect the two kinks in the outer ring to travel more slowly than the single kink in the inner ring. Instead, space-time plots (not shown) indicate that, again, the kinks in both rings move together at equal speeds and the anti-kinks in the outer ring move together at a slower speed. When a third pair is excited at $I_b = 0.54 I_c$, the Eck voltage of the inner ring does not change. Finally, at $I_b = 0.57 I_c$ the pairs disappear and the outer

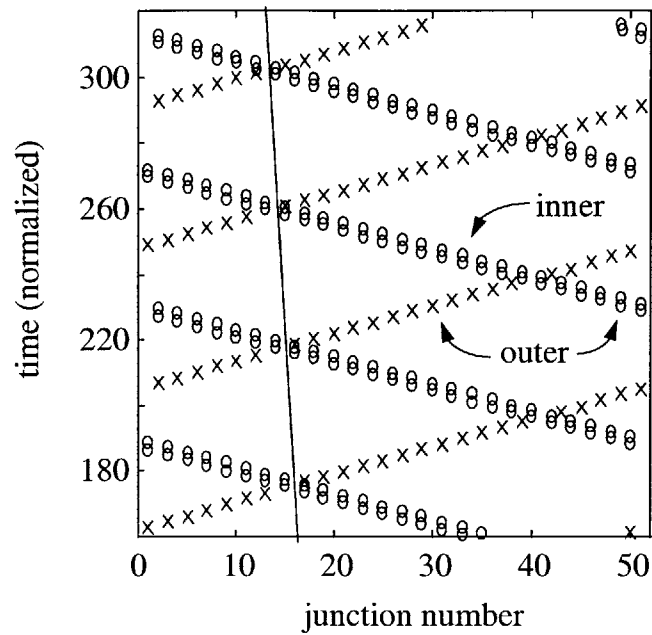


Figure 4-17: Space-time diagram of the kinks for $I_b = 0.45 I_c$ marked by a dashed line in Figure 4-16. The kinks are represented by open circles, while the anti-kink is marked by crosses. The kinks in the two rings are phase-locked (note the parallel lines of circles). The anti-kink travels more slowly, causing its point of intersection with the kink to precess.

ring switches to a uniform whirling state [11]. The inner branch persists up to higher current and jumps at $I_b = 0.72 I_c$.

4.5 Analysis for Resonances in Coupled Rings

In Section 4.3 on inductively coupled rows, we used an ansatz for the phase solutions to obtain the voltages at which in-phase and anti-phase resonances could occur. In the case of coupled rings, however, we have seen that the two rings are not always voltage-locked. In addition, there are many new resonances observed in this system. Using simulations, we have been able to write down a list of the appropriate ansatz for each case. However, this would be a very inefficient way to analyze the system. Therefore, we will take the approach presented in Section 3.5 on single rings. We do not assume a particular form of the phase solutions, but we will take advantage of the fact that, for the resonances of which interest us, there are only a few spatial wavelengths present in the phase solutions.

For the purpose of analysis, we will assume that the parameters of the two rings are identical. In addition, we neglect $M_{h,x}$, which according to simulations results, does not influence the essential nature of the dynamical solutions. Then the governing equations become:

$$\mathcal{N}[\phi_j] - M_v \mathcal{N}[\psi_j] = \Lambda_j^2 \nabla^2 \phi_j + \mathbf{I}_b \quad (4.27)$$

$$\mathcal{N}[\psi_j] - M_v \mathcal{N}[\phi_j] = \Lambda_j^2 \nabla^2 \psi_j + \mathbf{I}_b \quad (4.28)$$

where $M_v > 0$ and

$$\mathcal{N}[\phi_j] = \ddot{\phi}_j + \Gamma \dot{\phi}_j + \sin \phi_j \quad (4.29)$$

$$\nabla^2 \phi_j = \phi_{j+1} - 2\phi_j + \phi_{j-1} \quad (4.30)$$

with the boundary conditions:

$$\phi_{j+N} = \phi_j + 2\pi M_1 \quad (4.31)$$

$$\psi_{j+N} = \psi_j + 2\pi M_2 \quad (4.32)$$

Make again the transformation

$$\varphi_j = \phi_j - 2\pi \frac{M_1}{N} j \quad (4.33)$$

$$\varsigma_j = \psi_j - 2\pi \frac{M_2}{N} j. \quad (4.34)$$

So that now φ_j and ς_j obey periodic boundary conditions: $\varphi_{j+N} = \varphi_j$ and $\varsigma_{j+N} = \varsigma_j$. Again, we can write a discrete Fourier series for the functions $\varphi_j, \varsigma_j, \sin[\varphi_j + (2\pi M_1/N)j]$, and $\sin[\varsigma_j + (2\pi M_2/N)j]$:

$$\varphi_j = \sum_{k=\langle N \rangle} P_k(t) e^{ik(2\pi/N)j} \quad (4.35)$$

$$\varsigma_j = \sum_{k=\langle N \rangle} Q_k(t) e^{ik(2\pi/N)j} \quad (4.36)$$

$$\sin[\varphi_j + (2\pi M_1/N)j] = \sum_{k=\langle N \rangle} F_k(t) e^{ik(2\pi/N)j} \quad (4.37)$$

$$\sin[\varsigma_j + (2\pi M_2/N)j] = \sum_{k=\langle N \rangle} G_k(t) e^{ik(2\pi/N)j}. \quad (4.38)$$

Again, the discrete Laplacian will simplify to

$$\nabla^2 \varphi_j = \sum_{k=\langle N \rangle} (-\omega_k^2) P_k(t) e^{ik(2\pi/N)j} \quad (4.39)$$

$$\nabla^2 \varsigma_j = \sum_{k=\langle N \rangle} (-\omega_k^2) Q_k(t) e^{ik(2\pi/N)j} \quad (4.40)$$

where $\omega_k^2 = \Lambda_j^2 \sin^2(k\pi/N)$.

Now we can write amplitude equations similar to those of the single ring. For $k = 0$, we have

$$\ddot{P}_0 + \Gamma \dot{P}_0 + F_0 - M_v [\ddot{Q}_0 + \Gamma \dot{Q}_0 + G_0] = I_b \quad (4.41)$$

$$\ddot{Q}_0 + \Gamma \dot{Q}_0 + G_0 - M_v [\ddot{P}_0 + \Gamma \dot{P}_0 + F_0] = I_b \quad (4.42)$$

For the $k \neq 0$ equations we have

$$\ddot{P}_k + \Gamma \dot{P}_k + F_k - M_v[\ddot{Q}_k + \Gamma \dot{Q}_k + G_k] = -\omega_k^2 P_k \quad (4.43)$$

$$\ddot{Q}_k + \Gamma \dot{Q}_k + G_k - M_v[\ddot{P}_k + \Gamma \dot{P}_k + F_k] = -\omega_k^2 Q_k \quad (4.44)$$

From the calculation in Appendix B, the expressions for F_0 and G_0 will be

$$F_0 = -\frac{1}{2} p_{M_1} \sin(P_0 - \theta_{M_1}) \quad (4.45)$$

$$G_0 = -\frac{1}{2} q_{M_2} \sin(Q_0 - \alpha_{M_2}) \quad (4.46)$$

Substituting this into (4.41) and (4.42) gives:

$$\ddot{P}_0 + \Gamma \dot{P}_0 - p_{M_1} \sin(P_0 - \theta_{M_1}) = \left(\frac{1}{1 - M_v} \right) I_b \quad (4.47)$$

$$\ddot{Q}_0 + \Gamma \dot{Q}_0 - q_{M_2} \sin(Q_0 - \alpha_{M_2}) = \left(\frac{1}{1 - M_v} \right) I_b. \quad (4.48)$$

The phases θ_{M_1} and α_{M_2} are from writing $P_{M_1} = (-i/2)p_{M_1}e^{i\theta_{M_1}}$ and $Q_{M_2} = (-i/2)q_{M_2}e^{i\alpha_{M_2}}$ in polar coordinates.

Our linearization which gave F_0 and G_0 neglects the coupling of all but one mode to the DC equations. Although the nonlinear term actually couples *all* of the modes, the system is made more analytically tractable by including only the most important term. Already we know that these approximations for F_0 and G_0 cannot explain every aspect of the experimental and numerical data. For example, in both experiments and simulations, we see shifts in the IV curve of *ring 1* when P_{M_1} is not at all large. This sometimes happens when ring 1 is on the whirling branch, and ring 2 is in its Eck step. The actual voltage of the DC whirling branch solution seems to be influenced by the fact that ring 2 is on a resonance. These observations are in conflict with equations (4.47- 4.48), which imply that the DC IV curve of ring 1 can *only* be influenced through P_{M_1} . On the other hand, the more tractable system of modal equations can provide some valuable insight into the system dynamics, as we will see.

We can also substitute the expressions for F_k , G_k , F_{M_1} , and G_{M_2} into equations (4.43) and (4.44). Since they make the equations so long, though, the substitution is left until later.

Applying the same algebra as we did for the $k = 0$ equations, we can write

$$\ddot{P}_k + \Gamma \dot{P}_k + \bar{\omega}_k^2 P_k = -F_k - M_v \bar{\omega}_k^2 Q_k \quad (4.49)$$

$$\ddot{Q}_k + \Gamma \dot{Q}_k + \bar{\omega}_k^2 Q_k = -G_k - M_v \bar{\omega}_k^2 P_k \quad (4.50)$$

where we define

$$\bar{\omega}_k^2 = \frac{\omega_k^2}{1 - M_v^2}. \quad (4.51)$$

If P_k and Q_k are excited with periodic oscillations which are either equal in frequency or are integer multiples of each other, then linear combinations of P_k and Q_k can be periodic. In these cases, the normal modes of the system are in-phase and anti-phase modes:

$$X_k = \frac{P_k + Q_k}{2} \quad (4.52)$$

$$Y_k = \frac{P_k - Q_k}{2} \quad (4.53)$$

By adding and subtracting equations (4.49) and (4.50), we obtain equations for X_k and Y_k :

$$\ddot{X}_k + \Gamma \dot{X}_k + \bar{\omega}_k^2 (1 + M_v) X_k = \frac{1}{2} (F_k + G_k) \quad (4.54)$$

$$\ddot{Y}_k + \Gamma \dot{Y}_k + \bar{\omega}_k^2 (1 - M_v) Y_k = \frac{1}{2} (F_k - G_k) \quad (4.55)$$

For now, we do not write the functions F_k and G_k in terms of X_k and Y_k . Their form will depend the DC voltages of the rings and must be considered by the case. Depending on F_k and G_k , equations (4.54 - 4.55) look promising; the equations for

X_k and Y_k will be uncoupled in some cases. These coordinates are referred to as the normal modes of the system. When a system can be diagonalized in this way, it is always possible to find an initial condition such that only one of the normal modes is independently excited. In our system, the solution will still be a linear combination of the normal modes unless P_k and Q_k are equal in magnitude and oscillate at the same frequencies. Depending on the values of M_1 and M_2 , this requirement selects certain combinations of the DC voltages which will enable a single in-phase or anti-phase oscillation to be excited.

4.5.1 Coupled Rings with $M_1 = M_2$

In the special case where $M_1 = M_2 = M$, then the two rings can be voltage locked. Although equations (4.47) and (4.48) are uncoupled, since the bias currents are identical then the first order solutions have equal voltages. As in the single ring case, a perturbative solution of (4.47) and (4.48) will give $P_0 = \nu t + \theta$ and $Q_0 = \nu t + \alpha$. The phases θ and α are integration constants. If we analyze the $k = M$ mode, we should be able to obtain results similar to those published in [28], where we started with an ansatz for voltage-locked rows. For the $k = M$ case, we have

$$\begin{aligned} F_M &= \frac{1}{2}[-ie^{i\nu t}e^{i\theta} + P_{2M}e^{-i\nu t}e^{-i\theta}] \\ G_M &= \frac{1}{2}[-ie^{i\nu t}e^{i\alpha} + Q_{2M}e^{-i\nu t}e^{-i\alpha}]. \end{aligned} \quad (4.56)$$

As we know from the single ring case, the modes P_{2M} and Q_{2M} will be associated with HV steps. To compare with the results of [28] on Eck steps, we will consider only the first drive terms for now, setting $P_{2M} = Q_{2M} = 0$. If $\theta = \alpha$, then only the drive on X_M ($F_M + G_M$) is nonzero. If instead $\theta = \alpha + \pi$, then only the drive on Y_M is nonzero. Consider the consequences of these two cases. First, for $\theta = \alpha$, the system is being driven to one of its normal modes, X_M . Without driving, Y_M should decay to zero. For Y_M to equal zero, the following must be true (1) P_M and Q_M must have identical frequencies in time, (2) P_M and Q_M must have equal magnitudes, and

(3) the phases must be related by $\theta_M = \alpha_M$. (Recall that $P_M = (-i/2)p_M e^{i\theta_M}$ and $Q_M = (-i/2)q_M e^{i\alpha_M}$). For $\theta = \alpha + \pi$, the value of X_M should decay to zero, which results in the same characteristics (1) and (2) above, but (3) instead is $\theta_M = \alpha_M + \pi$. Thus, the phases θ and α determine which mode is driven and as a result the relative phases of P_M and Q_M .

When the frequency ν of the driving function ($F_M \pm G_M$) is equal to the natural frequency on the left-hand-side of equations (4.54) and (4.55), then the amplitudes can become large. For the in-phase X_M mode, these resonances can occur at the DC voltages

$$\nu = \bar{\omega}_M \sqrt{1 + M_v} \quad (4.57)$$

while for the anti-phase Y_M mode the resonances are at:

$$\nu = \bar{\omega}_M \sqrt{1 - M_v}. \quad (4.58)$$

The damping shift of the resonance frequency is neglected for simplicity. For small M_v , these are the frequencies predicted from the ansatz analysis in [28].

The agreement with [28] makes sense, since in this paper, we assumed not only that the rows were voltage locked, but also that the basic solutions were exactly $P_0 = \nu t + \theta$ and $Q_0 = \nu t + \alpha$. For the in-phase resonance, $\theta - \alpha = 0$ was chosen, while for the anti-phase resonance, $\theta - \alpha = \pi$ was adopted. The ansatz was also restricted to only the $k = M$ mode in order to calculate the resonant frequency for in-phase and anti-phase excitations.

In the open-ended system of [28], no HV steps appeared. An intuitive explanation as to why they do not appear in open-ended systems (with only a DC drive) is based on the association of HV steps with excited kink/anti-kink pairs. If a pair is excited somewhere in the middle of the array, the kink and anti-kink will be swept in opposite directions by the bias current. At the array edges, they can escape. However, in both single and coupled rings, these types of excitations can survive. For the HV steps, equations (4.54) and (4.55) should be re-written, since F_k and G_k can be combined

in this case to functions of X_k and Y_k . For voltage-locked states,

$$F_k \pm G_k = \frac{1}{2}[P_{k-M}e^{i\nu t}e^{i\theta} + P_{k+M}e^{-i\nu t}e^{-i\theta}] \pm \frac{1}{2}[Q_{k-M}e^{i\nu t}e^{i\alpha} + Q_{k+M}e^{-i\nu t}e^{-i\alpha}]. \quad (4.59)$$

When $\theta = \alpha$,

$$F_k + G_k = \frac{1}{2}[X_{k-M}e^{i\nu t}e^{i\theta} + X_{k+M}e^{-i\nu t}e^{-i\theta}] \quad (4.60)$$

$$F_k - G_k = \frac{1}{2}[Y_{k-M}e^{i\nu t}e^{i\theta} + Y_{k+M}e^{-i\nu t}e^{-i\theta}]. \quad (4.61)$$

When $\theta = \alpha + \pi$

$$F_k + G_k = \frac{1}{2}[Y_{k-M}e^{i\nu t}e^{i\theta} + Y_{k+M}e^{-i\nu t}e^{-i\theta}] \quad (4.62)$$

$$F_k - G_k = \frac{1}{2}[X_{k-M}e^{i\nu t}e^{i\theta} + X_{k+M}e^{-i\nu t}e^{-i\theta}]. \quad (4.63)$$

Thus, no choice of θ and α can make one of the drives on X_k or Y_k zero, as before. However, if $\theta = \alpha$ then the equations (4.54) and (4.55) are at least uncoupled. Then the appropriate value of ν will excite one or the other of the X_k or Y_k modes. The appropriate values of ν for these HV steps, based on the same approach used for calculating single ring HV steps [34], should be

$$\nu = (\bar{\omega}_k + \bar{\omega}_{k+M})(1 \pm M_v)^{1/2} \quad (4.64)$$

for $k + M$ excited pairs, or, for $k - M$ excited pairs,

$$\nu = (\bar{\omega}_k + \bar{\omega}_{k-M})(1 \pm M_v)^{1/2}. \quad (4.65)$$

4.5.2 Coupled Rings with $M_1 \neq M_2$

We now consider the harder cases where $M_1 \neq M_2$, which appear in the coupled rings. In this case, the rings are not necessarily voltage locked, so we let $P_0 = \nu_1 t + \theta$ and

$$Q_0 = \nu_2 t + \alpha.$$

We first write the equations for the $k = M_1 \neq M_2$ mode as

$$\ddot{X}_{M_1} + \Gamma \dot{X}_{M_1} + \bar{\omega}_{M_1}^2 (1 + M_v) X_{M_1} = \frac{1}{2} (F_{M_1} + G_{M_1}) \quad (4.66)$$

$$\ddot{Y}_{M_1} + \Gamma \dot{Y}_{M_1} + \bar{\omega}_{M_1}^2 (1 - M_v) Y_{M_1} = \frac{1}{2} (F_{M_1} - G_{M_1}). \quad (4.67)$$

From the single ring calculations (see Appendix B), we know

$$F_{M_1} = \frac{1}{2} [-i e^{i(\nu_1 t + \theta)} + P_{2M_1} e^{-i(\nu_1 t + \theta)}] \quad (4.68)$$

$$G_{M_1} = \frac{1}{2} [Q_{M_1 - M_2} e^{i(\nu_2 t + \alpha)} + Q_{M_1 + M_2} e^{-i(\nu_2 t + \alpha)}]. \quad (4.69)$$

This means that the X_{M_1} and Y_{M_1} coordinates are coupled. Substituting $P_k = X_k + Y_k$ and $Q_k = X_k - Y_k$ into the equations above gives

$$F_{M_1} = \frac{1}{2} [-i e^{i(\nu_1 t + \theta)} + (X_{2M_1} + Y_{2M_1}) e^{-i(\nu_1 t + \theta)}] \quad (4.70)$$

$$G_{M_1} = \frac{1}{2} [(X_{M_1 - M_2} - Y_{M_1 - M_2}) e^{i(\nu_2 t + \alpha)} + (X_{M_1 + M_2} - Y_{M_1 + M_2}) e^{-i(\nu_2 t + \alpha)}] \quad (4.71)$$

Unfortunately, no choice of the driving phases θ or α can eliminate one of the drives on X_{M_1} or Y_{M_1} ($F_{M_1} \pm G_{M_1}$), or even uncouple the equations.

However, ν_1 and ν_2 can be chosen so that $F_{M_1} + G_{M_1}$ drives equation (4.66) at its resonance, $\bar{\omega}_{M_1} (1 + M_v)^{1/2}$. This resonance is, of course the Eck resonance of ring 1, which means that we must have $\nu_1 = \bar{\omega}_{M_1} (1 + M_v)^{1/2}$. For the voltage of ring 2, there are two possibilities which will drive a resonance of mode $k = M_1$. These correspond to the two possible HV steps discussed for single rings. Either M_1 kink/anti-kink pairs can become excited, or $M_1 - M_2$ pairs can become excited. In the first case, modes $k = M_1$ and $k = M_1 + M_2$ are large, while in the second case, modes $k = M_1 - M_2$ and $k = M_1$ are large. These two possible states will both allow the mode $k = M_1$ to be at resonance, matching ring 1, which is on its $k = M_1$ Eck step. The two possible HV steps actually multiply into four when the possible phase relationships between

the rings are considered. Even though we are discussing the resonance of mode X_{M_1} , meaning that $\theta_{M_1} = \alpha_{M_1}$, we should not assume that all of the other $\theta_k = \alpha_k$. Then the four possible values of ν_2 which will contribute to the resonance of X_{M_1} are (in sets of two closely spaced steps):

$$\nu_2 = \begin{cases} \bar{\omega}_{M_1}(1 + M_v)^{1/2} + \bar{\omega}_{M_1+M_2}(1 + M_v)^{1/2}, & \text{for } X_{M_1+M_2} \text{ excited.} \\ \bar{\omega}_{M_1}(1 + M_v)^{1/2} + \bar{\omega}_{M_1+M_2}(1 - M_v)^{1/2}, & \text{for } Y_{M_1+M_2} \text{ excited.} \end{cases} \quad (4.72)$$

$$\nu_2 = \begin{cases} \bar{\omega}_{M_1}(1 + M_v)^{1/2} + \bar{\omega}_{M_1-M_2}(1 + M_v)^{1/2}, & \text{for } X_{M_1-M_2} \text{ excited.} \\ \bar{\omega}_{M_1}(1 + M_v)^{1/2} + \bar{\omega}_{M_1-M_2}(1 - M_v)^{1/2}, & \text{for } Y_{M_1-M_2} \text{ excited.} \end{cases} \quad (4.73)$$

In experiments, it might be difficult to distinguish between the sets of in-phase and anti-phase resonances, unless *both* appeared, as did the V_+ and V_- Eck steps in Section 4.2, for example. Similarly, it might also be difficult to distinguish the Eck step (ν_1) corresponding to a resonance of X_{M_1} from the anti-phase resonance of Y_{M_1} unless they both appeared. For the case of a Y_{M_1} resonance, the set of HV steps must also occur at slightly different voltages. These are found by replacing $\bar{\omega}_{M_1}(1 + M_v)^{1/2}$ with $\bar{\omega}_{M_1}(1 - M_v)^{1/2}$ in the above equations. The values of ν_1 and ν_2 for X_{M_1} and Y_{M_1} resonances are closely spaced for typical values of $M_v \approx 0.1 - 0.2$.

Despite the fact that $M_1 \neq M_2$, we see that phase-locked resonances are possible for the individual spatial modes. If the two rings are on their respective Eck steps, the spatial modes $k = M_1$ and $k = M_2$ will be excited in *both* rings. This fact is very clear upon re-examining equations (4.49) and (4.50). If instead, one of the rings (ring 2 for example) moves to an HV step, then the DC voltages of both rings can drive a phase-locked resonance of mode $k = M_1$. The exact value of the HV step depends on several possible phase-shifts between the rings, but centers on either $\nu_2 \approx \omega_{M_1} + \omega_{M_1+M_2}$ for M_1 excited pairs in ring 2, or $\nu_2 \approx \omega_{M_1} + \omega_{M_1-M_2}$ for $M_1 - M_2$ excited pairs in ring 2. Out of all the possible HV steps that ring 2 could have, these two (or two ‘sets’, counting all the in-phase/anti-phase possibilities) are the only ones which can maintain a *minimum* number of spatial components in the solution. In

addition, the rings can phase lock. Modes $k = M_1$ and $k = M_2$ are driven when the rings are on their Eck steps. If ring 2 switches to an HV step, then the excited modes will be either $k = M_1$ and $k = M_1 + M_2$, or $k = M_1$ and $k = M_1 - M_2$.

In experiments where $M_1 \neq M_2$, we see large steps (indicating resonances) with one ring on its Eck resonance while the other ring has an HV step. For example, if the inner ring is on its Eck step with $M_{\text{in}} = 1$, then based on the above discussion, any HV steps which appear in the outer ring should happen at approximately

$$\nu_{\text{out}} = \omega_1 + \omega_{M_{\text{out}}+1}. \quad (4.74)$$

This is an easy example since any HV step in the outer ring *must* correspond to M_{in} excited pairs— $M_{\text{in}} - M_{\text{out}}$ would give a negative number of excited anti-kinks for $M_{\text{in}} = 1$.

Figure 4-18 compares (4.74) with the observed steps in a coupled ring system with $N = 8$ junctions. Data for two different samples is presented in (a) and (b). The squares represent the values of the outer ring Eck voltages measured while $M_{\text{in}} = 0$. The solid fit to the Eck voltage data is the theory, in real units:

$$V_k \approx V_o \sin\left(\frac{k\pi}{N}\right) \quad (4.75)$$

where $V_o = \Phi_o/2\sqrt{L_s C}$ and $k = M_{\text{out}}$ is used. The effects of M_h and M_v are left out of (4.75) since the exact values of both Eck and HV steps depend on the phase relationship between the rings which cannot be experimentally determined. Instead, we simply fit the Eck voltages of the outer step to obtain V_o . This value of V_o is then used in equation (4.74) for the HV step voltages. The data for the HV steps is represented by filled circles. Equation (4.74) works well to fit the data, using the value of V_o determined from the Eck steps. Although the possibility that the rings can be oscillating in-phase or out-of-phase will change the theory (4.74) by up to 10%, the trend looks promising.

In theory, it should be possible to make three more plots like Fig. 4-18 of the steps

in the outer ring for different cases of M_{in} . In theory, it should also be possible to make a similar set of four plots of the inner ring HV steps for various cases of M_{out} . Unfortunately, relatively few HV steps are measured in our arrays. As in the case of single rings [34], the stability of the HV steps depends sensitively on the parameters β_c and Λ_J^2 , making it difficult to firmly establish patterns such as those speculated here.

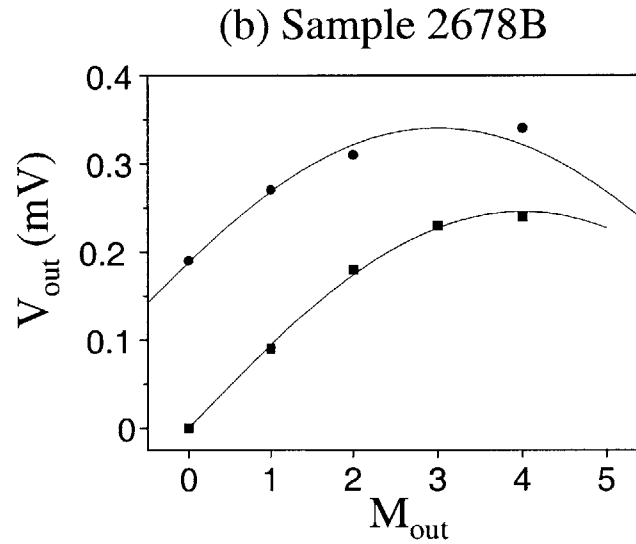
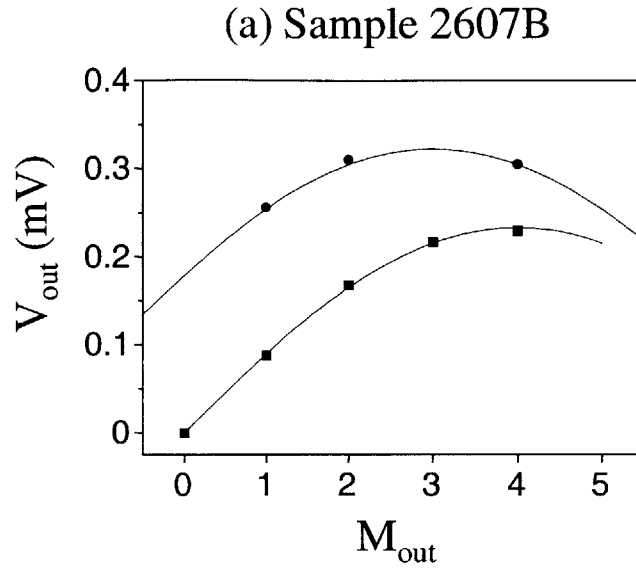


Figure 4-18: The Eck (squares) and HV (circles) steps of the outer ring for inductively coupled $N = 8$ rings. The Eck step voltages are for the case of $M_{\text{in}} = 0$, while the HV steps are for the case $M_{\text{in}} = 1$. The solid line fitting the Eck steps is from an approximation of the dispersion relation, equation (4.75). The fitting parameter for sample (a) is $V_o = 0.233$ mV, and for sample (b) is $V_o = 246$ mV. The solid line fitting the HV steps uses the value of V_o from the Eck steps and the HV formula (4.74).

4.5.3 Energy balance for coupled rings

In Fig. 4-15, we observe some interesting voltage shifts of the inner ring Eck step. Such voltage shifts are typical features of the data for coupled rings when the two rings are not voltage-locked. It appears as though the Eck voltage of the inner ring depends on the state of the outer ring. It is tempting to attribute the shift to the change from an in-phase to an anti-phase resonance. According to the modal analysis, the difference between an in-phase resonance and an anti-phase resonance corresponds to a small voltage shift. However, this does not seem to be the answer. Simulations of the shifts do not show a change in the relative phases of the ring oscillations. Also, the shifts have been observed experimentally when the rings both begin on the whirling branch and, as current is decreased, only *one* (ring 2) switches to an HV step. In this case, the other (ring 1) shows a shift of its whirling branch voltage. The rings started from a non-resonant whirling state. The shift of the ring 1 voltage, then, cannot be explained by a change of a resonance phase.

In addition, our modal equations for the DC IV curves in coupled systems (4.47) and (4.48) suggest that the IV curve of one ring is not directly influenced by the state of the other ring. Clearly, this is not the case, and some important terms may have been neglected in the modal analysis presented. On the other hand, even the simple modal analysis of Section 3.2.1 became very complicated very quickly, and including more terms may make it impossible to interpret. Instead, a more general power balance approach can be used to interpret some of the data with voltage shifts.

The logic is similar to that presented for a single ring. If we write the voltage across junction j in ring one as $V_{(1),j}$ and the voltage across junction j in ring two as $V_{(2),j}$, then the total power supplied by the source is just:

$$\mathcal{P}_s = I \sum_{j=\langle N \rangle} \langle V_{(1),j} \rangle + I \sum_{j=\langle N \rangle} \langle V_{(2),j} \rangle. \quad (4.76)$$

This must equal the total power absorbed by the passive impedances, which is:

$$\varphi_R = \frac{1}{R} \sum_{j=\langle N \rangle} \langle V_{(1),j}^2 \rangle + \frac{1}{R} \sum_{j=\langle N \rangle} \langle V_{(2),j}^2 \rangle \quad (4.77)$$

As described in the section on single rings, these expressions simplify to:

$$I_b[\langle \mathcal{V}_{(1),0} \rangle + \langle \mathcal{V}_{(2),0} \rangle] = \sum_{k=\langle N \rangle} \langle |\mathcal{V}_{(1),k}|^2 \rangle + \sum_{k=\langle N \rangle} \langle |\mathcal{V}_{(2),k}|^2 \rangle \quad (4.78)$$

The effect is that the sum of the total magnitude of $\vec{\mathcal{V}}_{(1)}$ and the total magnitude of $\vec{\mathcal{V}}_{(2)}$ is constrained to a surface. For a fixed bias current, I_b , if any component $\mathcal{V}_{(1),k}$ or $\mathcal{V}_{(2),k}$ is to increase, then the sum of the other components must decrease. Which components and how much is not specified. However, we are usually concerned with cases where relatively few k-modes (including the $k = 0$ modes) need to be considered.

For example, consider the IV in Fig. 4-15. As the bias current is increased from zero, the inner ring (ring 1) has an Eck step while the outer ring (ring 2) has no voltage. From simulations, we know to associate this state with the following: $\mathcal{V}_{(1),0} \neq 0$, $\mathcal{V}_{(1),\text{Min}} \neq 0$, and all other $\mathcal{V}_{(1),k}, \mathcal{V}_{(2),k} \approx 0$. At approximately $I = 7.2 \mu\text{A}$, the outer ring jumps to a non-zero DC voltage. At the same time, the inner ring shows a slight down-shift in its Eck voltage. It is this down-shift which will be considered. Since the jumps in voltage appear almost instantaneously in current, we will approximate that the radius of our surface is fixed while comparing the two states, defined as follows:

State **A** is defined by

$$\begin{aligned} \mathcal{V}_{(1),0} > 0, \quad \mathcal{V}_{(1),\text{Min}} > 0, \\ \|\vec{\mathcal{V}}_{(2)}\| = 0 \end{aligned}$$

State **B** is defined by

$$\begin{aligned} \mathcal{V}_{(1),0} > 0, \quad \mathcal{V}_{(1),\text{Min}} > 0, \\ \|\vec{\mathcal{V}}_{(2)}\| > 0. \end{aligned}$$

While the system is in State **A**, the surface is a circle. When the system jumps to state **B**, the surface becomes at least 3-dimensional. Since it is difficult to visualize

more than three dimensions, all of the new excited spatial components (including DC) of the outer ring can be lumped into one sum, $\|\vec{\mathcal{V}}_{(2)}\|$, making the surface a sphere. Without any additional constraints, it would be difficult to say how the energy was re-distributed among the three excited modes. It is conceivable that as the value of $\|\vec{\mathcal{V}}_{(2)}\|$ grows, the mode $\mathcal{V}_{(1),\text{Min}}$ decreases, leaving the DC voltage $\mathcal{V}_{(1),0}$ unchanged. However, there is an additional constraint on the relationship between $\mathcal{V}_{(1),0}$ and $\mathcal{V}_{(1),\text{Min}}$. To first order, this is given by the resonance curve of P_{Min} in response to $P_0 = \nu_1 t$, as in the single rings case also.

The schematic of Fig. 4-19 shows how such a resonance constraint might influence the relative magnitudes of the modes $\mathcal{V}_{(1),0}$ and $\mathcal{V}_{(1),M1}$ as a third mode is added. The intersection of the circle with the resonance curve gives larger values for $\mathcal{V}_{(1),0}$ and $\mathcal{V}_{(1),M1}$ than the intersection of the resonance curve with any point on the sphere for which $\|\vec{\mathcal{V}}_{(2)}\| > 0$. This will be true no matter what the exact shape of the resonance curve is, as long as the slope is positive in the $\mathcal{V}_{(1),0} - \mathcal{V}_{(1),M1}$ plane.

The situation is actually much more complicated than the above discussion implies. From our study of the coupled modal equations, we know that two things happen as ring 2 moves to an HV step. One is that the rings can now oscillate in in-phase or anti-phase states, and the resonance curve splits into two. The other is that the effective drive on the mode P_{M1} changes as Q_{M1} grows, which changes the height its resonance curves. The combination of these effects makes it difficult to predict how the DC voltage $\mathcal{V}_{(1),0}$ should shift. However, the fact that we see shifts in the DC IV curves of the rings in response to each other's states is made completely intelligible by the power balance requirement.

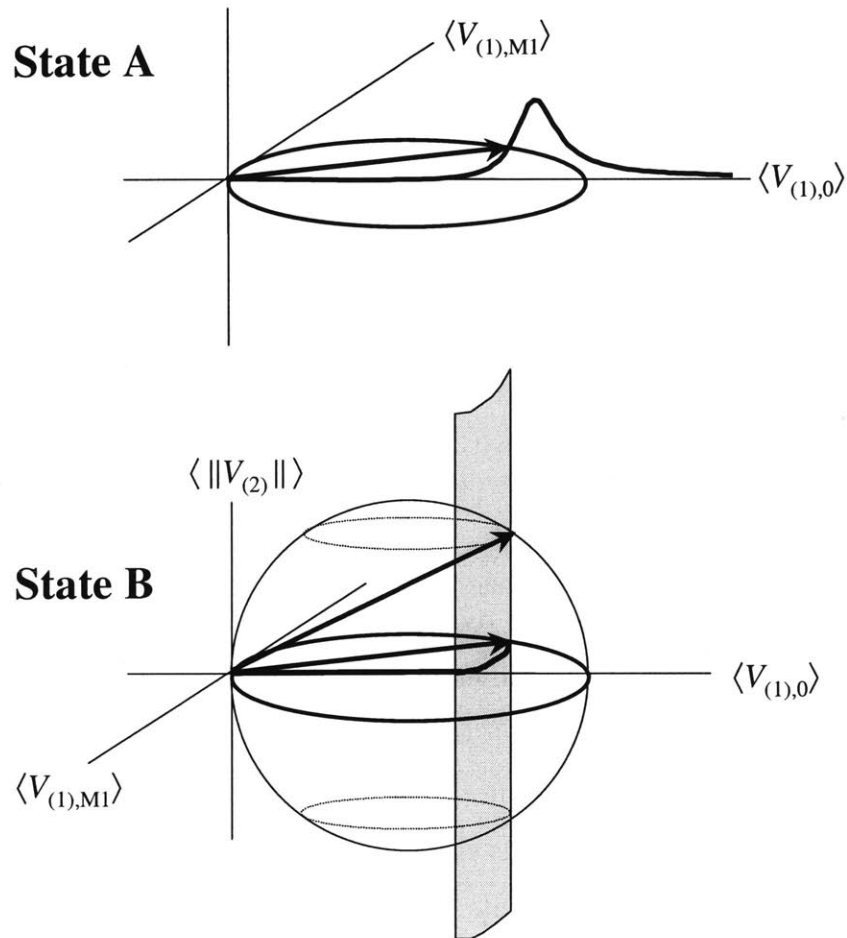


Figure 4-19: State **A** shows a schematic of the power balance constraint together with a resonance curve, for $\|\vec{\mathcal{V}}_{(2)}\| = 0$. State **B** shows the constraint when a non-zero $\|\vec{\mathcal{V}}_{(2)}\|$ is added. The resonance curve becomes a surface which intersects the sphere.

4.6 Summary of the results on Coupled Systems

We have studied the effect of inductively coupling two rings and two open-ended rows of Josephson junctions together. As described in Chapter 3, the single rings and rows exhibit several resonant oscillations as steps in the IV curve. For identical, symmetrically coupled oscillators, we expected the resonances in the system to split into two.

The splitting of the Eck resonance step was measured for the two coupled rows, which can be made with identical parameters. Numerical simulations were used to study the dynamics of the system when biased on the Eck steps. As in the case of single rows, the solutions on the Eck resonance are traveling waves with a single harmonic. The spatial wavelength is determined by the applied field. For the coupled system, the waves in each row can be in-phase or anti-phase. These two states have different frequencies, and give rise to the splitting of the Eck step. The traveling wave solution was also used as an ansatz in the governing equations for the system. By applying harmonic balance, we were able to derive the dispersion relation for the in-phase and anti-phase Eck resonances.

For inductively coupled rings, the dynamics can be much more complex, due to the fact that the two rings can have different numbers of trapped kinks. Study of the single rings showed that the resonance voltages, the excited spatial modes, and the frequency of oscillations in the system all depend on the number of trapped kinks. Indeed, measurements and simulations showed that the rings are not voltage locked when $M_1 \neq M_2$; one ring may stay on its Eck step while the other ring may switch to an HV resonance. However, the HV resonances which appear in such systems might be limited. Only a subset of the possible HV steps of a given ring was discovered in our measurements. The analysis presented in Section 4.5.2 offers a possible explanation.

We have extended the modal analysis of Chapter 3 to the system inductively coupled rings. The method was especially useful for this system, since it does not require a starting ansatz. Therefore, many of the different combinations of Eck and HV steps in the two rings could be considered. We found that, when $M_1 \neq M_2$, both

rings should have quasi-periodic solutions, even on their Eck steps. The $k = M_1$ and $k = M_2$ modes will be excited in *both* rings. This matches the results of numerical simulations. In addition, if ring 2 switches to an HV step, the analysis shows that, for certain numbers of excited pairs, the two rings can still phase-lock in the $k = M_1$ mode. The excited pairs are such that either the total number of kinks in ring 2 equals M_1 , or the total number of anti-kinks in ring 2 equals M_1 . The suggested pattern is consistent with experimental data for HV step voltages.

Another prominent feature of our data on coupled rings is the observation of voltage shifts in one ring when the other ring changes its dynamic state such that kinks and anti-kinks are annihilated or excited. According to the modal analysis, the difference between an in-phase resonance and an anti-phase resonance corresponds to a small voltage shift. In simulations, however, it is not clear that this can explain the shifts. Some experiments contradict this explanation as well. Therefore, we have extended the power balance approach presented in Chapter 3 to the coupled rings. Unfortunately, the power balance constraint is not very restrictive and only shows the plausibility of such voltage shifts. However, it does offer a nice interpretation for the shifts. A fixed energy input to the system must be shared among the spatial modes. For the coupled system, the total number of modes is doubled, as the energy is shared by both rings. If one ring suddenly changes its dynamic state such that large-amplitude resonances are excited, the energy available to the DC mode of the other ring decreases, and the DC voltage will decrease.

Chapter 5

Josephson Junction Arrays as Oscillators

When multiple oscillators are to be used as AC power sources, the output of the individual oscillators must be phase-locked and in-phase. Circuit level power combination has been done for Gunn diodes [7] and for various Josephson junction systems (Table 5.1). However, the conditions under which nonlinear oscillators phase-lock are not fully understood and is the subject of ongoing research in many fields. Phase-locking has been particularly important to the superconducting electronics community, since single junctions produce such small output power. As a result, significant progress has been made on the subject of phase-locking in Josephson systems. Series arrays of junctions phase-lock in the presence of a load [45]. Large amplitude sinusoidal oscillations are most easily obtained when the junctions are coupled to a resonator [54], similar to the transistor dielectric resonator oscillator. Unfortunately the resonator limits the tunability of the system. Two-dimensional square arrays can also be phase-locked. When there are no horizontal junctions present, the phase locking mechanism between rows is purely magnetic in nature [28]. When horizontal junctions are present, these elements contribute to the inter-row coupling [47]. When the system is biased on an LC resonance, the rows become phase-locked and produce large-amplitude, nearly sinusoidal voltage oscillations. In this case, the resonance frequency is usually tunable by an external magnetic field. The success of circuit-

level power combining methods in Josephson systems is indicated by the high output power levels of the largest arrays in Table 5.1. However, this approach is limited due to the size constraints imposed by high frequency operation. In order to assume lumped-element behavior, the system dimensions must be much less than a quarter-wavelength, preferably on the order of $\lambda/10$. At 100 GHz, for example, the Josephson junction array should not exceed $750 \mu\text{m}$. If more junctions are desired, a distributed structure is necessary. Several researchers have coupled small lumped-element groups of junctions into a waveguide (stripline) structure at intervals of $\lambda/2$ [19, 48, 54]. The combining efficiency in this case is limited by waveguide losses [19].

In this research, we will investigate two new network geometries for Josephson junction oscillators. First, we will use our understanding of the dynamics of parallel arrays and inductively coupled parallel arrays to assess whether these devices have potential as oscillators. Next we will measure triangular arrays, with three junctions in a cell. This system was proposed by Yukon and Lin [49, 50] as an alternative to the large two-dimensional arrays studied by other groups. We will provide the experiments to complement their work and the analysis of Barahona *et al.* in [47]. Our experiments will include DC as well as on-chip AC measurements.

Table 5.1: JOSEPHSON JUNCTION OSCILLATORS

Geometry	Measurement Type	Power@frequency	bandwidth	ref.
Short Josephson Junctions				
Jos. point contact	ac detection	1 pW @ 9 GHz	unknown	[52]
9 series JJ	on-chip detection	3.6 μ W @ 330 GHz	unknown	[54]
20 series JJ	on-chip detection	1.8 μ W @ 300 GHz	200-500 GHz	[53]
20 series JJ	on-chip detection	0.5 μ W @ 312 GHz	unknown	[54]
40 series JJ	ac chip detection?	1 μ W @ 350 GHz	350-450	[55]
500 series JJ	on-chip detection	47 μ W @ 394 GHz	300-500 GHz	[48]
3 series SQUIDS	ac detection	unknown	67-73 GHz	[56]
Long Josephson Junctions				
LJJ	ac detection	1 pW @ 120 GHz	80-120 GHz	[57]
LJJ	on-chip detection	420 nW @ 560 GHz	560-970 GHz	[62]
2 series LJJ	on-chip detection	430 nW @ 320 GHz	100-500 GHz	[58]
2 series LJJ	ac detection	42 pW @ 9 GHz	unknown	[59]
300 series LJJ	ac detection	550 nW @ 200 GHz	185-315 GHz	[60]
1968 series LJJ	on-chip detection	0.16 mW @ 240 GHz	100-300 GHz	[61]
2 stacked LJJ	ac detection	32 pW @ 11 GHz	unknown	[63]
2 stacked LJJ	on-chip detection	10 nW @ 410 GHz	170-410 GHz	[64]
2D Arrays of Josephson Junctions				
10x10 square array	on-chip detection	0.4 μ W @ 150 GHz	60-210 GHz	[18]
10x10 square array	ac detection	0.2 μ W @ 85 GHz	53-230 GHz	[19]
10x10 square array	on-chip detection	56 nW @ 147 GHz	unknown	[65]
10x10 square array	on-chip detection	73 nW @ 220 GHz	100-290 GHz	[66]
12x1 triangle array	ac detection	90 pW @ 80 GHz	75-80 GHz	[67]

5.1 Underdamped Parallel Arrays

Measurements of long, discrete, one-dimensional Josephson junction arrays show resonant steps in the presence of a magnetic field (Section 3.3). Numerical simulations based on the discrete sine-Gordon show that the solutions on the steps are periodic traveling waves, and power spectra of the voltages consist of a small number of harmonic peaks, which may be exploited for possible oscillator applications. In order to predict the oscillation amplitudes and the distributed power among the modes, the nonlinearity in the system must be carefully treated. Perturbation techniques [11, 72] clarify the role of the nonlinearity in driving the resonance and have been used to predict step voltages in Josephson systems. Combined with an appropriate ansatz, they also provide expressions for the oscillation amplitude [28, 42, 43]. However, the analytic expressions obtained included only the first harmonic and were implicit. In the following sections, we use a two-mode extension of the harmonic balance method to predict the resonant frequencies as well as the mode amplitudes at resonance. These formulas are analytic and include the dependence on magnetic field. With a matched load condition, a theoretical upper limit on the available output power of the underdamped Josephson oscillator can be calculated.

5.1.1 Simulations and phase solutions

Numerical simulations are used to find an appropriate ansatz for the phase solutions at resonance. The governing equations which model our open-ended row arrays have been derived already, in normalized form as

$$\ddot{\phi}_j + \Gamma \dot{\phi}_j + \sin \phi_j = I_b + \Lambda_J^2 (\phi_{j+1} - 2\phi_j + \phi_{j-1}) \quad (5.1)$$

for $j = 1, \dots, N$ and $\Gamma = \beta_c^{-1/2}$. With only self-inductance, the boundary conditions for an open-ended row are simply

$$\phi_0(t) = \phi_1(t) - 2\pi f \quad \text{and} \quad \phi_{N+1}(t) = \phi_N(t) + 2\pi f \quad (5.2)$$

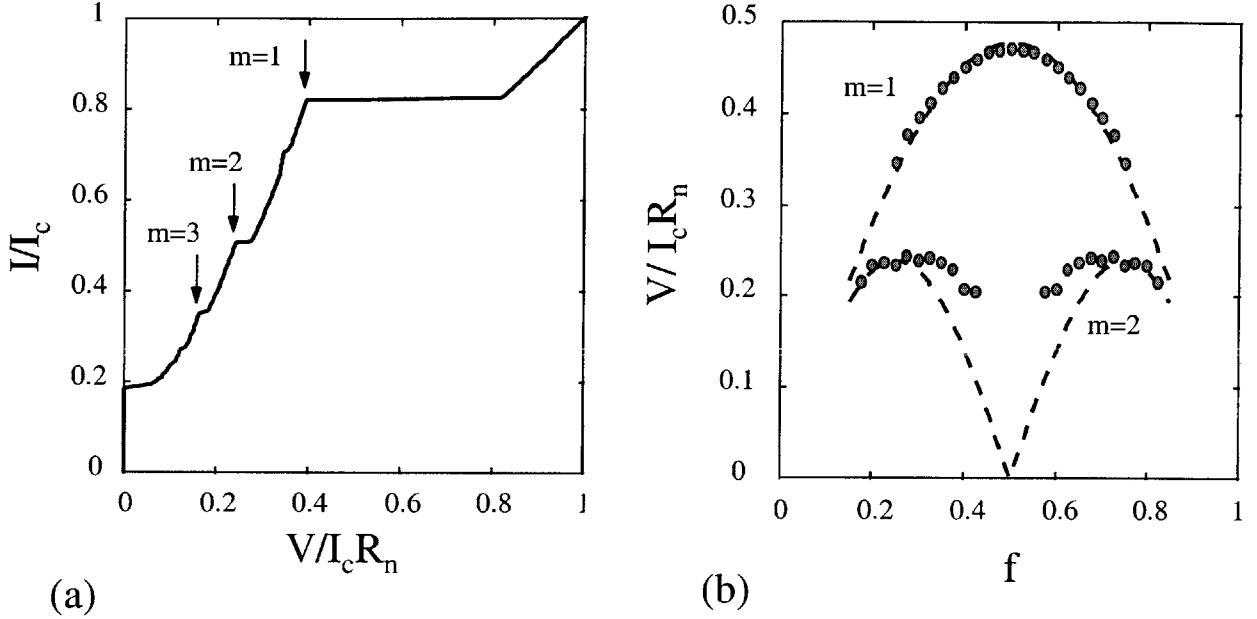


Figure 5-1: (a) Simulated current-voltage characteristic for a 54-junction array at $f = 0.3$. The three most prominent steps are marked. (b) Points taken from the top of the steps show the tunability of the first two steps with magnetic field. The parameters are the experimental values: $\beta_c = 16$ ($\Gamma = 0.25$) and $\Lambda_J^2 = 0.92$.

for all t , where artificial junctions ϕ_0 and ϕ_{N+1} are introduced at the endpoints so that (5.1) is valid at $j = 1$ and N as well [11].

With (5.1–5.2), current-voltage characteristics are numerically obtained at different f values using the parameters Λ_J and Γ from our experiments. Figure 5-1(a) shows the results for $f = 0.3$. The curve reproduces the measured one in Fig. 3-11 well, and at least three steps (indexed by m) are clear. In a manner similar to Fig. 3-12, the f -dependence of the step voltage locations is shown in Fig. 5-1(b). There are slight differences, but the main features and voltage values are represented well.

Simulations allow us to study the solutions in detail. We are especially interested in the system dynamics when biased on top of a step. In Fig. 5-2(a–c) the phase of the junction $j = 27$ (located in the middle of the array) on the $m = 1, 2, 3$ step, respectively, is shown as a function of time. The junction appears to be in a periodic motion. Its phase increases rapidly when a kink (vortex) passes by, and it oscillates for the period between passing vortices. In a mechanical analog of a junction as an

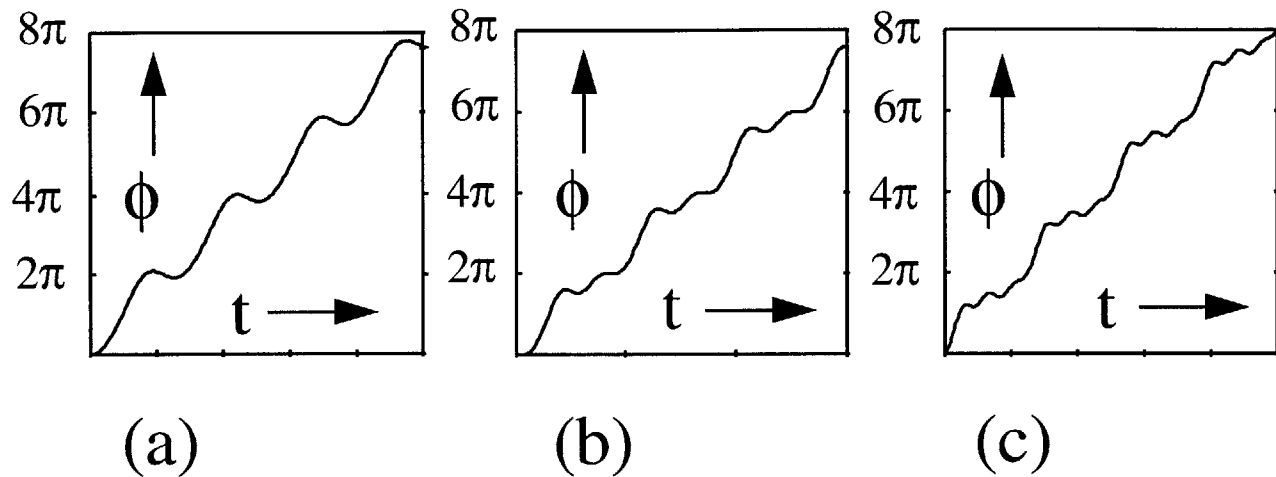


Figure 5-2: Time evolution of the phase of a junction $j = 27$ in the center of a 54-junction array, biased on the (a) $m = 1$, (b) $m = 2$, and (c) $m = 3$ steps, respectively.

underdamped pendulum [31], a sudden overturn of the pendulum is followed by an overshoot, and the pendulum “rings” several times until the next kink passes by.

Figure 5-2 shows that the solution on the step m corresponds to m such ringings. This can be quantified by studying the harmonic content of the voltages (3.3). Fourier spectra of the voltages are shown in Fig. 5-3(a-c), respectively. On the step m , the first m harmonics are dominant, and the higher harmonics have rapidly decaying magnitudes. Despite the presence of other harmonics, the steps are indexed by the ringing frequency, m .

Similar plots for the other junctions inside the array appear identical to ϕ_{27} , except for a certain shift in the time axis. This suggests that the solutions are well approximated by traveling waves. Near both ends of the array, reflections from the ends change this picture. The boundary effects, however, decay within 4–5 junctions from the end, and appear to play only a minor role in our long arrays.

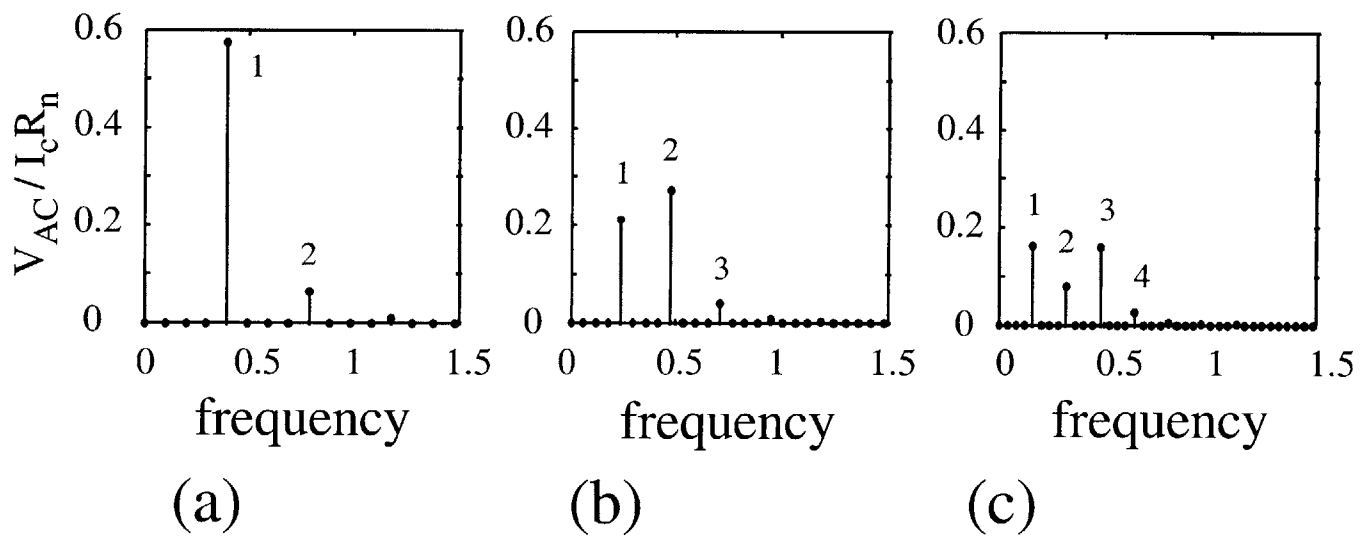


Figure 5-3: Fourier spectra of the voltage corresponding to Fig. 5-2(a-c), with (a) step $m=1$, (b) step $m=2$, and (c) step $m=3$. Voltages are proportional to the time derivative of the phase in Fig. 5-2.

5.1.2 Analysis of super-harmonics

Using the results on single rings, we can easily estimate the DC voltages at which the sub-steps appear by allowing the flux in the dispersion relation of [8] to be tunable. That is, by substituting $f = M/N$, the normalized DC step voltages occur at

$$\nu = 2\Lambda_J \sin(m\pi f)/m, \quad m = 1, 2, \dots \quad (5.3)$$

This fits the data well, as can be seen by the dashed lines in Fig. 3-12. The dispersion relation of [8] for rings can also be obtained from the modal equations in Section 3.2.1 (see Appendix C), which is a satisfying consistency check on that approach to the system analysis.

Although the modal analysis serves well in dealing with the various resonant frequencies of the system, we might also consider the modal amplitudes at resonance, especially for applications. When the equations are linearized as was done in Section 3.2.1 and only the coupling between a few modes is included, then the analytical solutions for the mode amplitudes become unrealistically large. This was even apparent when the resonance curve for mode P_M was plotted with the power balance constraint in Fig. 3-16. The predicted amplitudes do not agree with numerical results and become too large to justify the linearization.

Therefore, we have used another approach to cope with larger amplitudes. Since we are specifically considering the open-ended row system, we will no longer require the state variables to have a discrete Fourier Series expansion. We look for traveling wave solutions of the discrete sine-Gordon equation (5.1) of the form

$$\phi_j(t) = \phi(x) = x + \psi(x) \quad (5.4)$$

where

$$x = \omega t + 2\pi f j \quad (5.5)$$

is the moving coordinate with the wave, and $\psi(x + 2\pi) = \psi(x)$. The fundamental frequency ω is proportional to the DC voltage through the Josephson voltage-

phase relation (3.3) while the spatial wavenumber is imposed by the external field. If the modulation were absent ($\psi \equiv 0$), then the boundary conditions (5.2) would be satisfied exactly. Since ψ is not vanishing, they are satisfied only on average, and there should be a correction to (5.4). We neglect this boundary effect and will show that the simplification still leads to good estimates of the measurements and simulations. (In a circular array (5.2) is replaced by the periodic boundary conditions: $\phi_{j+N}(t) = \phi_j(t) + 2\pi M$ where M is an integer [11]. There can be exact solutions of the form (5.4,5.5) with $f = M/N$.)

The periodic function ψ can be expanded into Fourier modes

$$\psi(x) = \sum_{m=-\infty}^{\infty} A_m e^{imx} \quad (5.6)$$

with $A_{-m}^* = A_m$. We set $A_0 = 0$, without loss of generality, by shifting the origin of time. The phase ϕ is an increasing function of x , but the nonlinear term $\sin \phi$ is 2π -periodic and can be expanded as

$$\sin \phi(x) = \sum_{m=-\infty}^{\infty} F_m e^{imx} \quad (5.7)$$

with $F_{-m}^* = F_m$. The coefficients F_m can be computed in terms of $A_{\pm 1}, A_{\pm 2}, \dots$ from the usual Fourier-Bessel expansions, and therefore provide coupling among the modes. By substituting (5.4,5.6,5.7) into (5.1), we obtain a coupled system of modal equations.

$$(\delta_m + im\Gamma\omega)A_m + F_m = 0 \quad (5.8)$$

where

$$\delta_m = \omega_m^2 - (m\omega)^2, \quad (5.9)$$

and

$$\omega_m = 2\Lambda_J \sin(m\pi f). \quad (5.10)$$

The index $m = 1, 2, \dots$ for (5.8–5.10). In addition, the balance of the DC terms in

(5.1) results in

$$I_b/I_c = \Gamma\omega + F_0. \quad (5.11)$$

The first term on the right hand side is proportional to ω , and hence to the DC voltage. This term describes the ohmic line in the I - V plane. The second term is also a function of ω through the A_m 's, and describes the deviation of the I - V curve from the ohmic line.

The super-harmonic resonance [35] may occur in the algebraic system (5.8,5.11) and lead to the creation of resonant steps in the I - V curve. For small Γ , the magnitude of A_m would generically become large near $\delta_m = 0$, that is, near

$$\omega = \omega_m/m, \quad m = 1, 2, \dots \quad (5.12)$$

Then F_0 also becomes large, and the I - V deviates substantially from the ohmic line near these frequencies (or corresponding voltages). This argument neglects the dependence of the coupling terms F_m on the complex amplitudes A_m , but explains our measurements quite well. We plot (5.12) for $m = 1, 2$ as dashed curves in Figs. 3-12 and 5-1(b). The agreement is good without a fitting parameter.

The right hand side of (5.12) is the phase velocity of the m th mode on the discrete lattice. The left hand side can be viewed as the kink velocity. Then, the relation can be viewed as the phase-locking condition of the kink velocity and the phase velocity of the m th mode [9, 11]. In the absence of the coupling terms F_m , a resonance occurs when the kink lattice moves at the same velocity as one of the modes. We note that these resonance frequencies ω are distinct for different m because of the sinusoidal dependence of the dispersion relation (5.10) on m . If the second order difference in (5.1) were replaced by a second spatial derivative, the dispersion relation would depend linearly on m , and the phase velocities of all the modes would be identical. Consequently, there would be only one kink velocity that can excite modes, and we would observe only one resonance voltage. This explains why only the Eck step (among this type of step) is observed in a long continuous junction. In this sense, our observation of the $m > 1$ steps is due to the discreteness of the system.

We also note that, in some parameter regime, the resonating modes may be sub-harmonics of the fundamental frequency. Sub-harmonic resonances of order n can be sought by generalizing (5.6) to

$$\psi(x) = \sum_{m=-\infty}^{\infty} A_m e^{imx/n}. \quad (5.13)$$

This is still a traveling wave but has an n times longer period. In a similar manner to the above discussion, one may expect resonances when

$$0 = \omega_{m,n}^2 - (m\omega/n)^2 \quad \text{i.e.} \quad \omega = n\omega_{m,n}/m \quad (5.14)$$

where

$$\omega_{m,n} = 2\Lambda_J \sin(2m\pi f/n). \quad (5.15)$$

The resonances with $m = 1$ and $n = 1, 2, 3$ have been observed by Caputo *et al.* [36].

There was no need to analyze the coupling terms F_m to determine the resonant voltages, but it becomes necessary when the AC components A_m are wanted. These mode amplitudes are important information for possible oscillator applications because one can then estimate the power available from the device. Since analysis of the modal equations in general appears formidable, we focus only on the steps $m = 1$ and 2, and make several approximations.

First, as we see in the spectra in Fig. 5-3(a,b), A_3 and higher modes have much smaller magnitudes on these two steps, so they will be neglected. Then,

$$\begin{aligned} \phi(x) &= x + (A_1 e^{ix} + \text{c.c.}) + (A_2 e^{2ix} + \text{c.c.}) \\ &= x + a_1 \sin(x + \theta_1) + a_2 \sin(2x + \theta_2) \end{aligned} \quad (5.16)$$

where

$$A_m = -(i/2)a_m e^{i\theta_m}. \quad (5.17)$$

The *harmonic balance* method, which is commonly used for approximating a finite amplitude solution, would neglect A_2 as well. Thus, the ansatz (5.16) can be thought

of an extension of the method to a multi-harmonic case. Including two harmonics, however, introduces coupling terms between them, and makes the problem substantially harder. By the Fourier-Bessel expansion, the coupling is expressed as

$$F_0 = \sum_{n=-\infty}^{\infty} J_{-(2n+1)}(a_1)J_n(a_2) \sin [n\theta_2 - (2n + 1)\theta_1] \quad (5.18)$$

and

$$\begin{aligned} F_m &= -(i/2) \sum_n J_{m-(2n+1)}(a_1)J_n(a_2)e^{i(n\theta_2+(m-2n-1)\theta_1)} \\ &+ (i/2) \sum_n J_{-m-(2n+1)}(a_1)J_n(a_2)e^{-i(n\theta_2-(m+2n+1)\theta_1)} \end{aligned} \quad (5.19)$$

for $m \neq 0$, and J_m are Bessel functions.

To make analytical progress we simplify the coupling by taking only the most dominant terms (for small a 's) and neglecting all the others. This results in

$$F_1 = -(i/2)J_0(a_1)J_0(a_2), \quad F_2 = -(i/2)J_1(a_1)J_0(a_2)e^{i\theta_1}. \quad (5.20)$$

The higher order Bessel functions $J_2(a_1)$, $J_3(a_1)$, ... and $J_1(a_2)$, $J_2(a_2)$, ..., are neglected, which can be justified in the range, say, $|a_1| < 2$ and $|a_2| < 1$. We substitute them into (5.8) for $m = 1, 2$ and obtain

$$(J_0(a_1)/a_1)^2 = (\delta_1^2 + \Gamma^2\omega^2)/J_0^2(a_2), \quad \tan \theta_1 = -\Gamma\omega/\delta_1 \quad (5.21)$$

and

$$(J_0(a_2)/a_2)^2 = (\delta_2^2 + 4\Gamma^2\omega^2)/J_1^2(a_1), \quad \tan(\theta_2 - \theta_1) = -2\Gamma\omega/\delta_2. \quad (5.22)$$

It is convenient to think of ω as the control parameter and determine a_1 , a_2 , θ_1 and θ_2 . The arguments of tangent are defined between 0 and π . As ω increases from 0, δ_1 and δ_2 decrease monotonically, and change sign from positive to negative at the resonance frequencies. Thus, θ_1 decreases from π to 0, with the crossover $\theta_1 = \pi/2$

at $\omega = \omega_1$. Similarly, $(\theta_2 - \theta_1)$ decreases from π to 0, and crosses $\pi/2$ at $\omega = \omega_2/2$.

The amplitude equations of (5.21,5.22) are more complicated. It follows from (5.22) that $a_2 = 0$ when $a_1 = 0$. That is, the second mode is excited only in the presence of the first mode. On the other hand, the first mode can be excited alone since $a_1 > 0$ in (5.21) when $a_2 = 0$. The feedback from the second mode through $J_0(a_2)$ in (5.21) is not essential when considering a_1 .

To extract more information we make a further approximation. We first linearize the Bessel functions on the right hand sides, i.e. $J_1(a_1) \approx a_1/2$ and $J_0(a_2) \approx 1$. (Consequently, F_1 becomes independent of A_2 , and the feedback from the second mode is neglected. Then, (5.21) reduces to the equations obtained through the method of harmonic balance [28].)

On the left hand sides of (5.21,5.22), the function $J_0(a)/a$ is monotonically decreasing from ∞ to zero as a increases from 0 to the first zero of J_0 , which is $a^* \approx 2.4$. Thus, for any ω , a can be found within 0 and a^* . Approximating the function crudely by $J_0(a)/a \approx 1/a$ would make the range of a unbounded. This is not desirable near the resonances. We could include the next term from the expansion of J_0 , but this would make the following algebra more complicated. Alternatively, we replace the function by another one which has the same asymptotic behavior as $a \rightarrow 0$ and a bounded domain for a . We use

$$(J_0(a)/a)^2 \approx 1/a^2 - 1/4. \quad (5.23)$$

This has a slightly different saturation amplitude at $a^* = 2$ but overall the approximation is good; the error in a introduced by this replacement is less than 5% for $a < 0.7$ and at most 20% when a saturates. In return for the error introduced at this stage, we obtain simple expressions for the amplitudes as

$$a_1 = (b_1^2 + 1/4)^{-1/2} \quad \text{and} \quad a_2 = (b_2^2 + 1/4)^{-1/2}, \quad (5.24)$$

where

$$b_1^2 = \delta_1^2 + \Gamma^2 \omega^2 \quad \text{and} \quad b_2^2 = 4(\delta_2^2 + 4\Gamma^2 \omega^2)/a_1^2. \quad (5.25)$$

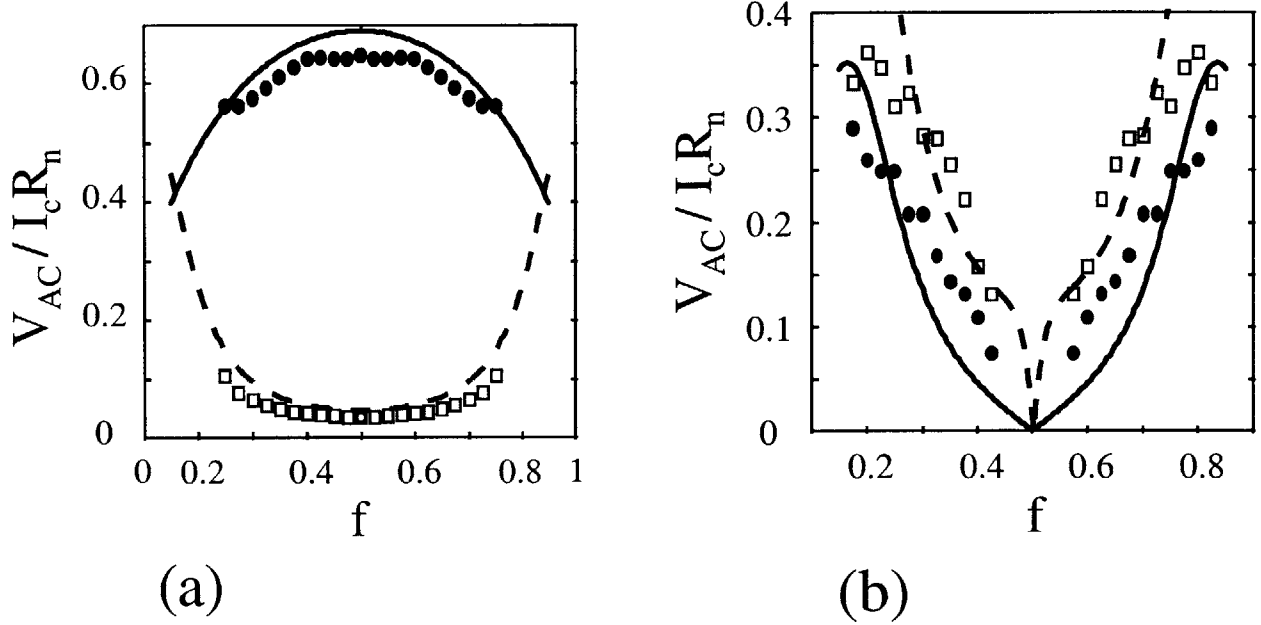


Figure 5-4: Amplitudes of the first two AC voltage harmonics on (a) Eck step and (b) the $m = 2$ step vs. f . The theory (5.24) is represented by a solid (dashed) line for the first (second) harmonic. Filled circles and open squares show the amplitude of the first and second harmonics, respectively, from simulations. The values of Λ_J and Γ are the same as in Fig. 5-1.

Once the phases and amplitudes of the modes are determined, the instantaneous voltage is obtained from the time-derivative of (5.16). In our normalization,

$$V/I_c R_n = \Gamma\omega [1 + a_1 \cos(x + \theta_1) + 2a_2 \cos(2x + \theta_2)]. \quad (5.26)$$

Thus, the DC voltage and the AC amplitude of the mode m are

$$V_{DC}/I_c R_n = \Gamma\omega \quad \text{and} \quad V_{AC}/I_c R_n = \Gamma\omega m a_m. \quad (5.27)$$

In Fig. 5-4, we compare the amplitude estimate with simulations. On the first two steps, the peak AC voltage amplitudes for the first two Fourier modes are obtained from simulations, shown as data points. The estimates of the resonance frequencies $\omega = \omega_1$ and $\omega_2/2$ from (5.12) are used. The theoretical curves show a reasonable agreement with the data on the Eck step. On the second step the comparison is

worse, but the overall magnitude and f -dependence are estimated fairly, considering the several approximations made during the derivation.

The maximum AC voltage oscillation of the first mode on the Eck step is achieved at $f = 0.5$. The maximum of the second mode on the second step happens near the lower critical frustration ($f \approx 0.2$). The vertical axes in Fig. 5-4 are shown in terms of AC voltages. Converted back to the amplitudes, $a_1 < 1.75$ and $a_2 < 0.4$ on the Eck step for $0.2 < f < 0.8$. This is thought to be within the validity of the assumptions. On the second step, $a_1 < 1.8$ for $0.15 < f < 0.45$, but a_2 exceeds unity when $f < 0.25$. The bending of the theoretical curves in (b) when $f < 0.25$ may be attributed to the large predicted magnitude of a_2 . Including terms involving $J_1(a_2)$ in the modal equations would be necessary to make a better estimate in the region.

Generally, our assumption is violated when a_1 saturates in (5.24), or when b_1^2 becomes small. On the Eck peak $b_1^2 \approx (2\Gamma\Lambda_J \sin(\pi f))^2$, so the assumption breaks down for very small Γ and/or Λ_J . Similarly, a_2 exceeding unity indicates that we need more coupling terms included from (5.8). On the $m = 2$ step, $a_2 < 1$ is fulfilled when $\Gamma^2\omega_2^2[1 + \Gamma^2\omega_2^2 + 4(\omega_1^2 - \omega_2^2/4)^2] > 3/4$. Again, small Λ_J and/or Γ make it easier to violate the criterion. Thus, the validity of our approximations is limited to when $\Gamma\Lambda_J$ is relatively large and resonances are not so strong.

5.1.3 Power at resonances

The calculation of the mode amplitudes provides a theoretical upper limit for the power available from the Josephson oscillator at resonance. If we assume a matched load condition, then the power dissipated in the load is just the power dissipated in the matched resistance. Using the RCSJ model and assuming sinusoidal voltage oscillations, this corresponds to $P = V_{AC}^2/8R_{arr}$, where $R_{arr} = R_n/N$ is the array resistance. The power available from mode m is then

$$\frac{P_m}{I_c^2 R_n} = \frac{N}{8} \left(\frac{V_{AC}}{I_c R_n} \right)^2 = \frac{N}{8} (\Gamma \omega m a_m)^2 \quad (5.28)$$

with a_m estimated in (5.24) of Section 3.7. Therefore, the vertical axis of Fig. 5-4 is also $\sqrt{8P_m/N I_c^2 R_n}$, and the f -dependence of the powers can be read directly from the figure. When biasing on the Eck step, the largest power and the highest frequency are obtained at $f = 0.5$. When the system is biased on the second-harmonic ($m = 2$) step, the largest power is obtained near $f = 0.2$, and the highest frequency is achieved near $f = 0.25$.

We take our experimental values ($I_c R_n = 0.93$ mV and $R_n = 16.6 \Omega$) and the maximum amplitudes in Fig.5-4 ($V_{AC,1} = 0.65 I_c R_n$ on the Eck step and $V_{AC,2} = 0.36 I_c R_n$ on the second step). This predicts a maximum of about 150 nW from the first harmonic at the first resonance and 46 nW from the second harmonic at the second resonance. These numbers are much smaller than previous estimates [18], and, according to measurements [19, 57], are probably more realistic.

Our simulation and analysis show that multiple Fourier modes are excited on the new steps $m > 1$. For possible applications as oscillators, this is not desirable since the AC power is therefore distributed among the modes, instead of being concentrated in one mode, as at the Eck step. Usually in such a case one could simply increase the drive, to increase the output at the desired frequency. However, in this system the driving current is limited because if it is increased beyond the top of the step, the resonance becomes unstable. Furthermore, since the maximum output power is small for a single row, methods are needed to combine power from multiple rows while

preserving the frequency content of the resonance.

Both discrete rows of underdamped Josephson junctions and continuous long junctions operating at the Eck step have already been proposed as high frequency oscillators [10, 73]. Although no single experiment has directly compared the two systems, studies indicate that the output power levels are comparable, while the output impedance of the discrete system may be advantageously higher [10]. In order to increase power levels in either case, additional oscillators are required. Stacks of continuous long junctions have been fabricated and measured [74, 75, 76], as well as the analogous inductively coupled discrete arrays [28, 37]. However, in both systems, the power is only increased if the oscillating elements are phase-locked and in-phase. The existence of in-phase as well as anti-phase states have been well established for both discrete and continuous systems, through numerics [77], simulations [38, 71], and experiments [28, 78]. Unfortunately, in both cases the anti-phase pattern is preferred at the Eck step [28, 78], and the output oscillations of adjacent elements almost completely cancel. In addition, the difficulty (and necessity) of fabricating identical oscillators in the case of continuous stacks limits the possibility for improving this system.

On the other hand, the presence of higher harmonic resonances in discrete systems may actually be an advantage in terms of power combining. As observed in [37], when the discrete system is biased on the stable $m = 2$ peak, the fundamental oscillations of the rows are anti-phase (shifted by π), but the second harmonics are still in-phase. Thus, the output power from the second mode is enhanced. It is important to note that such modes do not exist in uniform continuous long junctions. So although the power level of a single row biased in this state is lower than the oscillators mentioned above, the potential for power-combining in this state is much greater. Simulations indicate that this in-phase resonance for the second mode is stable for many coupled rows [37], which is promising for oscillator applications.

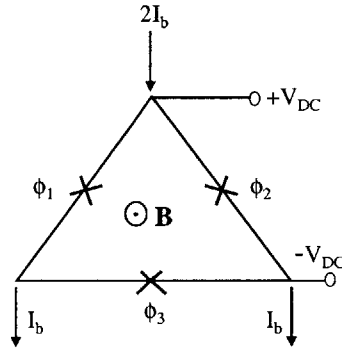


Figure 5-5: A single triangle cell.

5.2 Triangular Arrays

5.2.1 DC Measurements

Triangular arrays have been proposed as a possible alternative for obtaining useful AC power from Josephson networks [49]. A single triangular cell is shown in Fig. 5-5. DC current is applied to the vertical junctions, and the average DC voltage V_{DC} is measured across the vertical junctions. A row of triangular cells is shown in Fig. 5-6.

According to the analysis of Yukon and Lin, strong $L_s C$ and $L_J C$ resonances can occur in systems with three junctions per cell. The $L_s C$ resonance is similar to that associated with the Eck step in parallel arrays. There is no counterpart of the $L_J C$ resonance in parallel arrays, since it is related to the presence of the new third junction, which receives no DC bias ¹ [47, 49]. These resonances correspond to large-amplitude AC oscillations of the junction voltages. The phase differences between the oscillating junctions are determined by the magnetic field, just as for the case of parallel (2 junction/ cell) arrays. At $f = 1/2$, adjacent vertical junctions oscillate

¹We call the junctions in triangular arrays which receive no DC bias “horizontal” and the junctions which receive a DC bias “vertical”, since, in this thesis, the DC bias is usually drawn in the vertical direction on the page.

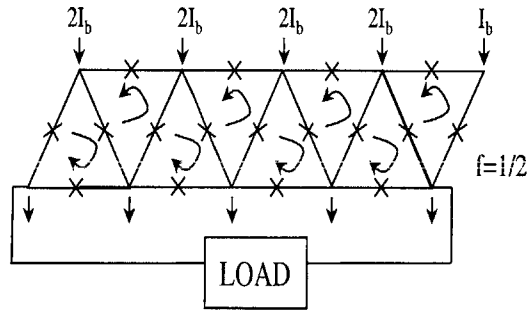


Figure 5-6: Triangular cell row, with load connected across horizontal junctions. Bias resistors are used to inject the current. The directions of the circulating currents at $f = 1/2$ are shown.

exactly out-of-phase. However, it is the relative phases of the horizontal junctions which are of interest in this system. Yukon and Lin used numerical simulations to show that at $f = 1/2$, the horizontal junctions along the same line oscillated exactly in-phase. This in-phase oscillation is stabilized and tuned by the DC bias on the vertical junctions. For example, in Fig. 5-6, all of the horizontal junctions along the bottom of the row oscillate in-phase. Therefore, the authors suggested connecting a load across the *horizontal* junctions, as shown in the figure. For N_h horizontal junctions, this supplies N_h times the voltage of a single junction to the load. If the load is either matched to or voltage-biased by the array, the delivered power will be multiplied by N_h . Since the voltage-bias regime corresponds to the case where the source impedance (the array) is much less than the load impedance, this is where typical systems ($50\ \Omega$ loads) might operate.

The DC IV curves of a single cell and an 8-cell array (unloaded) are shown in Fig. 5-7. For both the single cell and the array, the parameters are $\beta_c = 230$ and $\Lambda_J^2 = 2.4$. The lower voltage step is associated with an $L_J C$ resonance, while the upper step is associated with an $L_s C$ resonance [49]. The currents are normalized to

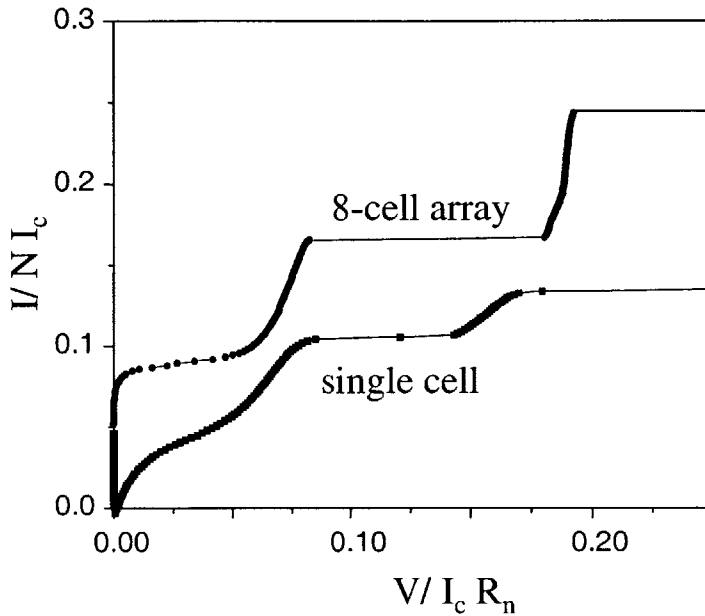


Figure 5-7: Current-Voltage characteristics of a single triangular cell and of an 8-cell array. The parameters are $\beta_c = 230$ and $\Lambda_J^2 = 2.4$, and $f = 0.5$.

the number of vertical junctions so that the systems can be compared. The observed steps are characteristics of single cells, and their position does not change significantly with the number of array cells. Measurements of two different cell sizes, however, show that the upper step voltage depends strongly on the cell geometry, while the lower step is only slightly affected. The steps appear only in the presence of a magnetic field, when the average applied flux per cell is approximately one-half. They are stable for a range on $f = 0.3 - 0.7$. Figure 5-8 shows the range of stability and the step voltage variation, by plotting the step voltage together with the array critical current versus frustration. Both are periodic in field. As usual, the critical current is largest at $f = 0$, while the steps maximize at $f = 0.5$. These steps also appear in measurements of high critical current density junctions, where $\beta_c \approx 10 - 20$. At low temperatures the high current density samples have Λ_J^2 values well below 1. We found that the upper step, corresponding to the $L_s C$ resonance, is only stable when the temperature is raised such that $\Lambda_J^2 > 0.3$ (approximately).

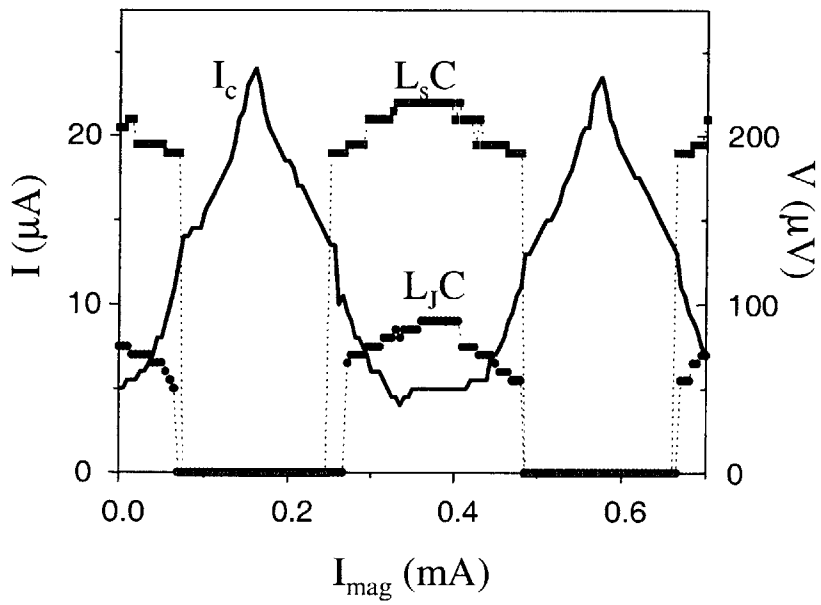


Figure 5-8: Step voltage versus field is compared to the critical current versus field for the 8-cell triangular array.

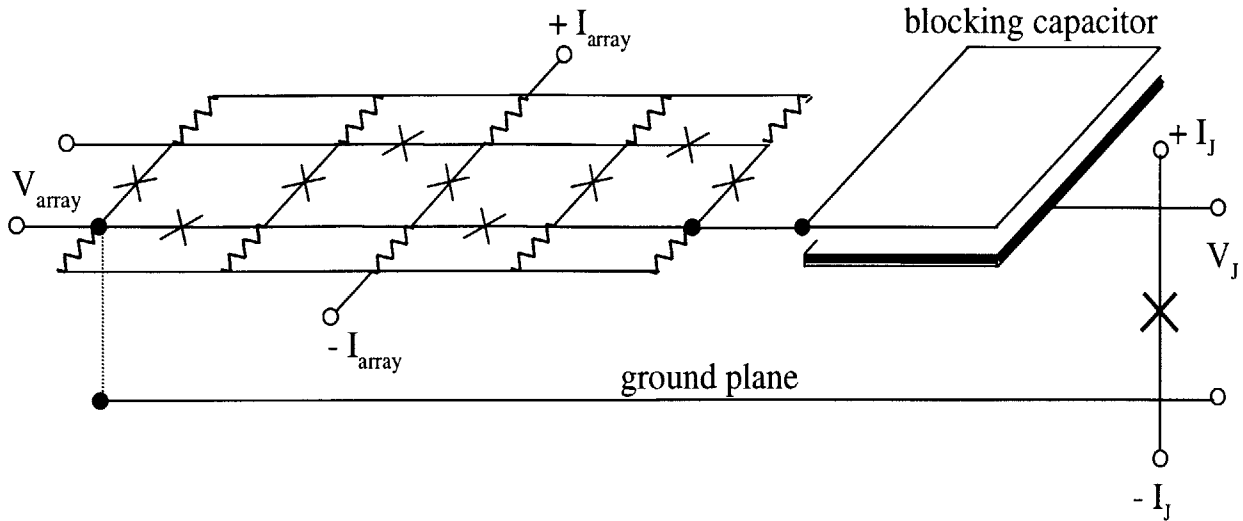


Figure 5-9: Triangular array coupled to a detector junction.

5.2.2 AC Measurements: on-chip and off-chip

DC measurements have confirmed the presence of an $L_s C$ resonance in the triangular cell arrays. The AC power from horizontal junctions has been successfully tested two different ways. Both detection methods involved collaborations with other groups.

The AC output of a Josephson array can be detected on-chip by using another Josephson junction. If AC power at a single frequency is coupled into a single overdamped junction, then Shapiro steps [68] will appear in the detector junction IV characteristic. The voltage position of the step is related to the AC bias frequency by the Josephson relation. Likewise, the AC bias frequency is determined by the DC bias of the Josephson junction array source. The height of the step is related to the power of the radiation. By simulating a single Josephson junction and the coupling circuit to an ideal AC source (which in this case represents the triangular row), the power coupled out from the array can be estimated. This scheme was first successfully used on Josephson networks by Benz [69] and was later improved by Cawthorne [66].

Our preliminary measurements of the AC power from a triangular row use the

exact coupling circuit and detector junction designed by Professor Lobb and Fred Cawthorne at the University of Maryland, Department of Physics. Their original system was also fabricated by HYPRES, and their results on 2D square arrays are published in reference [66]. A schematic of the triangular array coupled to a detecting junction is shown in Fig. 5-9. The arrays measured have 20 cells, or 10 horizontal junctions. The blocking capacitor has dimensions $376 \times 181 \mu\text{m}^2$ and has a capacitance of approximately $C_B = 14 \text{ pF}$. A ground plane is placed under the array to decrease the self inductance of the loops and to provide a low-inductance connection from the array to the detector. The ground plane is narrowed to a strip under the blocking capacitor, as suggested by Cawthorne *et al.* in [66], leading to a parasitic capacitance from the blocking capacitor to ground of only $C_G = 0.5 \text{ pF}$. Both the detector junction and the array junctions are $3 \times 3 \mu\text{m}^2$ and are shunted with approximately $R_{\text{sh}} = 1.1 \Omega$. For $j_c = 1300 \text{ A/cm}^2$, this gives an overdamped system with $\beta_c = 0.15$. We estimate the loop inductance as roughly $L_s \approx \mu_o \sqrt{A}/3.7$, where A is the loop area and the factor of 3.7 is due to the ground plane [79]. With the loop area $A = 18 \times 18 \mu\text{m}^2$, $L_s \approx 6.2 \text{ pH}$. Thus, $\Lambda_J^2 = 0.45$. Due to the presence of a ground plane, magnetic field must be applied to the array using a control wire. The wire is not included in the schematic of Fig. 5-9, but is placed along the line of the top row of horizontal junctions and is superconducting.

Using measurements of the array critical current versus field, as in Fig. 5-8, we determine that the value of $I_{\text{ctrl}} = 0.92 \text{ mA}$ in the control wire produces $f = 1/2$ in the array. Since these arrays are overdamped, the $L_s C$ and $L_J C$ resonant steps are not very pronounced and cannot be used to determine f . When the array is biased at a nonzero voltage and $f = 1/2$, the theory and simulations of [49, 50] indicate that the horizontal junctions should oscillate in-phase and couple power to the detector. This is confirmed by the observation of Shapiro steps in the detector junction. Figure 5-10 shows the detector junction IV curves for both $I_{\text{array}} = 0$ and $I_{\text{array}} = 6.6 \text{ mA}$. When $I_{\text{array}} = 0 \text{ mA}$, no Shapiro steps appear. Other structure is visible in the IV curve, resulting from the dynamics of the single junction with the load that it sees. In the IV curve on the right, a clear step appears at $V_J = 0.41 \text{ mA}$. The dotted

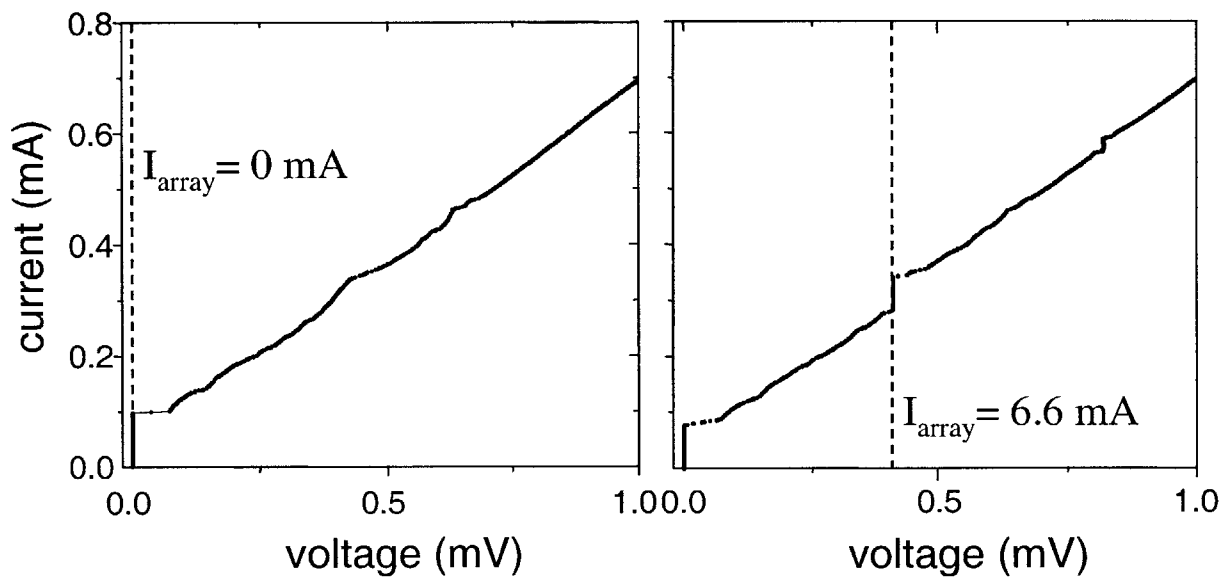


Figure 5-10: IV curves of the detector junction when the triangular array is biased at $I_{\text{array}} = 0 \text{ mA}$, in the left IV, and $I_{\text{array}} = 6.6 \text{ mA}$, on the right. The dotted line shows the measured array voltage, which also matches the voltage of the primary Shapiro step. For $I_{\text{array}} = 6.6 \text{ mA}$, the primary Shapiro step occurs at $V_J = 0.41 \text{ mV}$, and a second step is visible at $V_J = 0.82 \text{ mV}$.

line shows the measured voltage across the triangular array when it is biased with $I_{\text{array}} = 6.6$ mA. The fixed array voltage exactly matches the voltage of the Shapiro step. A second Shapiro step is also visible at $V_J = 0.82$ mA. When the array voltage is moved (by changing I_{array}), the Shapiro step in the detector junction also changes.

Figure 5-11 shows an IV of the triangular array at $f = 0$. (Due to the large damping, there is no visible change in the array IV as f is increased, and the step associated with the $L_s C$ resonance in underdamped arrays is not visible). The region within the dotted lines indicates the range of array bias values which produce a measurable Shapiro step in the detector junction. The voltage range corresponds to a bandwidth of 24 – 227 GHz. This wide range implies that the array produces AC power even when not biased at a particular resonance voltage. However, the height of the Shapiro step varies within the bandwidth of Fig. 5-11, and the power which can be coupled from the array is not uniform within that bandwidth. To estimate the power which is coupled from the horizontal junctions of the array, numerical simulations of the detector junction should be matched to the IV curves of Fig. 5-10. On the other hand, direct measurements of the power can be obtained using off-chip detectors.

Off-chip detection is usually more desirable, since then linewidth measurements are also possible. We collaborated with Dr. Pasquiline Caputo and Professor A. Ustinov² at the Institute for Thin Film and Ion Technology at KFA in Juelich, Germany to assist with designs for off-chip detection. The laboratory at KFA was equipped with a cryogenic probe with rectangular waveguides for the frequency range of 80–120 GHz. The room temperature receiver is operated as a radiometer with a fixed detector bandwidth. The power from the triangular row is coupled into the rectangular waveguide via a finline antenna. The exponentially tapered finline antenna transforms a stripline impedance into a rectangular waveguide [80]. A schematic of the design is shown in Fig. 5-12. In the figure, $M0 - M3$ are superconductor layers of the HYPRES process [20]. In order to obtain a good impedance match, the stripline impedance Z_s at the input of the antenna was calculated in the limit when the stripline width w is

²Present address: University of Erlangen, Germany.

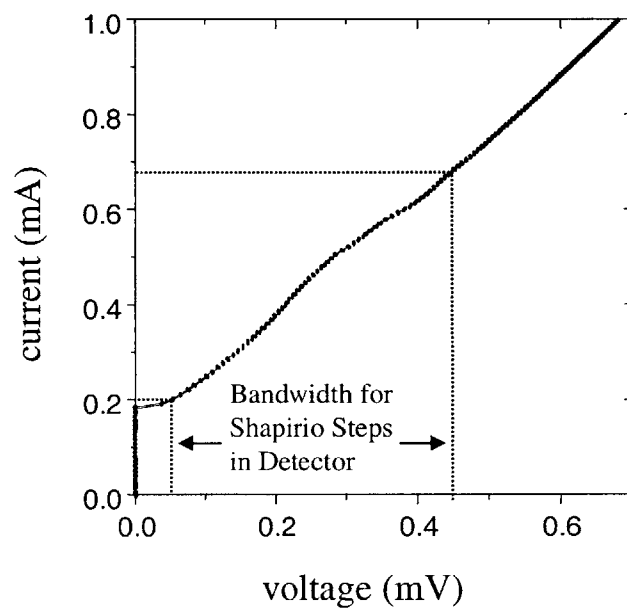


Figure 5-11: IV curve of the triangular array, when the detector junction is left unbiased. The region within the dotted lines indicates the range of bias for which Shapiro steps can be measured in the detector junction. The range of voltages is 0.05 – 0.47 mV, corresponding to a bandwidth of 24 – 227 GHz.

larger than the dielectric height h ($w/h > 2$)[81]

$$Z_s = \frac{377}{\sqrt{\epsilon_r}} \left(\frac{w}{h} + 0.883 + \frac{\epsilon_r + 1}{\pi \epsilon_r} \left[\ln \left(\frac{w}{2h} + 0.94 \right) + 1.451 \right] + 0.165 \frac{\epsilon_r - 1}{\epsilon_r^2} \right)^{-1} \quad (5.29)$$

where $\epsilon_r = 3.5$ is the dielectric constant for SiO_2 and $h = 0.65 \mu\text{m}$ with HYPRES. In this calculation, the stripline is treated as a normal conductor. The width of the stripline was then chosen to match the impedance looking into the triangular row. A 12-cell row was used, coupling 6 horizontal junctions across the antenna electrodes. The impedance of the array was calculated by replacing the junctions with parallel R_nC circuits. Much better models for the junction impedance are now available [51]. However, this effort at impedance matching sufficed for our preliminary experiment. The high current density junctions ($j_c = 1000 \text{ A/cm}^2$) with areas of $3 \times 3 \mu\text{m}^2$ have an impedance of approximately 4Ω at 100 GHz. In this model, then, the array impedance is 24Ω at the expected operating frequency. Therefore a stripline width of $w = 5 \mu\text{m}^2$ was chosen for the start of the finline antenna.

Figure 5-13 shows the measurements by Dr. P. Caputo at KFA of the power versus the triangular array bias at $f = 1/2$. Radiation is detected at 75 GHz when the array is biased on the L_sC resonance step. The detector bandwidth is 0.9 GHz, but is wider than the peak in Fig. 5-13. The radiation is a maximum at $f = 1/2$ and decays to zero at $f = 0, \pm 1$. This shows that, as predicted by Yukon and Lin [50], the applied field can change the relative phases of the horizontal junctions. The detected power is a maximum when the horizontal junctions are oscillating in-phase at $f = 1/2$. The maximum power from the array is estimated to be 90 pW, after taking into account losses ($\approx 13 \text{ dB}$) in the finline antenna and waveguide coupling.

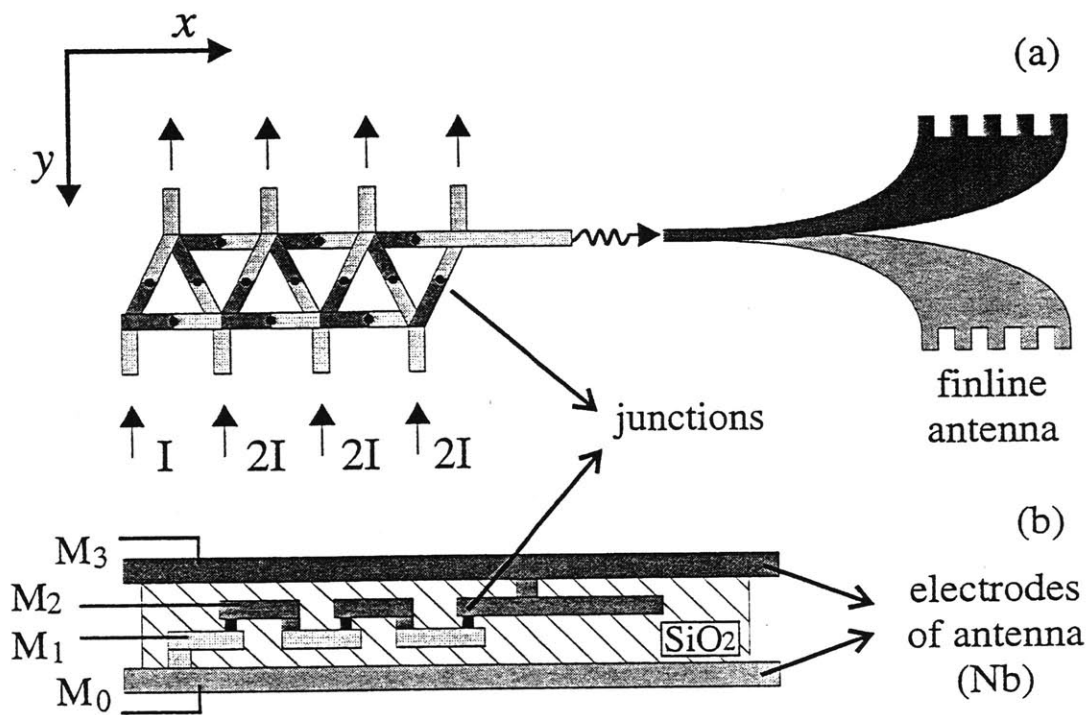


Figure 5-12: (a) Schematic top view of a 6 cell triangular array with the finline antenna which couples the array signal to the 80 – 120 GHz rectangular waveguide, and (b) cross-sectional view of the horizontal junctions of the array inserted in the microstripline and ending in the antenna.

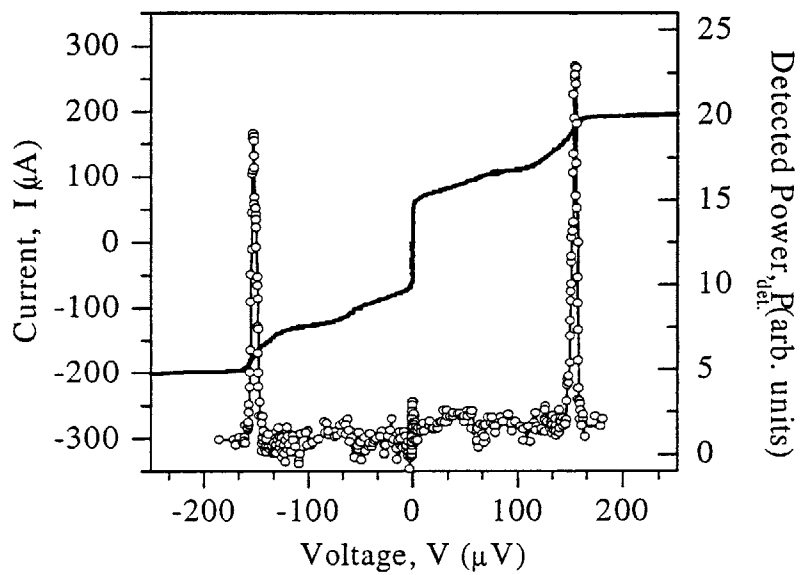


Figure 5-13: Measurement by Dr. P. Caputo of radiation emission from a 12 cell array. The IV curve is shown together with the detected radiation power at frequency 75 GHz. The detector bandwidth is 0.9 GHz.

5.3 Conclusions

Josephson systems are natural DC to AC converters. In this chapter, we investigated the AC power which might be produced by two specific Josephson junction networks.

Based on extensive experimental and numerical results on parallel rows (Chapter 3), we developed analytical expressions for the AC voltage amplitudes at resonance. The analysis assumed an infinitely long array with no load. If the system could be perfectly matched to a load, then the power in this AC mode will be shared with the load. Therefore, this represents an *upper limit* on the power available to a load from a single row at resonance. Our calculations suggest that, for underdamped junctions made in HYPRES technology, the power is only in the 50 – 150 nW range. More recently, analysis which carefully includes the effect of various loads on parallel rows shows that the power delivered to a matched load could be better than our estimate by a factor of two [51].

A second Josephson oscillator array was investigated through both DC and AC experiments. The simulations and analysis of Yukon and Lin [50] suggested that arrays with three junctions per cell might have unique advantages as high frequency oscillators. These triangular arrays operate at $f = 1/2$ and power is coupled from the horizontal junctions. This configuration allows one to couple from a whole series of junctions which oscillate in-phase. We successfully measured power from the horizontal junctions by two different methods. In collaboration with Dr. Cawthorne and Professor Lobb at the University of Maryland, we used an on-chip detector junction and measured Shapiro steps. Also, in collaboration with Dr. Caputo and Professor Ustinov at KFA in Juelich, Germany, we placed a finline antenna across the horizontal row of junctions and coupled power off-chip, to a room temperature receiver. Both experiments demonstrated a proof-of-concept, and future work should include improved matching to measure the maximum available power.

Chapter 6

Future Work

In this thesis research, several open questions and future research directions have been identified.

A particularly exciting new question is that of the mechanism creating the negative differential resistance in single rings. This feature is well characterized experimentally but is still not explained. In Section 3.3, detailed data sets for a system with $N = 8$ and $M = 3$ were presented. New plots might still be made from this data, emphasizing different aspects of the system response. The plots of the $N = 8$ with $M = 4$ data and the $N = 9$ with $M = 2$ data should also be carefully compared. The most definitive information will come from numerical simulations. If the negative differential resistance feature can be found in simulations, then the complete solution will be available for study. Effects which might be added to the simulations in order to find the feature include disorder in the junction critical currents, thermal noise, and the influence of the biasing circuit.

In coupled Josephson junction rings, some of the more interesting effects do appear in numerical simulations, but could still benefit from future research. The voltage shifts exhibited by each ring in response to a change of the other ring's dynamical state are not fully explained. The energy balance argument offered some intuition, but no concrete justification. In addition, the energy balance approach focuses on a regime where only a few spatial modes are excited. This is limited to the regime where $M\Lambda_J^2/N > 1$. All of the experimental results and most of the simulations

were in this regime. However, we also studied coupled rings with $N = 51$ junctions which were in a highly discrete regime. Voltage shifts appeared in these simulated IV curves as well, but were in a different direction than in the less discrete systems. As the voltage shifts are considered in the future, it might be helpful to remember that the behavior of the coupled system can be qualitatively different in these two regimes.

Another issue which might be pursued in the future is the precession of the kink/anti-kink collision region in the $N = 51$ junction coupled rings. Simulations conducted by J. Weisenfeld and Professor Strogatz at Cornell University [82] indicated that, as N is lowered and the system becomes less discrete, the collision region is not as well-defined. Instead, the solutions in the ring with $M = 0$ and a single excited pair show that the $k = 1$ spatial mode is strongly excited, due to the kink and the anti-kink motion. However, the solution is quasi-periodic. The two frequencies may be the in-phase and anti-phase resonances. These effects are almost certainly due to the single kink in the other ring, which breaks the symmetry of the $M = 0$ excited pair solutions. Future research might include a study of the cross-over from a highly discrete system where precession can be identified to the non-discrete system where beating is observed.

The possibility of using Josephson junction arrays as AC sources was also addressed in this research. This thesis, however, presents only some preliminary work on this topic, and the suggestions for future work are numerous.

For parallel arrays to be used as oscillators, an upper limit on the power which is available at the resonance frequency was derived in Section 5.1.3. However, this calculation was for an unloaded array. The power (at the resonance frequency) which can actually be *delivered* to a load is more relevant, and has recently been calculated by Trías *et al.* in [51]. This theoretical power needs to be compared with experimental results. A related consideration is the possibility of using inductively coupled rows to deliver more power to a load. The oscillations of the two rows must be in-phase. In future research, the effect of a load on the stability of the in-phase oscillation might be considered.

The triangular arrays were tested both on-chip and off-chip, and power was successfully coupled from the horizontal junctions. An immediate goal might be to complete simulations of the triangular row coupled to the on-chip detector junction so that the delivered power can be estimated. The next step will be to design a better matching circuit to the detector junction, using the impedance models presented in [51].

In order to take advantage of the unique triangular array geometry, future designs must be adjusted. Our experimental results showed that overdamped triangular arrays delivered power over a wide bandwidth (not limited to the L_sC resonance). In fact, the L_sC resonance step was suppressed by the damping and the array IV did not change significantly with applied field. This can be the advantage of using overdamped triangular arrays—the power can be controlled by the applied magnetic field, independently of the frequency, which is controlled by the bias. However, the results of our preliminary experiments indicated that the applied field was not well-controlled, and the system should be re-designed to test this behavior of the triangular array. The experiment showed that the Shapiro step height was not uniform over the available bandwidth. In addition, the expected maximum of power at $f = 1/2$ and minimum at $f = 0$ was not observed. The Shapiro step height did not change with an identifiable pattern in f . We determined that this was due to the presence of non-uniform stray fields resulting from the bias circuit. This is not an issue in un-shunted underdamped arrays, since the bias currents are so much smaller. New designs should include a modified biasing circuit to remove this effect.

Appendix A

Experimental Parameters

Samples are fabricated by HYPRES [20], using a Nb-AlO_x-Nb trilayer process. The T_c of Niobium is approximately 9.2 K. The critical current densities produced by HYPRES range from approximately 100–1000 A/cm². HYPRES provides a measured critical current for each sample, and guarantees a uniformity of approximately 5%. We measure the junction normal-state resistance, which is marked “Resistive normal state” in Fig. A-1, when our sample is close to T_c . The actual critical current is then estimated from $I_c R_n = 1.9$ mV. In most designs, our junctions are $3 \times 3 \mu\text{m}^2$. The j_c can then be calculated and compared with the value provided by HYPRES. Usually, the comparison is within 5% for high j_c samples (~ 1000 A/cm²), but can be different by a factor of 2 for low j_c samples. Variations in the junction areas do not appear to be the cause of this difference. Once the I_c for $T = 0$ has been calculated, we assume that the junction critical current follows the Ambegaokar-Baratoff dependence [70]. The junction capacitance is calculated from $C = AC'$, where $C' = 38$ fF/ μm^2 is determined by HYPRES and A is the designed junction area. The Stewart-McCumber parameter can now be calculated from $\beta_c = R_n^2 C / L_J$, where $L_J(T) = \Phi_o / 2\pi I_c(T)$. The damping is defined by $\Gamma = \beta_c^{-1/2}$.

The loop inductance of a single cell in the array or ring can be measured by fitting the Eck step voltages to the theory [10]

$$V_E = \frac{\Phi_o}{\pi\sqrt{L_s C}} \sin(\pi f) \tag{A.1}$$

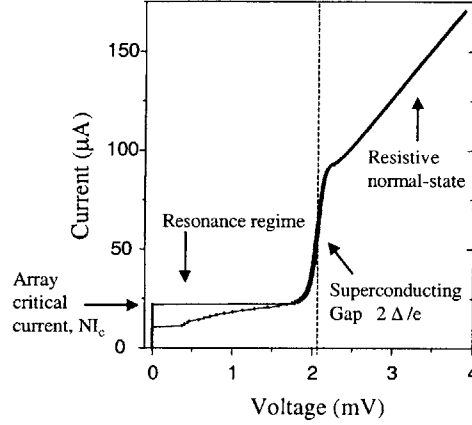


Figure A-1: $N=8$ ring, $M=0$. $T = 7.3$ K, $\beta_c = 162$, $\Lambda_J^2 = 4.29$.

For rings, we use $f = M/N$. The value of L_s is typically about 12 pH. By including two more fitting parameters, we can also estimate the values of the nearest-neighbor cell mutual inductances M_v and M_h [28]

$$V_{\pm} = \frac{\Phi_o}{\pi\sqrt{L_s C}} \left[\frac{1}{1 \mp M_v - 2M_h \cos(2\pi f)} \right]^{1/2} \sin(\pi f) \quad (\text{A.2})$$

The parameters M_v and M_h are the ratios of the mutual inductance to the cell self-inductance, and are typically about 0.15. The V_{\pm} refers to the fact that for a system of two coupled rings or rows, two Eck steps appear. This effect is discussed in more detail in Chapter 4.

Once the cell self-inductance is known, we can calculate the discreteness parameter, or 1-dimensional penetration depth, $\Lambda_J^2 = L_J/L_s$. For samples with $j_c \approx 100$ A/cm², the typical values range from $\Lambda_J^2 = 2 - 4$, while for $j_c \approx 1000$ A/cm², the discreteness can range from $\Lambda_J^2 = 0.2 - 0.4$.

Appendix B

Modal Expansion of Sine Terms

In this section, we derive a relationship between the discrete Fourier series coefficients of the nonlinear sine term (F_k) and the Fourier components of the phase (P_k).

Since the function $\varphi_j(t)$ is discrete and periodic,

$$\varphi_j = \sum_{k \in \langle N \rangle} P_k(t) e^{ik(2\pi/N)j} \quad (\text{B.1})$$

The function φ_j is physically a difference of phases between two superconductors. The phase must be a real function since it represents the phase of a complex variable. Thus, $P_k = P_{-k}^*$. Then

$$\begin{aligned} \varphi_j &= \sum_{-N/2}^{N/2-1} P_k e^{ik(2\pi/N)j} \\ &= P_0 + \sum_{k=1}^{N/2-1} [P_k e^{ik(2\pi/N)j} + P_k^* e^{-ik(2\pi/N)j}] \end{aligned} \quad (\text{B.2})$$

Writing $P_k = (-i/2)p_k e^{i\theta_k}$ in polar coordinates and defining $\xi \equiv j2\pi/N$,

$$\varphi_j = P_0 + \sum_{k=1}^{N/2-1} p_k \sin(k\xi + \theta_k) \quad (\text{B.3})$$

Similarly, since $\sin(\varphi_j + M\xi)$ is also real and periodic,

$$\sin[\varphi_j + M\xi] = F_0 + \sum_{k=1}^{N/2-1} [F_k e^{ik\xi} + F_k^* e^{-ik\xi}] \quad (\text{B.4})$$

We will also use the fact that

$$\sin(\varphi_j + M\xi) = -\frac{i}{2} e^{i(\varphi_j + M\xi)} + \frac{i}{2} e^{-i(\varphi_j + M\xi)} \quad (\text{B.5})$$

The first exponential term in equation (B.5) can be expanded into

$$\begin{aligned} e^{i(\varphi_j + M\xi)} &= e^{i(M\xi + P_0)} \prod_{k=1}^{N/2-1} e^{ip_k \sin(k\xi + \theta_k)} \\ &= e^{i(M\xi + P_0)} \prod_{k=1}^{N/2-1} \left[\sum_{l=-\infty}^{+\infty} J_l(p_k) e^{il(k\xi + \theta_k)} \right] \end{aligned} \quad (\text{B.6})$$

Assuming that the p_k are all much less than order one, we take only terms linear in p_k . Therefore only terms $l = 0, +1, -1$ will be considered. Furthermore, we will approximate that

$$\begin{aligned} J_0(p_k) &\approx 1 \\ J_1(p_k) &\approx p_k/2 \\ J_{-1}(p_k) &\approx -p_k/2 \end{aligned} \quad (\text{B.7})$$

Using these approximations, equation (B.6) becomes

$$e^{i(\varphi_j + M\xi)} \approx e^{i(M\xi + P_0)} \prod_{k=1}^{N/2-1} \left[1 + \frac{p_k}{2} e^{i(k\xi + \theta_k)} - \frac{p_k}{2} e^{-i(k\xi + \theta_k)} \right] \quad (\text{B.8})$$

which becomes, for only linear terms in p_k ,

$$e^{i(\varphi_j + M\xi)} \approx e^{i(M\xi + P_0)} \left[1 + \sum_{k=1}^{N/2-1} \left(\frac{p_k}{2} e^{i(k\xi + \theta_k)} - \frac{p_k}{2} e^{-i(k\xi + \theta_k)} \right) \right] \quad (\text{B.9})$$

$$e^{i(\varphi_j+M\xi)} \approx e^{i(M\xi+P_0)} + \frac{1}{2}e^{iP_0} \sum_{k=1}^{N/2-1} \left(p_k e^{i[\xi(k+M)+\theta_k]} - p_k e^{-i[\xi(k-M)+\theta_k]} \right) \quad (\text{B.10})$$

Now, equation (B.10) can be used to combine equations (B.4) and (B.5).

$$\begin{aligned} F_0 + \sum_{k=1}^{N/2-1} (F_k e^{ik\xi} + F_k^* e^{-ik\xi}) = & -\frac{i}{2} e^{i(M\xi+P_0)} \\ & - \left(\frac{i}{2} \right) \frac{e^{iP_0}}{2} \left[\sum_{k=M+1}^{N/2-1+M} p_{k-M} e^{i(k\xi+\theta_{k-M})} - \sum_{k=1-M}^{N/2-1-M} p_{k+M} e^{-i(k\xi+\theta_{k+M})} \right] \\ & + \frac{i}{2} e^{-i(M\xi+P_0)} \\ & + \left(\frac{i}{2} \right) \frac{e^{-iP_0}}{2} \left[\sum_{k=M+1}^{N/2-1+M} p_{k-M} e^{-i(k\xi+\theta_{k-M})} - \sum_{k=1-M}^{N/2-1-M} p_{k+M} e^{i(k\xi+\theta_{k+M})} \right] \end{aligned} \quad (\text{B.11})$$

Using this last equality, we balance the coefficients of $e^{ik\xi}$ to obtain the F_k . If $M = 0$, the e^{i0} coefficients are:

$$F_0 = (-i/2)e^{iP_0} + (i/2)e^{-iP_0} = \sin P_0 \quad (\text{B.12})$$

When $M \neq 0$,

$$\begin{aligned} F_0 &= \frac{1}{2}P_M^* e^{iP_0} + \frac{1}{2}P_M e^{-iP_0} \\ &= -\frac{1}{2}p_M \sin(P_0 - \theta_M) \end{aligned} \quad (\text{B.13})$$

When $M \neq 0$, the coefficients of $e^{iM\xi}$ give

$$F_M = \frac{1}{2}[-ie^{iP_0} + P_{2M}e^{-iP_0}] \quad (\text{B.14})$$

Balancing the coefficients of $e^{ik\xi}$ for $k \neq M$ and $k \neq 0$ gives

$$F_k = \frac{1}{2}[P_{k-M}e^{iP_0} + P_{k+M}e^{-iP_0}] \quad (\text{B.15})$$

It should be remembered that $P_k = P_{k+N}$. These substitutions will be made in the $N/2$ equations which relate the P_k variables.

Appendix C

Superharmonic Resonances from Modal Equations

In Section 3.5, the modal equations for the single ring were obtained. It was seen that the $k = M$ equation is always driven by the DC voltage, ν . Even off-resonance this drives the mode to oscillate at $P_M \sim e^{i\nu t}$. This non-zero amplitude in turn drives other modes which are multiples $k = mM$. We repeat the modal equations for this particular set of coupled modes. For $P_0 = \nu t$, we have

$$\ddot{P}_M + \Gamma \dot{P}_M + \omega_M^2 P_M = \frac{i}{2} e^{i\nu t} - \frac{1}{2} P_{2M} e^{-i\nu t} \quad (\text{C.1})$$

$$\ddot{P}_{2M} + \Gamma \dot{P}_{2M} + \omega_{2M}^2 P_{2M} = -\frac{1}{2} P_M e^{i\nu t} - \frac{1}{2} P_{3M} e^{-i\nu t} \quad (\text{C.2})$$

$$\ddot{P}_{3M} + \Gamma \dot{P}_{3M} + \omega_{3M}^2 P_{3M} = -\frac{1}{2} P_{2M} e^{i\nu t} - \frac{1}{2} P_{4M} e^{-i\nu t} \quad (\text{C.3})$$

⋮

The two driving terms on the right-hand-side (RHS) will have the same effect and so, to begin with, we consider only the first of these terms. For equation (C.1), the driving frequency is at ν , and so even off-resonance $P_M \sim e^{i\nu t}$. The P_M mode will be at resonance if the RHS frequency matches the natural frequency on the LHS— if $\nu = \omega_M$. For equation (C.2), the driving frequency is due to $e^{i\nu t}$ multiplied by $P_M \sim e^{i\nu t}$, which gives a total drive of 2ν . Then the mode P_{2M} will resonate when

$2\nu = \omega_{2M}$. For the equation (C.3), the driving on the RHS is due to the combination of $e^{i\nu t}$ and P_{2M} . The mode P_{2M} is driven at 2ν , as just discussed, giving a total drive on P_{3M} of 3ν . Thus P_{3M} will resonate when $3\nu = \omega_{3M}$. In general, for modal equation $k = mM$, the drive on the RHS is at $m\nu$. Then the resonances will occur at

$$\nu = \frac{\omega_{mM}}{m} \tag{C.4}$$

This is the same dispersion relation obtained in [11] and [8]. In both these references and this analysis, the ω_k are the resonant frequencies for linear modes of the system. In [11, 8], the linear modes are excited through phase-locking with the kinks circulating around the ring. In our case, the linear modes are excited through coupling of the modal equations to the DC drive. A very important point made in [11, 8] was that m was not restricted to the set of $\langle N \rangle$. This was because m represented the number of times that a junction could “ring” in between the passing of the kink, which can be arbitrarily large, depending on the kink speed.

This example illustrates an essential characteristic of truly nonlinear systems, which is that such systems can have more “modes” than degrees of freedom. In the linearized modal system of (3.20)-(3.18), there are only $k = \langle N \rangle$ independent spatial modes. This is consistent with the fact that there are only $j = N$ junctions. However, the work of [8] shows that other modes have physical meaning and can be observed.

Appendix D

Publications and Conference Proceedings

- Duwel, A.E., C.P. Heij, J.C. Weisenfeld, M.K.S. Yeung, E. Trías, S.J.K. Vardy, H.S.J. van der Zant, S.H. Strogatz, T.P. Orlando, “Interactions of topological kinks in two coupled rings of nonlinear oscillators,” *Phys. Rev. B* **58** (13) 8749, 1998.
- Duwel, A.E., E. Trías, T.P. Orlando, H.S.J. van der Zant, S. Watanabe, S. Strogatz, “Discreteness-induced resonances and ac voltage amplitudes in long one-dimensional Josephson junction arrays,” *J. Appl. Phys.*, **82** (9) 4661, 1997.
- Duwel, A.E., T.P. Orlando, S. Watanabe, H.S.J. van der Zant, “A novel phase-locked state in discrete Josephson Oscillators,” *IEEE Trans. Appl. Supercond.*, **7** 2897, 1997.
- Duwel, A.E., E. Trías, T.P. Orlando, H.S.J. van der Zant, S. Watanabe, S. Strogatz, “Resonance splitting in discrete planar arrays of Josephson junctions,” *J. Appl. Phys.*, **79** (10) 7864, 1996.
- Duwel, A.E., H.S.J. van der Zant and T.P. Orlando, “Discrete underdamped vortex flow devices,” *IEEE Trans. Appl. Supercond.* **5** 3357, 1995.

- Duwel, A.E., Underdamped Vortex Flow Devices. Master Thesis at the Massachusetts Institute of Technology. May, 1995.
- Van der Zant, H.S.J., M. Barahona, A.E. Duwel, E. Trías, T.P. Orlando, Shinya Watanabe, Steven Strogatz, “Dynamics of one-dimensional Josephson-junction arrays,” *Physica D* , 1-8, 1994.
- Orlando, T.P., H.S.J. van der Zant, J. White, E. Trías, A.E. Duwel, “Measurements of self-field effects in arrays of Josephson junctions”, in *Macroscopic Quantum Phenomena and Coherence in Superconducting Arrays*, edited by C. Giovannella and M. Tinkham, pp. 175-186, World Scientific, 1995.
- Barahona, M., E. Trías, T.P. Orlando, A.E. Duwel, H.S.J. van der Zant, S. Watanabe, S. Strogatz, “Resonances of dynamical checkerboard states in Josephson arrays with self-inductance,” *Phys. Rev. B* **55** (18) 989, 1997.
- Caputo, P., A.E. Duwel, T.P. Orlando, A.V. Ustinov, N.C.H. Lin, S.P. Yukon, “Experiments with Triangular Arrays of Josephson Junctions,” *Proceedings of the ISEC*, Berlin, 1997.
- Trías, E., A.E. Duwel, T.P. Orlando, “Circuit Models for Arrays of Josephson Oscillators with Loads,” *IEEE Trans. Appl. Supercond.* to be published.

Appendix E

Selected Reprints

- p.162 Duwel, A.E., C.P. Heij, J.C. Weisenfeld, M.K.S. Yeung, E. Trías, S.J.K. Vardy, H.S.J. van der Zant, S.H. Strogatz, T.P. Orlando, "Interactions of topological kinks in two coupled rings of nonlinear oscillators," *Phys. Rev. B* **58** (13) 8749, 1998.
- p.168 Duwel, A.E., E. Trías, T.P. Orlando, H.S.J. van der Zant, S. Watanabe, S. Strogatz, "Discreteness-induced resonances and ac voltage amplitudes in long one-dimensional Josephson junction arrays," *J. Appl. Phys.*, **82** (9) 4661, 1997.
- p.176 Duwel, A.E., E. Trías, T.P. Orlando, H.S.J. van der Zant, S. Watanabe, S. Strogatz, "Resonance splitting in discrete planar arrays of Josephson junctions," *J. Appl. Phys.*, **79** (10) 7864, 1996.
- p.183 Duwel, A.E., T.P. Orlando, S. Watanabe, H.S.J. van der Zant, "A novel phase-locked state in discrete Josephson Oscillators," *IEEE Trans. Appl. Supercond.*, **7** 2897, 1997.
- p.187 Duwel, A.E., H.S.J. van der Zant and T.P. Orlando, "Discrete underdamped vortex flow devices," *IEEE Trans. Appl. Supercond.* **5** 3357, 1995.

Interactions of topological kinks in two coupled rings of nonlinear oscillators

A. E. Duwel

Department of Electrical Engineering & Computer Science, Massachusetts Institute of Technology, Cambridge, Massachusetts 02143

C. P. Heij

Department of Applied Physics and DIMES, Delft University of Technology, P. O. Box 5046, 2628 CJ Delft, The Netherlands

J. C. Weisenfeld and M. K. Stephen Yeung

Department of Theoretical & Applied Mechanics, Cornell University, Kimball Hall, Ithaca, New York 14853

E. Trías

Department of Electrical Engineering & Computer Science, Massachusetts Institute of Technology, Cambridge, Massachusetts 02143

S. J. K. Várdy and H. S. J. van der Zant

Department of Applied Physics and DIMES, Delft University of Technology, P. O. Box 5046, 2628 CJ Delft, The Netherlands

S. H. Strogatz

Department of Theoretical & Applied Mechanics, Cornell University, Kimball Hall, Ithaca, New York 14853

T. P. Orlando

Department of Electrical Engineering & Computer Science, Massachusetts Institute of Technology, Cambridge, Massachusetts 02143

(Received 27 April 1998; revised manuscript received 19 June 1998)

Two discrete rings of nonlinear oscillators with topologically trapped kinks exhibit features due to coupling interactions between the rings. These interaction effects include phase locking between kinks in different rings, precession of the kink/antikink collision region, excitation of kink/antikink pairs, and time-dependent switching. We study these phenomena in simulations of two coupled discrete sine-Gordon equations, and in experiments on two inductively coupled rings of niobium Josephson junctions. [S0163-1829(98)06237-7]

I. INTRODUCTION

Discrete rings of coupled nonlinear oscillators have long served as model systems in studies of spatiotemporal pattern formation. Turing's pioneering analysis of morphogenesis¹ was largely concerned with instabilities and spatial patterns in a discrete ring of N cells, each governed by nonlinear chemical kinetics and coupled together by diffusion. Rings of nonlinear oscillators have also been used to model arrays of physical systems composed of phase-locked loops,²⁻⁴ lasers,⁵ Josephson junctions,^{6,7} pendula,⁸ chemical oscillators,⁹ and chaotic circuits.¹⁰

Certain kinds of rings have an interesting topological property: they can trap an integer number of kinks. To be concrete, consider an open-ended chain of pendula coupled to their nearest neighbors by torsional springs. Twist the chain a few times and then form a ring by connecting the first and last pendula by another torsional spring. Assuming that the springs remain intact, the net number of twists always remains constant, no matter how the system evolves. Winfree¹¹ calls this principle "the conservation of winding number." It holds whether the twists spread out or form localized kinks and antikinks. More generally, trapped kinks can occur in any ring of elements satisfying the following conditions: the state of each element involves a circular phase variable, and the state's amplitude does not vanish anywhere along the ring. Trapped kinks have been studied in

model rings of biological and chemical oscillators with strongly attracting limit cycles,^{11,12} and in long annular Josephson junctions.¹³⁻¹⁷

The dynamics are particularly rich if the oscillators are underdamped and the ring is discrete. Then, for small forcing, the twists remain localized. As these kinks propagate, they excite small-amplitude linear waves in their wake.^{13,19} When driven at certain speeds, a rotating kink can phase lock with its own radiation, leading to novel resonances that have recently been predicted⁶ and observed experimentally in discrete Josephson rings.²⁰ Because of the discreteness, it is also possible for kinks and antikinks to travel at different speeds in a single system, giving rise to quasiperiodic resonances with more complicated spatiotemporal patterns.^{7,21}

In this article, we explore a system of *two* discrete rings of underdamped oscillators, using inductively coupled Josephson junctions as an experimental realization. The nonlinear dynamics of two coupled discrete rings are almost uncharted. However the continuous counterpart, a stacked long Josephson junction ring system, has been studied experimentally,^{22,23} numerically,²⁴ and analytically.²⁵ An interesting feature is the phase locking between kinks and antikinks in the two rings. Such a phase-locking has been observed in continuous ring-systems.^{22,28} Together with the literature describing symmetries shared by (open-ended) continuous and discrete coupled systems,^{26,27} we approach the discrete coupled ring system with a certain intuition as to

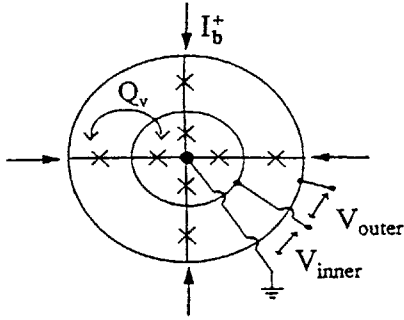


FIG. 1. Schematic of inductively coupled ring system. A uniform current I_b is fed into each node, as indicated by arrows and is extracted from the center island. In experiments, we measure the dc voltages V_{inner} and V_{outer} . Q_v is the mutual inductance between two adjacent cells of the inner and outer rings.

the types of phenomena which might be observed.

Besides the phenomena seen in single discrete rings (trapping of kinks, resonances between kinks and linear waves in the same ring), we report fascinating effects that occur because of interactions *between* the rings. Our results include phase-locking between kinks in separate rings, a precession of the kink/antikink collision region in the ring, and an extreme sensitivity of excited states to the system parameters. We view this Josephson array as a model system for studying spatiotemporal dynamics of coupled oscillators, and more specifically for exploring kink interactions in discrete lattices, a topic that is also important in, e.g., the dynamics of dislocations and ferromagnetic domain walls.^{29,30}

II. THE SYSTEM

The layout of a discrete coupled ring system with N junctions per ring is shown in Fig. 1 for $N=4$. Current is fed into the nodes of the outer ring (shown by arrows), flows radially through the junctions and is extracted at the center island. The $Nb-AIO_x-Nb$ junctions are $3 \times 3 \mu\text{m}^2$, and the critical current densities of the samples measured are in the range of 100 A/cm^2 .³¹ The radius of the outer ring is $28 \mu\text{m}$. When the system is cooled in the presence of a perpendicular magnetic field to below the superconducting transition, the total flux bounded by the continuous superconducting rings becomes trapped in units of $\Phi_0 = h/2e$. A single unit of quantized flux is called a vortex if the flux is along the applied field and an antivortex if it is opposite. A vortex and antivortex correspond to a kink and antikink. If there are $m_{v,\text{in}}$ and $m_{v,\text{out}}$ kinks in the two rings, and $m_{a,\text{in}}$ and $m_{a,\text{out}}$ antikinks, then the net, conserved phase winding in each ring is $M_{\text{in}} = m_{v,\text{in}} - m_{a,\text{in}}$ and $M_{\text{out}} = m_{v,\text{out}} - m_{a,\text{out}}$.

We use ϕ_j and ψ_j to represent the phase of junction j in the outer ring and inner ring, respectively. The dynamics are governed by two coupled discrete sine-Gordon equations:

$$\mathcal{N}[\phi_j] - \Lambda_{\text{out}}^2 \nabla^2 \phi_j - I_b / I_c = Q_{v,\text{out}} \mathcal{N}[\psi_j] + Q_{h,\text{out}} (\mathcal{N}[\phi_{j+1}] + \mathcal{N}[\phi_{j-1}]), \quad (1)$$

$$\mathcal{N}[\psi_j] - \Lambda_{\text{in}}^2 \nabla^2 \psi_j - I_b / I_c = Q_{v,\text{in}} \mathcal{N}[\phi_j] + Q_{h,\text{in}} (\mathcal{N}[\psi_{j+1}] + \mathcal{N}[\psi_{j-1}]), \quad (2)$$

where $\mathcal{N}[\varphi(t)] \equiv \ddot{\varphi} + \Gamma \dot{\varphi} + \sin \varphi$ returns the total normalized current through a junction in response to its phase $\varphi(t)$, and $\nabla^2 \varphi_j = \varphi_{j+1} - 2\varphi_j + \varphi_{j-1}$ is the discrete Laplacian. The bias current is normalized to the Josephson supercurrent, I_c . Γ measures the damping in the system. In our normalization, the Josephson relation gives the instantaneous voltage at a junction as: $\dot{\varphi}_j \Gamma = V_j / I_c R_n$, where R_n is the junction's normal-state resistance. Experimentally, we measure the dc voltage across a ring, which is proportional to the spatiotemporally averaged $\langle \dot{\varphi} \rangle$. The parameters $\Lambda_{\text{in}}^2 = L_j / L_{\text{in}}$ and $\Lambda_{\text{out}}^2 = L_j / L_{\text{out}}$ are the ratios of the Josephson inductance $L_j = \Phi_0 / 2\pi I_c$ to the cell inductances, L_{in} and L_{out} . (Due to the planar geometry, we have $L_{\text{in}} < L_{\text{out}}$.) These ratios measure the spatial extent of localized kinks in each ring. The magnetic coupling between the two rings is dominated by the mutual inductance of adjacent cells in each ring, Q_v (see Fig. 1). The nearest-neighbor coupling within a ring Q_h is also included. All inductances are normalized to the self-inductance of a cell, giving $Q_{v,x} = Q_v / L_x$ and $Q_{h,x} = Q_h / L_x$, where "x" refers to either "in" or "out."

The net twist trapped in a ring alters the otherwise periodic boundary conditions by

$$\phi_{j+N} = \phi_j + 2\pi M_{\text{out}}, \quad (3)$$

$$\psi_{j+N} = \psi_j + 2\pi M_{\text{in}}. \quad (4)$$

The governing equations are invariant to changes in M_{in} and M_{out} by $\pm N$.²¹ We will assume that $M_x \geq 0$, so that the number of excited pairs in a ring is simply $m_{a,x}$. Note that in our experiment M_{in} can be different from M_{out} .

Due to the magnetic coupling between rings, the motion of kinks and antikinks in one ring excites linear waves in *both* rings. When $M_{\text{in}} \neq M_{\text{out}}$ (and $m_{a,\text{in}} = m_{a,\text{out}} = 0$), two linear waves are excited with wave numbers $\kappa_1 = 2\pi M_{\text{out}} / N$ and $\kappa_2 = 2\pi M_{\text{in}} / N$; however, the amplitudes of the linear waves in each ring may be different. The inductive coupling also causes splitting of the dispersion relation for these linear waves. When $M_{\text{in}} = M_{\text{out}}$, the calculation is the same as for an open-ended system, which, for m kinks or antikinks ($\kappa = 2\pi m / N$), gives an approximate dispersion relation^{32,27}

$$\omega^{\pm}(m, x) \approx \frac{2\Lambda_x |\sin(m\pi/N)|}{\sqrt{1 - 2Q_{h,x} \cos(2m\pi/N) \mp Q_{v,x}}}. \quad (5)$$

This expression was derived for equal numbers of m kinks or antikinks in coupled *identical* sine-Gordon systems, for small Γ . We will use Eq. (5) as a semiquantitative estimate in the more general cases. It should be noted that the dispersion (5) is considered to be valid when kinks trapped in a given ring are closely packed and overlap one another, i.e., $m\Lambda_x / N \gg 1$. If they are well-separated and localized (i.e., $m\Lambda_x / N \ll 1$), then one expects a correction term that becomes significant when Λ_x becomes small.^{6,20} The difference in the dispersion relation depending on packing of the kinks has been recently studied more carefully by Zheng *et al.*³³ as well as by Strunz and Elmer.³⁴

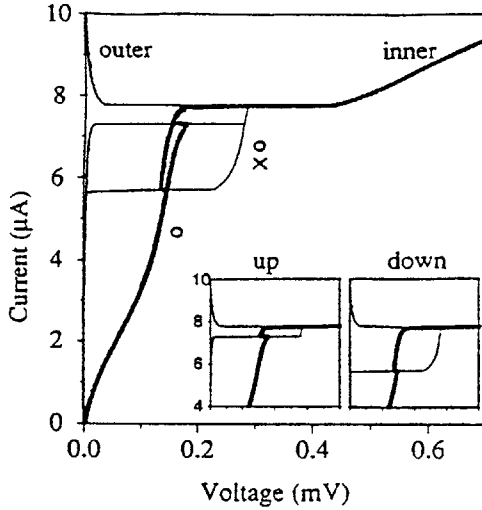


FIG. 2. Current-voltage curves for the $N=4$ system with $M_{in}=1$ and $M_{out}=0$. The sample parameters are $L_{in}=21$ pH, $L_{out}=26$ pH, and $j_c(T=0)=139$ A/cm². $T=7.22$ K, giving $\Gamma=0.0823$, $\Lambda_{in}^2=2.55$, $\Lambda_{out}^2=2.07$.

III. EXPERIMENTAL FEATURES OF THE SYSTEM

We first choose a case where $M_{in}=1$ and $M_{out}=0$ in order to introduce some of the interesting features of our system. Figure 2 shows simultaneous measurements of the inner and outer ring voltages while the bias current is varied. In the figure, we use an open circle to represent kinks and a cross to represent the antikink. As the bias current is increased from zero, the single kink trapped in the inner ring begins to move, producing an average dc voltage across the inner ring junctions. Meanwhile, the outer ring, which has no trapped kinks, remains superconducting.

Since the system is discrete, the kink phase locks with linear waves in the system.²⁰ As the kink's rotational speed ω/κ approaches the phase velocity for these linear waves, $\omega^\pm(m, x)/\kappa$, further increases in the bias current tend to increase the amplitudes of the excited linear waves rather than the speed of the kink. As a result, steps of almost constant voltage appear in the IV. When $m_{v,x}=M_x$ so that there are no antivortices, we refer to the corresponding resonant step as a flux flow step (FFS). This is the discrete analog to the Eck step,³⁵ which is also called a FFS, in continuous systems.³⁶

As the inner ring approaches a constant voltage at the FFS, we can assume (and numerical simulations confirm) that the excited linear waves in both rings have significant amplitudes. When the current is monotonically increased from zero, at approximately $I_b=7.2$ μ A the outer ring's superconducting state becomes unstable, and a step appears. The up path of the IV is shown separately in the left inset of Fig. 2. This instability can be associated with the excitation of a kink/antikink pair.^{21,37} To lowest order, the contributions of the kinks and antikinks in a given ring simply add up, resulting in voltage steps at $\omega = \omega^\pm(m_v, x) + \omega^\pm(m_a, x)$.²¹ We refer to these as high-voltage steps (HVS), since they are similar in nature to the corresponding FFS but are higher in voltage.

As soon as the outer ring switches to the HVS, the voltage of the inner ring (on a FFS) shifts to a slightly lower value. The step which appears on the up path of the outer ring IV

has approximately twice the voltage of the inner ring step. This is consistent with the picture that the outer ring kink and antikink move at nearly equal speeds and in opposite directions, producing twice the dc voltage of the kink moving in the inner ring. The sudden shift in the inner ring FFS voltage (which is clearer in the inset) indicates that the inner ring kink slows down when a pair appears in the outer ring. This suggests that the inner ring kink may have slowed to phase lock with the kink in the outer ring and that together they travel at a speed corresponding to ω^- .

At still higher driving current, the excited pair disappears again as the FFS in the inner ring becomes unstable. At this point (near 7.75 μ A), the outer ring switches back to the superconducting state and the inner ring switches to a uniform whirling state.⁷ On the down path (the right inset of Fig. 2 with current decreasing monotonically from 10 μ A), a pair is again excited in the outer ring and persists as the current bias is decreased even below 7.2 μ A, causing hysteresis in the IV. Surprisingly, the voltage of this HVS gradually decreases to well below twice the voltage of the inner ring FFS. When the pair disappears from the outer ring, the inner ring kink speeds up again, as indicated by the shift in the FFS voltage at $I=5.6$ μ A.

The experiments show two surprising results. First, a shift to a lower voltage occurs in the FFS as soon as the outer ring is on the HVS. This adjustment of the kink velocity clearly illustrates the existence of interactions between the two rings. Second, the voltage of the FFS is not exactly half of the voltage of the HVS. This observation indicates that not the whole array is phase-locked. We have performed many simulations to study these aspects in more detail. Some results will be presented in the next section.

IV. SIMULATIONS: KINK AND ANTIKINK INTERACTIONS

In order to better understand the interactions described by the data in Fig. 2, we have simulated the system with parameters similar to our experiments. However, we find that simulations of systems with larger N , where the kinks are very localized and easy to identify, are the most elucidating. Figure 3 shows an IV characteristic from a simulation. In this case, there are $N=51$ junctions in each ring. For a range of bias currents ($I_b < 0.57 I_c$), kink/antikink pairs are excited in the outer ring. The inset shows the relative motions of the kinks and the antikink when one pair is excited in the outer ring.

In Fig. 3, we plot the average dc voltage for each ring vs bias current. As the current is increased, the kinks move faster, and the dc voltage increases. The inner ring FFS reaches a maximum at a voltage of $0.0151 I_c R_n$. The outer ring has a phase-winding of zero, but exhibits HVS. The first step in the outer ring at $0.0297 I_c R_n$ is due to a single excited pair. As in the experiment, the voltage of the FFS step jumps to a lower voltage value when the outer ring switches to the HVS.

Along the FFS, we find that the average voltage of the outer ring is not quite twice that of the inner ring's, indicating that the speeds of the two kinks and the antikink are not identical. Figure 4 plots the space-time portrait of the motion at $I_b=0.45 I_c$. The two kinks, drawn as open circles, travel

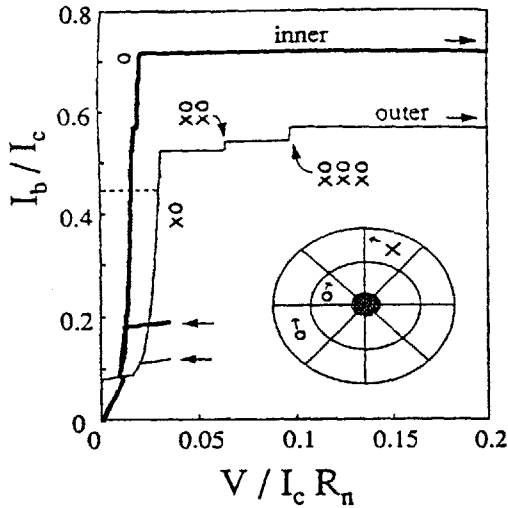


FIG. 3. Simulated IV characteristic for parameters: $M_{in}=1$, $M_{out}=0$, $N=51$, $\Gamma=0.1$, $\Lambda_{out}^2=1.76$, $\Lambda_{in}^2=2.55$, $Q_{v,out}=0.08$, $Q_{v,in}=0.12$, $Q_{h,in}=0.12$, and $Q_{v,in}=0.17$. The nearly constant voltage steps correspond to the motion of the kinks (represented by open circles) and antikinks (represented by crosses) at their maximum speeds. The inset shows the relative motion of the kinks and the antikink for one excited pair in the outer ring.

at approximately the same speed with a constant phase separation between them. Hence, we see that the coupling gives rise to phase-locking between kinks of the same sign in different rings.

A more dramatic interaction effect is the precession of the collision region between the kink and antikink in the outer ring. The antikink travels in the opposite direction and moves more slowly than the kink. As it periodically collides with the kink, the interaction perturbs its motion slightly. Because of the difference in their speeds, they collide at a different location for each revolution, and the collision region precesses around the ring, as shown from the solid line

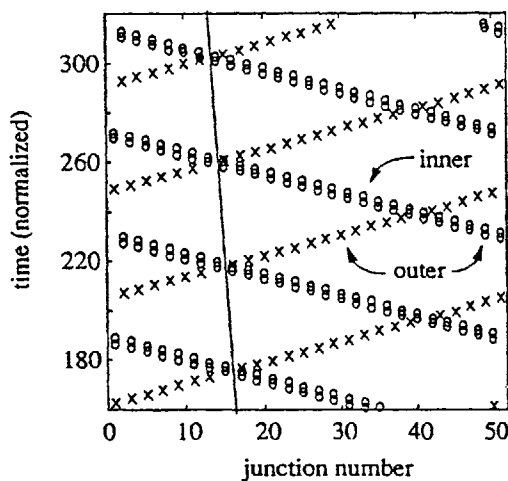


FIG. 4. Space-time diagram of the kinks for $I_b=0.45 I_c$ marked by a dashed line in Fig. 2. The kinks are represented by open circles, while the antikink is marked by crosses. The kinks in the two rings are phase locked (note the parallel lines of circles). The antikink travels more slowly, causing its point of intersection with the kink to precess.

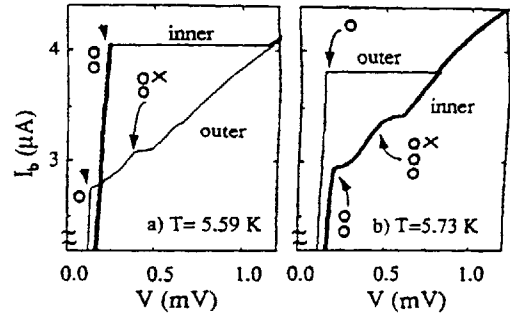


FIG. 5. Measured IV characteristic with $N=4$. These close-ups begin at a bias current of $2.2 \mu\text{A}$, when both rings are on FFS. The sample parameters are $L_{out}=26 \text{ pH}$, $L_{in}=21 \text{ pH}$, and $j_c(T=0)=83.3 \text{ A/cm}^2$. $M_{in}=2$ and $M_{out}=1$. (a) $T=5.59 \text{ K}$, giving $\Gamma=0.0507$, $\Lambda_{in}^2=2.67$, and $\Lambda_{out}^2=2.23$. A kink/antikink pair is excited in the outer ring at $I_b=2.75 \mu\text{A}$, causing an HVS. (b) $T=5.73 \text{ K}$, giving $\Gamma=0.0514$, $\Lambda_{in}^2=2.74$, and $\Lambda_{out}^2=2.29$. A kink/antikink pair is excited in the inner ring at $I_b=2.9 \mu\text{A}$.

in Fig. 4. Slopes of the lines indicate that $\omega(m_{v,in})=\omega(m_{v,out})=0.0151$, and $\omega(m_{a,out})=0.0146$. The difference $\omega(m_{v,out})-\omega(m_{a,out})$ gives the precession rate of the kink/antikink collision region. This difference may be attributed to the two kinks traveling at a higher speed which approaches $\omega^+(1,out)$ in Eq. (5) while the speed of the antikink approaches $\omega^-(1,out)$.³⁸

When the current is increased above $I_b=0.52 I_c$, a second pair is excited in the outer ring and a voltage step appears at $0.065 I_c R_n$. At this point, the inner ring voltage shifts to a slightly higher value. Since the system is discrete, we might expect the two vortices in the outer ring to travel more slowly than the single vortex in the inner ring. Instead, space-time plots (not shown) indicate that, again, the kinks in both rings move together at equal speeds and the antikinks in the outer ring move together at a slower speed. When a third pair is excited at $I_b=0.54 I_c$, the FFS voltage of the inner ring does not change. Finally, at $I_b=0.57 I_c$ the pairs disappear and the outer ring switches to a uniform whirling state.⁷ The inner branch persists up to higher current and jumps at $I_b=0.72 I_c$.

V. EXPERIMENTS: A SYSTEM WITH MANY STATES

Now we study the system when there are nonzero phase windings in *both* of the rings ($M_x \neq 0$). To illustrate, $M_{in}=2$ and $M_{out}=1$ are used in Fig. 5, which shows a close-up of the FFS in both rings above $I_b=2.2 \mu\text{A}$. There are two kinks (drawn as open circles) trapped in the inner ring and one in the outer ring. As the current bias is increased along the FFS, the amplitudes of excited linear waves grow until at least one of the FFS destabilizes. At this point, one or both rings may switch to a HVS with the excitation of one or more kink/antikink pairs.

In Fig. 5(a) the HVS occurs at $I_b=2.75 \mu\text{A}$, when a kink/antikink pair is excited in the outer ring, causing the voltage across the outer ring to increase. The IV steepens as the two kinks and the single antikink reach their maximum speeds. In both experiments and simulations, we observe additional steps at voltages corresponding to: $\omega=n_v \omega^\pm(m_v, x) + n_a \omega^\pm(m_a, x)$, where n_v and n_a are integers. Although

there are many possible combinations of FFS and HVS states for the system of two rings, we observe only a limited set of states. In fact, for the case $n_a = n_v = 1$, our measurements of $N=4$ and $N=8$ systems exhibit only one out of the possible HVS for a given M_{in} and M_{out} .

Even more intriguing is the fact that, unless $M_{in} = M_{out}$, HVS appear in only one ring at a time. An interesting question, then, is *which ring* will have an excited pair and when. The answer depends on temperature, which directly affects the parameters Λ_x and Γ . Figure 5(b) shows the IV at a slightly higher temperature, corresponding to an increase of Λ_x and Γ by only 1.3 percent from the IV in Fig. 5(a). At this temperature an HVS appears in the inner ring instead.

We find that for every distinct combination of $M_{in} \neq M_{out}$, a parameter regime where pairs are excited only in the outer ring, another parameter regime where pairs are excited only in the inner ring, and a transition region in temperature from one state to the other. The reason for a transition from one state to another as the parameters are varied is related to the stability of the states. In fact, we observe similar transitions among many of the possible dynamical states of the system. For a given M_{in} and M_{out} , each ring can be in one of the following states: (1) $V=0$, (2) FFS, (3) HVS, and (4) whirling branch (admittedly a simplified picture, for the purpose of discussion), leading to 16 possibilities for the system. Which of these possible states appears depends on both the driving current and the system parameters. As seen in Fig. 2, more than one state can be stable for a given driving current when the system is hysteretic.

We find a surprising feature in the evolution of the coupled ring IV curves as the temperature is varied. As the temperature is monotonically changed, the range of bias currents for which a given state is stable can shrink to almost zero until a new state appears at that current value. At this transition temperature, there is no visible hysteresis in the IV curves. This situation is illustrated in Fig. 2. At about $I_b = 7.75 \mu\text{A}$, the system switches from a combination of [in=FFS, out=HVS] to [in=whirling branch, out=zero voltage], with no hysteresis. While this may turn out to be a simple coincidence, the result can be dramatic experimentally. The tiniest bit of AC drive added to the input current

can switch the system between two largely different voltage outputs. In the future, these transitions will be studied in more detail.

VI. SUMMARY

We have studied the dynamics of two inductively coupled Josephson rings. Different numbers of kinks (vortices) can be trapped in each of the rings. A generic feature of our data is that voltage shifts in one ring occur when the other ring changes its dynamic state such that kinks and antikinks are excited or annihilated. Numerical simulations show that a phase locking occurs between the kinks in separate rings but the antikinks may move at different velocities. The two rings are therefore not completely phase-locked and a precession of the kink/antikink collision region occurs.

The dynamics is especially complicated when each ring contains kinks but not of the same number. Our experiments show that kinks and antikinks are only excited in one ring at the time. In which ring these pairs are excited depends on the system parameters (i.e., the temperature in the experiment). Many details of the interaction effects between the two coupled rings are not understood at present. For instance, we cannot quantitatively explain the voltage shifts that occur when kinks and antikinks are excited in the other ring. Nor do we have a complete picture of the intriguing transitions between dynamical states which occur at a single point in parameter space and are characterized by a sudden absence of hysteresis in the IV curve. The present paper only presents an exploration of the interesting interaction effects between kinks in two coupled rings of nonlinear oscillators. As such, a system of two coupled Josephson rings is an ideal model for further studies.

ACKNOWLEDGMENTS

The research was supported in part by the NSF Graduate Fellowship program and NSF Grants DMR-9610042 and DMS-9500948. We thank L. Mahadevan for useful discussions. We are especially grateful to Shinya Watanabe for his critical review of the manuscript.

¹A. M. Turing, *Philos. Trans. R. Soc. London. Ser. B* **237**, 37 (1953).

²G. Goldsztein and S. H. Strogatz, *Int. J. Bifurcation Chaos Appl. Sci. Eng.* **5**, 983 (1995).

³M. de Sousa Vieira, A. J. Lichtenberg, and M. A. Lieberman, *Int. J. Bifurcation Chaos Appl. Sci. Eng.* **4**, 1563 (1994).

⁴V. S. Afraimovich, V. I. Nekorkin, G. V. Osipov, and V. D. Shalfeev, *Stability. Structures and Chaos in Nonlinear Synchronization Networks* (World Scientific, Singapore, 1994).

⁵M. Silber, L. Fabiny, and K. Wiesenfeld, *J. Opt. Soc. Am. B* **10**, 1121 (1993).

⁶A. V. Ustinov, M. Cirillo, and B. A. Malomed, *Phys. Rev. B* **47**, 8357 (1993).

⁷S. Watanabe, H. S. J. van der Zant, S. H. Strogatz, and T. P. Orlando, *Physica D* **97**, 429 (1996).

⁸M. Levi, in *Analysis, Et Cetera*, edited by P. Rabinowitz and E.

Zehnder (Academic Press, New York, 1990), p. 471.

⁹I. R. Epstein and M. Golubitsky, *Chaos* **3**, 1 (1993).

¹⁰J. F. Heagy, T. L. Carroll, and L. M. Pecora, *Phys. Rev. Lett.* **73**, 3528 (1994); J. F. Heagy, L. M. Pecora, and T. L. Carroll, *ibid.* **74**, 4185 (1995).

¹¹A. T. Winfree, *The Geometry of Biological Time* (Springer, New York, 1980), p. 127.

¹²G. B. Ermentrout, *J. Math. Biol.* **23**, 55 (1985); G. B. Ermentrout and J. Rinzel, *ibid.* **11**, 269 (1981).

¹³A. Davidson, B. Dueholm, B. Kryger, and N. F. Pedersen, *Phys. Rev. Lett.* **55**, 2059 (1985).

¹⁴K. Maginu, *SIAM (Soc. Ind. Appl. Math.) J. Appl. Math.* **43**, 225 (1983).

¹⁵A. V. Ustinov, T. Dorderer, R. P. Huebener, N. F. Pedersen, B. Mayer, and V. A. Oboznov, *Phys. Rev. Lett.* **69**, 1815 (1992).

¹⁶I. V. Vernik, N. Lazarides, M. P. Sorensen, A. V. Ustinov, and N.

- F. Pedersen, *J. Appl. Phys.* **79**, 7853 (1996).
- ¹⁷N. Martucciello, J. Mygind, V. P. Koshelets, A. V. Shchukin, L. V. Filippenko, and R. Monaco, *Phys. Rev. B* **57**, 5444 (1998).
- ¹⁸J. F. Currie, S. E. Trullinger, A. R. Bishop, and J. A. Krumhansl, *Phys. Rev. B* **15**, 5567 (1977).
- ¹⁹M. Peyrard and M. D. Kruskal, *Physica D* **14**, 88 (1984).
- ²⁰H. S. J. van der Zant, T. P. Orlando, S. Watanabe, and S. H. Strogatz, *Phys. Rev. Lett.* **74**, 174 (1995).
- ²¹S. Watanabe, S. H. Strogatz, H. S. J. van der Zant, and T. P. Orlando, *Phys. Rev. Lett.* **74**, 379 (1995).
- ²²P. Barbara, A. V. Ustinov, and G. Costabile, *Phys. Lett. A* **191**, 443 (1994).
- ²³E. Goldobin, A. Wallraff, N. Thyssen, and A. V. Ustinov, *Phys. Rev. B* **57**, 130 (1998).
- ²⁴A. Petraglia, A. V. Ustinov, N. F. Pedersen, and S. Sakai, *J. Appl. Phys.* **77**, 1171 (1995).
- ²⁵A. Wallraff, E. Goldobin, and A. V. Ustinov, *J. Appl. Phys.* **80**, 6523 (1996).
- ²⁶S. Sakai, P. Bodin, and N. F. Pedersen, *J. Appl. Phys.* **73**, 2411 (1993).
- ²⁷A. Petraglia, N. F. Pedersen, P. L. Christiansen, and A. V. Ustinov, *Phys. Rev. B* **55**, 8490 (1997).
- ²⁸R. D. Parmentier, P. Barbara, G. Costabile, A. D'Anna, B. A. Malomed, and C. Soriano, *Phys. Rev. B* **55**, 15 165 (1997).
- ²⁹N. Flytzanis, S. Crowley, and V. Celli, *Phys. Rev. Lett.* **39**, 891 (1977).
- ³⁰A. R. Bishop and T. F. Lewis, *J. Phys. C* **12**, 3811 (1979).
- ³¹Samples were fabricated by HYPRES, Inc. in Elmsford, NY.
- ³²A. E. Duwel, E. Trías, T. P. Orlando, H. S. J. van der Zant, S. Watanabe, and S. H. Strogatz, *J. Appl. Phys.* **79**, 7864 (1996).
- ³³Zhigang Zheng, Bambi Hu, and Gang Hu (unpublished).
- ³⁴T. Strunz and F. Elmer, *cond-mat/9805287* (1998) (unpublished).
- ³⁵R. E. Eck, D. J. Scalapino, and B. N. Taylor, *Phys. Rev. Lett.* **13**, 15 (1964).
- ³⁶N. F. Pedersen and A. V. Ustinov, *Supercond. Sci. Technol.* **8**, 389 (1995).
- ³⁷G. Costabile, S. Pagano, and R. D. Parmentier, *Phys. Rev. B* **36**, 5225 (1987).
- ³⁸In smaller systems where the kink or antikink spacing becomes of the order of the ring size, this interaction-induced precession is more difficult to identify. However, the excited linear waves clearly show the presence of both frequencies, even when the rings are identical, and a beat frequency, $\omega^+(m_s) - \omega^-(m_s)$, appears.

Discreteness-induced resonances and ac voltage amplitudes in long one-dimensional Josephson junction arrays

A. E. Duwel^{a)}

Department of Electrical Engineering and Computer Science, MIT, Cambridge, Massachusetts 02143

Shinya Watanabe

Center for Chaos and Turbulence Studies, Niels Bohr Institute, Blegdamsvej 17, Copenhagen, 2100, Denmark

E. Triás and T. P. Orlando

Department of Electrical Engineering and Computer Science, MIT, Cambridge, Massachusetts 02143

Herre S. J. van der Zant

Department of Applied Physics, Delft University of Technology, P.O. Box 5046, 2628 CJ Delft, The Netherlands

Steven H. Strogatz

Department of Theoretical and Applied Mechanics, Cornell University, Kimball Hall, Ithaca, New York 14853

(Received 11 April 1997; accepted for publication 20 June 1997)

New resonance steps are found in the experimental current-voltage characteristics of long, discrete, one-dimensional Josephson junction arrays with open boundaries and in an external magnetic field. The junctions are underdamped, connected in parallel, and dc biased. Numerical simulations based on the discrete sine-Gordon model are carried out, and show that the solutions on the steps are periodic trains of fluxons, phase locked by a finite amplitude radiation. Power spectra of the voltages consist of a small number of harmonic peaks, which may be exploited for possible oscillator applications. The steps form a family that can be numbered by the harmonic content of the radiation, the first member corresponding to the Eck step. Discreteness of the arrays is shown to be essential for appearance of the higher order steps. We use a multimode extension of the harmonic balance analysis, and estimate the resonance frequencies, the ac voltage amplitudes, and the theoretical limit on the output power on the first two steps. © 1997 American Institute of Physics. [S0021-8979(97)00919-5]

I. INTRODUCTION

Josephson junction systems have a natural application as millimeter- and submillimeter-wave oscillators. To facilitate their use, however, ongoing research must address several issues. To produce oscillators with narrow linewidths and high power, we must study the harmonic content and oscillation amplitudes of Josephson sources. Furthermore, the conditions under which many Josephson oscillators can be phase locked to produce higher output power continue to challenge researchers.

ac power has been measured from both continuous long Josephson junctions and discrete arrays of short junctions. In underdamped Josephson systems, the ac oscillation amplitudes are expected to be largest at certain resonant frequencies. Much analytical work has been done to predict the frequency of these resonances. The success of these analyses can be assessed by studying the dc current-voltage ($I-V$) characteristics. Steps appear in the $I-V$ when increases of the current bias over a certain range do not produce increases in the dc voltage. Instead, the input power drives large-amplitude ac oscillations. The frequency of these oscillations is related to the dc voltage by the Josephson relation,

$\omega = 2\pi V/\Phi_0$, where Φ_0 is the flux quantum, while the spatial wave number is determined by the applied magnetic field, $k = 2\pi f$, where f is the applied flux per unit cell normalized to Φ_0 . The oscillations can be approximated as the normal modes to the linearized system. This approach has been used successfully, to predict resonance frequencies, or steps in the $I-V$ characteristics of many different geometries of Josephson systems. The dependence of the step voltage on applied magnetic field can be included, thus giving a dispersion relation for the associated oscillations. In the discrete case, the dispersion relation is nonlinear, and higher mode waves are expected to produce distinct steps in the $I-V$.^{1,2} One of the limitations of these linear analyses is that the predicted oscillations are necessarily single harmonic, since the normal modes of the linearized Josephson system are simply Fourier modes. In addition, the absence of a driving force in the linearized system precludes any calculation of the oscillation amplitudes.

In order to predict oscillation amplitudes and the distribution of power among excited modes, the nonlinearity in the system must be more carefully treated. Perturbation techniques^{3,4} clarify the role of the nonlinearity in driving the resonance and have been used to predict step voltages in Josephson systems. Combined with an appropriate ansatz, they also provide expressions for the oscillation

^{a)}Electronic mail: duwel@bardeen.mit.edu

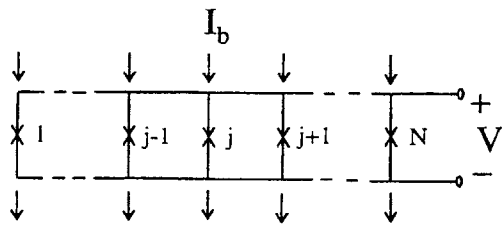


FIG. 1. Schematic of an open-ended parallel array. A uniform current I_b is applied at each of the upper nodes and extracted at the lower nodes.

amplitude.⁵⁻⁷ However, analytic expressions for the ac amplitudes so far include only the first harmonic and are implicit.⁵

In this article we use experiments, simulations, and non-linear analysis to investigate the properties of discrete, planar arrays of Josephson junctions connected in parallel. Both experiments and simulations yield several resonant steps in the $I-V$. Simulations indicate that on these steps, a traveling wave pattern dominates the oscillations of junctions in the array. In contrast to the linear picture, these resonances correspond to excitations of more than one mode, though the harmonic content is still limited. Similar states have already been reported in discrete rings,⁸ indicating that boundary conditions play a minor role. In inductively coupled arrays with open ends, the second harmonic resonance was also observed experimentally.⁹ We use a two-mode extension of the harmonic balance method to predict the resonant frequencies as well as the mode amplitudes at resonance. Our formulas are analytic and include the dependence on magnetic field. With a matched load condition, a theoretical upper limit on the available output power of the underdamped Josephson oscillator is calculated.

II. MEASUREMENTS OF ARRAYS

We have measured single-row arrays of $N=54$ junctions connected in parallel. Figure 1 shows a schematic of our device. A bias current I_b is applied at each upper node of the array and extracted from each bottom node as shown. We use resistors to distribute the bias current as evenly as possible. The voltage across the array is measured at an edge. The array is placed above a superconducting ground plane, and a separate control line (not shown) is used to apply a magnetic field. We will discuss the applied field in terms of the *frustration*, f (the flux applied to a single loop of the array, normalized to the flux quantum). Because the system is discrete, we expect its properties to be periodic in f with period $f=1$.¹⁰ In this experiment, the applied flux is proportional to the control current.

Samples were fabricated using a Nb trilayer process.¹¹ The junctions are $3 \times 3 \mu\text{m}^2$ with a critical current density of $j_c(T=0) = 1270 \text{ A/cm}^2$. Device parameters have been determined using the diagnostic procedures described by van der Zant *et al.*¹² For our samples at 7.2 K, the normal-state resistance $R_n = 16.6 \Omega$, the self-inductance of a loop $L_s = 6.4 \text{ pH}$, the nearest-neighbor inductive coupling $M_h = 0.11 L_s$, the junction capacitance $C = 340 \text{ fF}$, and the Josephson induc-

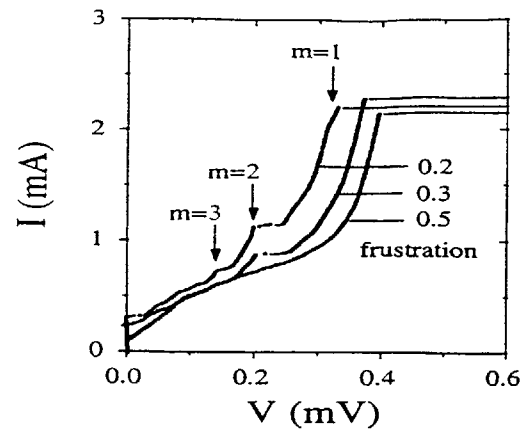


FIG. 2. Current vs voltage of a 54-junction array on a ground plane at three values of $f=0.2, 0.3$, and 0.5 . The temperature is 7.2 K so that $I_c R_n = 0.93 \text{ mV}$. The three steps indicated by the arrows are labeled by m values corresponding to the number of dominant harmonics in the mode.

tance $L_J = \Phi_0 / (2\pi I_c) = 5.9 \text{ pH}$. We use the normal-state resistance to calculate the Stewart-McCumber parameter, $\beta_c = 16$. The sub-gap resistance is not as well defined at these high temperatures but approaches the value of R_n . For the discreteness parameter, we calculate $\Lambda_J^2 = L_J / L_s = 0.92$.

Figure 2 shows the voltage across an array when the current is uniformly injected. Three $I-V$ curves are presented, for $f=0.2, 0.3$, and 0.5 . The most prominent feature is the sharp Eck step, which is the steepest part of the $I-V$, just before the switch to the gap voltage (not shown). We label this step " $m=1$ " for the reason given in the next section. In the regime where β_c is small (overdamped) or Λ_J is large (less discrete), this is the only step observed. For our underdamped and discrete samples, however, additional steps appear below the Eck voltage. We index these steps with $m=2, 3$, etc. In this article we are mostly concerned with the Eck step $m=1$ and, among the new steps, the clearest one with $m=2$. The study of the second step sheds light on the finer steps with $m>2$.

The voltage locations of the peaks experimentally vary with f , as seen in Fig. 2. More systematically, we show the dependence of the first two steps in Fig. 3. The Eck peak voltage is found to be periodic in f with period $f=1$ and to be approximately symmetric with respect to $f=0.5$. This is consistent with previous observations.¹⁰ At $f=0.5$, the Eck step reaches its highest voltage value. For a smaller f , there is a threshold frustration, below which the Eck step does not appear. This cutoff f_{c1} , known as the lower critical field or frustration, is the minimum applied flux density for vortices to enter an array.¹⁰ The value is quite large for our system, $f_{c1} \approx 2/(\pi^2 \Lambda_J) = 0.2$. The voltage location of the second step shows roughly the same f periodicity and symmetry as the Eck step. This second step, however, achieves the maximum voltage near $f=0.25$, and it disappears near $f=0.5$ and for approximately $f < f_{c1}$.

The Eck ($m=1$) steps are ubiquitous in one-dimensional parallel arrays as well as in continuous long junctions. In contrast, the other steps ($m>1$) do not appear in long continuous junctions, but do appear in discrete arrays when Λ_J

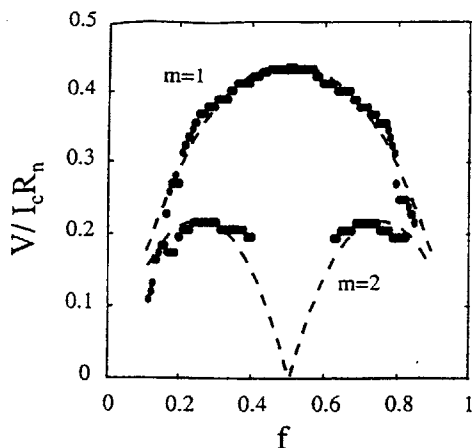


FIG. 3. Step voltages of the 54-junction array vs the frustration, f , for the modes $m=1$ and $m=2$. The dashed curves are plots of Eq. (13).

is small. In our arrays, we find Λ_J must be less than unity for the $m=2$ step to appear. Similar steps have been observed also in highly discrete circular arrays⁸ and open-ended arrays consisting of two rows that are inductively coupled.⁵

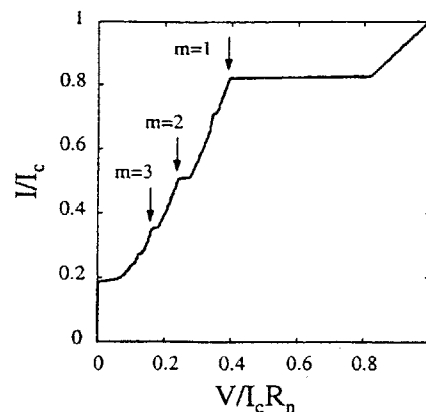
In open-ended arrays with a smaller N , Fiske steps¹³ may be observed in a similar part of the I - V below the Eck voltage. We emphasize, however, that they are qualitatively different. Fiske resonances can be described as standing waves (cavity modes) resulting from boundary reflections. The wavelength of the modes is restricted by the boundary geometry and, consequently, the resonance voltage locations do not depend strongly on f . At a certain value of f , only even or only odd modes are excited. As N becomes large, for a given value of damping, these Fiske resonances disappear due to damping of the edge reflections. None of these features apply for the Eck step as well as the $m > 1$ steps, which are tunable in f . Thus, the new steps are expected to belong to the same family as the Eck step.

III. SIMULATIONS

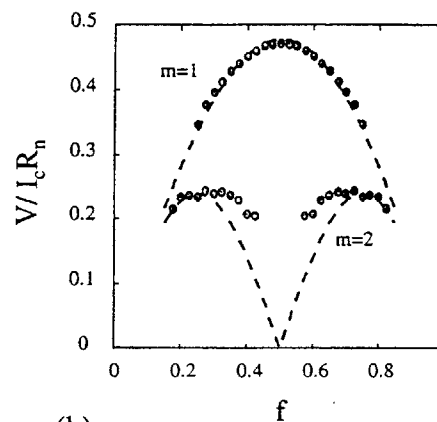
The governing equations which model our arrays are derived by applying Kirchhoff's current laws and using the resistively shunted junction (RSJ) model for the current through a single junction. We normalize the current to I_c , the voltage to $I_c R_n$, and time to $\sqrt{L_J C}$ (inverse plasma frequency). The equations are given in terms of the gauge-invariant phase differences across the junctions, ϕ_j , where $j=1, \dots, N$ indexes the junction's position. For simplicity we neglect all the cell inductances except the self-inductance, which results in the damped, driven, discrete sine-Gordon model:

$$\ddot{\phi}_j + \Gamma \dot{\phi}_j + \sin \phi_j = I_b / I_c + \Lambda_J^2 (\phi_{j+1} - 2\phi_j + \phi_{j-1}) \quad (1)$$

for $j=1, \dots, N$ and $\Gamma = \beta_c^{-1/2}$. Our numerical code can include longer range inductances as necessary, up to the full inductance matrix.¹⁴ However, our analysis in the next section uses mainly Eq. (1). Simulating the same equations allows us to make a direct comparison with our analysis. The simpler system not only illuminates the essential mechanism



(a)



(b)

FIG. 4. (a) Simulated current-voltage characteristic for a 54-junction array at $f=0.3$. The three most prominent steps are marked. (b) Voltages corresponding to the top of the steps show the tunability of the first two steps with magnetic field. The parameters are the experimental values: $\beta_c=16$ ($\Gamma=0.25$) and $\Lambda_J^2=0.92$.

responsible for the observed steps but also reproduces the measurements reasonably well, as we will show in this section.

With only self-inductance, the boundary conditions are simply

$$\phi_0(t) = \phi_1(t) - 2\pi f \quad \text{and} \quad \phi_{N+1}(t) = \phi_N(t) + 2\pi f \quad (2)$$

for all t , where artificial junctions ϕ_0 and ϕ_{N+1} are introduced at the end points so that Eq. (1) is valid at $j=1$ and N as well.¹⁵ The fourth-order Runge-Kutta scheme with a time-step $\Delta t=1$ is used for integrating the system. The instantaneous voltage at junction j is simply proportional to the rate of the change of ϕ_j , and is given in our normalization by

$$V/I_c R_n = \Gamma d\phi_j / dt. \quad (3)$$

With Eqs. (1-3), current-voltage characteristics are numerically obtained at different f values using the parameters Λ_J and Γ from our experiments. Figure 4(a) shows the results for $f=0.3$. The curve reproduces the measured one in Fig. 2 well, and at least three steps (indexed by m) are clear. (There is also a small step just below the $m=1$ step which we think arises from a different mechanism.) In a manner similar to Fig. 3, the f dependence of the step voltage loca-

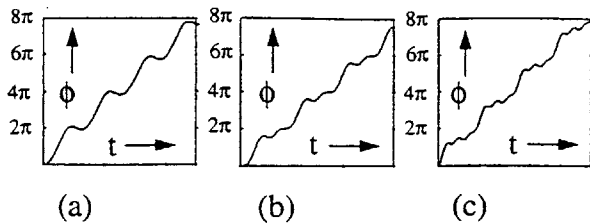


FIG. 5. Time evolution of the phase of a junction $j=27$ in the center of an array, biased on the (a) $m=1$, (b) $m=2$, and (c) $m=3$ steps, respectively. Note the increased frequency content as the mode number increases.

tions is shown in Fig. 4(b). There are slight differences, but the main features and voltage values are represented well.

Simulations allow us to study the solutions in detail. We are especially interested in the system dynamics when biased on top of a step. In Figs. 5(a)–(c) the phase of the junction $j=27$ (located in the middle of the array) on the $m=1,2,3$ step, respectively, is shown as a function of time. The junction appears to be in a periodic motion. Its phase increases rapidly when a vortex (kink) passes by, and it oscillates for the period between passing vortices. In a mechanical analog of a junction as an underdamped pendulum,¹⁶ a sudden overturn of the pendulum is followed by an overshoot, and the pendulum “rings” several times until the next vortex passes by.

It appears in Fig. 5 that the solution on the step m corresponds to m such ringings. This can be quantified by studying the harmonic content of the voltages [Eq. (3)]. Fourier spectra of the voltages are shown in Figs. 6(a)–(c), respectively. On the step m , the first m harmonics are dominant, and the higher harmonics have rapidly decaying magnitudes. Despite the presence of other harmonics, the steps are indexed by the ringing frequency, m .

Similar plots for the other junctions inside the array appear identical to ϕ_{27} , except for a certain shift in the time axis. This suggests that the solutions are well approximated by traveling waves. Near both ends of the array, reflections from the ends change this picture. The boundary effects, however, decay within 4–5 junctions from the end, and appear to play only a minor role in our long arrays.

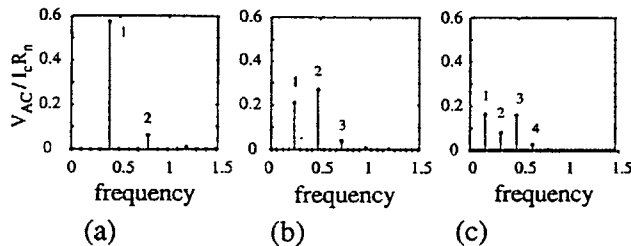


FIG. 6. Fourier spectra of the voltage corresponding to Figs. 5(a)–(c), with (a) step $m=1$, (b) step $m=2$, and (c) step $m=3$. Voltages are proportional to the time derivative of the phase in Fig. 5. The average slope of the phase plots corresponds to the dc voltage and is determined by the fundamental harmonic. The dc voltage was subtracted before computing the Fourier spectra. Note that only m harmonics are dominant for the m th step.

Such traveling wave solutions, consisting of a vortex and ringing, have been found in circular arrays with the periodic boundary conditions.^{1,15,17} In these systems, a vortex is trapped in a ring and, as it circulates, it creates an oscillatory wake, which phase locks back to the vortex. It is not surprising that a nearly identical situation may arise in a linear array with open boundaries, if the array is sufficiently long. Instead of a single circulating vortex, a vortex lattice propagates through the array. A junction is swept periodically by a vortex in both cases. There is, however, one major difference between the two geometries. The magnetic field in the array (which controls the vortex spacing) can be continuously tuned in the linear geometry while it is restricted to multiples of Φ_0 in a circular array due to the flux quantization.

IV. ANALYSIS

In this section we seek a more analytical description of the system, and estimate dc voltages at each step and the amplitudes of the ac voltage components. The simulations in the previous section suggest that finding traveling wave solutions to the governing Eq. (1) is the key to the estimates, but this task is not simple in practice.

The Eq. (1) may be viewed as a variation, in two respects, from the *integrable* sine-Gordon partial differential equation,

$$\phi_{tt} + \sin\phi = \phi_{xx} \quad (4)$$

which possesses traveling kink solutions as exact solutions. First, Eq. (1) is no longer a conservative equation, as it includes the external drive (bias current I_b) and the loss ($\Gamma\dot{\phi}_j$) terms. The added terms also break the integrability and exact solutions are no longer known. A perturbation approach¹⁸ in the *conservative limit* ($I_b, \Gamma \rightarrow 0$) has been developed to approximate a kink solution.

Second, the spatial derivative in Eq. (4) is discretized in Eq. (1). In general, nonlinear wave equations discretized on lattices may exhibit qualitatively different solutions from their continuous counterparts, and study of such discreteness-induced effects is an active current topic in its own right.¹⁹ For sine-Gordon systems, in particular, Eq. (1) was studied by Refs. 19, 20, and 21 without a loss term or a drive, and it was found that propagation of a kink introduces a background radiation which greatly influences the speed of the kink. As far as we are aware, however, there has been no attempt to estimate the amplitudes of the induced radiation, especially in the driven case.

Strunz and Elmer¹⁷ recently transformed Eq. (1) into a system of coupled modal equations and pointed out that the superharmonic resonance leads to creation of the radiated waves. They expanded a traveling wave form into Fourier modes, which may not be the best expansion basis but is a convenient one. Since our Fourier spectrum in Fig. 6 shows only a small number of peaks, we may truncate most modes and still obtain reasonable predictions. With this goal in mind, we review the analysis of Ref. 17 in Sec. IV A. The coupling terms among modes are truncated and analyzed in

Sec. IV B, and we estimate the ac voltage amplitudes on the steps. The available power from the array is then evaluated in Sec. IV C.

A. Resonance mechanism and voltages

We look for traveling wave solutions of the discrete sine-Gordon Eq. (1) of the form

$$\phi_j(t) = \phi(x) = x + \psi(x), \quad (5)$$

where

$$x = \omega t + 2\pi f j \quad (6)$$

is the moving coordinate with the wave, and $\psi(x + 2\pi) = \psi(x)$. The fundamental frequency ω is proportional to the dc voltage through the Josephson voltage-phase relation (3) while the spatial wave number is imposed by the external field. If the modulation were absent ($\psi \equiv 0$), then the boundary conditions (2) would be satisfied exactly. Since ψ is not vanishing, they are satisfied only on average, and there should be a correction to Eq. (5). We neglect this boundary effect and will show that the simplification still leads to good estimates of the measurements and simulations. (In a circular array Eq. (2) is replaced by the periodic boundary conditions: $\phi_{j+N}(t) = \phi_j(t) + 2\pi M$ where M is an integer.¹⁵ There can be exact solutions of the form [Eqs. (5) and (6)] with $f = M/N$.)

The periodic function ψ can be expanded into Fourier modes

$$\psi(x) = \sum_{m=-\infty}^{\infty} A_m e^{imx} \quad (7)$$

with $A_{-m}^* = A_m$. We set $A_0 = 0$, without loss of generality, by shifting the origin of time. The phase ϕ is an increasing function of x , but the nonlinear term $\sin\phi$ is 2π -periodic and can be expanded as

$$\sin\phi(x) = \sum_{m=-\infty}^{\infty} F_m e^{imx} \quad (8)$$

with $F_{-m}^* = F_m$. The coefficients F_m can be computed in terms of $A_{\pm 1}, A_{\pm 2}, \dots$ from the usual Fourier-Bessel expansions, and therefore provide coupling among the modes. By substituting Eqs. (5), (7), and (8) into Eq. (1), we obtain a coupled system of modal equations.

$$(\delta_m + im\Gamma\omega)A_m + F_m = 0, \quad (9)$$

where

$$\delta_m = \omega_m^2 - (m\omega)^2 \quad (10)$$

and

$$\omega_m = 2\Lambda_J \sin(m\pi f). \quad (11)$$

The index $m = 1, 2, \dots$ for Eqs. (9)–(11). In addition, the balance of the dc terms in Eq. (1) results in

$$I_b/I_c = \Gamma\omega + F_0. \quad (12)$$

The first term on the right hand side is proportional to ω , and hence to the dc voltage. This term describes the ohmic line in

the I - V plane. The second term is also a function of ω through the A_m 's, and describes the deviation of the I - V curve from the ohmic line.

The superharmonic resonance²² may occur in the algebraic system (9,12) and lead to the creation of resonant steps in the I - V curve. For small Γ , the magnitude of A_m would generically become large near $\delta_m = 0$, that is, near

$$\omega = \omega_m/m, \quad m = 1, 2, \dots \quad (13)$$

Then F_0 also becomes large, and the I - V deviates substantially from the ohmic line near these frequencies (or corresponding voltages). This argument neglects the dependence of the coupling terms F_m on the complex amplitudes A_m , but explains our measurements quite well. We plot Eq. (13) for $m = 1, 2$ as dashed curves in Figs. 3 and 4(b). The agreement is good without a fitting parameter.

The right hand side of Eq. (13) is the phase velocity of the m th mode on the discrete lattice. The left hand side can be viewed as the vortex velocity. Then, the relation can be viewed as the phase-locking condition of the vortex velocity and the phase velocity of the m th mode.^{1,15} In the absence of the coupling terms F_m , a resonance occurs when the vortex lattice moves at the same velocity as one of the modes. We note that these resonance frequencies ω are distinct for different m because of the sinusoidal dependence of the dispersion relation (11) on m . If the second order difference in Eq. (1) were replaced by the second spatial derivative as in Eq. (4), the dispersion relation would depend linearly on m , and the phase velocities of all the modes would be identical. Consequently, there would be only one vortex velocity that can excite modes, and we would observe only one resonance voltage. This explains why only the Eck step (among this type of step) is observed in a long continuous junction. In this sense, our observation of the $m > 1$ steps is due to the discreteness of the system.

We also note that, in some parameter regime, the resonating modes may be sub harmonics of the fundamental frequency. Sub-harmonic resonances of order n can be sought by generalizing Eq. (7) to

$$\psi(x) = \sum_{m=-\infty}^{\infty} A_m e^{imx/n}. \quad (14)$$

This is still a traveling wave but has an n times longer period. In a similar manner to the above discussion, one may expect resonances when

$$0 = \omega_{m,n}^2 - (m\omega/n)^2, \quad \text{i.e.,} \quad \omega = n\omega_{m,n}/m, \quad (15)$$

where

$$\omega_{m,n} = 2\Lambda_J \sin(2m\pi f/n). \quad (16)$$

The resonances with $m = 1$ and $n = 1, 2, 3$ have been observed by Caputo *et al.*²³

B. Amplitudes at resonances

There was no need to analyze the coupling terms F_m in the previous section to determine the resonant voltages, but it becomes necessary when the ac components A_m are wanted.

These mode amplitudes are important information for possible oscillator applications because one can then estimate the power available from the device.

One way to calculate the amplitudes is to linearize the coupled modal Eqs. (9) with respect to A_m . One would obtain a linear algebraic system with coupling between neighboring modes only. We have tried this approach, but the estimated magnitudes became too large to justify the linearization, and they did not agree well with the numerically obtained mode amplitudes.

Therefore, we have used another approximation that can cope with larger amplitudes. Since analysis of the modal equations in general appears formidable, we focus only on the steps $m=1$ and 2, and make several approximations.

First, as we see in the spectra in Fig. 6(a,b), A_3 and higher modes have much smaller magnitudes on these two steps, so they will be neglected. Then,

$$\begin{aligned}\phi(x) &= x + (A_1 e^{ix} + \text{c.c.}) + (A_2 e^{2ix} + \text{c.c.}) \\ &= x + a_1 \sin(x + \theta_1) + a_2 \sin(2x + \theta_2),\end{aligned}\quad (17)$$

where

$$A_m = -(i/2) a_m e^{i\theta_m}.\quad (18)$$

The *harmonic balance* method, which is commonly used for approximating a finite amplitude solution, would neglect A_2 as well. Thus, the ansatz (17) can be thought of as an extension of the method to a multiharmonic case. Including two harmonics, however, introduces coupling terms between them, and makes the problem substantially more difficult. By the Fourier-Bessel expansion, the coupling is expressed as

$$F_0 = \sum_{n=-\infty}^{\infty} J_{-(2n+1)}(a_1) J_n(a_2) \sin[n\theta_2 - (2n+1)\theta_1]\quad (19)$$

and

$$\begin{aligned}F_m &= -(i/2) \sum_n J_{m-(2n+1)}(a_1) J_n(a_2) e^{i(n\theta_2 + (m-2n-1)\theta_1)} \\ &+ (i/2) \sum_n J_{-m-(2n+1)}(a_1) J_n(a_2) \\ &\times e^{-i(n\theta_2 - (m+2n+1)\theta_1)}\end{aligned}\quad (20)$$

for $m \neq 0$, and J_m are Bessel functions.

To make analytical progress we simplify the coupling by taking only the most dominant terms (for small a 's) and neglecting all the others. This results in

$$\begin{aligned}F_1 &= -(i/2) J_0(a_1) J_0(a_2), \\ F_2 &= -(i/2) J_1(a_1) J_0(a_2) e^{i\theta_1}.\end{aligned}\quad (21)$$

The higher order Bessel functions $J_2(a_1)$, $J_3(a_1)$, ... and $J_1(a_2)$, $J_2(a_2)$, ... are neglected, which can be justified in the range, say, $|a_1| < 2$ and $|a_2| < 1$. We substitute them into Eq. (9) for $m=1,2$ and obtain

$$\begin{aligned}(J_0(a_1)/a_1)^2 &= (\delta_1^2 + \Gamma^2 \omega^2) / J_0^2(a_2), \\ \tan \theta_1 &= -\Gamma \omega / \delta_1\end{aligned}\quad (22)$$

and

$$\begin{aligned}(J_0(a_2)/a_2)^2 &= (\delta_2^2 + 4\Gamma^2 \omega^2) / J_1^2(a_1), \\ \tan(\theta_2 - \theta_1) &= -2\Gamma \omega / \delta_2.\end{aligned}\quad (23)$$

It is convenient to think of ω as the control parameter and determine a_1 , a_2 , θ_1 and θ_2 . The arguments of tangent are defined between 0 and π . As ω increases from 0, δ_1 and δ_2 decrease monotonically, and changes sign from positive to negative at the resonance frequencies. Thus, θ_1 decreases from π to 0, with the crossover $\theta_1 = \pi/2$ at $\omega = \omega_1$. Similarly, $(\theta_2 - \theta_1)$ decreases from π to 0, and crosses $\pi/2$ at $\omega = \omega_2/2$.

The amplitude equations of (22) and (23) are more complicated. It follows from Eq. (23) that $a_2=0$ when $a_1=0$. That is, the second mode is excited only in the presence of the first mode. On the other hand, the first mode can be excited alone since $a_1 > 0$ in Eq. (22) when $a_2=0$. The feedback from the second mode through $J_0(a_2)$ in Eq. (22) is not essential when considering a_1 .

To extract more information we make a further approximation. We first linearize the Bessel functions on the right hand sides, i.e. $J_1(a_1) \approx a_1/2$ and $J_0(a_2) \approx 1$. (Consequently, F_1 becomes independent of A_2 , and the feedback from the second mode is neglected. Then, Eq. (22) reduces to the equations obtained through the method of harmonic balance.⁵)

On the left hand sides of Eqs. (22) and (23), the function $J_0(a)/a$ is monotonically decreasing from ∞ to zero as a increases from 0 to the first zero of J_0 , which is $a^* \approx 2.4$. Thus, for any ω , a can be found within 0 and a^* . Approximating the function crudely by $J_0(a)/a \approx 1/a$ would make the range of a unbounded. This is not desirable near the resonances. We could include the next term from the expansion of J_0 , but this would make the following algebra more complicated. Alternatively, we replace the function by another one which has the same asymptotic behavior as $a \rightarrow 0$ and a bounded domain for a . We use

$$[J_0(a)/a]^2 \approx 1/a^2 - 1/4.\quad (24)$$

This has a slightly different saturation amplitude at $a^*=2$ but overall the approximation is good; the error in a introduced by this replacement is less than 5% for $a < 0.7$ and at most 20% when a saturates. In return for the error introduced at this stage, we obtain simple expressions for the amplitudes as

$$a_1 = (b_1^2 + 1/4)^{-1/2} \quad \text{and} \quad a_2 = (b_2^2 + 1/4)^{-1/2},\quad (25)$$

where

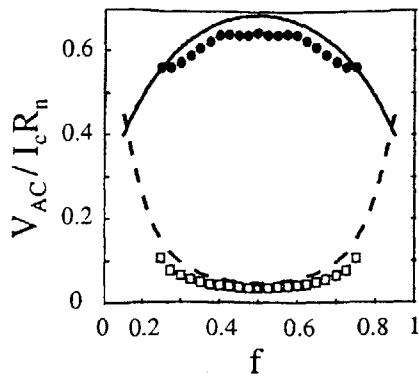
$$b_1^2 = \delta_1^2 + \Gamma^2 \omega^2 \quad \text{and} \quad b_2^2 = 4(\delta_2^2 + 4\Gamma^2 \omega^2) / a_1^2.\quad (26)$$

Once the phases and amplitudes of the modes are determined, the instantaneous voltage is obtained from the time derivative of Eq. (17). In our normalization,

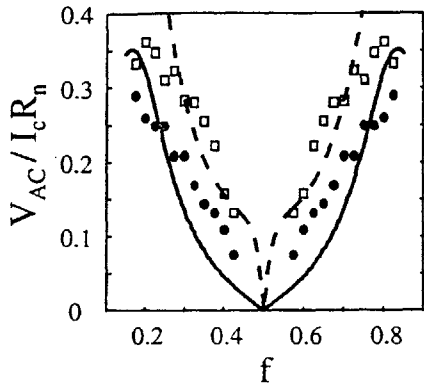
$$V/I_c R_n = \Gamma \omega [1 + a_1 \cos(x + \theta_1) + 2a_2 \cos(2x + \theta_2)].\quad (27)$$

Thus, the dc voltage and the ac amplitude of the mode m are

$$V_{DC}/I_c R_n = \Gamma \omega \quad \text{and} \quad V_{AC}/I_c R_n = \Gamma \omega m a_m.\quad (28)$$



(a)



(b)

FIG. 7. Amplitudes of the first two ac voltage harmonics on (a) the $m=1$ (Eck) step and (b) the $m=2$ step vs f . The theory (25) is represented by a solid (dashed) line for the first (second) harmonic. Filled circles and open squares show the amplitude of the first and second harmonics, respectively, from simulations. The values of Λ_J and Γ are the same as in Fig. 4. As expected, the amplitude at the second frequency is quite small on the $m=1$ step (a), while the amplitudes of the first two harmonics are comparable on the $m=2$ step (b).

In Fig. 7, we compare the amplitude estimate with simulations. On the first two steps, the peak ac voltage amplitudes for the first two Fourier modes are obtained from simulations, shown as data points. The estimates of the resonance frequencies $\omega = \omega_1$ and $\omega_2/2$ from Eq. (13) are used. The theoretical curves show a reasonable agreement with the data on the Eck step. On the second step the comparison is worse, but the overall magnitude and f dependence are estimated fairly, considering the several approximations made during the derivation.

The maximum ac voltage oscillation of the first mode on the Eck step is achieved at $f=0.5$. The maximum of the second mode on the second step happens near the lower critical frustration ($f \approx 0.2$). The vertical axes in Fig. 7 are shown in terms of ac voltages. Converted back to the amplitudes, $a_1 < 1.75$ and $a_2 < 0.4$ on the Eck step for $0.2 < f < 0.8$. This is thought to be within the validity of the assumptions. On the second step, $a_1 < 1.8$ for $0.15 < f < 0.45$, but a_2 exceeds unity when $f < 0.25$. The bending of the theoretical curves in (b) when $f < 0.25$ may be attributed to the large predicted

magnitude of a_2 . Including terms involving $J_1(a_2)$ in the modal equations would be necessary to make a better estimate in the region.

Generally, our assumption is violated when a_1 saturates in Eq. (25), or when b_1^2 becomes small. On the Eck peak $b_1^2 \approx (2\Gamma\Lambda_J \sin(\pi f))^2$, so the assumption breaks down for very small Γ and/or Λ_J . Similarly, a_2 exceeding unity indicates that we need more coupling terms included from Eq. (9). On the $m=2$ step, $a_2 < 1$ is fulfilled when $\Gamma^2 \omega_2^2 [1 + \Gamma^2 \omega_2^2 + 4(\omega_1^2 - \omega_2^2/4)^2] > 3/4$. Again, small Λ_J and/or Γ make it easier to violate the criterion. Thus, the validity of our approximations is limited to when $\Gamma\Lambda_J$ is relatively large and resonances are not so strong.

C. Power at resonances

The calculation of the mode amplitudes provides a theoretical upper limit for the power available from the Josephson oscillator at resonance. If we assume a matched load condition, then the power dissipated in the load is just the power dissipated in the matched resistance. Using the RSJ model and assuming sinusoidal voltage oscillations, this corresponds to $P = V_{ac}^2 / 8R_{arr}$, where $R_{arr} = R_n / N$ is the array resistance. The power available from mode m is then

$$\frac{P_m}{I_c^2 R_n} = \frac{N}{8} \left(\frac{V_{ac}}{I_c R_n} \right)^2 = \frac{N}{8} (\Gamma \omega a_m)^2 \quad (29)$$

with a_m estimated in Eq. (25). Therefore, the vertical axis of Fig. 7 is also $\sqrt{8P_m / NI_c^2 R_n}$, and the f dependence of the powers can be read directly from the figure. When biasing on the Eck step, the largest power and the highest frequency are obtained at $f=0.5$. When the system is biased on the second step, the largest power is obtained near $f=0.2$, and the highest frequency is achieved near $f=0.25$.

We take our experimental values ($I_c R_n = 0.93$ mV and $R_n = 16.6 \Omega$) and the maximum amplitudes in Fig. 7 ($V_{ac,1} = 0.65 I_c R_n$ on the Eck step and $V_{ac,2} = 0.36 I_c R_n$ on the second step). This predicts a maximum of about 150 nW from the first harmonic at the first resonance and 46 nW from the second harmonic at the second resonance. These numbers are much smaller than previous estimates,²⁴ and, according to measurements,^{25,26} are probably more realistic.

Our simulation and analysis show that multiple Fourier modes are excited on the new steps $m > 1$. For possible applications as oscillators, this is not desirable since the ac power is therefore distributed among the modes, instead of being concentrated in one mode, as at the Eck step. Usually in such a case one could simply increase the drive, to increase the output at the desired frequency. However, in this system the driving current is limited because, if it is increased beyond the top of the step, the resonance becomes unstable. Furthermore, since the maximum output power is small for a single row, methods are needed to combine power from multiple rows while preserving the frequency content of the resonance.

Both discrete rows of underdamped Josephson junctions and continuous long junctions operating at the Eck step have already been proposed as high frequency oscillators.^{10,27} Although no single experiment has directly compared the two

systems, studies indicate that the output power levels are comparable, while the output impedance of the discrete system may be advantageously higher.¹⁰ In order to increase power levels in either case, additional oscillators are required. Stacks of continuous long junctions have been fabricated and measured,²⁸⁻³⁰ as well as the analogous inductively coupled discrete arrays.^{5,9} However, in both systems, the power is only increased if the oscillating elements are phase locked and in phase. The existence of in-phase as well as anti-phase states has been well established for both discrete and continuous systems, through numerics,³¹ simulations,^{2,32} and experiments.^{5,33} Unfortunately, in both cases the anti-phase pattern is preferred at the Eck step,^{5,33} and the output oscillations of adjacent elements almost completely cancel. In addition, the difficulty (and necessity) of fabricating identical oscillators in the case of continuous stacks limits the possibility for improving this system.

On the other hand, the presence of higher harmonic resonances in discrete systems may actually be an advantage in terms of power combining. As observed in Ref. 9, when the discrete system is biased on the stable $m=2$ peak, the fundamental oscillations of the rows are anti phase (shifted by π), but the second harmonics are still in phase. Thus, the output power from the second mode is enhanced. It is important to note that such modes do not exist in uniform continuous long junctions. So, although the power level of a single row biased in this state is lower than the oscillators mentioned above, the potential for power combining in this state is much greater. Simulations indicate that this in-phase resonance for the second mode is stable for many coupled rows,⁹ which is promising for oscillator applications.

V. SUMMARY

We have observed experimentally and through simulations new resonance steps in long one-dimensional Josephson junction arrays in the underdamped and discrete regime. They emerge in the $I-V$ characteristic below the Eck voltage, and are tunable in the magnetic field f . We have shown that the resonance mechanism can be explained by neglecting the boundary effects and assuming a traveling wave solution. Fourier components of the solution resonate to create a wave form which appears to consist of a kink and radiation, phase locked to each other. We have employed a two-mode extension of the harmonic balance method in order to simplify the coupling of the modes. We have derived an analytic formula for not only the resonance voltages but also the amplitudes of the modes. Finally, we used these results to predict the power available from such Josephson oscillators and discuss its dependence on the system parameters.

ACKNOWLEDGMENTS

The authors thank Mauricio Barahona, Alexey Ustinov, Andreas Wallraff, and Pasquilina Caputo for valuable dis-

cussions. They also acknowledge the support of the NSF Graduate Fellowship program and NSF Grants Nos. DMR-9402020, DMS-9057433, and DMS-9500948. The authors appreciate the partial support of the Dutch Foundation for Fundamental Research on Matter.

- ¹A. V. Ustinov, M. Cirillo, and B. A. Malomed, *Phys. Rev. B* **47**, 8357 (1993).
- ²A. Petraglia, N. F. Pedersen, P. L. Christiansen, and A. V. Ustinov, preprint (1995).
- ³S. Watanabe, S. Strogatz, H. S. J. van der Zant, and T. P. Orlando, *Phys. Rev. Lett.* **74**, 379 (1995).
- ⁴K. Yoshida, K. Hamasaki, and F. Irie, *Jpn. J. Appl. Phys.* **18**, 373 (1979).
- ⁵A. E. Duwel, E. Trias, T. P. Orlando, H. S. J. van der Zant, S. Watanabe, and S. H. Strogatz, *J. Appl. Phys.* **79**, 7864 (1996).
- ⁶I. O. Kulik, *Sov. Phys. JETP* **24**, 1307 (1967).
- ⁷K. Enpuku, K. Yoshida, and F. Irie, *J. Appl. Phys.* **52**, 344 (1981).
- ⁸H. S. J. van der Zant, T. P. Orlando, S. Watanabe, and S. H. Strogatz, *Phys. Rev. Lett.* **74**, 174 (1995).
- ⁹A. E. Duwel, T. P. Orlando, S. Watanabe, and H. S. J. van der Zant, *IEEE Trans. Appl. Supercond.* **7**, 2897 (1997).
- ¹⁰H. S. J. van der Zant and T. P. Orlando, *J. Appl. Phys.* **76**, 7606 (1994).
- ¹¹Hypres, Inc., Elmsford, NY 10523.
- ¹²H. S. J. van der Zant, R. A. M. Reuveur, T. P. Orlando, and A. W. Kleinsasser, *Appl. Phys. Lett.* **65**, 2102 (1994).
- ¹³H. S. J. van der Zant, D. Berman, and T. P. Orlando, *Phys. Rev. B* **49**, 12945 (1994).
- ¹⁴E. Trias, M.S. thesis, MIT, 1995.
- ¹⁵S. Watanabe, H. S. J. van der Zant, S. H. Strogatz, and T. P. Orlando, *Physica D* **97**, 429 (1996).
- ¹⁶S. H. Strogatz, *Nonlinear Dynamics and Chaos* (Addison-Wesley, 1994), pp. 106-113.
- ¹⁷T. Strunz and F. J. Elmer, in *Physics of Sliding Friction*, edited by B. N. J. Persson and E. Tosatti (Kluwer, Dordrecht, 1996), pp. 149-161.
- ¹⁸R. D. Parmentier, in *The New Superconducting Electronics*, edited by H. Weinstock and R. W. Ralston (Kluwer, Dordrecht, 1993), pp. 221-248, Sec. 3.2 and references therein.
- ¹⁹D. B. Duncan, J. C. Eilbeck, H. Feddersen, and J. A. D. Wattis, *Physica D* **68**, 1 (1993).
- ²⁰M. Peyrard and M. D. Kruskal, *Physica D* **14**, 88 (1984).
- ²¹R. Boesch, C. R. Willis, and M. El-Batanouny, *Phys. Rev. B* **40**, 2284 (1989).
- ²²A. H. Nayfeh and D. T. Mook, *Nonlinear Oscillations* (Wiley-Interscience, New York, 1979).
- ²³P. Caputo, A. V. Ustinov, N. Iosad, and H. Kohlstedt, *J. Low Temp. Phys.* **106**, 353 (1997).
- ²⁴S. P. Benz and C. J. Burroughs, *Appl. Phys. Lett.* **58**, 2162 (1991).
- ²⁵A. V. Ustinov, H. Kohlstedt, and P. Henne, *Phys. Rev. Lett.* **77**, 3617 (1996).
- ²⁶P. Booi and S. P. Benz, *Appl. Phys. Lett.* **64**, 21163 (1994).
- ²⁷N. F. Pedersen and A. V. Ustinov, *Supercond. Sci. Technol.* **8**, 389 (1995).
- ²⁸G. Carapella, G. Costabile, G. Filatrella, M. H. Manscher, J. Mygind, N. A. Nordahn, N. F. Pedersen, and A. Petraglia, *IEEE Trans. Appl. Supercond.* **7**, 2411 (1997).
- ²⁹A. V. Ustinov, H. Kohlstedt, and C. Heiden, *Appl. Phys. Lett.* **65**, 1457 (1994).
- ³⁰S. Sakai, A. V. Ustinov, H. Kohlstedt, A. Petraglia, and N. F. Pedersen, *Phys. Rev. B* **50**, 12905 (1994).
- ³¹N. Grønbech-Jensen, D. Cai, and M. R. Samuelsen, *Phys. Rev. B* **48**, 16160 (1993).
- ³²S. Sakai, P. Bodin, and N. F. Pedersen, *J. Appl. Phys.* **73**, 2411 (1993).
- ³³R. Monaco, A. Polcari, and L. Capogna, *J. Appl. Phys.* **78**, 3278 (1995).

Resonance splitting in discrete planar arrays of Josephson junctions

A. E. Duwel,^{a)} E. Trías, and T. P. Orlando
*Department of Electrical Engineering and Computer Science, Massachusetts Institute of Technology,
Cambridge, Massachusetts 02139*

Herre S. J. van der Zant
*Department of Applied Physics, Delft University of Technology, Lorentzweg 1, 2628 CJ Delft,
The Netherlands*

Shinya Watanabe
*Center for Chaos and Turbulence Studies, Niels Bohr Institute, Blegdamsvej 17, DK-2100, Copenhagen Ø,
Denmark*

Steven H. Strogatz
Theoretical and Applied Mechanics, Kimball Hall, Cornell University, Ithaca, New York 14853-1503

(Received 11 December 1995; accepted for publication 8 February 1996)

We have measured and modeled the dynamics of inductively coupled discrete arrays of niobium Josephson junctions. We see splitting of the Eck step in the current-voltage characteristic. Numerical simulations reproduce this splitting and are used to find an approximate solution for the junction phases at resonance. Using the technique of harmonic balance, we find an analytic expression for the resonance frequencies and the voltages that match this splitting. We can also predict the amplitude of these oscillations. The analytical results describe both the experiments and simulations well. © 1996 American Institute of Physics. [S0021-8979(96)07010-7]

I. INTRODUCTION

Recent studies indicate that parallel arrays of underdamped Josephson junctions can perform well as submillimeter local oscillators.¹ These devices also present an advantage over their continuous-junction counterparts due to a significant improvement in the output impedance. However, the radiation linewidths of both continuous and discrete devices are expected to be large (on the order of 1 MHz).¹ It has been suggested that inductive coupling between two long, continuous junctions might cause phase locking and thereby reduce the linewidth. Simulations confirm that phase-locking does occur, and that two stable states are possible.²⁻⁴ In the symmetric mode, the gauge-invariant phase differences across the junctions have periodic oscillations which are in phase with each other. In the anti-symmetric mode, the phase oscillations of the two junctions are shifted by π . The presence of these two states is experimentally observed by voltage steps in the current-voltage characteristic.^{5,6} The linewidth-narrowing effect has also been measured in such coupled Josephson junctions.⁶

Discrete planar arrays of Josephson junctions can be inductively coupled as well, and we will show in this paper that the effects are similar to those seen in vertically stacked junctions.

We develop an analysis based on a traveling wave solution for the phase. This solution increases linearly with time and space but has an additional sinusoidal component and phase shift. Harmonic balance is then used to determine the resonance frequencies. This analysis, which differs from the usual explanation of Eck voltages, describes both the experiments and simulations well.

In section II the physical properties of the junctions are described. Section III shows the experimental splitting of the coupled discrete arrays. The simulations and analysis are described and compared with the experiments in section IV. The results are discussed in section V and briefly summarized in section VI.

II. SAMPLES

Our inductively coupled devices consist of two rows of 54 parallel junctions, as depicted in the inset of Fig. 1. Superconducting leads at the device edges allow us to measure voltages across either or both rows. The bias current is carried to the device through superconducting wires and is applied uniformly (at positions indicated by arrows in Fig. 1) through resistors. A typical current-voltage characteristic (I - V) is shown in Fig. 1. In the following sections, we will only show the regime of interest, marked as the resonance regime. Our samples exhibit voltage steps in this regime at temperatures near 8.2 K.

Samples were fabricated with a Nb trilayer process.⁷ Device parameters have been determined using the diagnostic techniques described by van der Zant *et al.*⁸ on a nine-junction parallel array. A measurement of the normal-state resistance (at temperatures close to the critical temperature) is used to find the critical current at zero temperature, by $I_c(0)R_n = 1.9$ mV. Using the Ambegaokar-Baratoff relation,⁹ we then know $I_c(T)$. This, in turn, allows us to calculate the temperature dependence of the Josephson inductance, $L_J = \Phi_0 / (2\pi I_c)$, where Φ_0 is the flux quantum. As described in Refs. 8 and 10, we can use measurements of the Fiske mode voltages to find the value of $L_s C$, the product of the junction capacitance, C and the self-inductance, L_s , of a single loop in the array. This measurement also provides an estimate of M_n , the ratio of the nearest-neighbor coupling to

^{a)}Electronic mail: duwel@mit.edu

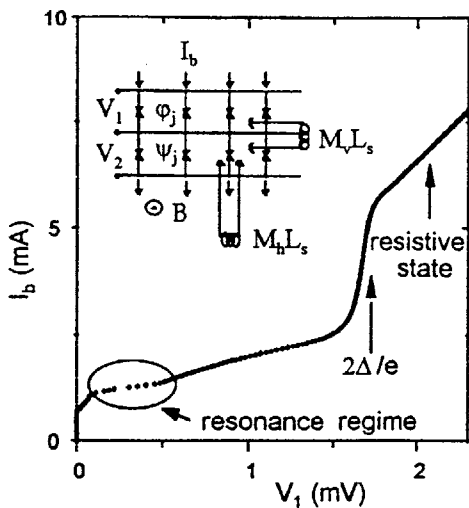


FIG. 1. A typical I - V of the 2×54 array. The voltage is measured across a single row of the array, at $T = 8.2$ K ($I_c R_n = 1.75$ mV). The inset depicts a circuit model of an inductively coupled planar array. The junction phases are designated ϕ_j in the top row of the array, and in the bottom row they are ψ_j . The mutual inductance between two horizontally adjacent cells of the array is $M_h L_s$. Likewise, $M_v L_s$ is the inductance of vertically adjacent cells.

the self-inductance.¹¹ We can then estimate L_s by using the capacitance prescribed in our designs. Alternatively, L_s can be found by measuring the array critical current vs frustration and fitting the slope of the linear portion to $\alpha = \Lambda_j^2 / [1.43(1 - 2M_h)]$, where $\Lambda_j^2 = L_j / L_s$.⁸ We define the frustration as the applied flux per unit cell (a loop of the array), normalized to the flux quantum,

$$f = \frac{\Phi_{\text{app}}}{\Phi_0} = \frac{M_{\text{ctrl}} I_{\text{ctrl}}}{\Phi_0} \quad (1)$$

When the sample is above a ground-plane, a magnetic field is applied by placing a current-carrying wire adjacent to the array. The current through the wire is designated as I_{ctrl} , and the flux coupling into the array is $M_{\text{ctrl}} I_{\text{ctrl}}$.

We have used the diagnostic techniques to find device parameters at these temperatures. For our samples at 8.2 K, $R_n = 15.3 \Omega$, $j_c(T=0) = 1378$ A/cm², $A = 9 \mu\text{m}^2$, $L_s = 8.5$ pH, $M_h = 0.13 L_s$, $C = 342$ fF, $L_j = 9.95$ pH. We use the normal-state resistance to calculate the Stewart-McCumber parameter, $\beta = 8.1$. The sub-gap resistance is not as well defined at these high temperatures but approaches the value of R_n . For the discreteness parameter, we calculate $\Lambda_j^2 = 1.2$.

For devices placed above a ground plane, all of the inductances are noticeably temperature-dependent. We have seen experimentally that the magnitude of the coupling decreases slightly with decreasing temperature. Changes in L_s and M_h are visible in our Fiske mode measurements, while changes in L_s , M_h , and M_v affect the following measurements of coupled arrays. The temperature dependence of the inductances can be modeled well by including the effects of temperature on the screening currents in the ground plane.¹²

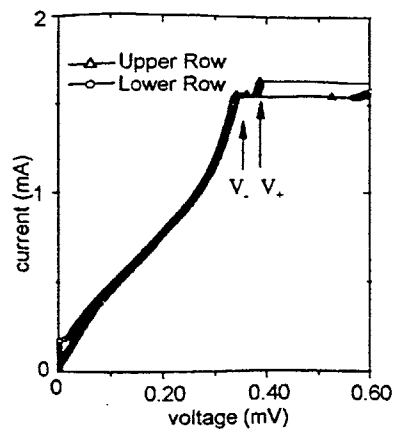


FIG. 2. Measurements of an inductively coupled array, $N = 2 \times 54$, on a ground plane. The triangles represent the voltage values measured across the top row, while the circles are voltage values across the bottom row. The measurements are taken at 8.2 K ($I_c R_n = 0.5$ mV) and $f = 0.55$.

III. MEASUREMENTS OF ARRAYS

Figure 2 shows the voltage across each row of a 2×54 array (above a ground plane) when the current is uniformly injected and $f = 0.55$. Two steps clearly appear in the I - V when the voltage is measured across a single row. The voltage values at the tops of the steps are labeled V_+ and V_- in the figure. Near the steps, the voltages across each row are the same, and the rows are said to be voltage-locked. When the voltage is measured across both rows, two steps are again seen, but at twice the voltage.

In Fig. 3, we plot the voltage positions of V_+ and V_- vs frustration. The voltages are periodic in magnetic field, with period $f = 1$, which is an effect of the discreteness. The steps appear sharp at high values of f (near $f = 0.5$). Near $f = 0$ and $f = 1$, the steps are unstable and difficult to define. The asymmetry in the data reflects this. (The solid lines are a theoretical fit, discussed in the next section, which uses parameters obtained from diagnostics.) Our devices are nearly symmetric, so that we can estimate the vertical nearest-

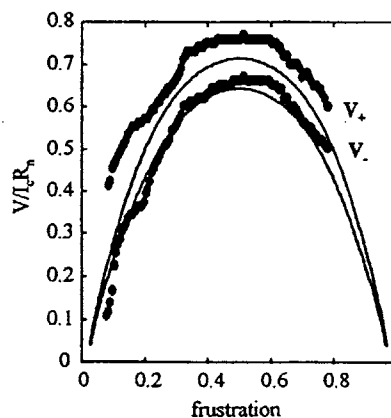


FIG. 3. The measured voltages of both steps vs frustration, for an array of $N = 2 \times 54$. This data was taken across one row of an array at $T = 8.2$ K. The solid line shows the model (Eq. 17), with $\beta = 8.1$, $\Lambda_j^2 = 1.2$, $M_v = 0.13$ and $M_h = 0.13$. The voltage is normalized to $I_c R_n = 0.5$ mV.

neighbor coupling, M_v , to be approximately equal to M_h . The theory provides a qualitative picture of the data and seems to match best at high f .

The two steps appear to be stable experimentally only in a limited parameter range, with $\beta=8-20$ and $\Lambda_j^2=1-1.5$. Although we have observed splitting in samples with much larger β and Λ_j , we did not see voltage locking between the rows.¹³ We find that, at the required temperatures, the output resistance is large, $r_0=8.5 \Omega$. The steps appear in a voltage range of $V_- = 0.05-0.34$ mV and $V_+ = 0.21-0.39$ mV, corresponding to bandwidths of 140 MHz and 87 MHz, respectively. There is a threshold field value below which no steps appear. This corresponds to a control current value of $I_{th}=0.3$ mA. We measure the period of the control current to be $I_{per}=1.6$ mA for the configuration shown in Fig. 1(a). In accordance with Eq. 1, we also observed that I_{per} decreases for stronger coupling, M_{ctrl} .

IV. SIMULATIONS AND ANALYSIS

Dynamical equations for the system are given in terms of the gauge-invariant phase differences across the junctions. As labeled in Fig. 1(a), we refer to the phases of junctions in the top row as ϕ_j and in the bottom row as ψ_j , where j indexes the junction's position in the array. The governing equations are derived by applying Kirchoff's current laws and the RSJ model for the current through a single junction. With only nearest-neighbor inductances, the gauge-invariant phase differences in the upper and lower row junctions, ϕ_j and ψ_j , satisfy

$$\begin{aligned} \mathcal{N}[\phi_j] - M_h(\mathcal{N}[\phi_{j+1}] + \mathcal{N}[\phi_{j-1}]) - M_v \mathcal{N}[\psi_j] \\ = I_b/I_c + \Lambda_j^2(\phi_{j+1} - 2\phi_j + \phi_{j-1}) \end{aligned} \quad (2)$$

and

$$\begin{aligned} \mathcal{N}[\psi_j] - M_h(\mathcal{N}[\psi_{j+1}] + \mathcal{N}[\psi_{j-1}]) - M_v \mathcal{N}[\phi_j] \\ = I_b/I_c + \Lambda_j^2(\psi_{j+1} - 2\psi_j + \psi_{j-1}) \end{aligned} \quad (3)$$

respectively, where

$$\mathcal{N}[\phi(t)] \equiv \ddot{\phi} + \Gamma \dot{\phi} + \sin \phi$$

is a functional which returns the total (normalized) current through a junction in response to its phase $\phi(t)$. Also, $\Gamma = \beta^{-1/2}$ and time has been normalized by $\tau = \sqrt{L_j C}$. Note that the inter-row coupling is provided only through terms involving M_v . If $M_h = M_v = 0$ (no inductive coupling), then the equations reduce to two independent discrete sine-Gordon equations. The above equations hold for all junctions in the array, except for $j=1$ and N . At the boundaries of the top row,

$$\begin{aligned} \mathcal{N}[\phi_1] - M_h(\mathcal{N}[\phi_2] + \mathcal{N}[\phi_1]) - M_v \mathcal{N}[\psi_1] \\ = I_b/I_c + \Lambda_1^2(\phi_2 - \phi_1 + 2\pi f), \end{aligned} \quad (4)$$

$$\begin{aligned} \mathcal{N}[\phi_N] - M_h(\mathcal{N}[\phi_{N-1}] + \mathcal{N}[\phi_N]) - M_v \mathcal{N}[\psi_N] \\ = I_b/I_c + \Lambda_N^2(\phi_{N-1} - \phi_N - 2\pi f). \end{aligned} \quad (5)$$

Similar equations hold for the lower row of junctions.

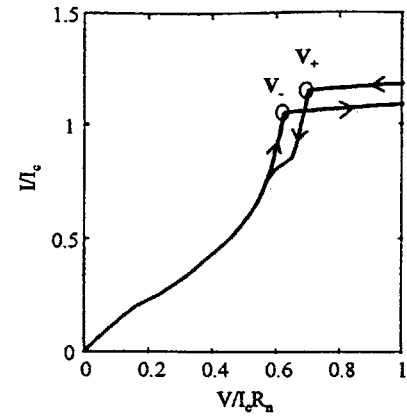


FIG. 4. Simulated current-voltage characteristic for an inductively coupled array of 2×54 junctions at $f=0.55$. The voltage across a single row is plotted. The parameters used are $\beta=10.8$ and $\Lambda_j^2=1.56$.

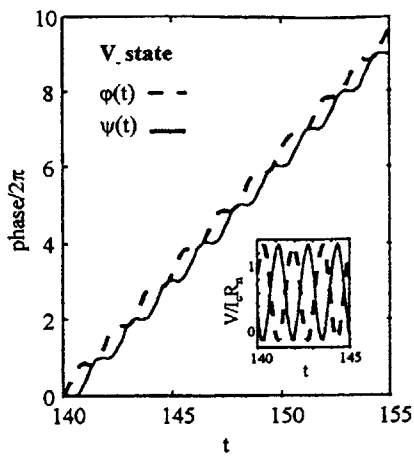
We have written Eqs. 2–5 in a form which emphasizes the spatial coupling introduced by nearest-neighbor inductances. However, to do numerical simulations, we write the system in a more compact form, similar to reference 3, which we will briefly describe. The junction phases constitute a $2N$ element vector, where the first N elements are the phases of the upper row and the last N elements are the phases of the lower row. Then the left side of Eqs. 2–5 can be expressed as the vector product of a $(2N \times 2N)$ inductance matrix, \bar{M} , and $\mathcal{N}[\bar{\phi}]$, while the spatial derivative on the right side can be written in terms of a matrix operator. Non-zero elements of the inductance matrix produce coupling. For example, the elements $(j,2j)$ and $(2j,j)$ are assigned a value of $-M_v$. All mutual inductances can be included by changing the inductance matrix, \bar{M} . We retain only the nearest-neighbor terms, noting that use of the complete inductance matrix gives nearly identical results.

We use a fourth-order Runge–Kutta scheme to solve the system. In order to implement this technique, we reduce the equations to two first-order systems by making the substitution, $\bar{v} = d\bar{\phi}/dt$. The coupled systems $d\bar{v}/dt$ and $d\bar{\phi}/dt$ are then integrated in equal time intervals. For damping and discreteness parameters approximating those of our experimental system, numerically simulated I - V 's also exhibit two voltage steps, as shown in Fig. 4.

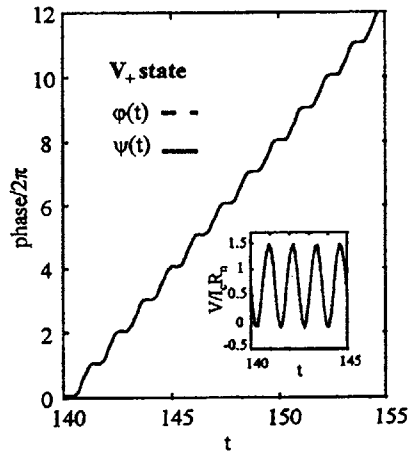
The figure shows the voltage measured across a single row. Note that both steps appear, even when the voltage is measured across only one row. In the simulations, the voltages of both rows are identical. This contrasts with our experiments, where the voltages of the rows are different for small bias currents. There also appears to be more hysteresis on the steps than in experiments. This is perhaps because we have not included thermal fluctuations in our simulations. In experiments, thermal fluctuations cause switching, making it difficult to trace the entire step.

A. Simulations

The numerical phase solutions, $\phi_j(t)$ and $\psi_j(t)$, provide valuable information which is not available through our experiments. We will use these to better describe the junction



(a)

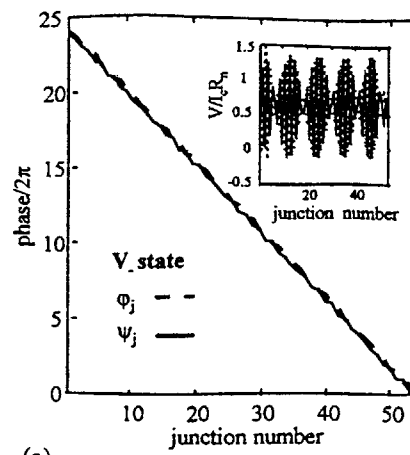


(b)

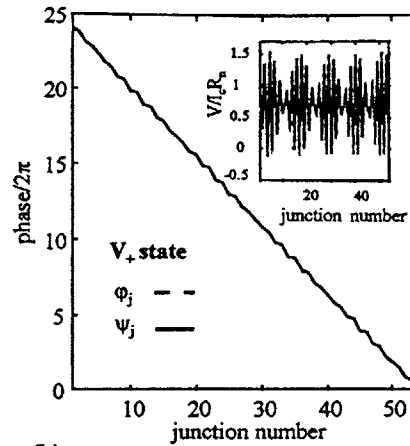
FIG. 5. (a) Phase evolution in time near the middle of the array ($j=25$), for the system with $N = 2 \times 54$ biased at point V_- . The upper row is represented by a dashed line, while the lower row corresponds to the solid line. The inset shows the corresponding voltage vs time for each row. (b) For the system biased at point V_+ , we show the phase evolution in time near the middle of the array ($j=25$). Dashed and solid lines correspond to the upper and lower rows, respectively. The inset shows the corresponding voltage vs time for each row. Time is normalized in steps of τ .

dynamics when the system is biased on a step and to specify the influence of magnetic field on the step voltage.

While we bias the system of 2×54 junctions at the top of a voltage step (at the points marked as V_- and V_+), Figs. 5(a) and 5(b) show the phase evolution in time for a single set of vertically adjacent junctions near the middle of the array ($j=25$). The junction phases, $\phi_{25}(t)$ and $\psi_{25}(t)$, can be approximated by the sum of a linear function in time and a small periodic oscillation. In the V_- state (Fig. 5(a)), the linear part of the phase plots show an offset between the rows, while the sinusoidal part is phase-shifted. However, in the V_+ state (Fig. 5(b)), the rows have no relative offsets or phase-shifts, and the plots of each row are indistinguishable. A linear fit through the points shows that the average $\phi_j(t)$ and $\psi_j(t)$ have slopes proportional to the step voltage. This is consistent with the fact that the dc voltage is calculated by taking a time average of $d\phi/dt$ for the first row and $d\psi/dt$



(a)



(b)

FIG. 6. (a) Phase vs junction number, j , at a fixed time, for the system with $N = 2 \times 54$ biased at V_- . The upper row is represented by a dashed line, while the lower row corresponds to the solid line. The inset shows the corresponding voltage vs j . (b) For the system biased at V_+ , we show the phase vs junction number, j , at a fixed time. Dashed and solid lines correspond to the upper and lower rows, respectively. The inset shows the corresponding voltage vs j . Since the solutions are in phase, they appear as one line in the plots.

for the second row. In the insets, we plot the voltage vs time. The oscillation is sinusoidal, with a single frequency ω which is equal to the slope of the linear fits. We find that the oscillation becomes more complicated when the system is not biased on a step. At voltages below the lower step, more frequency components appear in the oscillation. At these voltages, there is generally a phase-shift between the rows, but it is not clear that the phase-shift remains constant in time. At voltages above the upper step, the oscillations continue at a single frequency but with much smaller amplitude. The phase solutions in this regime appear to be whirling modes, as described in Ref. 14, and adjacent junctions in each row are always out-of-phase.

We find that the spatial distribution of phases across the array exhibits similar behavior. In Figs. 6(a) and 6(b), we plot the phase versus junction number, at a given point in time. The function is almost linear with an approximate slope of $2\pi f$. The insets show the instantaneous voltage vs

junction number for each row. These plots are reminiscent of under-sampled sine waves. Thus, the functional form of the wave is more easily determined by examining the voltage vs time plots of successive junctions. We find that the spatial oscillation is also sinusoidal, with a wave number of $2\pi f$. Again, on the lower-voltage step (Fig. 6(a)), the oscillations of each row are phase-shifted with respect to the other, whereas the oscillations are in-phase on the higher voltage step (Fig. 6(b)). Although it is more difficult to see in the figures, we find that there is again an offset between the rows for the lower step and not for the higher step.

In summary, the simulations indicate that solutions for the phases at these points of the I - V can be well approximated by

$$\phi_j(t) = \chi_j(t) + \theta + c + a \sin(\chi_j + \theta) \quad (6)$$

and

$$\psi_j(t) = \chi_j(t) - \theta + c + a \sin(\chi_j - \theta), \quad (7)$$

where

$$\chi_j(t) = \omega t + 2\pi f j. \quad (8)$$

The phase difference between the rows is given by 2θ ; e.g. $\theta=0$ for the symmetric in-phase state (V_-) and $\theta=\pi/2$ for the anti-symmetric state (V_+). The constant a represents the amplitude of the oscillations. The constant c denotes the phase difference between the linear rotating part and the sinusoidal oscillation part of the wave form.

The above traveling wave solution works well throughout most of the array. Near the array edges, we do see some reflections, and the junction oscillations no longer look sinusoidal. However, the simulations show that these effects damp out within a few junctions from the edge.

B. Analysis

In this section we substitute the suggested solutions, Eq. 6, into the governing Eq. 2 to determine relationships among the parameters a , c , θ , ω and I_b for a given f .

To clarify the discussion, we will carry out our analysis neglecting M_h in Eqs. 2 and 3 and then at the end show how M_h can be included. Substitution of Eq. 6 yields

$$\begin{aligned} \omega^2 a [\sin(\chi_j + \theta) - M_v \sin(\chi_j - \theta)] - \Gamma \omega a [\cos(\chi_j + \theta) \\ - M_v \cos(\chi_j - \theta)] - \Gamma \omega (1 - M_v) - \omega_1^2 a \sin(\chi_j + \theta) \\ + I_b/I_c = \sin[\chi_j + \theta + c + a \sin(\chi_j + \theta)] + M_v \sin[\chi_j \\ - \theta + c + a \sin(\chi_j - \theta)], \end{aligned} \quad (9)$$

where

$$\omega_1^2 = 4\Lambda_j^2 \sin^2(\pi f). \quad (10)$$

The non-linear terms on the right-hand side can be expanded into a Fourier-Bessel series,¹⁵

$$\begin{aligned} \sin[\chi_j \pm \theta + c + a \sin(\chi_j \pm \theta)] \\ = \sum_{m=-\infty}^{\infty} J_m(a) \sin[(m+1)(\chi_j \pm \theta + c) - mc]. \end{aligned} \quad (11)$$

Using this expansion, we can apply the method of harmonic balance to Eq. 9. This method neglects all the harmonics in Eq. 9 except the zeroth and the first, and balances the coefficients of these two modes. This method was previously used in the Josephson junction context in order to study a single junction,¹⁵ a simple in-phase solution of two-dimensional arrays,¹⁶ and single-harmonic solutions in two-dimensional arrays.¹⁷ It was also applied to the study of zero-field steps and the Fiske steps in one-dimensional continuous junctions.^{18,19}

After some algebraic manipulation, balancing of the dc terms yields

$$I_b = I_c (1 + M_v) [\Gamma \omega - J_1(a) \sin c]. \quad (12)$$

Balancing the $\cos \chi_j$ terms, we find

$$\begin{aligned} \sin \theta [-\omega_1^2 a + \omega^2 a (1 + M_v)] + \cos \theta [-\Gamma \omega a (1 - M_v)] \\ = \sin \theta [J_0(a) (1 + M_v) \cos c] \\ + \cos \theta [J_0(a) (1 - M_v) \sin c] \end{aligned} \quad (13)$$

while balancing the $\sin \chi_j$ terms gives

$$\begin{aligned} \sin \theta [\Gamma \omega a (1 + M_v)] + \cos \theta [-\omega_1^2 a + \omega^2 a (1 - M_v)] \\ = \sin \theta [-J_0(a) (1 + M_v) \sin c] \\ + \cos \theta [J_0(a) (1 - M_v) \cos c]. \end{aligned} \quad (14)$$

From Eq. 3, we obtain the same equations except θ is replaced by $-\theta$. Since Eq. 12 does not involve θ , it is unchanged. However, Eqs. 13 and 14 are changed, and we obtain a total of five constraints for the parameters, a , c , θ , ω and I_b/I_c for each f .

It is easy to see, however, that the five equations can never be satisfied simultaneously when $\sin \theta \neq 0$ and $\cos \theta \neq 0$. This means that the ansatz is consistent if and only if $\sin \theta = 0$ or $\cos \theta = 0$, in accordance with our numerical observation. In this case, Eqs. 12–14 reduce to

$$[\Gamma \omega - J_1(a) \sin c] (1 + M_v) = I_b/I_c, \quad (15)$$

$$\Gamma \omega a + J_0(a) \sin c = 0, \quad (16)$$

$$\omega^2 a (1 \pm M_v) = \omega_1^2 a + J_0(a) (1 \pm M_v) \cos c, \quad (17)$$

where the $-$ sign is taken for $\sin \theta = 0$ (in-phase) and the $+$ sign is taken for $\cos \theta = 0$ (anti-phase). Equation 15 simply computes I_b once the other parameters are obtained. Thus we have only two equations for a , c , ω . The parameter c can be eliminated from Eqs. 16 and 17, and we obtain a single equation

$$(J_0(a)/a)^2 = (\omega \Gamma)^2 + (\omega^2 - \omega_{\pm}^2)^2, \quad (18)$$

where

$$\omega_{\pm}^2 = \frac{\omega_1^2}{1 \mp M_v} = \frac{4\Lambda_j^2}{1 \mp M_v} \sin^2(\pi f).$$

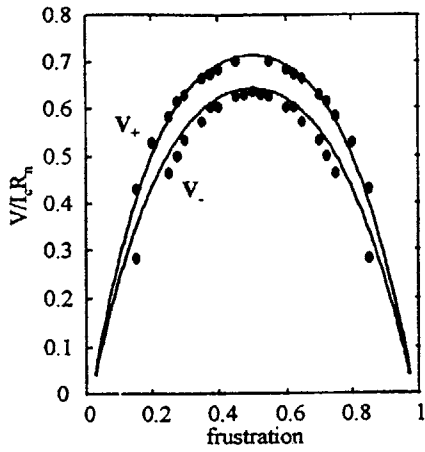


FIG. 7. Voltage positions of flux flow steps in simulated I - V 's (solid circles). The voltage is normalized to $I_c R_n$. The solid line represents the theory of Eq. 19.

As ω is varied, we obtain a one-parameter family of roots for a . Thus we supplement the equation with a "resonance condition" $da/d\omega=0$, which maximizes the oscillation amplitude, a . Solved with the condition, Eq. 18 gives us the resonance frequency

$$\omega^2 = \omega_{\pm}^2 - \Gamma^2/2. \quad (19)$$

The amplitude of the oscillations is then given implicitly by

$$\left(\frac{J_0(a)}{a}\right)^2 = \omega_{\pm}^2 \Gamma^2 - \frac{\Gamma^4}{4}. \quad (20)$$

Finally Eq. 15 gives the corresponding I_b . When we include horizontal nearest-neighbors in our equations, the form of the resonance frequencies, Eq. 19, and amplitude, Eq. 20 remain the same. However, ω_{\pm} is replaced by

$$\omega_{\pm}^2 = \frac{4\Lambda_J^2}{1 \mp M_v - 2M_h \cos(2\pi f)} \sin^2(\pi f). \quad (21)$$

In Fig. 7, the theory is compared with simulation results for $\beta=10.8$ and $\Lambda_J^2=1.56$. We see that the resonant voltages are predicted well by this theory. Our experimental data in Fig. 3 has similar trends, but the voltage values do not match the theory as well. We have found better fits to the data by modifying the values of β and M_h (within the uncertainty of our diagnostic results) used for the theoretical curve.

As observed, the resonance condition we imposed appears appropriate to calculate the steps. However, one may also choose an alternative supplementary condition, $dI/d\omega=0$. This is perhaps a more intuitive condition to calculate a step in the I - V , but it does not lead to an analytical estimate for the frequency. Nonetheless, the roots can be found by numerically solving the algebraic system, and it is determined that the resonant frequency is extremely close to (but larger than) ω in Eq. 19 when Γ is small. Thus, we may choose either condition, and our results are altered little by the choice.

V. DISCUSSION

In this section we discuss the resonance mechanism for the peaks and the harmonic balance approach taken in the previous section to explain the resonant voltages.

The resonance mechanism confirms the usual physical explanation given for Eck steps in both continuous and discrete systems.^{1,20} The applied field injects an array of vortices into the system. A bias current forces the vortices to move, producing a voltage across the open ends. As the bias current is increased, the vortices move faster, until the "limiting velocity" is reached. For a system of two rows, vortex arrays move through both rows. In this case, the rows are coupled and have two limiting velocities, giving rise to two different vortex patterns (the rows are either in-phase or out-of-phase).

The limiting velocity is commonly derived as the phase velocity of linear oscillations (electromagnetic waves) in the media. The continuous version of this system has been analyzed by several authors, and analytic expressions for the resonance frequencies have been found.³ These show good agreement with experimental data.^{5,21} In discrete systems, a similar strategy has been successful for a single-row, circular system,²² and is being extended to multi-row systems.²³

Based on these previous works, we would like to make the explanation of the limiting velocity more complete. In particular, there are several obstacles to be overcome in order to make the analyses consistent. (1) The analyses assume $\sin \phi \approx \phi$ and $I_b \ll 1$, neither of which is appropriate at the peaks. (2) Why can the limiting velocity of the vortices, which are nonlinear objects, be identified as the phase velocity of linear oscillations? Several attempts have been made^{10,1,24} to explain the interaction (phase-locking) mechanism between the vortices and the oscillation, but it is still far from complete. Furthermore, these linearization approaches are not capable of predicting the height of the peak since one needs to know the finite amplitude of oscillations around the vortices.

The harmonic balance approach in the previous section appears promising to deal with these questions. In our ansatz Eq. 6, we have both a stretched vortex (approximated by a linear function of χ) and a finite amplitude oscillation (only the first harmonic of χ is retained). Equation 18 describes their interaction; the vortex velocity ω significantly affects the amplitude of the harmonics a . In Eq. 15 we see the effect on the I - V curve; if $a=0$, then $I_b \propto \omega$, corresponding to the ohmic line. Deviation from the line is thus attributed to increase in a .

In the present paper, we have only showed that the harmonic balance approach recovers the resonant frequencies predicted by the linearization analysis. We have not yet carefully compared the predicted amplitude a and the peak bias current I_b . In a preliminary study, the amplitude a , obtained by solving the system (Eqs. 15–17) with a resonance condition, appears to agree with the amplitude in Fig. 5 within 10%. Also, the range of applicability of the ansatz needs to be studied; we may need to describe the vortex more accurately. However, assumption of the traveling wave constrains the functional form of the solutions to be $\phi_j(t) = \chi_j + \theta + c + f(\chi_j + \theta)$ where f is a periodic function.

Therefore, a systematic improvement of the ansatz is in principle possible by expanding f into Fourier series, and taking higher order harmonics.

VI. SUMMARY

We have observed that, in long inductively coupled arrays of Josephson junctions, two Eck steps appear in the I - V . These steps correspond to arrays of vortices traveling through the system. The wave is nearly a single harmonic, with a well-defined amplitude and dispersion relation. We have found that the lower step corresponds to an anti-symmetric state where the voltages are oscillating out of phase between the two rows. However, the upper step corresponds to a symmetric state, where the oscillating voltages are in-phase. We have found an ansatz for the voltage states which is close to numerical observations. We can analytically predict the dc voltages of these resonant states and numerically predict the amplitude of the ac voltages.

The upper step can have important technological implication. When the system is biased in this state, the ac voltages add, increasing the power output. The two-row device will also have higher output impedance than its continuous, stacked junction counterpart. These qualities make this device desirable for oscillator applications. As in a single discrete array, the frequencies can be tuned with a control current and are stable for a relatively wide range of bias currents.^{1,25} Although the bandwidth is approximately the same as for the single array, a larger output resistance may increase the linewidth. However, phase locking between the two rows is expected to reduce the linewidth, and such measurements will be helpful.

ACKNOWLEDGMENTS

We thank Mauricio Barahona, Joel Phillips, and Alexy Ustinov for valuable discussions. We also thank Jay Sage and Dave Feld at Lincoln Laboratories for their generous help. We acknowledge the support of the NSF Graduate Fel-

lowship program and NSF Grant Nos. DMR-9402020, DMS-9057433, and DMS-9500948. We appreciate the partial support of the Dutch Foundation for Fundamental Research on Matter.

- ¹H. S. J. van der Zant and T. P. Orlando, *J. Appl. Phys.* **76**, 7606 (1994).
- ²N. Grønbech-Jensen, M. R. Samuelsen, P. S. Lomdahl, and J. A. Blackburn, *Phys. Rev. B* **42**, 3976 (1990).
- ³S. Sakai, P. Bodin, N. F. Pedersen, *J. Appl. Phys.* **73**, 2411 (1993).
- ⁴A. V. Ustinov, H. Kohlstedt, and C. Heiden, *IEEE Trans. Appl. Supercond.* **5**, 2743 (1995).
- ⁵A. V. Ustinov, H. Kohlstedt, M. Cirillo, N. F. Pedersen, G. Hallmanns, and C. Heiden, *Phys. Rev. B* **48**, 10 614 (1993).
- ⁶T. Holst, J. Bindslev Hansen, N. Grønbech-Jensen, and J. A. Blackburn, *Phys. Rev. B* **42**, 127 (1990).
- ⁷HYPRES, Inc., Elmsford, NY 10523.
- ⁸H. S. J. van der Zant, R. A. M. Receveur, T. P. Orlando, and A. W. Kleinsasser, *Appl. Phys. Lett.* **65**, 2102 (1994).
- ⁹V. Ambegaokar and A. Baratoff, *Phys. Rev. Lett.* **10**, 486 (1963).
- ¹⁰H. S. J. van der Zant, D. Berman, T. P. Orlando, and K. A. Delin, *Phys. Rev. B* **49**, 12 945 (1994).
- ¹¹In this paper, we have taken M_h to be a positive number, so that the mutual inductance matrix element is $m = -M_h$.
- ¹²A. E. Duwel, Master thesis, The Massachusetts Institute of Technology, 1995.
- ¹³A. E. Duwel, H. S. J. van der Zant, and T. P. Orlando, *IEEE Trans. Appl. Supercond.* **5**, 3357 (1995).
- ¹⁴S. Watanabe, S. Strogatz, H. S. J. van der Zant, and T. P. Orlando, *Phys. Rev. Lett.* **74**, 379 (1995).
- ¹⁵K. Wiesenfeld, E. Knobloch, R. F. Miracky, and J. Clarke, *Phys. Rev. A* **29**, 2102 (1984).
- ¹⁶K. Wiesenfeld, S. Benz, and P. Booi, *J. Appl. Phys.* **76**, 3835 (1994).
- ¹⁷G. Filatrella and K. Wiesenfeld, *J. Appl. Phys.* **78**, 1878 (1995).
- ¹⁸I. O. Kulik, *Sov. Phys. JTEP* **24**, 1307 (1967).
- ¹⁹K. Enpuku, K. Yoshida, and F. Irie, *J. Appl. Phys.* **52**, 344 (1981).
- ²⁰R. E. Eck, D. J. Scalapino, and B. N. Taylor, *Phys. Rev. Lett.* **13**, 15 (1964).
- ²¹S. Sakai, A. V. Ustinov, H. Kohlstedt, A. Petraglia, and N. F. Pedersen, *Phys. Rev. B* (to be published).
- ²²A. V. Ustinov, M. Cirillo, and B. A. Malomed, *Phys. Rev. B* **47**, 8357 (1993).
- ²³A. Petraglia and N. F. Pedersen, preprint (unpublished).
- ²⁴S. Watanabe, H. S. J. van der Zant, S. H. Strogatz, and T. P. Orlando, *Phys. D* (submitted).
- ²⁵D. Berman, H. S. J. van der Zant, and T. P. Orlando, *IEEE Trans. Appl. Supercond.* **4**, 168 (1994).

A Novel Phase-Locked State in Discrete Josephson Oscillators

Amy E. Duwel and Terry P. Orlando
Massachusetts Institute of Technology, Cambridge, MA

Shinya Watanabe
Center for Chaos & Turbulence Studies, Niels Bohr Institute, Copenhagen, Denmark

Herre S. J. van der Zant
Delft University of Technology, Delft, The Netherlands

Abstract—We have measured a novel phase-locked state in discrete parallel arrays of Josephson junctions which can be used for oscillator applications. Previous Josephson junction oscillators have been based on the Eck step, where a large-amplitude wave of nearly a single harmonic travels through the system. Multi-row systems biased on the Eck step could improve the output power, but their in-phase oscillations are difficult to stabilize. A new in-phase state which is very stable has been measured as a step in the dc I-V characteristic of one and two row systems. Simulations show that large-amplitude oscillations of two harmonics characterize the state. The rows are phase-locked and in-phase for the higher harmonic. We present an analytic expression for the oscillation frequencies and their magnetic tunability.

I. INTRODUCTION

Long Josephson junctions and Josephson junction arrays have potential for microwave oscillator applications. Underdamped long Josephson junctions biased on the Eck step produce oscillations at frequencies proportional to the step voltage. Radiation from these devices has been measured, at power levels of $5 \mu\text{W}$ at 440 GHz [1] and linewidths of about 1 MHz. Discrete parallel arrays of short junctions also produce an Eck step and are expected to radiate at frequencies proportional to the step voltage [2]. Although the discrete version is not expected to significantly improve upon the power level or linewidth of long junction oscillators, the output impedance more closely matches typical microwave circuit loads. Various configurations have been proposed to improve the oscillator power and linewidth, including series arrays of short junctions, two-dimensional arrays of short junctions, stacked long junctions, and shorted arrays of short junctions. The proposed geometries increase the number of junctions across which the output voltage is measured. If the output junctions can be phase-locked in-phase, then the power and possibly the linewidth of the oscillator are improved. In addition, these devices have an increased output impedance which can be controlled.

Recent studies of underdamped discrete parallel arrays and stacked long junctions have shown that the output junctions can be phase-locked in a state with very large amplitude oscillations [3], [4]. Measurements of two discrete rows and of two stacked junctions show that, in both systems, the Eck step splits into two states. The lower voltage state corresponds to oscillations in the two rows which are exactly out-of-phase, while the higher voltage state corresponds to in-phase oscillations. Biased in the in-phase state, the oscillator power is expected to double (for two rows). For an arbitrary number N of rows oscillating in-phase, the power should be N times the power of a single row [5]. However, the in-phase state of the Eck step is difficult to stabilize experimentally, and the out-of-phase state can produce at most the power of a single row oscillator (if N is odd).

In contrast, we have found a new state in discrete arrays which is stable experimentally and, according to simulations, produces voltage oscillations which are in-phase across all the output junctions. This state is manifested as a step in the dc I-V curve at a voltage which is below the Eck step. Simulations indicate that oscillations occur at a frequency corresponding to the step voltage and at twice this frequency. It is this second harmonic which is in-phase between the rows. We have measured this state in single and double rows of 54 junctions per row. We find that it is analogous to the sub-structure observed in discrete ring arrays [6] and is possible only in discrete systems. Simulations of arrays with up to 5 rows show that all rows are phase-locked, and that the higher harmonic adds in-phase. Thus, the output power to a matched load should scale as the number of rows. In addition, the linewidth is still expected to scale as $1/N$ [5]. Although ac measurements must be made to verify these characteristics, our studies indicate that this device has potential for oscillator applications.

II. EXPERIMENTS

We have measured arrays of two rows ($N = 2$), with 54 junctions per row. Fig. 1 shows a schematic of our device. Resistors are used at positions indicated by the arrows in Fig. 1 to make the applied bias current as uniform as possible. The voltage of each row can be measured separately at the array edge. The array is placed above a superconducting ground plane, and a separate control wire is used to apply a magnetic field. Because the system is discrete, we expect its properties to be periodic with

Manuscript received August 27, 1996.

A. E. Duwel, 617-253-0393, duwel@bardeen.mit.edu.

This work was supported by the NSF Graduate Fellowship program and NSF Grant Nos. DMR-9402020, DMS-9057433, and DMS-9500948, with the partial support of the Dutch Foundation for Fundamental Research on Matter.

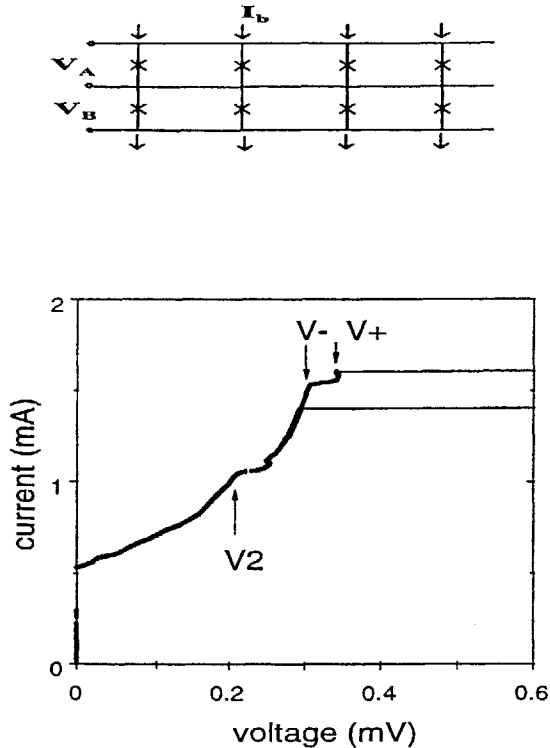


Fig. 2. Current-Voltage characteristic of 54x2 array. $\beta = 14$ and $\Lambda_J^2 = 0.68$. V^- and V^+ are the split Eck peak, while $V2$ is the second harmonic state.

magnetic field. Thus we will discuss the applied field in terms of frustration, which is the flux applied to a single loop of the array, normalized to the flux quantum, $f = \Phi_{\text{app}}/\Phi_0$. The applied flux is proportional to the control current.

Samples were fabricated using a Nb trilayer process [7]. The junctions are $3 \times 3 \mu\text{m}^2$ with a critical current density of $j_c(T=0) = 1400 \text{ A/cm}^2$. Device parameters have been determined using the diagnostic procedures described by van der Zant *et al.* [8]. We find that the normal-state resistance $R_n = 15.3 \Omega$, the self-inductance of a single loop in the array $L_s = 8.5 \text{ pH}$, the nearest-neighbor coupling ratios (to L_s) $M_h = M_v = 0.13$, the capacitance $C = 342 \text{ fF}$, and the Josephson inductance, $L_J = \Phi_0/(2\pi I_c(T=0)) = 2.8 \text{ pH}$. Our measurements were taken at $T = 7.4 \text{ K}$. At this temperature, the Stewart-McCumber damping parameter $\beta = R_n^2 C/L_J = 14$ and the discreteness parameter $\Lambda_J^2 = L_J/L_s = 0.68$.

Previous measurements of this particular device at a higher temperature ($\beta = 8.1$ and $\Lambda_J^2 = 1.2$) have already been reported [3]. We now lower the temperature so that Λ_J^2 is less than one, and additional resonances appear in the I-V. The most prominent of these is marked as $V2$ in the I-V of Fig. 2. The split Eck step is also marked as V^- and V^+ . Fig. 2 shows the voltage across a single row of the array. Measurements of the second row are identical except at very low voltages. All of the resonances respond periodically to a changing magnetic field. In Fig. 3 we plot this behavior. The $V2$ step has twice the period and about half the amplitude of the Eck step. It can be tuned

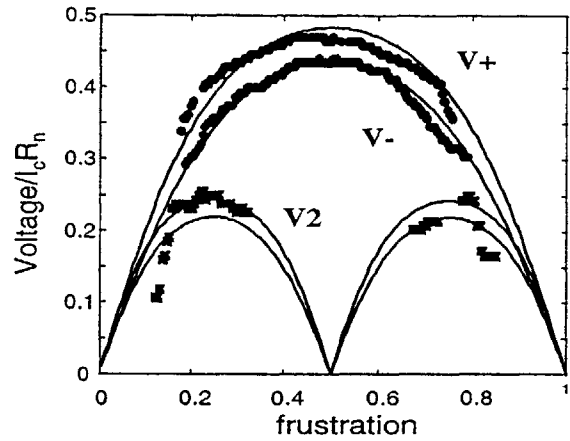


Fig. 3. Magnetic tunability of step voltages. The solid lines are Eq. 5 for $m = 1$ and $m = 2$, with $\beta = 14$ and $\Lambda_J^2 = 0.9$. The symbols are data points.

in a voltage range of about $0.12 - 0.25 \text{ mV}$. Since it is the second harmonic being considered, this corresponds to a bandwidth of $120 - 240 \text{ GHz}$.

III. SIMULATIONS

The governing equations for the system are derived by applying Kirchoff's current laws and using the RSJ model for the current through a single junction. We normalize the current to I_c , the voltage to $I_c R_n$, and time to $\sqrt{L_J C}$. With $\Gamma = \beta^{-1/2}$, our equations become

$$\begin{aligned} \mathcal{N}[\phi_j] - M_h(\mathcal{N}[\phi_{j-1}] + \mathcal{N}[\phi_{j+1}]) - M_v \mathcal{N}[\psi_j] \\ = I_b/I_c + \Lambda_J^2(\phi_{j+1} - 2\phi_j + \phi_{j-1}) \end{aligned} \quad (1)$$

and

$$\begin{aligned} \mathcal{N}[\psi_j] - M_h(\mathcal{N}[\psi_{j-1}] + \mathcal{N}[\psi_{j+1}]) - M_v \mathcal{N}[\phi_j] \\ = I_b/I_c + \Lambda_J^2(\psi_{j+1} - 2\psi_j + \psi_{j-1}) \end{aligned} \quad (2)$$

where ϕ_j and ψ_j represent the gauge-invariant phase differences across the upper row and lower row junctions respectively. The functional $\mathcal{N}[\phi_j(t)] \equiv \dot{\phi}_j(t) + \Gamma \phi_j(t) + \sin \phi_j(t)$ returns the total current through junction j . For consistency in comparing with theory, we include only nearest-neighbor inductances, M_h and M_v . We integrate using a fourth-order Runge-Kutta scheme. Our method is described in more detail in [3].

Figure 4 shows a simulated I-V curve with the same features found in the experimental measurements. In this simulation, frustration = 0.3, $\beta = 14$, $\Lambda_J^2 = 0.9$. The discreteness parameter used is slightly larger than that calculated for experiments, since smaller values of Λ_J^2 yield more fine-structure than that which appears in experiments. The Eck step (V^+ and V^-) and the $V2$ step are marked. These steps are tunable with frustration, as in our experiments. In Fig. 5 we plot the phase vs. time of the middle junction in each row while the system is biased at the top of the $V2$ step. The inset shows the

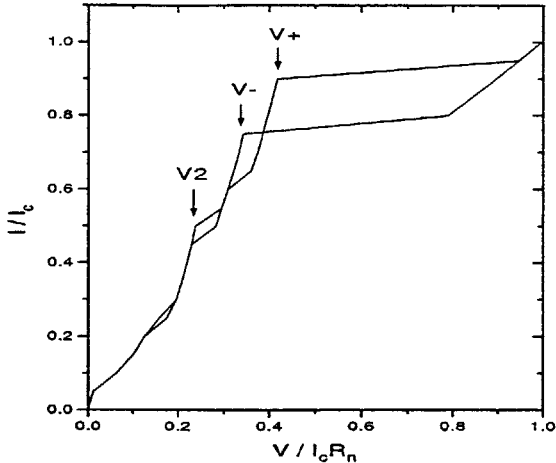


Fig. 4. Simulated Current-Voltage characteristic which shows the same features as experiments. $\beta = 14$ and $\Lambda_j^2 = 0.9$.

voltage vs. time. Two harmonics dominate the time evolution of the junctions. The lower harmonic, which has a frequency corresponding to the step dc voltage, is out-of-phase between the two rows. The second harmonic is in-phase. This relationship becomes clearer when we take the Fourier transform of the voltage signals. Fig. 6 compares the Fast Fourier Transform of the ac voltage from a single row to the transform of the sum of both rows. When the voltage across the two rows is added, the amplitude of the second harmonic doubles, while the lower harmonic disappears. Simulations for up to 5 rows of 54 junctions show that the voltage across N rows scales as N . However, preliminary results on a 10-row array suggest that there is a slight phase-shift between rows which causes a saturation of the second harmonic voltage amplitude across larger arrays. Simulations also indicate that the oscillation amplitude in the V_2 state is about three times smaller than the oscillation amplitude on the Eck step of a single row. Thus, it is necessary to bias three rows on the V_2 step to obtain equivalent voltage output.

IV. DISCUSSION

Substructures on the flux-flow part of the I - V characteristics have already been observed in single-row discrete rings [6]. In this system, a vortex was trapped and driven with a dc current, forcing it to travel with a constant velocity around the ring. The resonance frequencies in the system were first presented by Ustinov *et al.* [9] by linearizing the governing equation and calculating the dispersion relation. Petgrelia *et al.* extended the analysis to include an arbitrary number of inductively coupled rows by deriving such a relation for the linearized system of coupled equations [11]. For two rows, the leading order term reads:

$$\omega_r^2 = \frac{4\Lambda_j^2 \sin^2(\kappa_r p/2)}{1 \mp M_v - 2M_h \cos(\kappa_r p)} \quad (3)$$

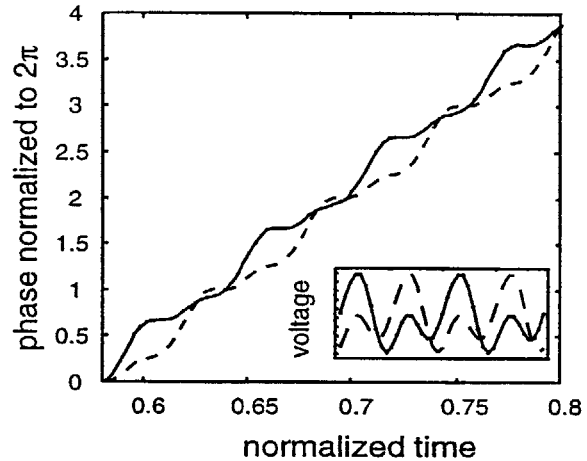


Fig. 5. Phase vs. time of vertically adjacent junctions in a 2x54 array biased at V_2 . Inset shows voltage vs. time of the two junctions.

The parameter κ_r is the wavenumber and p is the lattice spacing. In an annular system, this linear wave was phase-matched to the kink by a condition

$$\omega_r/\kappa_r = \omega/\kappa, \quad (4)$$

where ω and κ are the kink rotation frequency and its wavenumber, respectively. The kink frequency ω is proportional to the dc voltage while κ is determined by the periodic geometry. (For M vortices trapped in an n -junction ring, $\kappa = 2\pi M/(np)$.) Therefore, the condition predicts a discrete set of special voltages, that were identified with the observed resonant steps.

When the phase-matching condition (4) is fulfilled, the solutions would appear as a traveling wave, with a waveform being a superposition of a kink and a small amplitude oscillation. Such a traveling wave was found to be the dominant type of solutions not only on the resonant steps but generally in the flux-flow region [10]. Then, the functional form of the solutions is tightly restricted and can be written in the form: $\phi_j(t) = \xi + \Phi(\xi)$ where $\xi = \omega t + \kappa p j$ is a moving coordinate with a kink, and Φ is the 2π -periodic part of the waveform function. Starting from this traveling wave assumption, the interaction between the kink and the “linear” wave can be quantitatively taken into account. The function Φ is first expanded into Fourier modes, and the system can be rewritten in terms of these modes. The modal equations then appear as a coupled system driven by a kink [12].

These traveling wave solutions are not sensitive to the boundary conditions, and the same resonance mechanism is expected also in the arrays with open boundaries [3]. Instead of a periodically circulating kink, an evenly-spaced train of vortices propagates through the system in this case. The solution is still of the above form, but the wavelength $\kappa = 2\pi f$ can now be continuously tuned. (This continuous dependence on f distinguishes this type of step from Fiske steps, which could occur in a similar voltage

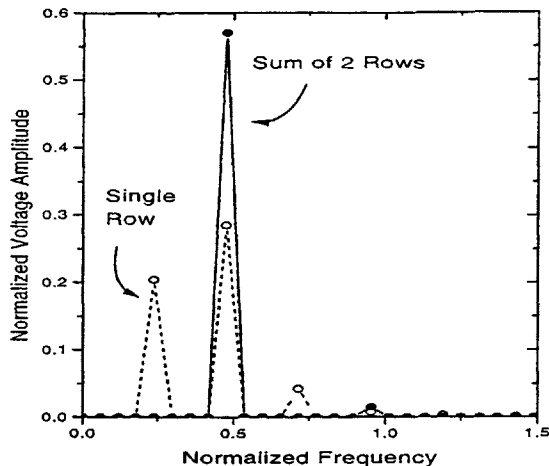


Fig. 6. Fast Fourier Transform of AC voltage signals. The dotted line represents the output of a single row. The solid line is obtained by adding the ac voltage across two rows and then computing the transform. The voltage is normalized to $I_c R_n$ and the frequency is normalized to $\Phi_0/(2\pi I_c R_n)$.

region of the I - V for shorter arrays but at fixed resonant voltages.) We have indeed observed the splitting of the Eck peak in a system of two coupled arrays, and explained the resonance from this approach [3]. The Eck peak in a discrete array corresponds to the resonance between the kink and the first harmonic of the waveform function Φ . Therefore, the higher harmonics were neglected and the harmonic balance approximation was carried out.

The new step we have found in Fig. 2 corresponds to when the second harmonic also has a non-negligible amplitude. The analysis of the modal equations is still possible in principle, but generally becomes complicated when higher harmonics are involved. Assuming that the coupling between modes are negligible and that the amplitudes of the modes are small, the resonance of the m -th Fourier mode is expected to occur at:

$$V_m = \frac{\Phi_0}{m\pi\sqrt{L_s C}} \left| \frac{\sin(m\pi f)}{1 \mp M_v - 2M_h \cos(2m\pi f)} \right|^{1/2} \quad (5)$$

in terms of voltage [12]. To first order, the linear analysis [11] would also yield this result. We compare the expression to our data in Fig. 3. By using a slightly larger value of $\Lambda_j^2 = 0.9$ we obtain a reasonable fit for both Eck peak and the V2 steps. We do not know if this discrepancy between the parameters can be explained by taking the coupling and the amplitudes of the modal equations into account. In addition, no splitting of the $m = 2$ step is observed; the reason is also to be studied further.

V. CONCLUSIONS

We have found a new phase-locked state in parallel arrays of Josephson junctions. This state has been measured as a step in the I - V characteristic of two row arrays with 54 junctions per row. The step is tunable with magnetic field and has half the period of the Eck step. Simulations for up to 5 row arrays indicate that, in this state, the

junctions undergo large amplitude oscillations with two harmonics. The higher harmonic is in-phase for all the rows, and the ac voltage of the system is N times the ac voltage of a single row biased on this step. Unfortunately, simulations show that the oscillation amplitude of a single row biased in this state is three times smaller than when the row is biased on the Eck step. Thus the array must be relatively large to improve upon the power output of single row oscillators. However, additional rows are expected to narrow the linewidth by a factor of $1/N$. The higher output impedance of a larger system is also important for coupling to typical microwave circuit loads.

ACKNOWLEDGMENTS

We thank Enrique Trías, Steve Strogatz, Mauricio Barahona, and Alexey Ustinov for helpful discussions.

REFERENCES

- [1] V. P. Koshelets, A. V. Shchukin, I. L. Lapytskaya, and J. Mygind, "Spectral linewidth of autonomous and injection locked flux-flow oscillators," *Phys. Rev. B*, vol. 51 (10), pp. 6536-6541, March, 1995.
- [2] H. S. J. van der Zant and T. P. Orlando, "Eck peak in underdamped discrete superconducting vortex flow devices," *J. Appl. Phys.*, vol. 76 (11), pp. 7605-7612, December, 1994.
- [3] A. E. Duwel, E. Trias, T. P. Orlando, H. S. J. van der Zant, S. Watanabe, and S. Strogatz, "Resonance splitting in discrete planar arrays of Josephson junctions," *J. Appl. Phys.*, vol. 79 (10), pp. 7864-7870, May, 1996.
- [4] A. V. Ustinov, H. Kohlstedt, and C. Heiden, "Possible phase locking of vertically stacked Josephson flux-flow oscillators," *Appl. Phys. Lett.*, vol. 65 (11), pp. 1457-1459, September, 1994.
- [5] S. P. Benz and C. J. Burroughs, "Two-dimensional arrays of Josephson junctions as voltage-tunable oscillators," *Supercond. Sci. Technol.*, vol. 4, pp. 561-567, 1991.
- [6] H. S. J. van der Zant, T. P. Orlando, S. Watanabe, and S. H. Strogatz, "Kink propagation in a highly discrete system: observation of phase locking to linear waves," *Phys. Rev. Lett.*, vol. 74 (1), pp. 174-177, January, 1991.
- [7] HYPRES, Inc. Elmsford, NY 10523.
- [8] H. S. J. van der Zant, R. A. M. Receveur, T. P. Orlando, and A. W. Kleinsasser, "One-dimensional parallel Josephson-junction arrays as a tool for diagnostics," *Appl. Phys. Lett.*, vol. 65 (16), pp. 2102-2104, October, 1994.
- [9] A. V. Ustinov, M. Cirillo, and B. A. Malomed, *Phys. Rev. B*, vol. 47, pp. 8357, 1993.
- [10] S. Watanabe, H. S. J. van der Zant, S. H. Strogatz, and T. P. Orlando, "Dynamics of circular arrays of Josephson junctions and the discrete sine-Gordon equation," *Physica D*, in press.
- [11] A. Petraglia, N. F. Pedersen, P. L. Christiansen, and A. V. Ustinov, "Comparative dynamics of 2D shorted arrays and stacked Josephson junctions," pre-print.
- [12] T. Strunz and F. J. Elmer, "On the sliding dynamics of the Frenkel-Kontorova Model," *Physics of Sliding Friction*, Kluwer Academic Publishers, The Netherlands, pp. 149-161, 1996.

Discrete Underdamped Vortex Flow Devices

A. E. Duwel, H. S. J. van der Zant, T. P. Orlando
Massachusetts Institute of Technology, Cambridge, MA 02139

Abstract— Vortex flow devices consisting of discrete arrays of underdamped Josephson junctions have been fabricated and measured. These devices and their long, continuous junction counterparts are based on the ability to magnetically control the Eck voltage in an underdamped system. We find that both transistor and oscillator parameters are improved by placing the arrays above a superconducting ground plane and by connecting two arrays in series. We developed models for the device behavior which numerically account for the measured parameters. Our models also suggest that junctions with smaller capacitances will further improve the device parameters.

I. INTRODUCTION

Parallel arrays of Josephson junctions behave, in many ways, like long, continuous junctions. Both structures may be used as superconducting circuit elements, such as transistors, oscillators, phase shifters, and amplifiers. These systems also serve as valuable models for high temperature superconducting devices.

Josephson junctions can be designed to operate in two different regimes. These are distinguished by the value of the McCumber parameter, β_c . Overdamped junctions, where $\beta_c < 1$, have been studied and function well as superconducting transistors. Transistors made from long, overdamped junctions have shown gains of about 10 and transresistances of about 0.2Ω [1], [2]. Parallel arrays of Josephson junctions have been fabricated with gains of about 1.2 and transresistances of 0.43Ω [3].

Although underdamped junctions ($\beta_c > 1$) exhibit more complicated dynamics, they also offer promising device characteristics. Long, underdamped junctions have been designed as transistors and as oscillators. Transresistances of the order of 0.01Ω [4] and available output power levels of about 20 nW at 260 GHz [5] have been achieved. However, the output impedance levels are less than 1Ω . Parallel arrays of underdamped junctions compete with

these devices, operating with transresistances of about 1.8Ω , expected power levels of about 10 nW, and output impedances of the order of 10Ω [6]. In this paper, we discuss the operation of the underdamped array as a vortex flow device and present simple models for its output parameters. We have also measured two variations on the underdamped array, and we show that, in both systems, the device parameters are improved.

II. SAMPLES

Samples were fabricated with a Nb trilayer process.¹ All of the devices which we discuss are on the same chip, and their physical parameters are measured at a temperature of 4.2 K. Each Josephson junction has an area of $8 \mu\text{m}^2$ and a capacitance, C , of 300 fF. We measured the normal-state resistance, R_n , to be about 275Ω . Taking the $I_c R_n$ product to be 1.75 mV at 4.2 K, we find that the critical current, $I_c = 6.4 \mu\text{A}$. This gives a value for the Josephson inductance, $L_J = \Phi_0/2\pi I_c$, of 51 pH. The McCumber parameter; $\beta_c = R_n^2 C / L_J$, is about 445 at 4.2 K, indicating that the junctions are highly underdamped.

Each of the devices on the chip can be subjected to a magnetic field through coupling to a superconducting control wire. The amount of magnetic flux supplied to the device, Φ_{app} , depends on the strength of the mutual inductive coupling, M_{ctrl} , and can be written as

$$\Phi_{\text{app}} = \frac{I_{\text{ctrl}} M_{\text{ctrl}}}{\Phi_0} \quad (1)$$

where I_{ctrl} is the amount of current in the control wire, and we have normalized the applied flux to one flux quantum, Φ_0 .

III. UNDERDAMPED VORTEX FLOW DEVICE

Figure 1 shows a schematic of the vortex flow device, which consists of 54 Josephson junctions, connected in parallel by superconducting Nb wires. A bias current, I_b , is applied uniformly to each junction, and the voltage is measured with superconducting leads at one end of the array. The control current providing a magnetic field runs

¹Hypres, Inc. Elmsford, NY 10523

Manuscript received October 16, 1994.

A. E. Duwel, e-mail duwel@mit.edu.

This work was conducted under the auspices of the Consortium for Superconducting Electronics with the partial support of the Advanced Research Projects Agency (MDA 972-90-C-0021) and National Science Foundation Graduate Research Fellowships.

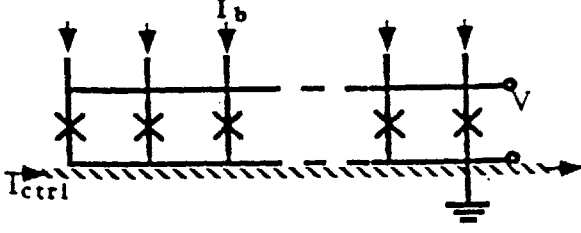


Fig. 1. A schematic drawing of the vortex flow device.

parallel to the edge of the array and is about 500 nm above it.

The magnetic field from I_{ctrl} injects vortices into the array. The bias current causes the vortices to move, thereby producing a voltage across the array, V , proportional to the vortex velocity. For a fixed I_{ctrl} , increasing I_b causes an increase in velocity, until the limiting electromagnetic phase velocity in the array is reached. At this point, increasing I_b further does not move the voltage beyond V_E , the Eck voltage [7]. Thus there is a steep rise in the current, as shown in Fig. 2. For sufficiently high I_b , the voltage jumps to the gap voltage, V_g .

When I_b is held constant and I_{ctrl} is increased, V_E initially increases due to the higher density of injected vortices. However, as the inset shows, V_E is periodic in I_{ctrl} , with period I_{per} , which reflects the fact that the properties of an array are periodic in magnetic field. The lighter line in the inset is the result of a linear analysis for V_E [6] and is given by

$$V_E = \frac{\Phi_0}{\pi\sqrt{L_s C}} \left| \sin\left(\frac{\pi\Phi_{app}}{N-1}\right) \right| \quad (2)$$

where L_s is the self inductance of a single loop (cell) in the array, and $N-1$ is the number of cells in the array. The value of L_s is determined from the diagnostic methods described in reference [8]. For this sample, L_s is 16 pH.

From equations (1) and (2), we see that the array may be used as a current-controlled voltage source. The device is biased at I_b , with input current I_{ctrl} and output voltage V_E . The maximum output voltage is inversely proportional to $\sqrt{L_s C}$ and the transresistance, $r_m = \partial V_E / \partial I_{ctrl}$, increases as $M_{ctrl} / \sqrt{L_s C}$ increases. The transresistance depends on the operating point and can be obtained graphically by taking the slope of the tangent to the $V_E(I_{ctrl})$ curve. For $V_E \approx 0.75V_{E,max}$, we obtain $r_m = 1.75\Omega$. The threshold current, discussed in detail in reference [6], can be modeled simply as: $I_{th} = 3.6I_c\sqrt{L_J/L_s}$. For this device, we have $I_{th} = 0.05$ mA, which matches the theory well. The output resistance, r_0 , is given by the slope of $V(I_b)$ as the voltage approaches V_E . This parameter affects the oper-

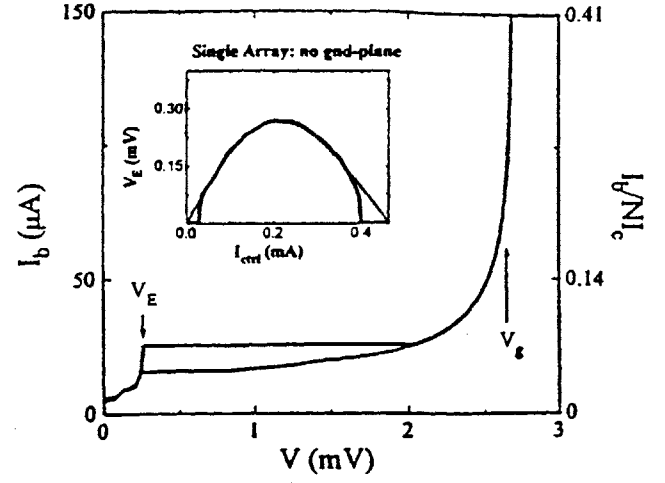


Fig. 2. Current vs. voltage curves of Josephson junction array at 4.2K. V_E is the Eck voltage and V_g is the gap voltage. The inset figure compares the transistor characteristic to theory.

ating range of the transistor and should be as small as possible.

This underdamped array may also be used as a current-controlled oscillator. The control current determines V_E , which, according to the Josephson relation, corresponds to a frequency, $\nu = V_E / \Phi_0$. For our device, V_E ranges from 0 to 0.27 mV, giving a bandwidth of 130 GHz. Based on the linewidth of a single junction oscillator [6], [9], we expect the array linewidth to be proportional to r_0 : The output impedance can be estimated by modeling the junction array as a transmission line, giving $Z_0 = \sqrt{L_s/C} \approx 10\Omega$. The maximum attainable power, $P = V_{E,max} I_{E,max}$, is about 8 nW. A summary of these device parameters is given in Table I.

Our simple models suggest that we can improve the output voltage and maximum power by decreasing L_s and C . We also expect higher voltages and possibly smaller linewidths from two arrays connected in series. In the following sections, we discuss configurations which address both of these issues.

TABLE I
DEVICE PARAMETERS (T=4.2K)

Parameter	Single Array no gnd-plane	Single Array on gnd-plane	Coupled Arrays on gnd-plane
$V_{E,max}$ (mV)	0.27	0.5	0.91
r_m (Ω)	1.75	0.53	1.5
r_0 (Ω)	0.62	<0.1	3.3
I_{th} (mA)	0.05	0.09	0.1
I_{per} (mA)	0.45	2.0	2.0
B (GHz)	130	240	240
P (nW)	8	35	29

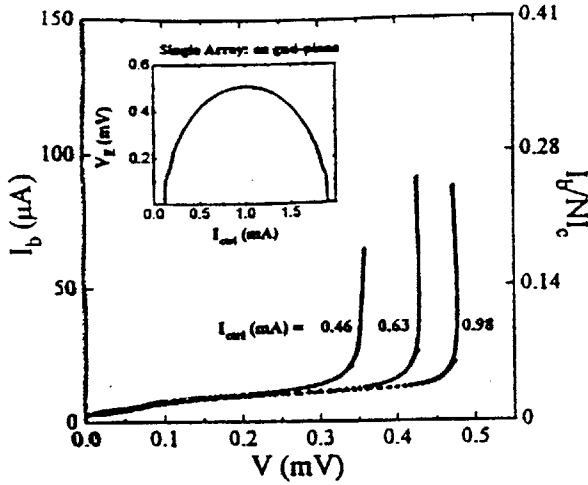


Fig. 3. Current vs. voltage curves of Josephson junction array above a superconducting ground plane. Measurements are at 4.2 K and various I_{ctrl} . The inset figure shows the I - V for the device when biased as a transistor.

IV. DEVICES ON GROUND PLANE

In order to lower L_s , we placed the same array of Josephson junctions about 200 nm above a superconducting ground plane. Our diagnostic measurements indicate that the effective inductance in the presence of a ground plane, L_{eff} , is lower than L_s , by a factor of about four.

This change in L_s has a clear effect on the transistor characteristics of the device. Equation (1) predicts that V_E will double for $L_{eff} = L_s/4$. This is almost exactly what we observe, as shown in the inset of Fig. 3. As expected, I_{th} is also approximately twice as large. The period of V_E has increased by a factor of about four, which corresponds to a decreased effective coupling, $M_{eff} = M_{ctrl}/4$. The transresistance, which is proportional to $M_{ctrl}/\sqrt{L_s}$, is half as large as before. We can quantitatively account for the smaller mutual and self-inductances by modeling the control line as an infinitely long wire, each cell of the array as a square loop, and the ground plane as an infinite, perfectly conducting sheet.

The higher output voltage levels also improve the performance of the oscillator. The bandwidth is twice as large, and the maximum power has more than doubled. This is because the current levels are also much higher, as seen in the $V(I_b)$ characteristics of Fig. 3. Here, the curves for several different control current values are presented. (Note that data points after the switch to the gap voltage are not included). Near V_E , the slopes become quite steep, and the decreased r_0 gives narrower linewidths.

The presence of the superconducting ground plane improves all of the device parameters except the transresistance. We have successfully modeled these trends in our data, and we can use this knowledge to further optimize the device performance.

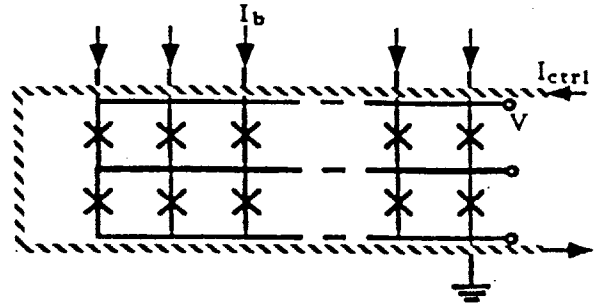


Fig. 4. Schematic of two arrays connected in series.

V. COUPLED DEVICE ON GROUND PLANE

Additional output voltage is obtained by connecting two arrays of 54 Josephson junctions in series. The control wire is now placed along both edges of the device and is again 500 nm above it. This structure also lies above a superconducting ground plane and is illustrated in Fig. 4.

At 4.2 K, the $V(I_b)$ curves for this device look similar to the single array on the ground plane. However, there is a much more gradual rise in the current near V_E , resulting in higher output resistances. The voltage across the coupled arrays is twice that of the single array, which is the expected result of placing two equal voltages in series.

Differences in the transfer characteristics of all three devices can be seen clearly in Fig. 5, where their transistor curves are presented. The currents are normalized to I_{per} , the values of which are given in Table I. The period of the coupled arrays is the same as that of the single array on the ground-plane. Since the output voltages are larger, r_m increases.

Despite the higher voltage levels, the frequency of the Josephson oscillations does not change, and the bandwidth is the same. The power decreases slightly due to a decrease in I_E . The large rise in the output resistance causes the linewidth to increase. This change in r_0 implies that these arrays are dynamically more complex than our previous structures.

Inductively coupled arrays are the discrete version of long, continuous stacked Josephson junctions. In the stacked junctions, two Eck voltages have been predicted and observed [10]–[12], corresponding to two limiting electromagnetic phase velocities. A simple analysis of the discrete system predicts

$$V_{E1,E2} = \frac{\Phi_0}{\pi\sqrt{L_s C}} |\sin(\frac{\pi\Phi_{app}}{N-1})| [1 \pm M] \quad (3)$$

where M is the strength of the coupling between adjacent cells of the two arrays, and we have neglected other coupling effects for simplicity. The result is that there are now two modes of oscillation. In the antisymmetric mode, the corresponding junctions in each row oscillate

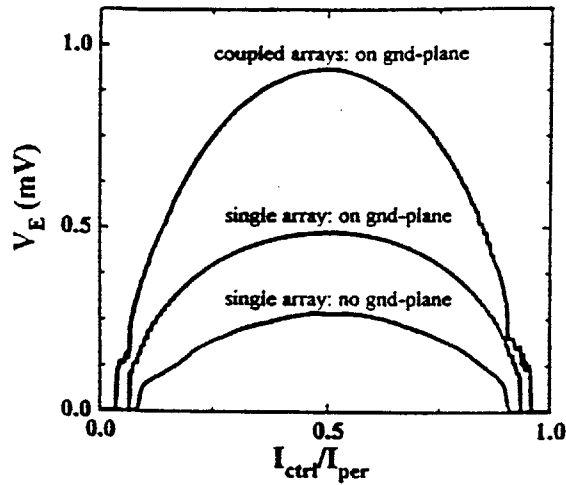


Fig. 5. Transistor characteristics of each device at 4.2 K. The currents are scaled to the current interval of one period, I_{per} .

with equal amplitude but out of phase, and the characteristic frequency (or voltage, V_{E1}) is higher than in the single array. In the symmetric mode, the rows oscillate in phase, and the characteristic frequency is lower.

Two voltages are visible in our $V(I_b)$ curves at temperatures above about 6 K, but do not appear at 4.2 K. Fitting equation (3) to data taken at 7.2 K required that $M \approx 0.5L_p$. Based on measurements of the nearest-neighbor coupling in a single array [8], this value is higher than we expected. By including other nearest-neighbor inductances, the value of M used in the fits is lowered. However, the match between the theory and measurements is not as good as in our previous devices, and more work is needed to fully understand the dynamics of this system.

VI. CONCLUSION

We have measured the device characteristics of arrays of underdamped Josephson junctions connected in parallel. We demonstrated that it is possible to model the performance of these devices and thus optimize their parameters for specific applications. This was achieved by manipulating the inductances of single arrays. We used a superconducting ground plane to lower the inductance values, which improved all of the parameters except the transresistance. It is clear from our models that the devices can also be improved by using smaller junctions or junctions with lower capacitances. In addition to optimizing the device parameters, a study of the noise performance of these devices must still be conducted.

We attempted to further refine the device parameters by connecting two arrays in series. This configuration achieved higher voltage levels and transresistances, but the output resistance was degraded. The power and bandwidth were relatively unaffected. These inductively coupled arrays may be promising for some applications, but the dynamics must be more carefully studied before this

potential can be realized.

ACKNOWLEDGMENT

We thank Enrique Trias and Joel Phillips for valuable discussions.

REFERENCES

- [1] D. P. McGinnis, J. B. Beyer, and J. E. Nordman, "A Modified Superconducting Current Injection Transistor and Distributed Amplifier Design," *IEEE Trans. Mag.*, vol. 25, pp. 1262-1265, March 1989.
- [2] B. J. Van Zeghbroeck, "Superconducting Current Injection Transistor", *Appl. Phys. Lett.*, vol. 42 (8), pp. 736-738, April 1983.
- [3] D. Berman, H. S. J. van der Zant, and T. P. Orlando, "Discrete Superconducting Vortex Flow Transistors," *IEEE Trans. Appl. Superconductivity*, vol. 4, pp. 161-168, September 1994.
- [4] D. P. McGinnis, J. E. Nordman, and J. B. Beyer, "Optimization of Circuit Parameters for the Vortex Flow Transistor," *IEEE Trans. Mag.*, vol. 23, pp. 699-702, March, 1987.
- [5] Y. M. Zhang, D. Winkler, and T. Claeson, "Detection of MM and SUBMM Wave Radiation from Soliton and Flux-Flow Modes in a Long Josephson Junction," *IEEE Trans. Appl. Superconductivity*, vol. 3 (1), pp. 2520-2523, March, 1993.
- [6] H. S. J. van der Zant and T. P. Orlando, "The Eck Peak in Underdamped Discrete Superconducting Vortex Flow Devices," *J. Appl. Phys.*, vol. 76 (11), December, 1994.
- [7] R. E. Eck, D. J. Scalapino, and B. N. Taylor, "Self-Detection of the ac Josephson Current," *Phys. Rev. Lett.*, vol. 13 (1), pp. 15-18, July, 1964.
- [8] H. S. J. van der Zant, R. A. M. Receveur, and T. P. Orlando, "One-Dimensional Parallel Josephson Junction Arrays as a Tool for Diagnostics," *Appl. Phys. Lett.*, October, 1994.
- [9] J. B. Hansen, "Noise in Superconducting Josephson Junctions," in *Non-Linear Superconductive Electronics and Josephson Devices*, G. Costible, S. Pagano, N. F. Pedersen, and M. Russo, Eds. New York: Plenum Press, 1991, pp. 161-180.
- [10] S. Sakai, A. V. Ustinov, H. Kohlstedt, A. Petraglia, and N. F. Pedersen, "Theory and Experiment on Electromagnetic Wave Propagation Velocities in Stacked Superconducting Tunnel Structures," to be published.
- [11] A. V. Ustinov, H. Kohlstedt, and C. Heiden, "Magnetic Flux Dynamics in Stacked Josephson Junctions," to be published.
- [12] N. Grønbech-Jensen, M. R. Samuelsen, P. S. Lomdahl, and J. A. Blackburn, "Bunched Soliton States in Weakly Coupled Sine-Gordon Systems," *Phys. Rev. B*, vol. 42 (7), pp. 3976-3980, September, 1990.

Bibliography

- [1] N. Flytzanis, S. Crowley and V. Celli, Phys. Rev. Lett. 39, 891 (1977).
- [2] A. R. Bishop and T. F. Lewis, J. Phys. C 12, 3811 (1979).
- [3] M. Levi, in *Analysis, Et Cetera*, editors P. Rabinowitz and E. Zehnder (Academic Press, New York, 1990), p.471.
- [4] A.C. Scott, Am. J. Phys, **37** (52) 1969.
- [5] H. Funakubo, Y. Kashimori, T. Kambara, IEEE Internat. Conf. Neural Networks, **1** 318 (1997).
- [6] R. Traub, J. Jefferys, in *Neural Modeling and Neural Networks*, editor F. Ventriglia (Pergamon Press, New York, 1994), p. 111.
- [7] J. Tuovinen, N.R. Erickson, IEEE Trans. Micr. Th. Tech, **43** (4) 962 (1995).
- [8] H.S.J. van der Zant, T.P. Orlando, S. Watanabe, and S.H. Strogatz, Phys. Rev. Lett. 74, 174 (1995).
- [9] A.V. Ustinov, M. Cirillo, and B.A. Malomed, Phys. Rev. B 47, 8357 (1993).
- [10] H. S. J. van der Zant and T. P. Orlando, J. Appl. Phys. 76 (11), 7606 (1994).
- [11] S. Watanabe, H.S.J. van der Zant, S.H. Strogatz, T.P. Orlando, Physica D 97, 429 (1996).
- [12] P. Barbara, A.V. Ustinov, G. Costabile, Phys. Lett. A 191, 443 (1994).
- [13] E. Goldobin, A. Wallraff, N. Thyssen, A.V. Ustinov, Phys. Rev. B 57, 130 (1998).

- [14] A. Petraglia, A.V. Ustinov, N.F. Pedersen, S. Sakai, *J. Appl. Phys.* 77, 1171 (1995).
- [15] A. Wallraff, E. Goldobin, A.V. Ustinov, *J. Appl. Phys.* 80, 6523 (1996).
- [16] R.D. Parmentier, P. Barbara, G. Costabile, A. D'Anna, B.A. Malomed, and C. Soriano, *Phys. Rev. B* **55** 15 165 (1997).
- [17] R.A. York, *Critical Review*, **CR54** 63 (1995).
- [18] S.P. Benz, C.J. Burroughs, *Appl. Phys. Lett.* 58 (19), 2162 (1991).
- [19] P. Booi, S.P. Benz, *Appl. Phys. Lett.* 64 (16), 21163 (1994).
- [20] Samples were fabricated by HYPRES, Inc. in Elmsford, NY.
- [21] T.P. Orlando, K.A. Delin, *Foundations of Applied Superconductivity*. (Addison-Wesley, New York, 1991).
- [22] M. Remoissnet, *Waves Called Solitons: Concepts and Experiments*. (Springer, Berlin, 1994).
- [23] R. Bock, *Influence of Induced Magnetic Fields on the Static and Dynamic Properties of Multijunction Josephson Interferometers*, Massachusetts Institute of Technology, M. S. thesis, 1993.
- [24] KIC Layout Editor, public software distributed by S.R. Whiteley, available through ftp at swordfish.eecs.berkeley.edu.
- [25] R.E. Eck, D.J. Scalapino, and B.N. Taylor, *Phys. Rev. Lett.* 13 (1), 15 (1964).
- [26] S. Watanabe, S.H. Strogatz, H.S.J. van der Zant, and T.P. Orlando, *Phys. Rev. Lett.* 74, 379 (1995).
- [27] A. Duwel, S. Watanabe, E. Trías, T.P. Orlando, H.S.J. van der Zant, S.H. Strogatz, *J. Appl. Phys.* **82** (9) 4661 (1997).

- [28] A.E. Duwel, E. Trías, T.P. Orlando, H.S.J. van der Zant, S. Watanabe, and S.H. Strogatz, *J. Appl. Phys.* **79**, 7864 (1996).
- [29] H. S. J. van der Zant, D. Berman, and T. P. Orlando, *Phys. Rev. B* **49** (18), 12945 (1994).
- [30] E. Trías, *Inductance Effects in Two-Dimensional Arrays of Josephson Junctions*, Massachusetts Institute of Technology, M. S. thesis, 1995.
- [31] S.H. Strogatz, *Nonlinear Dynamics and Chaos*. (Addison-Wesley, New York, 1994).
- [32] T. Strunz and F.J. Elmer, in *Physics of Sliding Friction*, edited by B.N. J. Persson and E. Tosatti (Kluwer, Dordrecht, 1996), pp. 149-161.
- [33] S. Watanabe and J.W. Swift, *Journal of Nonlinear Science*, **7**, 503-536 (1997).
- [34] S. Watanabe, *Nonlinear Dynamics of one-dimensional Josephson junction arrays*, Massachusetts Institute of Technology, Ph. D. thesis, 1995.
- [35] A.H. Nayfeh and D.T. Mook, *Nonlinear Oscillators* (Wiley-Interscience, New York, 1979).
- [36] P. Caputo, A.V. Ustinov, N. Iosad, and H. Kohlstedt, *J. Low Temp. Phys.* **106** 353 (1997).
- [37] A. E. Duwel, T. P. Orlando, S. Watanabe, H. S. J. van der Zant, *IEEE Trans. Appl. Supercond*, **7** 2897 (1997).
- [38] S. Sakai, P. Bodin, N.F. Pedersen, *J. Appl. Phys.* **73** 2411 (1993).
- [39] K. Wiesenfeld, E. Knogloch, R.F. Miracky, and J. Clarke, *Phys. Rev. A* **29**, 2102 (1984).
- [40] K. Wiesenfeld, S. Benz, and P. Booi, *J. Appl. Phys.* **76**, 3835 (1994).
- [41] G. Filatrella and K. Wiesenfeld, *J. Appl. Phys.* **78**, 1878 (1995).

- [42] I.O. Kulik, Sov. Phys. JTEP **24**, 1307 (1967).
- [43] K. Enpuku, K. Yoshida, and F. Irie, J. Appl. Phys. **52**, 344 (1981).
- [44] A.E. Duwel, C.P. Heij, J.C. Weisenfeld, M.K.S. Yeung, E. Trías, S.J.K. Várdu, H.S.J. van der Zant, S.H. Strogatz, T.P. Orlando, Phys. Rev. B, **58** (13) 8749 (1998).
- [45] S. Watanabe, S.H. Strogatz, Physica D **74** 197 (1994).
- [46] A. Kawakami, Y. Uzawa, Z. Wang, IEEE Trans. Appl. Supercond, **7** (1997).
- [47] M. Barahona, E. Trías, T.P. Orlando, A.E. Duwel, H.S.J. van der Zant, S. Watanabe, S. Strogatz, Phys. Rev. B **55** (18) 989 (1997).
- [48] S. Han, B. Bi, W. Zhang, J.E. Lukens, Appl. Phys. Lett, **64** 1424 (1994).
- [49] S.P. Yukon, N.C.H. Lin, in *Macroscopic Quantum Phenomena and Coherence in Superconducting Networks*, editors C. Giovannella and M. Tinkham (World Scientific, Singapore, 1995) p. 351.
- [50] S.P. Yukon, N.C.H. Lin, IEEE Trans. Appl. Supercond, **5** 2959 (1995).
- [51] E. Trías, T.P. Orlando, A.E. Duwel, IEEE Trans. Appl. Supercond, to be published (1998).
- [52] Vernet, G., R. Adde, Appl. Phys. Lett, **19** (6) 195 (1971).
- [53] Bi, B., J. Lukens, K. Wan, IEEE Trans. Appl. Sup, **3** (1) 2303 (1993).
- [54] Kawakami, A., Z. Wang, IEICE Trans. Electron, **E79 C** (9) 1242 (1996).
- [55] K.-L. Wan, A.K. Jain, and J.E. Lukens, Appl. Phys. Lett, **54** 1805 (1989).
- [56] Kapluneko, V.K., J. Myngid, N.F. Pedersen, A.V. Ustinov, J. Appl. Phys, **73** (4) 2019 (1993).
- [57] Ustinov, A.V., H. Kohlstedt, P. Henne, Phys. Rev. Lett, **77** (17) 3617 (1996).

- [58] Zhang, Y.M., D. Winkler, and T. Claeson, Appl. Phys. Lett, **62** (24), 3195 (1993).
- [59] Finnegan, T.F., S. Wahlsten, Appl. Phys. Lett, **21** (11) 541 (1972).
- [60] Kiryu, S., W. Zhang, S. Han, S. Deus, J.E. Lukens, IEEE Trans. Appl. Sup. , **7** (2) 3107 (1997).
- [61] Booi, P., S.P. Benz, App. Phys. Lett. **68** (26), 3799 (1996).
- [62] Kohjiro, S., S. Kiryu, A. Shoji, T. Kikuchi, S. Kodaira, J. Inatani, Appl. Sup. , Edinburgh, 3-6 July, 1995, p. 1665.
- [63] Holst, T., B. Hansen, N. Gronbech-Jensen, J.A. Blackburn, Phys. Rev. B, **42** (1) 127 (1990).
- [64] Shitov, S.V., A.V. Ustinov, N. Iosad, and H. Kohlstedt, J. Appl. Phys, **80** (12) 7134 (1996).
- [65] Keck, M., T. Doderer, R. Mueller, R. Pfeifer, A. Laub, R.P. Huebener, T. Traeu-
ble, R. Dolata, T. Weimann, J. Niemeyer, IEEE Trans. Appl. Sup. , **7** (2) 3407 (1997).
- [66] Cawthorne, A.B., P. Barbara, C.J. Lobb, IEEE Trans. Appl. Sup, **2** (2) 3403 (1997).
- [67] P. Caputo, A.E. Duwel, T.P. Orlando, A.V. Ustinov, N.C.H. Lin, and S.P. Yukon, Proc. of ISEC Berlin, 1997.
- [68] S. Shapirio, Phys. Rev. Lett, **11** 80 (1963).
- [69] S.P. Benz, C.J. Burroughs, Supercon. Sci. Tech, **4** 561 (1991).
- [70] V. Ambegaokar and A. Baratoff, Phys. Rev. Lett. **10**, 486 (1963).
- [71] A. Petraglia and N. F. Pedersen, P. L. Christiansen, and A. V. Ustinov, Phys. Rev. B, **55** (13) 8490 (1997).

- [72] K. Yoshida, K. Hamasaki, and F. Irie, *Jap. J. Appl. Phys.* 18 (2), 373 (1979).
- [73] N.F. Pedersen, A.V. Ustinov, *Sup. Sci. Tech.* 8, 389 (1995).
- [74] G. Carapella, G. Costabile, G. Filatrella, M.H. Manscher, J. Mygind, N.A. Nordahn, N.F. Pedersen, A. Petraglia, *IEEE Trans. on Appl. Sup.* 7 (2), 2411 (1997).
- [75] A.V. Ustinov, H. Kohlstedt, C. Heiden, *Appl. Phys. Lett.* 65 (11), 1457 (1994).
- [76] S. Sakai, A.V. Ustinov, H. Kohlstedt, A. Petraglia, N.F. Pedersen, *Phys. Rev. B* 50, 12905 (1994).
- [77] N. Grønbech-Jensen, D. Cai, M.R. Samuelsen, *Phys. Rev. B* 48 (21), 16160 (1993).
- [78] R. Monaco, A. Polcari, L. Capogna, *J. Appl. Phys.* 78 (5), 3278 (1995).
- [79] A.E. Duwel, *Underdamped Vortex Flow Devices* Massachusetts Institute of Technology M. S. thesis, 1995.
- [80] B. Bhat, S.K. Koul, *Analysis, Design, and Applications of Fin Lines*, (Artech House, Norewood, MA, 1987).
- [81] K.C. Gupta, R. Garg, I.J. Bahl, *Microstrip lines and Slotlines*, (Artech House, 1979).
- [82] J. Weisenfeld, S.H. Strogatz, private communication.

2976-49